

*Tesis Doctoral en el programa de Doctorado*

AUTOMÁTICA Y ELECTRÓNICA

**PREDICTIVE DIRECT CONTROL TECHNIQUES OF THE  
DOUBLY FED INDUCTION MACHINE FOR WIND ENERGY  
GENERATION APPLICATIONS**

*Doctorando:*  
GONZALO ABAD BIAIN

*Director:*  
DR. MIGUEL ÁNGEL RODRÍGUEZ VIDAL



**Goi Eskola Politeknikoa / Escuela Politécnica Superior / Faculty of Engineering  
03 de julio de 2008**

## Abstract

This research project deals with the control of the doubly fed induction machine operating as a high power wind turbine generator. In the recent years, the predictive direct control techniques are emerging as a promising control solution for high power AC induction machine drives. For that reason, this project adopts the predictive direct control theory, to develop several new and competitive control methods for the doubly fed induction machine.

Firstly, this work begins with a presentation of the potential benefits of the proposed predictive direct control strategies, according to the state of the art in the field of high power induction machine drives. For prediction purposes, the model of the doubly fed induction machine is presented too.

Secondly, a new predictive direct torque control strategy is developed for the doubly fed induction machine based on the two level voltage source converter. The main feature of this control technique is that a particular attention is paid to reduce the torque and rotor flux ripples, operating at considerably low and constant switching frequency. In addition, the fast dynamic response capacity of “classic” direct control techniques is kept as well as the good tracking behavior.

After that, a new predictive direct power control strategy is developed for the doubly fed induction machine based on the two voltage source converter. It is based on the same control principles as the previously developed predictive direct torque control, but it further improves the ripple behavior of the machine at steady state operation conditions.

Next, a new predictive direct torque control strategy and a new predictive direct power control strategy are developed for the doubly fed induction machine, based on the three level NPC voltage source converter. In this case again, these control strategies presents the same benefits and features as the previously developed control strategies, added to the ability to operate with larger voltage levels and better quality waveforms than with the classical two level voltage source converter.

All the control strategies are successfully validated in a 15kW experimental platform, which integrates the doubly fed induction machine, the two level and the three level NPC converters and the digital controller based on a DSP/FPGA board.

Then, the distorted grid voltage situation is studied. Based on the control techniques developed during the thesis, some simple modifications will be proposed to address the problems provoked by grid disturbances such as, voltage unbalance and the presence of harmonic distortion.

Finally, the conclusions and the future work of the thesis are served.

## Acknowledgements

First of all, I would like to specially thank to my thesis supervisor Miguel Rodríguez, since without his support, this thesis will not be achieved. It has been a pleasure to work with you. On the other hand, I wish also to express my gratitude to all my colleagues of Garaia, during these years: Mikel Sanzberro, Jon Andoni Barrena, Jose María Canales, Josu Galarza, Igor Baraia, Gaizka Almundoz, Xabi Agirre, Itoitz Errasti, Olatz Gerrikagoitia, Haritz Milikua, Iker González, Izaskun Sarasola, Egoitz Arruti, Sergio Aurtenetxea, Ana Escalada, Gaizka Ugalde, Javier Poza, José Ramón Torrealday, Antonio Barbero.

Of course, I would like also to thank to my colleagues of CIDAE, Silverio Álvarez, Iñigo Garin, Ion Etxeberria, Raul Reyero, Maider Santos, Agurtzane Agirre, Amaia Lopez de Heredia, Haizea Gaztañaga, Alex Munduate, Elsa Díaz.

I wish to express my sincere gratitude to Professor M.P Kazmierkowski, for giving me the opportunity to stay in Warsaw University of Technology and for his attention. I would also like to thank to Grzegorz Iwanski, Mariusz Malinowski, Marek Jasinski, Patryk Antoniewicz, Paweł Wójcik, Wojciech Kołomyjski, Sebastian Styński, Dhurian, Krzysztof Rafal and Małgorzata Bobrowska for their support.

I appreciate the contributions made by the final year project of Aimar Pérez, Aaron Meaza, Iñigo Polo, Igor Bernas, Koldo Manero and Iban Ayarzagüena, to the experimental rigs used in this thesis.

To my friends from the gyms of Bergara and Mondragon, especially to Santi Galán, to all my very good friends from Bergara, and certainly, thank you very much to my family and my parents prominently, real encouragement, support and sustenance during these years.

## Agradecimientos

En primer lugar, quisiera hacer una mención especial a mi director de tesis Miguel Rodríguez, que sin él, ésta tesis no podría haber sido llevada a cabo. Es sin duda, todo un privilegio el haber podido trabajar contigo. Por otro lado, querría agradecer también a todos mis compañeros de Garaia durante éstos años de tesis: Mikel Sanzberro, Jon Andoni Barrena, Jose María Canales, Josu Galarza, Igor Baraia, Gaizka Almandoz, Xabi Agirre, Itoitz Errasti, Olatz Gerrikagoitia, Haritz Milikua, Iker González, Izaskun Sarasola, Egoitz Arruti, Sergio Aurtenetxea, Ana Escalada, Gaizka Ugalde, Javier Poza, José Ramón Torrealday, Antonio Barbero.

Por supuesto también a mis compañeros de CIDAE, Silverio Álvarez, Iñigo Garin, Ion Etxeberria, Raul Reyero, Maider Santos, Agurtzane Agirre, Amaia Lopez de Heredia, Haizea Gaztañaga, Alex Munduate, Elsa Díaz.

Agradecer también al profesor M.P Kazmierkowski por brindarme la oportunidad de hacer la estancia en Warsaw University of Technology y por la atención prestada tanto por él como por Grzegorz Iwanski, Mariusz Malinowski, Marek Jasinski, Patryk Antoniewicz, Paweł Wójcik, Wojciech Kołomyjski, Sebastian Styński, Dhurian, Krzysztof Rafal, Małgorzata Bobrowska.

A Aimar Pérez, Aaron Meaza, Iñigo Polo, Igor Bernas, Koldo Manero e Iban Ayarzagüena por contribuir mediante vuestro proyecto fin de carrera, a la realización de las plataformas experimentales utilizadas en ésta tesis.

A mis compañeros de los gimnasios de Mondragón y Bergara, especialmente a Santi Galán, a todos mis muy buenos amigos de Bergara y sin duda, muchas gracias a mi familia y de manera destacada a mis padres, verdadero aliento, apoyo y sustento durante éstos años.



# CONTENTS

Abstract .....	2
Acknowledgements .....	3
Agradecimientos .....	4
1 Introduction .....	11
1.1 Background .....	11
1.2 Framework of the Thesis .....	12
1.2.1 Variable Speed Wind Energy Systems .....	12
1.2.2 DFIM based Wind Energy Generation .....	15
1.2.3 Wind Turbine Control Requirements .....	17
1.2.4 DFIM Control, State of the Art .....	20
1.2.5 Potential Benefits of Predictive Direct Control Techniques .....	22
1.3 Thesis Objectives .....	23
1.4 Outline of the Thesis .....	23
2 High Power Wind Energy Generation .....	27
2.1 Introduction .....	28
2.2 Justification of High Power Medium Voltage Wind Turbine .....	28
2.2.1 Medium Voltage Drives for Industry Applications .....	28
2.2.2 Wind Turbine Manufacturers .....	32
2.2.3 Tendency of Wind Turbine Development .....	33
2.2.4 Conclusions of this section .....	35
2.3 High Power Medium Voltage Wind Turbine. Scenario Definition .....	35
2.4 Conclusions of the Chapter .....	37
3 Modeling of the Doubly Fed Induction Machine (DFIM) .....	40
3.1 Introduction .....	40
3.2 Dynamic Modeling of the DFIM .....	41
3.2.1 Space Vector Notation of the DFIM .....	42
3.2.2 $\alpha\beta$ Model .....	44
3.2.3 dq Model .....	47
3.2.4 State-Space Representation of $\alpha\beta$ Model .....	49
3.3 Dynamic Modeling of the DFIM Considering the Iron Loss .....	50
3.3.1 $\alpha\beta$ Model .....	50

---

3.3.2	dq Model.....	54
3.3.3	State-Space Representation of $\alpha\beta$ Model.....	57
3.4	DFIM at Steady State.....	59
3.4.1	Mode 1. Motoring at Hypersynchronous Speed.....	61
3.4.2	Mode 2. Generating at Hypersynchronous Speed.....	62
3.4.3	Mode 3. Generating at Subsynchronous Speed.....	63
3.4.4	Mode 4. Motoring at Subsynchronous Speed.....	64
3.5	Conclusions of the Chapter.....	64
4	Two Level Converter Based Direct Torque Control of the Doubly Fed Induction Machine .....	68
4.1	Introduction.....	69
4.2	Study of Voltage Vectors Effect on the Doubly Fed Induction Machine.....	70
4.3	“Classic” Direct Torque Control (DTC) of the Doubly Fed Induction Machine (DFIM) .....	74
4.3.1	Control Block Diagram.....	74
4.3.2	Vector Selection Strategy.....	75
4.4	Predictive DTC Strategy with Reduced Torque Ripple and Constant Switching Frequency.....	78
4.4.1	Control Block Diagram.....	78
4.4.2	First Vector Selection Strategy.....	78
4.4.3	Torque Ripple Minimization Criteria at Constant Switching Frequency.....	81
4.4.4	Further Improvements Oriented to Low Switching Frequency.....	82
4.5	Predictive DTC Strategy with Reduced Torque and Flux Ripples and Constant Switching Frequency.....	83
4.5.1	Control Block Diagram .....	83
4.5.2	First vector Selection Strategy.....	84
4.5.3	Second and Third Vector Selection Strategy at Constant Switching Frequency .....	85
4.5.4	Torque and Flux Ripple Reduction Criteria at Constant Switching Frequency .....	87
4.5.5	Switching Power Losses Reduction.....	89
4.6	Simulation results.....	92
4.6.1	Overview of the Simulation Experiments.....	92
4.6.2	Transient and Steady-State Behavior for DTC Control Strategy.....	93
4.6.3	Transient and Steady-State Behavior. Predictive DTC with Reduced Torque Ripple .....	97

4.6.4	Transient and Steady-State Behavior. Predictive DTC with Reduced Torque and Flux Ripples.....	102
4.6.5	Tracking behavior. Predictive DTC with Reduced Torque and Flux Ripples.....	108
4.7	Experimental Results.....	111
4.7.1	Overview of the Experimental Results.....	111
4.7.2	Experimental Rig.....	111
4.7.3	Steady state Operation Conditions.....	112
4.7.4	Transient Response.....	114
4.7.5	Tracking Behavior.....	116
4.7.6	Performance near Synchronism.....	118
4.8	Conclusions of the Chapter.....	120
5	Two Level Converter Based Direct Power Control of the Doubly Fed Induction Machine.....	123
5.1	Introduction.....	123
5.2	Conceptual Analysis of the Direct Power Control Technique.....	124
5.2.1	Stator Active and Reactive Power Dependence on the Fluxes.....	124
5.2.2	Study of the Voltage Effect on the Fluxes.....	125
5.2.3	Geometrical Study of the Rotor Voltage Vectors Effect on the Stator Active and Reactive Power.....	126
5.2.4	Analytical Study of the Rotor Voltage Vectors Effect on the Stator Active and Reactive Power.....	128
5.3	Predictive DPC Strategy with Reduced Power Ripple at Low Constant Switching Frequency.....	130
5.3.1	Control Block Diagram.....	130
5.3.2	First Vector Selection Strategy.....	131
5.3.3	Second and Third Vector Selection Strategy at Constant Switching Frequency.....	132
5.3.4	Power Ripple Reduction Criteria at Constant Switching Frequency.....	134
5.4	Experimental Results.....	135
5.4.1	Steady State Operation Conditions at 250Hz Switching Frequency.....	136
5.4.2	Comparison of the Steady State Behavior between Different Control Strategies.....	137
5.4.3	Comparison of the Transient Response Behavior Between the Vector Control and the Predictive DPC.....	140
5.5	Conclusions of the Chapter.....	142

---

6 Three Level NPC Converter Based Direct Power Control and Direct Torque Control of the Doubly Fed Induction Machine.....	146
6.1 Introduction.....	147
6.2 Predictive Direct Power Control Strategy (DPC) at Low Constant Switching Frequency .....	147
6.2.1 Model of the Doubly Fed Induction Machine and the Rotor Side Filter.....	148
6.2.2 Control Block Diagram.....	149
6.2.3 Sector and Region Calculation.....	150
6.2.4 First Vector Selection Strategy.....	152
6.2.5 Second and Third Vector Selection Strategy at Constant Switching Frequency .....	155
6.2.6 Derivative Expressions Calculation.....	157
6.2.7 Power Error Reduction Criteria at Constant Switching Frequency.....	159
6.2.8 Balancing of DC Bus Capacitors Voltages.....	160
6.2.9 Vector Sequence Definition. Reduction of the Commutations.....	161
6.2.10 Real Vector Definition.....	162
6.3 Experimental Results of Predictive DPC Strategy.....	163
6.3.1 Steady State Operation Conditions at 0.5kHz Constant Switching Frequency with and without Inductive Rotor Filter.....	164
6.3.2 Transient Response Capacity at 0.5kHz Constant Switching Frequency with Inductive Rotor Filter.....	165
6.3.3 Tracking behavior at 0.5kHz Constant Switching Frequency with Inductive Rotor Filter.....	166
6.3.4 Variable speed performance at 0.5kHz Constant Switching Frequency with Inductive Rotor Filter.....	167
6.3.5 Performance near the Synchronous Speed at 0.5kHz Constant Switching Frequency with Inductive Rotor Filter.....	169
6.4 Predictive Direct Torque Control Strategy (DTC) at Low Constant Switching Frequency .....	171
6.4.1 Control Block Diagram.....	171
6.4.2 First Vector Selection Strategy.....	172
6.4.3 Derivative Expressions Calculation.....	173
6.4.4 Power Error Reduction Criteria at Constant Switching Frequency.....	174
6.5 Experimental Results of Predictive DTC Strategy.....	175
6.5.1 Steady State Operation Conditions at 1kHz Constant Switching Frequency without Inductive Rotor Filter.....	175
6.6 Conclusions of the Chapter.....	178

7	Control of Doubly Fed Induction Machine based Wind Turbine under Distorted Grid Voltage Operation Conditions.....	182
7.1	Introduction.....	182
7.2	Wind Power Energy Generation System under Unbalanced Voltage Grid.....	184
7.2.1	Model of the Unbalanced Grid.....	185
7.3	Model of the Doubly Fed Induction Machine under Unbalanced Voltage Grid Conditions.....	187
7.4	Control of the Doubly Fed Induction Machine under Unbalanced Voltage Grid Conditions.....	191
7.4.1	Direct Power Control (DPC).....	191
7.4.2	Stator Current Negative Sequence Cancellation Strategy.....	193
7.4.3	Torque Oscillations Cancellation Strategy.....	195
7.5	Control of the Grid Side Converter under Unbalanced Voltage Grid Conditions.....	197
7.5.1	Direct Power Control (DPC) of the Grid Side Converter.....	198
7.5.2	Power References Generation Strategy. Negative Sequence Cancellation.....	199
7.6	Contribution to Balance the Grid Voltage Unbalance.....	201
7.7	Simulation Results.....	203
7.7.1	Unbalanced Voltage Situation.....	203
7.7.2	Unbalanced Voltage Situation under Presence of Harmonics .....	208
7.8	Conclusions of the Chapter.....	211
8	Conclusions and Future Research.....	215
8.1	Contributions.....	215
8.2	Conclusions.....	216
8.3	Future Research.....	217
8.4	Publications.....	218
	References.....	219

# Chapter 1

## 1 Introduction

### 1.1 Background

The integration of renewable energy, particularly wind energy, in the electrical grid, accounts for an increasing proportion of the entire energy generated, currently evolving towards a 32% share in Europe [1]. According to the ambitious plan of the European Wind Energy Association (EWEA) among others, the next challenge is to achieve 12% of the worldwide energy production from wind power by 2020.

Up until now strong efforts have been made to integrate this type of energy with the electrical system's operations and control, but given the growth estimates, integration is essential as it now runs the risk of destabilizing the electrical system.

When a large number of wind turbine generators connect to the system and replace a substantial number of conventional synchronous generators, they begin to affect different aspects of the system's behavior, potentially leading to destabilization of the system. A particular case to bear in mind arises during periods of small loads and high wind speed, the relative wind energy contribution is greatest in these circumstances.

In addition, wind power generators are confronted with increasing standards from the grid operators (REE Spain, E.ON Germany, Eltra Denmark, AESO Canada, CER Ireland [2]) in aspects as power quality, grid integration, control capacities, or voltage dips behaviors. Emerging wind turbine technology allows these systems to not only produce energy but also fulfill the most demanding regulation requirements.

Within variable speed wind generators, the most widely used are those based on a doubly feed induction generator, on synchronous generator and on squirrel cage induction generators [3]. Attending to the major wind turbine manufacturers, they are developing bigger and more efficient wind turbines, with 3.6-6MW prototypes already running.

This research project will deal with the doubly fed induction generator topology operating as a high power wind turbine, that nowadays is becoming as the leading for high power wind generators. This is mainly due to the fact that the power converter only has to handle only a fraction of the total power. On the contrary, the slip-rings and the voltage ride through capabilities

are the most recognized drawbacks of this system topology. Nevertheless, it seems that this is one of the major solutions of the wind turbine industry, which will cope with all the expectations and requirements of the wind power generation market.

## 1.2 Framework of the Thesis

### 1.2.1 Variable Speed Wind Energy Systems

Until the mid 1990s, most of the installed wind turbines were based on squirrel cage induction machines directly connected to the grid and the generation was always done at constant speed [4]. Nowadays, most of the installed wind turbines are based on a doubly-fed induction generator (DFIG) sharing the market with the wound rotor synchronous generators (WRSG) and the new arrival of the permanent magnet synchronous generators (PMSG) [5]. All of these machine solutions allow variable speed generation.

In this section, the evolution of the variable speed generation systems is roughly analysed. Attending to the generator used in the generation system of the wind turbine, the variable speed wind turbine basic topologies can be classified into three different categories:

#### 1.- Doubly Fed Induction Generator – Wound Rotor:

The doubly fed induction generator (DFIG) has been used for years, for variable speed drives. In this case, the stator is connected directly to the grid and the rotor is fed by a bidirectional converter that is also connected to the grid.

Using vector control techniques, a bidirectional converter assures energy generation at nominal grid frequency and nominal grid voltage independently of the rotor speed, [6]. The converter's main aim is to compensate the difference between the speed of the rotor and the synchronous speed with the sliding control.

The main characteristics may be summarized as follows:

- Limited operating speed range (-30% to +20%).
- Small scale power electronic converter. Reduced power losses, price ...
- Complete control of active power and reactive power exchanged with the grid.
- Need for slip-rings.
- Need for gear (normally two stage gear).

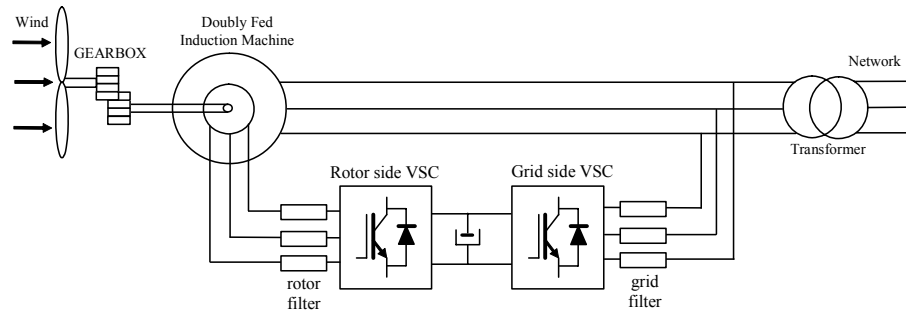


Fig. 1.1. Doubly fed induction machine based wind turbine.

## 2.- Full converter geared solutions

The full converter with gearbox configuration is used with permanent magnet synchronous generator (PMSG) and squirrel cage induction generator (SCIG). Using vector control techniques again, a bidirectional converter assures energy generation at nominal grid frequency and nominal grid voltage independently of the rotor speed.

The SCIG uses a two stage gearbox to connect the low-speed shaft to the high-speed shaft. Although nowadays the PMSG machine also uses a two stage gearbox, the objective is to decrease the gearbox from two stages to one, since the nominal speed of the machine is medium.

### Induction Generator – Squirrel Cage rotor: With main characteristics:

- Full operating speed range.
- No brushes on the generator (reduced maintenance).
- Full scale power electronic converter.
- Complete control of active power and reactive power exchanged with the grid.
- Need for gear (normally two stage gear).

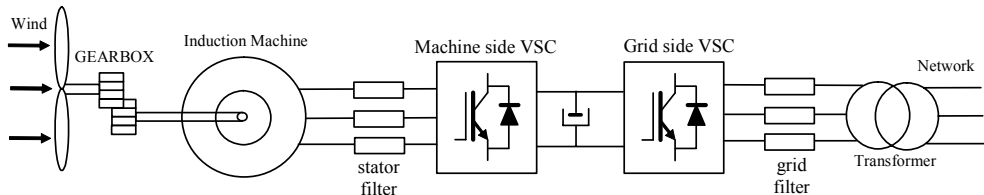


Fig. 1.2. Induction machine (SCIG) based wind turbine.

Synchronous Generator – Permanent Magnet: With main characteristics:

- Full operating speed range.
- No brushes on the generator (reduced maintenance).
- Full scale power electronic converter.
- Complete control of active power and reactive power exchanged with the grid.
- Possibility to avoid gear.
- Multipole generator.
- Permanent magnets needed in large quantities.
- Need for gear (normally one stage gear).

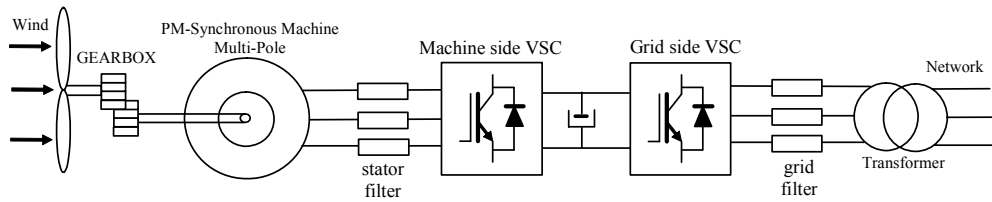


Fig. 1.3. Synchronous machine (PMSG) based wind turbine.

### 3.- Full converter direct drive solutions

Two solutions are proposed in the market:

Multipole permanent magnet generator (MPMG).

Multipole wound rotor synchronous generator (WRSG).

The multipole permanent magnet generator allows connecting the axis of the machine directly to the blades of the wind turbine. Using vector control techniques, a bidirectional converter assures energy generation at nominal grid frequency and nominal grid voltage independently of the rotor speed.

The biggest disadvantage of this technique is the size of the bidirectional converter which must be of the same power level as the alternator. Also, the harmonic distortion generated by the converter must be eliminated by a nominal power filters system. The advantage of this technique is the elimination of the mechanical converter (gearbox coupling) because the machine can operate at low speed. Another disadvantage is that the multipole machine requires an elevated number of poles, being the size of the machine bigger than the generators with the gearbox coupling.

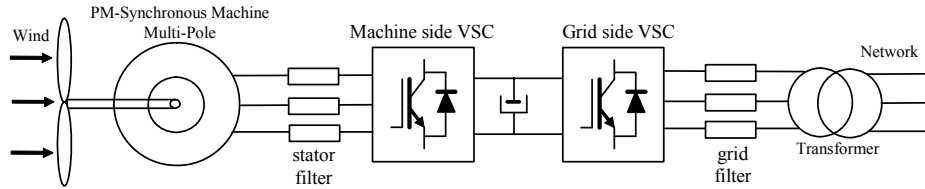


Fig. 1.4. Synchronous machine direct drive based wind turbine.

### 1.2.2 DFIM based Wind Energy Generation.

As mentioned in the background, among all different topologies of variable speed wind turbines, this thesis will be focused on the Doubly Fed Induction Machine (DFIM) based energy generation system. The standard DFIM considered is a wound rotor induction machine fed by slip rings [7] shown in Fig. 1.5.

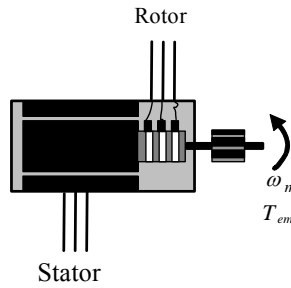


Fig. 1.5. Doubly Fed Induction Machine (DFIM)

There exist different supplying combinations for this machine reported in the literature.

- [8]-[10] proposes a configuration where a front end converter controls a DC link, connected to the rotor side voltage source converter and a stator side voltage source converter.

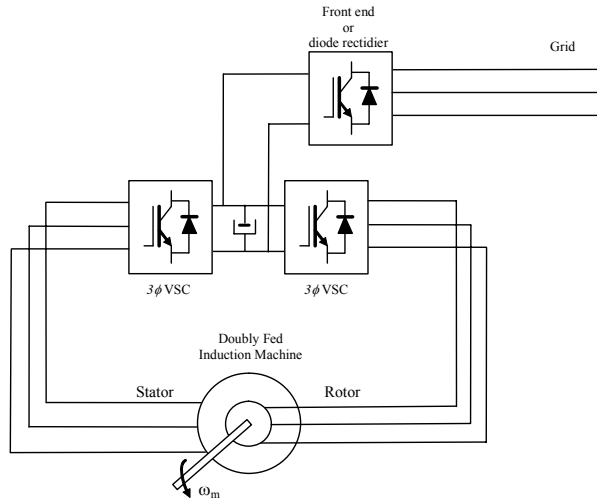


Fig. 1.6. Supplying topology proposed in [8]-[10].

- In [11], both rotor and stator are connected to the grid by to back to back converters, with the aim of optimizing the size of converters.

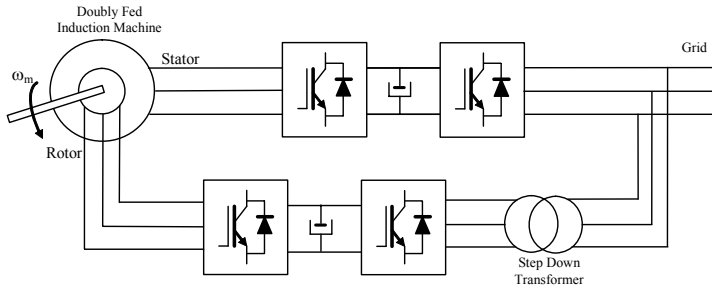


Fig. 1.7. Supplying topology proposed in [11].

However, the configuration adopted in this thesis connects the stator directly to the grid, and the rotor is fed by a reversible voltage source converter, as firstly proposed Peña et al. in [6] (Fig. 1.8).

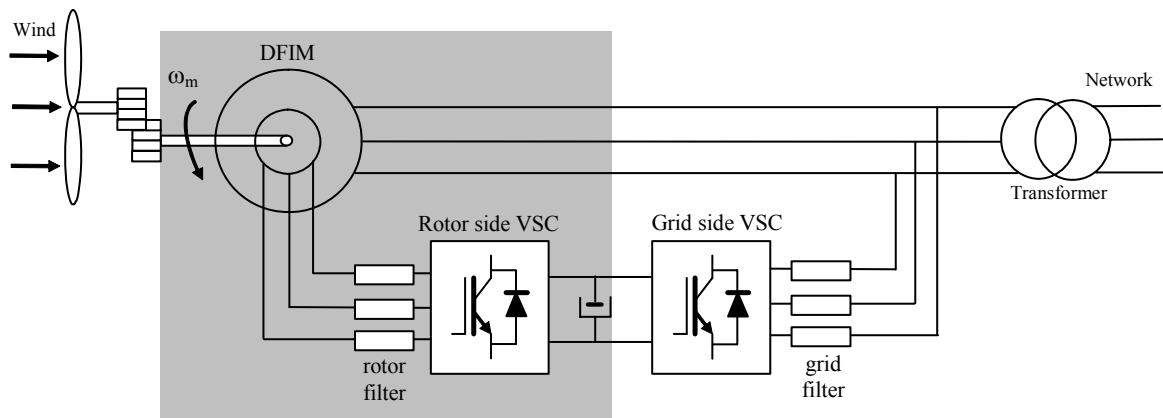


Fig. 1.8. General DFIM supply system. Rotor side control, with back to back converter configuration.

The stator side is supplied at constant frequency and constant three phase amplitude, since it is directly connected to the grid. The speed and the flow of active and reactive power through the rotor and the stator, is controlled by adjusting the amplitude, phase and frequency of the voltage introduced in the rotor.

This configuration is especially attractive as allows to the back to back power electronic converter dealing with approximately 30% of the generated power, reducing considerably the cost and the efficiency against full scale based topologies.

More specifically, this thesis will contribute to this research area by developing different control strategies of the **rotor side converter**, in order to cope with the most recent tendencies and requirements of the wind energy generation.

On the other hand, the grid side converter is not studied in this thesis, assuming reversible and constant DC link side of the back to back converter.

Added to this, different converter topologies will be considered, i.e. the “classic” two level converter and the three level NPC converter [12], [13].

### 1.2.3 Wind Turbine Control Requirements

The general control strategy of a variable speed wind turbine can be divided into three different control levels [14], as depicted in the next figure.

1. The control level I, regulates the flow of power between the grid and the machine [6], [15], [16].
  - The rotor-side converter is controlled in such a way that provides independent control of the electrical torque-stator active power and the stator reactive power.
  - The grid-side converter provides a decoupled control of active and reactive power flowing between the converter and the grid.
  - The crowbar converter protects the rotor-side converter when a voltage dip occurs.
2. The references for control level I are generated by control level II. In this level, two main operating modes are proposed:
  - Extract the maximum power from the wind, coordinating torque (stator active power) and pitch angle ( $\beta$ ) references, always keeping the wind turbine into the speed limits [17]-[19].
  - Respond to active and reactive power references from the higher control level [20].
3. Control level III is dedicated to the wind turbine grid integration. As occurs in control level II, several strategies are possible [21],[22]:
  - Provide ancillary services: voltage ( $V_{grid}$ ) and frequency ( $f_{grid}$ ) control (droop characteristics), or inertial response.
  - Respond to active and reactive power references from the grid operator or wind farm centralized control.

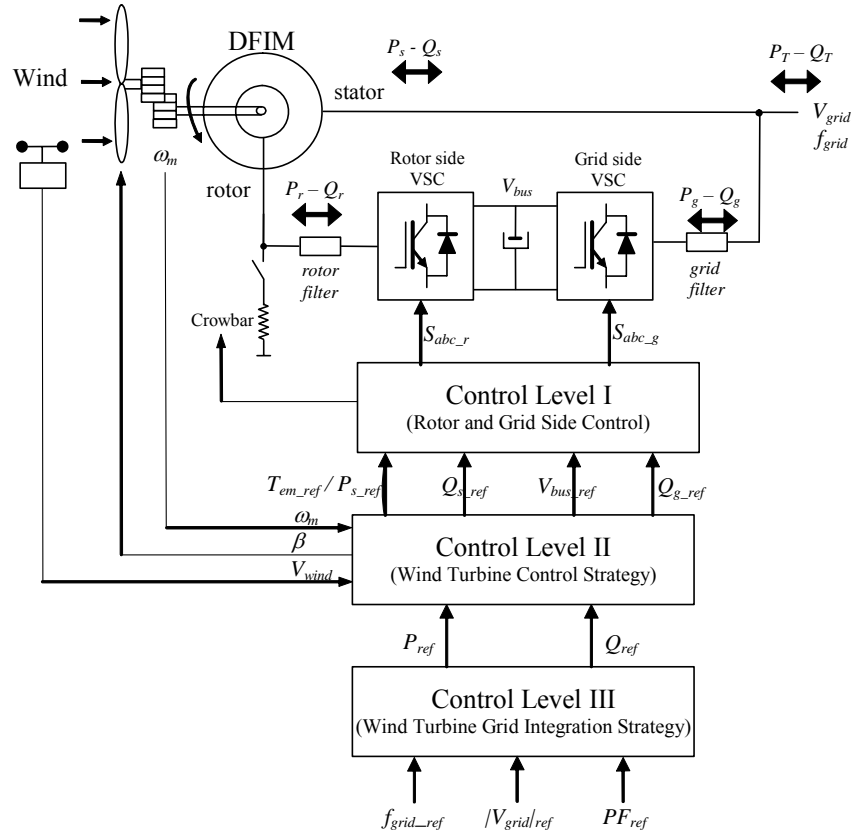


Fig. 1.9. General wind turbine control strategy based on DFIM

Consequently, as mentioned before, this thesis is focused on the control level I, and the proposed control strategies will be specially designed to address the following general purpose and specific requirements according with the wind turbine application.

### General control requirements:

**1.- Flexibility to control different magnitudes:** The control strategy should be able to control **different magnitudes** such as the stator active and reactive power, the rotor flux and the torque , in order to accomplish different demands of higher level control strategies. Under these circumstances, the control strategy should present appropriate steady-state, dynamic response and tracking behavior, according to the requirements of the wind energy generation system.

**2.- Generated power quality:** The control strategy should present the capacity to directly or indirectly deal with the **quality** of the **generated power**, in terms of the harmonic distortion of the stator and rotor currents (THD), current harmonic frequency spectrum, as well as the mechanical torque harmonic spectrum. This fact is especially interesting to accomplish the grid codes requirements and IEC standards [23] and to avoid non desired mechanical stresses along the direct drive of the wind turbine.

3.- General aspects: It is desired that the control strategy presents the following features [24]:

- Fast **dynamic response**.
- On line **implementation simplicity**.
- **Reduced tuning** and adjusting efforts of the **controllers**.
- **Robustness** against model uncertainties.
- **Reliability**.
- Good perturbation **rejection**.
- Etc...

On the other hand, considering the application where the control technique is going to be implemented it should meet the following specific control requirements:

#### **Specific control requirements:**

4.- Control oriented to the high power generation: In the market of the industrial drives [25]-[27], new applications requiring higher power levels, always have been accompanied with an increase of the voltage range levels, reaching at this moment the medium voltage. This tendency, have introduced several innovations (multilevel converter topologies, higher voltage levels, VSC-LCC...) that the control strategies need to consider. In this thesis, this framework is adopted, so the designed controls techniques will need to tackle the following two important difficulties.

- Reduced and **constant switching frequencies**, due to the semiconductor (HV-IGBTs, IGCTs) limitations of the power electronic converter.
- The main consequence of low switching frequency is that under some circumstances, the application could require **capacity** to **operate** with **high current** and torque **ripples** that yields to stability difficulties of the system.

5.- Stability under grid faults: It has been proved that in an wind energy generation environment, the DFIM based wind turbines present complicated behavior during grid faults. The control strategy should present sufficient **dynamic response** capacity and should be designed in order to address this problem [15], [16], [28]. For that purpose, grid codes are requiring increasing fault ride through capabilities to wind turbines.

### 1.2.4 DFIM Control, State of the Art

According to a general classification of the variable frequency induction machine control methods [29], the predictive direct control techniques developed in this thesis can be classified as a **vector based control** that belongs to the **direct control techniques with a circle flux trajectory**, as shown in Fig. 1.10.

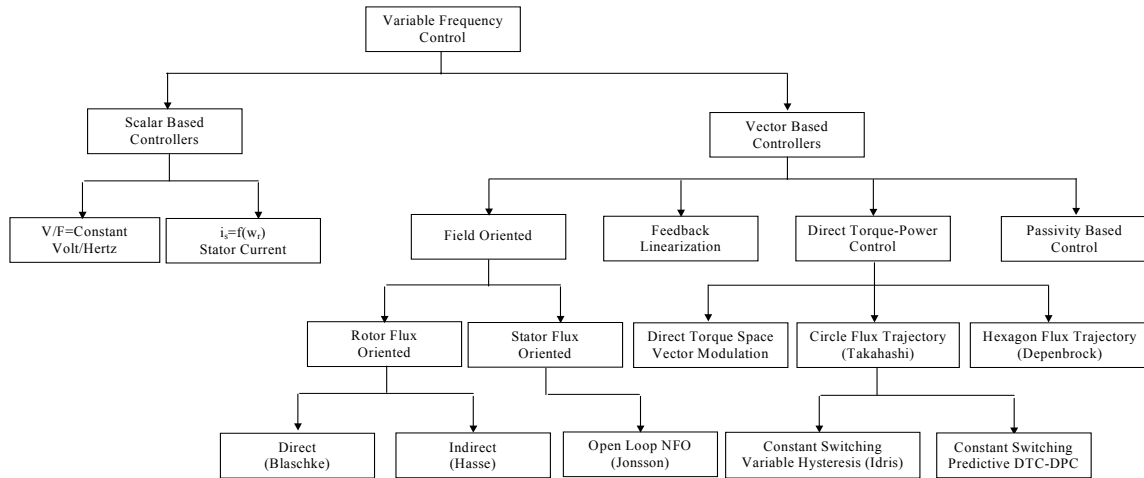


Fig. 1.10. General classification of the variable frequency induction machine control methods.

Hence, among all methods of control developed for the induction machine, the most widely used techniques may be classified within the Field Oriented Control (FOC) techniques and the Direct Control techniques. Although in 1971 F. Blaschke [30] presented the first publication on FOC, it seems to be accepted that the Direct Control techniques firstly introduced such as Direct Torque Control (DTC) by Takahashi [31] and Direct Self Control (DSC) by Depenbrock [32] achieve better steady-state and transient torque control conditions rather than FOC techniques [33], added to a simpler on-line implementation. Moreover, Direct Control techniques do not require current regulators, nor coordinate transformations or specific modulations like PWM or SVM for pulse generation, but they present some disadvantages compared to the FOC. For instance, the lack of direct current control, torque control difficulties at very low speeds and especially variable switching frequency behavior.

With regards to this last important drawback, in recent years, several authors have tackled the problem of improving the performance of a direct torque controlled induction machine, in the sense of imposing the average switching frequency of the voltage source converter. Thus, methods like Direct Mean Torque Control (DMTC) [34], Direct Torque Control with Space Vector Modulation (DTC-SVM) [35] and Direct Torque Control based on Discrete Space Vector Modulation (DTC-DSVM) [36], have already achieved constant switching frequency.

Furthermore, the methods proposed in [37], [38], [39] and [40] have extended the solution to reduce torque ripple at the same time imposing the switching frequency, as well as for different voltage-source multilevel converter topologies.

On the other hand, direct control techniques have also been developed in other machines, for example in the split-phase induction machine [41], in the synchronous machine achieving constant switching frequency [42], [43], in the brushless doubly fed induction machine [44], or the equivalent direct power control (DPC) strategies for several grid connected converter applications [45] and [46].

The present research work will focus the analysis on the Doubly Fed Induction Machine (DFIM), which is a common solution for variable speed wind turbines. Different control methods have been developed for this machine, thus, FOC has been performed by many authors, for example [6]. Direct torque control and direct power control methods without switching frequency imposition, have also been carried out in [47], [48] and [49].

These mentioned direct control techniques that achieve constant switching frequency behavior are based on predictive control with a prediction horizon equal to one sample period. In this thesis, the theoretical background developed by these authors will be employed to design new Predictive Direct Control techniques for the DFIM, at constant switching frequency. This control technique is based on a prediction of some magnitude evolutions of the machine. A different family of predictive control theory also exists, with a predictive horizon greater than one [50], that is based on the Model Predictive Control (MPC) for linear systems.

Finally, TABLE 1.I shows a chronology of the already developed Predictive Direct Control methods.

TABLE 1.I  
CHRONOLOGY OF DIRECT PREDICTIVE CONTROL METHODS FOR AC INDUCTION MACHINES

<b>Authors</b>	<b>Predictive Control Method</b>	<b>Predictive</b>	<b>Control Method</b>
E.Flach et al. in 1997 [34]	Direct Mean Torque Control	Induction Machine	2 Level Converter
J-K. Kang et al. in 1999 [37]	DTC	Induction Machine	2 Level Converter
C.A. Martins et al. in 2002 [39]	DTC	Induction Machine	4 Level Flying Capacitor Converter
J. Rodríguez et al. in 2004 [40]	DTC	Induction Machine	11 Level Cascaded Converter
M. Pacas et al. in 2005 [43]	DTC	PM Synchronous Machine	2 Level Converter

### 1.2.5 Potential Benefits of Predictive Direct Control Techniques

In this section, the choice of the predictive direct control method is justified as a control technique that meets the control requirements specified in section 1.2.3. In TABLE 1.II, a feature comparison is presented of the most widely used control methods for AC induction machines.

TABLE 1.II  
FEATURE COMPARISON OF DIFFERENT CONTROL METHODS

	Scalar Based Controller (V/F=Constant)	Field Oriented Control	Direct Torque-Power Control	Direct Torque with Space Vector Modulation	Predictive Direct Control
<b>Ripple reduction (quality)</b>	High	High	High	High	High
<b>Fast dynamic response</b>	Low	Medium	High	Medium	High
<b>On line implementation simplicity</b>	High	Low	High	Medium	Medium
<b>Reduced tuning efforts of controllers</b>	High	Low	High	Medium	High
<b>Robustness against model uncertainties</b>	Medium	High	High	High	Medium
<b>Reliability</b>	High	Medium	Medium	Medium	Medium
<b>Capacity to operate at low constant switching frequencies</b>	?	?	Low	?	High

Although apart from the V/F control, all the methods present similar characteristics, the predictive direct control method seems to be the most convenient method, since it able to operate at **low constant switching frequencies** with a very **fast dynamic response** and with a reasonably **on line implementation simplicity**. On the contrary, as a predictive method, the robustness against model uncertainties is lower than the other control methods, but as it will be demonstrated along this thesis, the proposed predictive direct control techniques will be specially designed to avoid this drawback.

Thus, comparing the predictive direct control method to the field oriented control and to the direct torque with space vector modulation, the predictive technique allows to obtain faster dynamic responses and ensures the capacity to operate at low constant switching frequencies, a characteristic not demonstrated for other control techniques.

On the other hand, the best advantage of the predictive direct control compared the “classic” direct torque control is the constant switching frequency behavior.

Finally, the scalar based controller has been excluded too, due to its “poorer” performances compared with the other control methods.

### **1.3 Thesis Objectives.**

The objective of this thesis is to develop, analyze and validate the control strategy that meets the requirements of a doubly fed induction machine based variable speed wind turbine operating in the high power range. Thus, these requirements are mainly specified in section 1.2.3, and are especially related to meet the requirements of grid codes for wind power generation.

Apart from validating the feasibility of the developed control strategy for the wind energy generation application, it can also be extensive to different applications.

### **1.4 Outline of the Thesis.**

The thesis is organized as follows:

**Chapter 1** The thesis is introduced, defining the most important characteristics of the designed control strategy. After that, the objectives of the thesis are presented and the related state of the art is studied.

**Chapter 2** The alternative high power medium voltage wind turbine approach is proposed. The power and voltage levels, the requirements and characteristics of the medium voltage converter as well as the doubly fed induction machine that composes the electrical drive of the high power medium voltage wind turbine are defined.

**Chapter 3** The dynamic model of the Doubly Fed Induction Machine, with and without considering the iron loss is presented, giving the differential equations and the state space equations of each model. After that, the four operation modes of the Doubly Fed Induction Machine at steady state are studied.

**Chapter 4** The Direct Torque Control (DTC) of the Doubly Fed Induction Machine based on the two level converter is studied. Three different DTC techniques are presented. The

first control technique is based on the “classic” DTC for induction machines. The second DTC technique achieves minimum torque ripple, at constant switching frequency. The last DTC technique, achieves reduced torque and flux ripples at “low” constant switching frequencies. Finally, simulation and experimental results are carried out of each control technique, focusing the analysis on the steady state performance, transient response and tracking behavior of the machine.

**Chapter 5** The Direct Power Control (DPC) of the Doubly Fed Induction Machine based on the two level converter is studied. In this case, the developed control technique achieves simultaneous ripple reduction of the directly controlled variables ( $P_s$  and  $Q_s$ ), at “low” constant switching frequency. To validate the control strategy, it will be experimentally compared to the most widely used control methods for the Doubly Fed Induction Machine in terms of steady state behavior and transient response capacity.

**Chapter 6** The Direct Torque and the Direct Power Control of the Doubly Fed Induction Machine based on the three level NPC converter is studied. Both DTC and DPC control strategies will be described, achieving simultaneous ripple reduction of both directly controlled variables. In addition, the rotor side inductive filter needed to meet the power quality requirements will be also taken into account by the proposed control strategy. To validate the control, experimental results will be served.

**Chapter 7** The distorted grid situation is studied. Based on the control techniques developed in precedent chapters, some simple modifications will be proposed to address the problems related to two main grid disturbances: voltage unbalance and the presence of voltage harmonic distortion.

**Chapter 8** The conclusions of the thesis are served accompanied by future work proposal.



## CONTENTS of Chapter 2

2	High Power Wind Energy Generation.....	27
2.1	Introduction.....	28
2.2	Justification of High Power Medium Voltage Wind Turbine.....	28
2.2.1	Medium Voltage Drives for Industry Applications .....	28
2.2.2	Wind Turbine Manufacturers .....	32
2.2.3	Tendency of Wind Turbine Development.....	33
2.2.4	Conclusions of this section .....	35
2.3	High Power Medium Voltage Wind Turbine. Scenario Definition .....	35
2.4	Conclusions of the Chapter.....	37

## Chapter 2

### 2 High Power Wind Energy Generation

*In this chapter, a high power wind energy generation system study is carried out. An alternative Medium Voltage (MV) high power wind turbine approach is proposed to the classical low voltage wind turbine solution, connected to the 690V grid. To justify this medium voltage high power wind turbine proposal, a state of the art based study will be served.*

*First, it will be shown that the most important industry manufacturers of high power drives, already develop medium voltage range solutions rather than low voltage solutions. Then, after analyzing the most important wind turbine manufacturers solutions, it will be stated that although nowadays the most widely installed wind turbine is the low voltage wind turbine, it is perceived a clear tendency to increase the power and a smoothly starting tendency to increase the operation voltage levels, basically in order to increase the efficiency of the wind turbines.*

*After justifying the medium voltage wind turbine approach, the high power and medium voltage wind turbine characteristics will be defined, providing power and voltage levels as well as the requirements and characteristics of the medium voltage converter and the doubly fed induction machine that composes the electrical drive of the wind turbine.*

## 2.1 Introduction

This chapter presents two main objectives. The first objective is to show the necessity of high power medium voltage wind turbines. This proposed high power and medium voltage wind turbine, among other specific requirements, demands a special control strategy. For that purpose, the predictive control strategies of subsequent chapters 4, 5 and 6 of this thesis have been designed. The second objective is to define and design the main characteristics of the electric drive, for the high power and medium voltage wind turbine generation system.

## 2.2 Justification of High Power Medium Voltage Wind Turbine

### 2.2.1 Medium Voltage Drives for Industry Applications

All the motor drives for industry applications are made of converters that use power semiconductors. The state of the art of the MV power semiconductors with turn-off capability is shown [52] in the next table.

TABLE 2.I

DEVICE RATINGS AND PACKAGE TYPES OF COMMON MV POWER SEMICONDUCTORS WITH TURN-OFF CAPABILITY

<b>Power Semiconductor</b>	<b>Manufacturer</b>	<b>Voltage Ratings [V]</b>	<b>Switching Power [MVA]</b>	<b>Case</b>
GTO	Mitsubishi	6500	36	Press-Pack
		4500	18	Press-Pack
	ABB	4500	18	Press-Pack
		6000	18	Press-Pack
	Eupec	3300	3.96	Module
		6500	3.90	Module
IGBT	Mitsubishi	3300	3.96	Module
		4500	4.05	Module
		6500	3.90	Module
	Hitachi	3300	3.96	Module
	Toshiba	3300	3.96	Press-Pack
		4500	9.45	Module
	ABB	3300	3.96	Module
		4500	13.50	Press-Pack
		6500	3.90	Module
IGCT	ABB	4500	18	Press-Pack
		4500	9.90	Press-Pack
		5500	9.90	Press-Pack
		6000	18.00	Press-Pack
	Mitsubishi	4500	18	Press-Pack
		6000	36	Press-Pack
		6500	9.75	Press-Pack

On the other hand, the most extended converter topologies for MV industrial application drives are:

1. 2 Level VSC (Fig. 2.1).
2. 3 Level NPC VSC (Fig. 2.2).
3. 4 Level Flying Capacitor VSC (Fig. 2.3).
4. Series Connected H Bridge VSC (Fig. 2.4).
5. Series Connected 3 Level NPC VSC (Fig. 2.5).
6. CSI (Fig. 2.6).

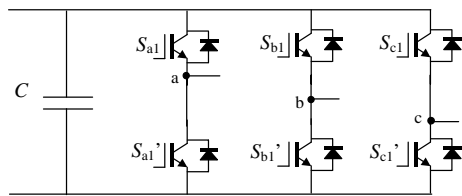


Fig. 2.1 2 Level VSC

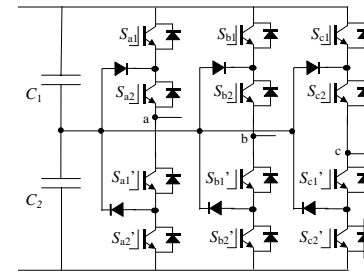


Fig. 2.2 3 Level NPC VSC

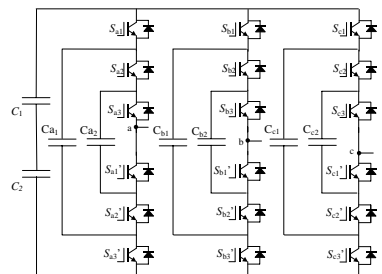


Fig. 2.3 4 Level Flying Capacitor VSC

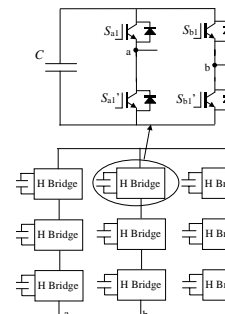


Fig. 2.4 Series Connected 9L H Bridge VSC

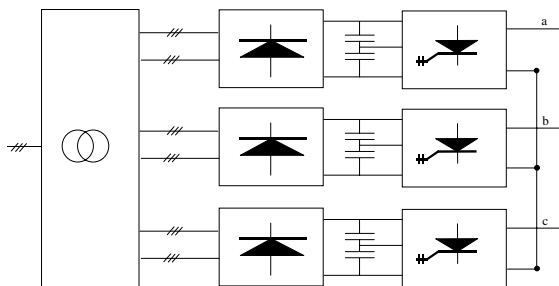


Fig. 2.5. SC3L-VSC

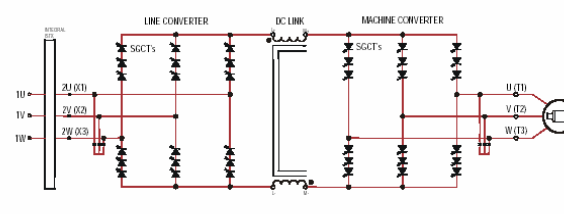


Fig. 2.6 Rockwell CSI with SCGTs.

The following table [52] shows the market overview about industrial MV drives, including the manufacturers.

TABLE 2.II  
MARKET OVERVIEW ABOUT INDUSTRIAL MV DRIVES.

Manufacturer	Type	Power	Voltage[kV]	Topology	Semicond.	Control
Ingeteam	Ingedrive ® MV	0.75-27MVA	2.3, 3.3, 4.16	3L-NPC	IGBT,IEGT,IGCT	?
	Perfect Harmony	0.3-31MVA	2.3-13.8	SC 9L HB	LV-IGBT	Vector Control
Asirobicon	Silcovert GN	3-20MVA	4.16	3L-NPC	IGCT	?
	Silcovert H	1-25MVA	2.2-13.8	CSI	Thyristors	?
	TM GE Dura-Bilt5i MV	4.8-9.6MVA	5	3-5L-NPC	IGBT	?
Toshiba Mitsubishi GE	TM GE 10 Tmdrive 70	6-40MVA	3.3	3L-NPC	IEGT	PWM
	Power Flex 7000	0.15-6.7MVA	2.3, 3.3, 4.1, 6.6	CSI	SGCT	Vector Control
Allen Bardley	Masterdrive MV	0.66-9.1MVA	2.3, 3.3, 4.16, 6, 6.16	3L-NPC	HV IGBT	Vector Control
	Masterdrive ML2	5-30MVA	3.3	3L-NPC	IGCT	Vector Control
Siemens	ACS 1000	0.3-5MVA	2.3, 3.3, 4.0	3L-NPC	IGCT	DTC
	ACS 5000	5.2-24MVA	6, 6.6, 6.9	3-5L-NPC	IGCT	DTC
	ACS 6000	3-27MVA	3, 3.3	3L-NPC	IGCT	DTC
	LCI	7-72MVA	2.1, 10	CSI	Thyristors	?
ABB	VDM5000	1.4-7.2MVA	2.3, 3.3, 4.2	2L-VSC	IGBT	Vector Control
	VDM6000	0.3-8MVA	2.3, 3.3, 4.2	4L-FLC	IGBT	Vector Control
	VDM7000	7.9-5MVA	3.3	3L-NPC	GTO	Vector Control
Converteam (Alstom)						

From all presented topologies it seems that the 2 Level, the 3 Level NPC and the 4 Level FC VSC are the most suitable for the DFIM control application, since they do not require different voltage sources. In addition, for drives of power order between 2 and 10 MW, the manufacturers operate at voltage levels between 2.2 and 13.8kV.

On the other hand, in general the ratio between the maximum voltage of the semiconductor and the application voltage (depends on the DC bus voltage), is chosen **around 0.6**.

In [53] with table 2.III comparison, different voltage levels for the NPC topology using different semiconductors are analyzed:

TABLE 2.III  
COMPARISON BETWEEN DIFFERENT NPC TOPOLOGIES FOR DIFFERENT SEMICONDUCTORS.

Semiconductor	Two Level NPC			Three Level NPC			Five Level NPC		
	V <sub>AC</sub>	Power	V <sub>DC</sub>	V <sub>AC</sub>	Power	V <sub>DC</sub>	V <sub>AC</sub>	Power	V <sub>DC</sub>
IGBT 1.2 kV-1.2 KA	510V	610kVA	720V	1000V	1.2kVA	1400V	2kV	2.4 MVA	2800V
IGBT 3.3 kV-1.2 KA	1.5 kV	1.8MVA	2100V	2.7kV	3.2MVA	3800V	5.7kV	6.8 MVA	8000V
IGBT 4.5 kV-1.2 KA	2 kV	2.4MVA	2800V	3.6kV	4.3MVA	5040V	7.8kV	9.4 MVA	11000V
IGCT 4.5 kV-3 KA	2 kV	3.5MVA	2800V	3.6kV	6.3MVA	5040V	7.8kV	23.4MVA	11000V
IGCT 6 kV-4 KA	2.7 kV	4.5MVA	3800V	4.8kV	8MVA	6800V	11kV	44MVA	15000V

When the application requires reaching higher voltage levels, it is possible to use series connected semiconductors. TABLE 2.IV shows a comparison of the voltage levels that can reach the most common topologies, using the higher voltage semiconductor.

TABLE 2.IV

COMPARISON BETWEEN DIFFERENT NPC TOPOLOGIES WITH SERIES CONNECTION OF SEMICONDUCTORS. (6500V IGBT OR IGCT)

Series Semiconductors	3 Level NPC		4 Level FC		5 Level NPC		6 Level FC	
	V <sub>AC</sub>	V <sub>DC</sub>						
1	4.6kV	6500V	6.9kV	9750V	9.2kV	13000V	11.5kV	16250V
2	9.1kV	13000V	13.8kV	19500V	18.4kV	26000V	23kV	32500V
3	13.8kV	19500V	21kV	29250V	27.5kV	39000V	34kV	48750V

## 2.2.2 Wind Turbine Manufacturers

On the other hand, paying attention to the wind turbine manufacturers, according to [54], there exist the following wind turbine generator manufacturers in Spain.

TABLE 2.V  
SPANISH WIND TURBINE MANUFACTURERS

Company	Power	Voltage	Generator	Special features
Aerogeneradores Canarios, S.A.	225kW, 660kW	400V, 690V	DFIM, Asynchronous	Siemens, ABB,Vestas
Bazán-Bonus	1.3MW	690V	Asynchronous	?
Desarrollos Eólicos, S.A -DESA	600 kW-1.5MW	?	?	?
Dewind Iberia, S.A.	600kW – 1.5MW	690V	DFIM	?
Ecotecnia MCC	150kW – 750kW	?	?	?
Enron Wind Iberica	1.5MW – 2MW	?	DFIM	?
Gamesa Eólica, S.A	850kW – 2MW	690V	DFIM	Ingecon W
Made tecnologías renovables	1.3MW-800kW	690V, 1000 V	Asynchronous-Synchronous	?
Neg Micon Iberica SAU	2MW - 400kW	690 V	Asynchronous	?
Nordex Ibérica	1.3MW – 250kW	690 V	Asynchronous	?
Acciona Wind Power	1500kW	12000 V	DFIM	Ingecon W

Also, there exist very important manufacturers abroad.

TABLE 2.VI  
WORLD'S LEADERS WIND TURBINE MANUFACTURERS

<b>Company</b>	<b>Power</b>	<b>Voltage</b>	<b>Generator</b>	<b>Special features</b>
General Electric (EE.UU)	2.5MW 2MW	?	Synchronous PM	Full Converter (Low Voltage Ride Thru) Working on a 5-7 MW project
Siemens	3.6 MW 2.3 MW 1.3 MW	690 V	Asynchronous	?
Vestas	4.5 MW 2.75 MW 3 MW 2 MW 1.8 MW	6000V 1000V 1000V 690V 690V	Asynchronous with OptiSpeed	Offshore Offshore Onshore Onshore
REpower (Germany)	5 MW 2 MW	950V(660VRotor) 690 V	DFIM	Offshore / Onshore Onshore
Enerkon (Germany)	4.5-6 MW 2 MW	?	Ring Generator Synchronous annular generator	?

Wind turbine manufacturers are developing bigger wind turbines, increasing their generated power. According to [55]-[56] among others, in less than ten years 10MW offshore wind turbines will be a reality. On the other hand, as shown in TABLE 2.V and TABLE 2.VI, DFIM based turbines are commonly used by most of the manufacturers.

Attending to the machine's connection voltage, recent developments show that some manufacturers (Vestas, Repower, Acciona) are increasing the voltage values together with the power increase. Consequently, the wind turbine evolution reveals that the tendency goes to bigger power turbines connected to higher voltage levels.

### 2.2.3 Tendency of Wind Turbine Development

In Fig. 2.7, the increase of power in variable speed wind turbine can be observed over the last few years [57]. According to leading authors of this research area [3], this fact occurs due to an increase of the efficiency of the wind turbines at higher power levels.

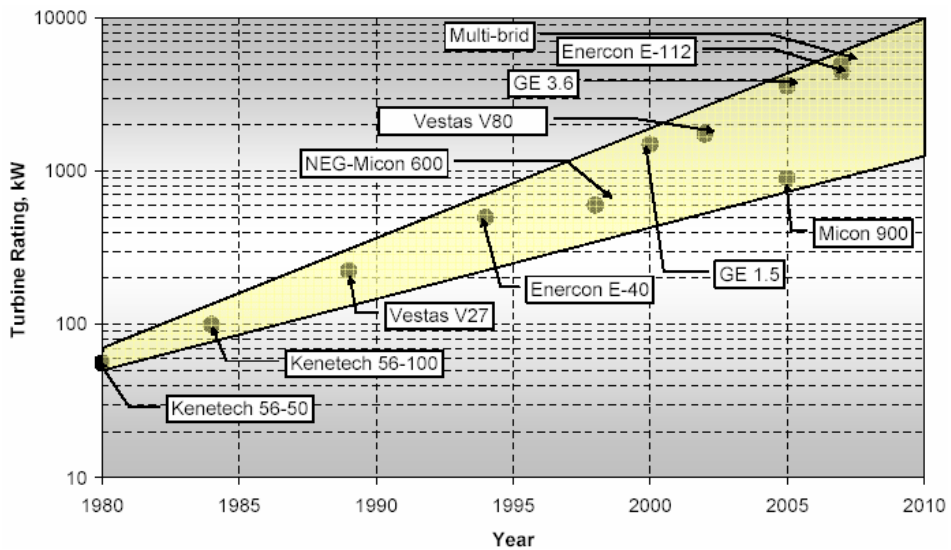


Fig. 2.7 Wind turbine power increase over the last 30 years [57].

On the other hand, as shown in section 2.2.1, all the manufacturers of motor drives for industry applications operate at medium voltage, for power levels higher than 1MW.

The medium voltage range is different according to the standard used, as listed in TABLE 2.VII. Historically for example, the park voltage in USA was 12.47kV and 13.8kV, although nowadays 34.5kV is starting to be used.

TABLE 2.VII  
VOLTAGE CLASSIFICATION

Region	Relevant Standard	Definition
Low Voltage < 600V		
North America	ANSI C84.1	208V, 120/240V, 480V, 575V 600V < Medium Voltage < 35kV 2.4kV, 4.16kV, 6.9kV, 12.47kV, 13.8kV, 21kV, 34.5kV
Low Voltage < 1000V		
Europe	IEC 60038	220V, 400V, 690V 1000V < Medium Voltage < 35kV 3.3kV, 6.6kV, 11kV, 22kV, 33kV

Finally, in [57] for instance different wind turbine comparison is carried out at low voltage and medium voltage, concluding that **“Wind turbines of MW are more economical at medium voltage rather than at low voltage”**. The main reasons can be summarized as follows:

- There is a substantial reduction in the cost of **pendant cables** for the MV systems compared to LV systems.
- The MV main breakers are significantly cheaper than LV, especially due to the **current** breaking requirement.
- Perceived technical risk associated with the MV converter innovations is mitigated by the fact that such technology is already common in motor drive applications.

#### 2.2.4 Conclusions of this section

As a result of the facts presented in this section it can be concluded with:

- The tendency of the wind turbine manufacturers is to increase the range of power in order to improve their efficiency.
- Wind turbines of MW are more economical at medium voltage rather than at low voltage.
- The most common converter topologies of MV industrial application motor drives are: Two level converter, Three level NPC converter and Four Level Flying Capacitor converter.

### 2.3 High Power Medium Voltage Wind Turbine. Scenario Definition

Considering to the facts presented in the previous section, the high power medium voltage variable speed wind turbine has been defined as depicted in Fig. 2.8.

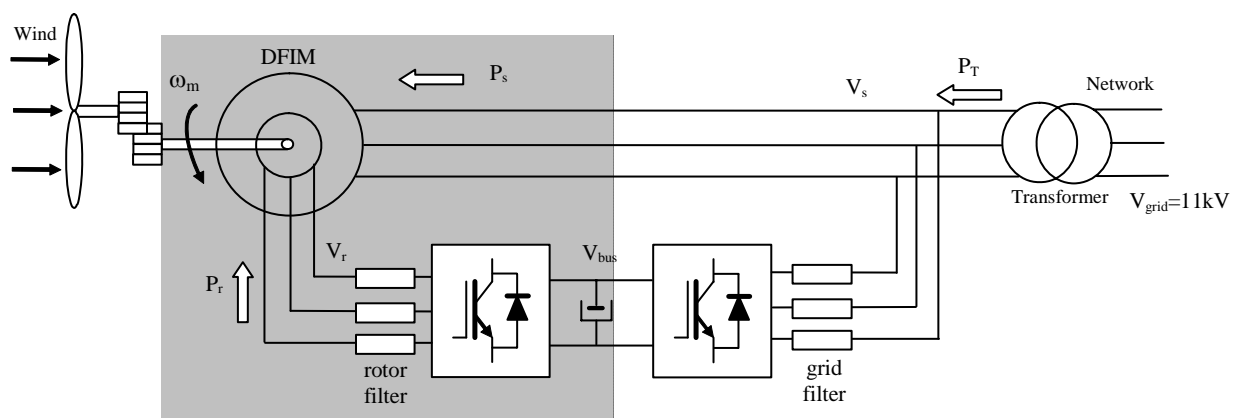


Fig. 2.8 General DFIM supply system. Rotor side control with back to back converter configuration.

The most important characteristics of the defined wind turbine are summarized as follows:

<b>DFIM</b>	<b>Converter</b>
$P_T = 10\text{MW}$	Three Level NPC VSC topology
$P_s = 7.5\text{MW}$	Back to back
$P_r = 2.5\text{MW}$	$V_{AC} = 3.3\text{kV}$
Stator Rotor turn factor 1/3	$V_{bus} = 5\text{kV}$
Model Parameters:	
$R_s = 2.6\text{m}\Omega$	IGBT 4500V-6500V
$L_{\sigma s} = 83\mu\text{H}$	$P_{conv} = 2.5\text{MW}$
$R_r = 2.9\text{m}\Omega$	$f_{switching} = 500\text{Hz}$
$L_{\sigma r} = 85\mu\text{H}$	$L_{rotor\_filter} = 2\text{mH}$
$L_h = 2.54\text{mH}$	
p = 2 pair of poles	

Hence, these values have been selected according to the following criteria:

- **$P_T$ :** Taking into account that nowadays the biggest wind turbine is 6MW, it is scheduled that in three years 10MW wind turbines could be a reality [55]- [57].
- **$P_s - P_r$ :** The nominal power interchanged by the rotor is 33% of the stator power.
- **$V_r$ :** 3.3kV is one of the most common voltages among motor drives manufacturers for 3MW (Note that only 1/3 of the rotor nominal voltage is reached).
- **$V_s$ :** The relation between the stator and the rotor voltages is wanted to be 1/3, in order to avoid the necessity of one more transformer and the same DC bus voltage requirement in both AC sides of the back to back converter, less filtering requirement in the rotor side converter, etc...
- **$V_{bus}$ :** 5kV of DC bus voltage is considered a sufficiently large voltage for both AC sides of the back to back converter. The rotor side converter will operate in the whole range of modulation indexes, depending on the speed. On the other hand, the grid side converter will mostly operate at voltage levels near the nominal value.
- **Model parameters:** Due to the difficulty to find the parameters of a 10MW machine, the parameters of a 2MW machine [49] have been employed. Nevertheless, no remarkable difference has been found in terms of stability for different model parameters.
- **Converter topology:** The three level NPC VSC topology is one of the most common topologies, according to TABLE 2.II and it fits with the required voltage levels, with power semiconductors greater than 4500V. However, with 5kV of DC bus voltage by

using 6500V IGBT, it would be also possible to use the two level converter topology, achieving slightly worse generated power quality.

- **$f_{switching}$ :** It is expected that the switching frequency of the IGBTs will be restricted at 3MW power. For that purpose, a considerably low frequency of 500Hz have been set, in order to define a severe scenario from the control strategy point of view, but at the same time, safe from the switching power losses of the semiconductor perspective.
- **$L_{rotor\_filter}$ :** The necessity of a filter in the rotor side converter is due to a low stator and rotor self inductances for high power machines. The inductance value has been chosen in order to obtain a generated stator current total harmonic distortion of **3%**, at the nominal power.

## 2.4 Conclusions of the Chapter

According to a study of the related state of the art, it has been shown that the natural tendency of the wind turbine development is to increase the power range, as well as to increase their operation voltage levels. For that reason, the high power medium voltage wind turbine characteristics have been defined, giving details such as the power, voltage and model parameters of the doubly fed induction machine, together with the topology of the back to back converter and its nominal ratings. It has been concluded that for a 10MW wind turbine, the appropriate AC voltage operating levels would be 3.3kV in both rotor and stator sides, while the converter topology will be a three level NPC VSC with semiconductors greater than 4500V, for instance IGBTs.

On the other hand, in order to secure a safe switching behavior for the power semiconductors, considerably low switching frequency is imposed. Thus, this fact will provoke the necessity of a rotor side filter to meet the power quality requirements of the grid codes.

Therefore, all these specific particularities together, will demand a specially designed control technique, with the capacity to tackle the requirements of this severe scenario, i.e. high power and medium voltage wind turbines.

*For that purpose, before starting to define the control techniques, the next chapter will deeply analyze the mathematical model of the doubly fed induction machine. It is very important, prior the design of the control strategy, the accurate knowledge of the system that is going to be controlled, establishing the mathematical expressions and relations provided by the so called: model of the doubly fed induction machine. After that, the control techniques will be based, among other aspects, on this mathematical model.*



## CONTENTS of Chapter 3

3	Modeling of the Doubly Fed Induction Machine (DFIM).....	40
3.1	Introduction .....	40
3.2	Dynamic Modeling of the DFIM.....	41
3.2.1	Space Vector Notation of the DFIM.....	42
3.2.2	$\alpha\beta$ Model.....	44
3.2.3	dq Model.....	47
3.2.4	State-Space Representation of $\alpha\beta$ Model .....	49
3.3	Dynamic Modeling of the DFIM Considering the Iron Loss .....	50
3.3.1	$\alpha\beta$ Model.....	50
3.3.2	dq Model.....	54
3.3.3	State-Space Representation of $\alpha\beta$ Model .....	57
3.4	DFIM at Steady State .....	59
3.4.1	Mode 1. Motoring at Hypersynchronous Speed .....	61
3.4.2	Mode 2. Generating at Hypersynchronous Speed.....	62
3.4.3	Mode 3. Generating at Subsynchronous Speed.....	63
3.4.4	Mode 4. Motoring at Subsynchronous Speed.....	64
3.5	Conclusions of the Chapter .....	64

# Chapter 3

## 3 Modeling of the Doubly Fed Induction Machine (DFIM)

*In this chapter different dynamic models of the DFIM are presented. They are useful for different purposes, but especially they are required to develop the predictive control strategies presented in next chapters. Hence, first the dynamic  $\alpha\beta$  and  $dq$  models of the DFIM are presented by using the space vector representation. After that, the dynamic  $\alpha\beta$  and  $dq$  models of the DFIM considering the iron losses of the machine are developed. Finally, the four operation modes of the DFIM at steady state are studied.*

### 3.1 Introduction

In this chapter, different dynamic models of the DFIM are presented considering the state of the art related to this field. The first dynamic model in the  $\alpha\beta$  version or in the  $dq$  version will be employed through the whole control techniques described in this thesis. The knowledge of the model of the machine is very important under this scenario, since these developed control techniques are based on a prediction of the machine's state. So for that purpose, the certainty and accurateness of the model will play an important role.

The second dynamic model, further considers the iron losses of the DFIM. This could be specifically useful if the control is oriented to applications that use small power DFIM where the iron losses can not be normally neglected, comparing to higher power machines.

Finally, since the DFIM depending on the application requirements can work at four different operation modes, the most interesting characteristics of the steady state behavior of each mode will be roughly presented.

### 3.2 Dynamic Modeling of the DFIM

The DFIM can be modeled by the next equivalent electric circuit [47].

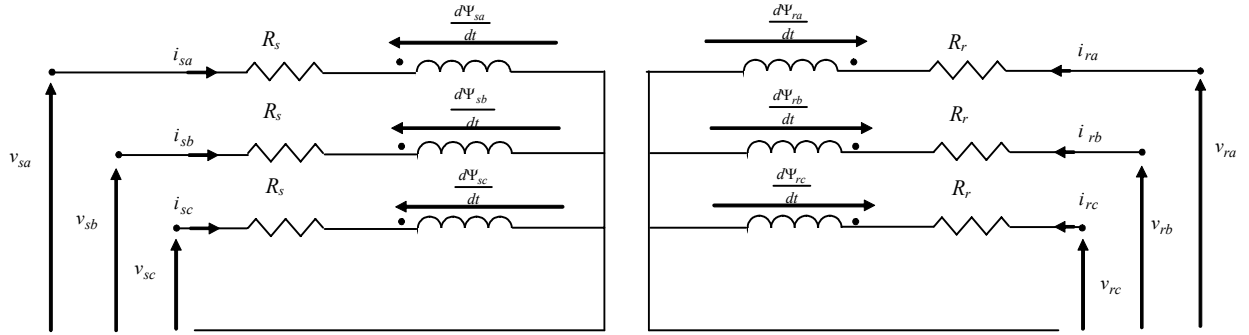


Fig. 3.1. DFIM electric equivalent circuit.

The stator voltages, current and fluxes of the machine can be described by the following electric equations [47].

$$\begin{aligned} v_{sa}(t) &= R_s \cdot i_{sa}(t) + \frac{d\Psi_{sa}(t)}{dt} \\ v_{sb}(t) &= R_s \cdot i_{sb}(t) + \frac{d\Psi_{sb}(t)}{dt} \\ v_{sc}(t) &= R_s \cdot i_{sc}(t) + \frac{d\Psi_{sc}(t)}{dt} \end{aligned} \quad (3.1)$$

where  $R_s$  is the stator resistance,  $i_{sa}(t)$ ,  $i_{sb}(t)$  and  $i_{sc}(t)$  are the stator currents of phase a, b and c.  $v_{sa}(t)$ ,  $v_{sb}(t)$  and  $v_{sc}(t)$  are the stator voltages and  $\Psi_{sa}(t)$ ,  $\Psi_{sb}(t)$  and  $\Psi_{sc}(t)$  are the stator fluxes. At steady-state operation conditions, the stator electric magnitudes vary sinusoidally with a constant pulsation of  $\omega_s$ .

Similarly, the rotor magnitudes are described by:

$$\begin{aligned} v_{ra}(t) &= R_r \cdot i_{ra}(t) + \frac{d\Psi_{ra}(t)}{dt} \\ v_{rb}(t) &= R_r \cdot i_{rb}(t) + \frac{d\Psi_{rb}(t)}{dt} \\ v_{rc}(t) &= R_r \cdot i_{rc}(t) + \frac{d\Psi_{rc}(t)}{dt} \end{aligned} \quad (3.2)$$

where  $R_r$  is the rotor resistance,  $i_{ra}(t)$ ,  $i_{rb}(t)$  and  $i_{rc}(t)$  are the rotor currents of phase a, b and c.  $v_{ra}(t)$ ,  $v_{rb}(t)$  and  $v_{rc}(t)$  are the rotor voltages and  $\Psi_{ra}(t)$ ,  $\Psi_{rb}(t)$  and  $\Psi_{rc}(t)$  are the rotor fluxes. At steady-state operation conditions the rotor magnitudes again vary sinusoidally but in this case, at constant pulsation  $\omega_r$ .

### 3.2.1 Space Vector Notation of the DFIM

The space vector notation, is a commonly extended tool to represent the flux, voltage and current magnitudes of the machine in a compact manner. Thus, a three phase magnitude ( $x_a$ ,  $x_b$  and  $x_c$ ) can be represented by a space vector ( $\vec{x}^s$ ) as follows [7]:

$$\vec{x}^s = x_\alpha + j \cdot x_\beta = \frac{2}{3} \left( x_a + a \cdot x_b + a^2 \cdot x_c \right) \quad (3.3)$$

Where

$$a = e^{j \frac{2\pi}{3}} \quad (3.4)$$

The constant 2/3 is chosen to scale the space vectors according to the maximum amplitude of the three phase magnitudes.

The subscript “s” denotes that the space vector is referred to the reference frame of the stator of the DFIM.

Added to this, thanks to the space vector notation, the three phase magnitudes may be represented by a rotating space vector, that can also be represented by two phase magnitudes ( $x_\alpha$  and  $x_\beta$ ) in the real-imaginary plane, as illustrated in Fig. 3.2.

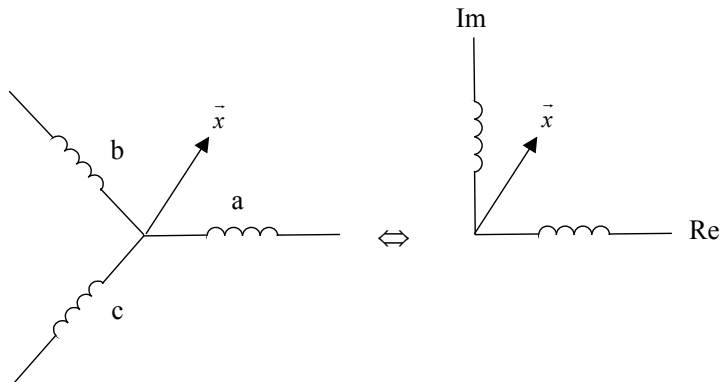


Fig. 3.2. Space vector principle.

Hence, in general a space vector can be expressed as:

$$\vec{x}^s = \hat{x} \cdot e^{j(\theta_s + \phi)} \quad (3.5)$$

Where  $\hat{x}$  is the amplitude,  $\phi$  is the phase shift and  $\theta_s$  is the rotation position that can be calculated from:

$$\theta_s = \int \omega_s dt \quad (3.6)$$

In general, three different reference frames are used to express the different magnitudes of the DFIM in space vector notation.

1. The stator reference frame (α-β): Aligned with the stator, the rotating speed of the frame is zero, and the space vector referenced to it, rotates at the synchronous speed  $\omega_s$ .
2. The rotor reference frame (D-Q): Aligned with the rotor, the rotating speed of the frame is the speed of the rotor  $\omega_m$ , and the space vector referenced to it rotates at the slip speed  $\omega_r$ .

$$\vec{x}^r = x_D + j \cdot x_Q = e^{-j\theta_m} \cdot \vec{x}^s \quad (3.7)$$

being

$$\theta_m = \int \omega_m dt \quad (3.8)$$

3. The synchronous reference frame (d-q): The rotating speed of the frame is the synchronous speed  $\omega_s$ , and the space vector referenced to it does not rotate, i.e. it presents constant real and imaginary parts.

$$\vec{x}^a = x_d + j \cdot x_q = e^{-j\theta_s} \cdot \vec{x}^s \quad (3.9)$$

or

$$\vec{x}^a = x_d + j \cdot x_q = e^{-j\theta_r} \cdot \vec{x}^r \quad (3.10)$$

being

$$\theta_r = \int \omega_r dt \quad (3.11)$$

and

$$\omega_r + \omega_m = \omega_s \quad (3.12)$$

The different reference frame representations are shown in Fig. 3.3.

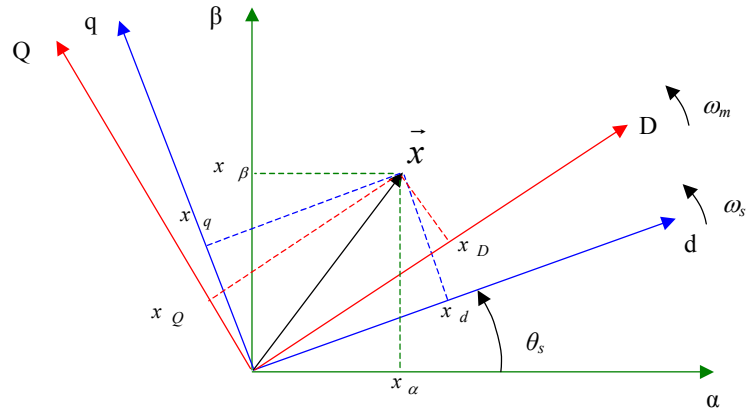


Fig. 3.3 Space vector representation in different reference frames.

### 3.2.2 $\alpha\beta$ Model

In this section, the model of the DFIM is developed using the space vector representation in the stator reference frame. Hence, the voltage equations (3.1) and (3.2) transformed to the space vector notation using expression (3.3), lead to:

$$\vec{v}_s^s = R_s \cdot \vec{i}_s^s + \frac{d\vec{\Psi}_s^s}{dt} \quad (3.13)$$

$$\vec{v}_r^r = R_r \cdot \vec{i}_r^r + \frac{d\vec{\Psi}_r^r}{dt} \quad (3.14)$$

where  $\vec{v}_s^s$  is the stator space voltage vector,  $\vec{i}_s^s$  is the stator current space vector and  $\vec{\Psi}_s^s$  is the stator flux space vector. The equation (3.13) is represented in stator coordinates.  $\vec{v}_r^r$  is the rotor voltage space vector,  $\vec{i}_r^r$  is the rotor current and  $\vec{\Psi}_r^r$  is the rotor flux space vector. The equation (3.14) is represented in rotor coordinates.

On the other hand, the relation between the fluxes and the currents, in space vector notation is:

$$\vec{\Psi}_s^s = L_s \cdot \vec{i}_s^s + L_h \cdot \vec{i}_r^s = L_s \cdot \vec{i}_s^s + L_h \cdot e^{j\theta_m} \cdot \vec{i}_r^r \quad (3.15)$$

$$\vec{\Psi}_r^r = L_h \cdot \vec{i}_s^r + L_r \cdot \vec{i}_r^r = L_h \cdot e^{-j\theta_m} \cdot \vec{i}_s^s + L_r \cdot \vec{i}_r^r \quad (3.16)$$

where  $L_s$  and  $L_r$  are the stator and rotor self inductances,  $L_h$  is the mutual inductance and they are related to the stator leakage inductance  $L_{\sigma s}$  and the rotor leakage inductance  $L_{\sigma r}$ , according to the following expressions.

$$L_s = L_{\sigma s} + L_h \quad (3.17)$$

$$L_r = L_{\sigma r} + L_h \quad (3.18)$$

Consequently, the  $\alpha\beta$  model of the DFIM is obtained by the equations in stator coordinates:

$$\vec{v}_s^s = R_s \cdot \vec{i}_s^s + \frac{d\vec{\Psi}_s^s}{dt} \quad (3.19)$$

$$\vec{v}_r^s = R_r \cdot \vec{i}_r^s + \frac{d\vec{\Psi}_r^s}{dt} - j \cdot \omega_m \cdot \vec{\Psi}_r^s \quad (3.20)$$

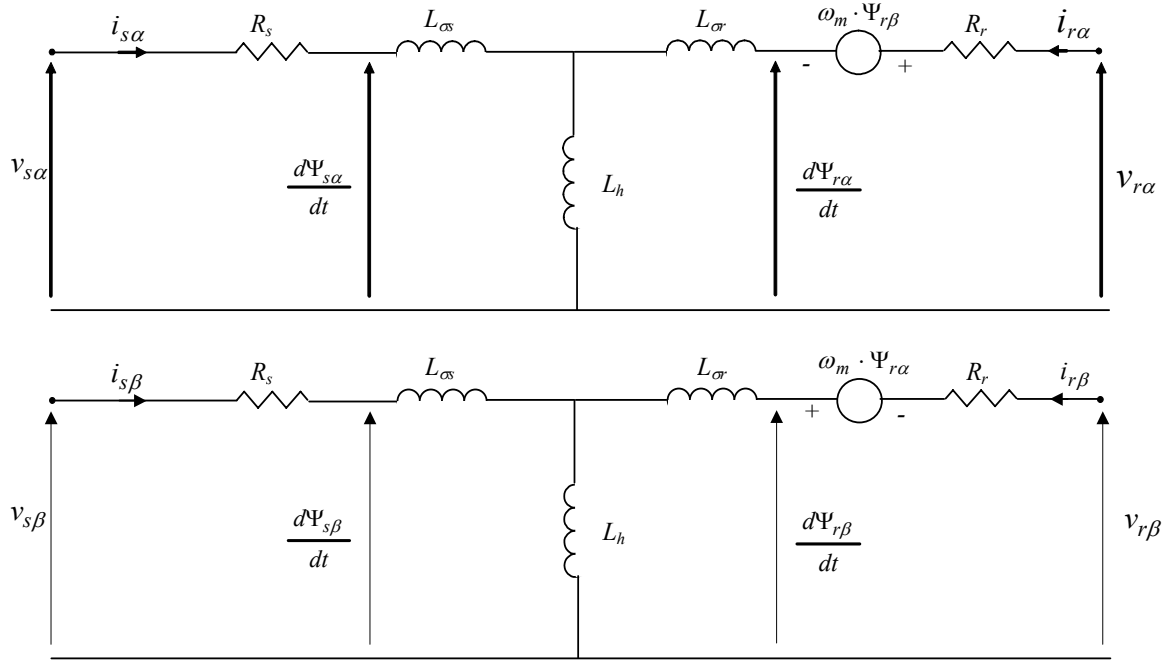
$$\vec{\Psi}_s^s = L_s \cdot \vec{i}_s^s + L_h \cdot \vec{i}_r^s \quad (3.21)$$

$$\vec{\Psi}_r^s = L_h \cdot \vec{i}_s^s + L_r \cdot \vec{i}_r^s \quad (3.22)$$

Note that:

$$\frac{d\vec{\Psi}_r^r}{dt} \cdot e^{j\theta_m} = \frac{d(\vec{\Psi}_r^r \cdot e^{j\theta_m})}{dt} - j \cdot \omega_m \cdot \vec{\Psi}_r^r \cdot e^{j\theta_m} \quad (3.23)$$

Fig. 3.4 shows the  $\alpha\beta$  model of the DFIM in stator coordinates.


 Fig. 3.4.  $\alpha\beta$  model of the DFIM in stator coordinates.

The electric power in the stator side and in the rotor side is calculated as follows:

$$P_s = \frac{3}{2} \operatorname{Re} \left\{ \vec{v}_s \cdot \vec{i}_s^* \right\} = \frac{3}{2} (v_{s\alpha} \cdot i_{s\alpha} + v_{s\beta} \cdot i_{s\beta}) \quad (3.24)$$

$$P_r = \frac{3}{2} \operatorname{Re} \left\{ \vec{v}_r \cdot \vec{i}_r^* \right\} = \frac{3}{2} (v_{r\alpha} \cdot i_{r\alpha} + v_{r\beta} \cdot i_{r\beta}) \quad (3.25)$$

$$Q_s = \frac{3}{2} \operatorname{Im} \left\{ \vec{v}_s \cdot \vec{i}_s^* \right\} = \frac{3}{2} (v_{s\beta} \cdot i_{s\alpha} - v_{s\alpha} \cdot i_{s\beta}) \quad (3.26)$$

$$Q_r = \frac{3}{2} \operatorname{Im} \left\{ \vec{v}_r \cdot \vec{i}_r^* \right\} = \frac{3}{2} (v_{r\beta} \cdot i_{r\alpha} - v_{r\alpha} \cdot i_{r\beta}) \quad (3.27)$$

Finally, the torque can be found from:

$$\begin{aligned} T_{em} &= \frac{3}{2} p \cdot \operatorname{Im} \left\{ \vec{\Psi}_r^* \cdot \vec{i}_r \right\} = \frac{3}{2} p \cdot \operatorname{Im} \left\{ \vec{\Psi}_s \cdot \vec{i}_r^* \right\} = \frac{3}{2} p \cdot \operatorname{Im} \left\{ \vec{\Psi}_s^* \cdot \vec{i}_s \right\} \\ &= \frac{3}{2} \frac{L_h}{L_r} p \cdot \operatorname{Im} \left\{ \vec{\Psi}_r \cdot \vec{i}_s^* \right\} = \frac{3}{2} \frac{L_h}{\sigma \cdot L_r \cdot L_s} p \cdot \operatorname{Im} \left\{ \vec{\Psi}_r^* \cdot \vec{\Psi}_s \right\} = \frac{3}{2} L_h \cdot p \cdot \operatorname{Im} \left\{ \vec{i}_s \cdot \vec{i}_r^* \right\} \end{aligned} \quad (3.28)$$

where  $\sigma = 1 - L_h^2 / (L_s \cdot L_r)$  is the leakage coefficient and  $p$  the pair of poles of the machine. Note that for simplicity in the notation, the superscript “s” has been removed from the power and torque expressions.

### 3.2.3 dq Model

In this section, the model of the DFIM is developed using the space vector representation in the synchronous reference frame. From equations (3.13) and (3.14), applying (3.9) and (3.10), the stator and rotor voltage equations yields:

$$\vec{v}_s^a = R_s \cdot \vec{i}_s^a + \frac{d\vec{\Psi}_s^a}{dt} + j \cdot \omega_s \cdot \vec{\Psi}_s^a \quad (3.29)$$

$$\vec{v}_r^a = R_r \cdot \vec{i}_r^a + \frac{d\vec{\Psi}_r^a}{dt} + j \cdot (\omega_s - \omega_m) \cdot \vec{\Psi}_r^a \quad (3.30)$$

From equations (3.15) and (3.16), the flux expressions yields:

$$\vec{\Psi}_s^a = L_s \cdot \vec{i}_s^a + L_h \cdot \vec{i}_r^a \quad (3.31)$$

$$\vec{\Psi}_r^a = L_h \cdot \vec{i}_s^a + L_r \cdot \vec{i}_r^a \quad (3.32)$$

Hence, the dq model of the DFIM in synchronous coordinates is represented in Fig. 3.5.

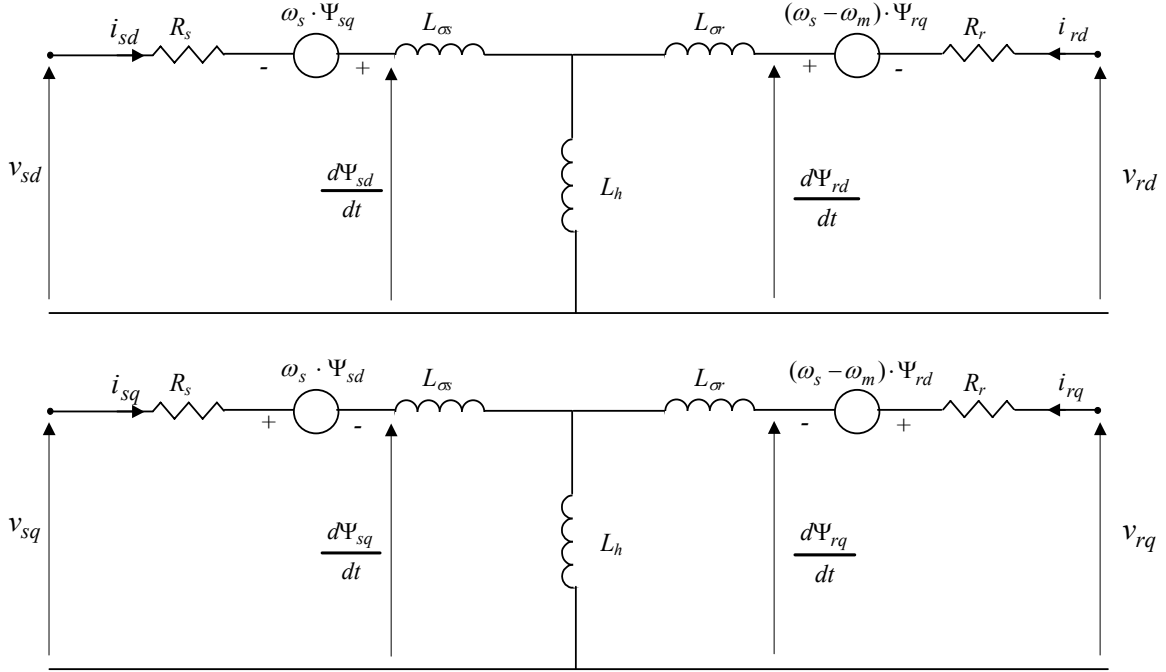


Fig. 3.5. dq model of the DFIM in synchronous coordinates.

The torque and the power expressions of this model, are equivalent to the  $\alpha\beta$  model:

$$P_s = \frac{3}{2} \operatorname{Re} \left\{ \vec{v}_s \cdot \vec{i}_s^* \right\} = \frac{3}{2} \left( v_{sd} \cdot i_{sd} + v_{sq} \cdot i_{sq} \right) \quad (3.33)$$

$$P_r = \frac{3}{2} \operatorname{Re} \left\{ \vec{v}_r \cdot \vec{i}_r^* \right\} = \frac{3}{2} \left( v_{rd} \cdot i_{rd} + v_{rq} \cdot i_{rq} \right) \quad (3.34)$$

$$Q_s = \frac{3}{2} \operatorname{Im} \left\{ \vec{v}_s \cdot \vec{i}_s^* \right\} = \frac{3}{2} \left( v_{sq} \cdot i_{sd} - v_{sd} \cdot i_{sq} \right) \quad (3.35)$$

$$Q_r = \frac{3}{2} \operatorname{Im} \left\{ \vec{v}_r \cdot \vec{i}_r^* \right\} = \frac{3}{2} \left( v_{rq} \cdot i_{rd} - v_{rd} \cdot i_{rq} \right) \quad (3.36)$$

$$\begin{aligned} T_{em} &= \frac{3}{2} p \cdot \operatorname{Im} \left\{ \vec{\Psi}_r^* \cdot \vec{i}_r \right\} = \frac{3}{2} p \cdot \operatorname{Im} \left\{ \vec{\Psi}_s \cdot \vec{i}_r^* \right\} = \frac{3}{2} p \cdot \operatorname{Im} \left\{ \vec{\Psi}_s^* \cdot \vec{i}_s \right\} = \\ &= \frac{3}{2} \frac{L_h}{L_r} p \cdot \operatorname{Im} \left\{ \vec{\Psi}_r \cdot \vec{i}_s^* \right\} = \frac{3}{2} \frac{L_h}{\sigma \cdot L_r \cdot L_s} p \cdot \operatorname{Im} \left\{ \vec{\Psi}_r^* \cdot \vec{\Psi}_s \right\} = \frac{3}{2} L_h \cdot p \cdot \operatorname{Im} \left\{ \vec{i}_s \cdot \vec{i}_r^* \right\} \end{aligned} \quad (3.37)$$

### 3.2.4 State-Space Representation of $\alpha\beta$ Model

A representation of the  $\alpha\beta$  model in state-space equations is very useful for simulation purposes. Rearranging the equations (3.19)-(3.22), and taking the fluxes as state-space magnitudes, the model of the DFIM is given by:

$$\frac{d}{dt} \begin{bmatrix} \Psi_{\alpha s} \\ \Psi_{\beta s} \\ \Psi_{\alpha r} \\ \Psi_{\beta r} \end{bmatrix} = \begin{bmatrix} -R_s & 0 & \frac{R_s \cdot L_h}{\sigma \cdot L_s \cdot L_r} & 0 \\ \frac{\sigma \cdot L_s}{\sigma \cdot L_s} & -R_s & 0 & \frac{R_s \cdot L_h}{\sigma \cdot L_s \cdot L_r} \\ 0 & \frac{\sigma \cdot L_s}{\sigma \cdot L_s} & 0 & \frac{R_s \cdot L_h}{\sigma \cdot L_s \cdot L_r} \\ \frac{R_r \cdot L_h}{\sigma \cdot L_s \cdot L_r} & 0 & \frac{-R_r}{\sigma \cdot L_r} & -\omega_m \\ \frac{R_r \cdot L_h}{\sigma \cdot L_s \cdot L_r} & 0 & \frac{R_r}{\sigma \cdot L_r} & \omega_m \end{bmatrix} \cdot \begin{bmatrix} \Psi_{\alpha s} \\ \Psi_{\beta s} \\ \Psi_{\alpha r} \\ \Psi_{\beta r} \end{bmatrix} + \begin{bmatrix} v_{\alpha s} \\ v_{\beta s} \\ v_{\alpha r} \\ v_{\beta r} \end{bmatrix} \quad (3.38)$$

If instead of the fluxes, the currents are chosen as state-space magnitudes, the equivalent model of the DFIM is expressed as follows:

$$\begin{aligned} \frac{d}{dt} \begin{bmatrix} i_{\alpha s} \\ i_{\beta s} \\ i_{\alpha r} \\ i_{\beta r} \end{bmatrix} = & \begin{bmatrix} -R_s & \frac{\omega_m \cdot L_h^2}{\sigma \cdot L_s \cdot L_r} & \frac{R_r \cdot L_h}{\sigma \cdot L_s \cdot L_r} & \frac{\omega_m \cdot L_h}{\sigma \cdot L_s} \\ \frac{-\omega_m \cdot L_h^2}{\sigma \cdot L_s \cdot L_r} & -R_s & \frac{-\omega_m \cdot L_h}{\sigma \cdot L_s} & \frac{R_r \cdot L_h}{\sigma \cdot L_s \cdot L_r} \\ \frac{R_s \cdot L_h}{\sigma \cdot L_s \cdot L_r} & \frac{-\omega_m \cdot L_h}{\sigma \cdot L_r} & \frac{-R_r}{\sigma \cdot L_r} & \frac{-\omega_m}{\sigma} \\ \frac{\omega_m \cdot L_h}{\sigma \cdot L_r} & \frac{R_s \cdot L_h}{\sigma \cdot L_s \cdot L_r} & \frac{\omega_m}{\sigma} & \frac{-R_r}{\sigma \cdot L_r} \end{bmatrix} \cdot \begin{bmatrix} i_{\alpha s} \\ i_{\beta s} \\ i_{\alpha r} \\ i_{\beta r} \end{bmatrix} + \\ & + \begin{bmatrix} \frac{1}{\sigma \cdot L_s} & 0 & \frac{-L_h}{\sigma \cdot L_s \cdot L_r} & 0 \\ 0 & \frac{1}{\sigma \cdot L_s} & 0 & -L_h \\ \frac{-L_h}{\sigma \cdot L_s \cdot L_r} & 0 & \frac{1}{\sigma \cdot L_r} & 0 \\ 0 & \frac{-L_h}{\sigma \cdot L_s \cdot L_r} & 0 & \frac{1}{\sigma \cdot L_r} \end{bmatrix} \cdot \begin{bmatrix} v_{\alpha s} \\ v_{\beta s} \\ v_{\alpha r} \\ v_{\beta r} \end{bmatrix} \end{aligned} \quad (3.39)$$

### 3.3 Dynamic Modeling of the DFIM Considering the Iron Loss

The models developed in the previous section do not take into account the core loss that may be present in the DFIM. In this section, the  $\alpha\beta$  and the dq models of the DFIM will be developed considering the iron loss. Traditionally, most of the models have ignored this phenomena causing inaccuracies in the control strategies based on these models. Consequently, in order to develop a model as close as possible to the real machine, the iron loss will be introduced in the machine's model equations. In general, low power machines present higher power loss than big power machines.

#### 3.3.1 $\alpha\beta$ Model

In this section, the model of the DFIM is developed using the space vector representation in the stator reference frame and considering the iron loss. The voltage equations (3.19) and (3.20) are still valid for this model:

$$\vec{v}_s^s = R_s \cdot \vec{i}_s^s + \frac{d\vec{\Psi}_s^s}{dt} \quad (3.40)$$

$$\vec{v}_r^r = R_r \cdot \vec{i}_r^r + \frac{d\vec{\Psi}_r^s}{dt} - j \cdot \omega_m \cdot \vec{\Psi}_r^s \quad (3.41)$$

The iron loss of the machine is modeled as a resistance in parallel to the mutual self inductance of each phase [58], as shown in Fig. 3.6.

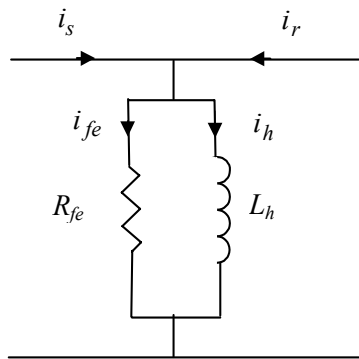


Fig. 3.6. Iron loss modeling.

This resistance  $R_{fe}$ , provokes an active current consumption ( $\vec{i}_{fe}^s$ ) but does not create flux. The flux is created by the current that goes through the mutual self inductance ( $\vec{i}_h^s$ ) and the leakage inductances. Hence, the flux expressions are given by:

$$\vec{\Psi}_s^s = L_{\sigma s} \cdot \vec{i}_s^s + L_h \cdot \vec{i}_h^s \quad (3.42)$$

$$\vec{\Psi}_r^s = L_h \cdot \vec{i}_h^s + L_{\sigma r} \cdot \vec{i}_r^s \quad (3.43)$$

Additionally, from the current and voltage relations, two more expressions are deduced:

$$\vec{i}_s^s + \vec{i}_r^s = \vec{i}_{fe}^s + \vec{i}_h^s \quad (3.44)$$

$$R_{fe} \cdot \vec{i}_{fe}^s = L_h \cdot \frac{d\vec{i}_h^s}{dt} \quad (3.45)$$

Fig. 3.7 shows the model of the DFIM in stator coordinates, considering the iron loss.

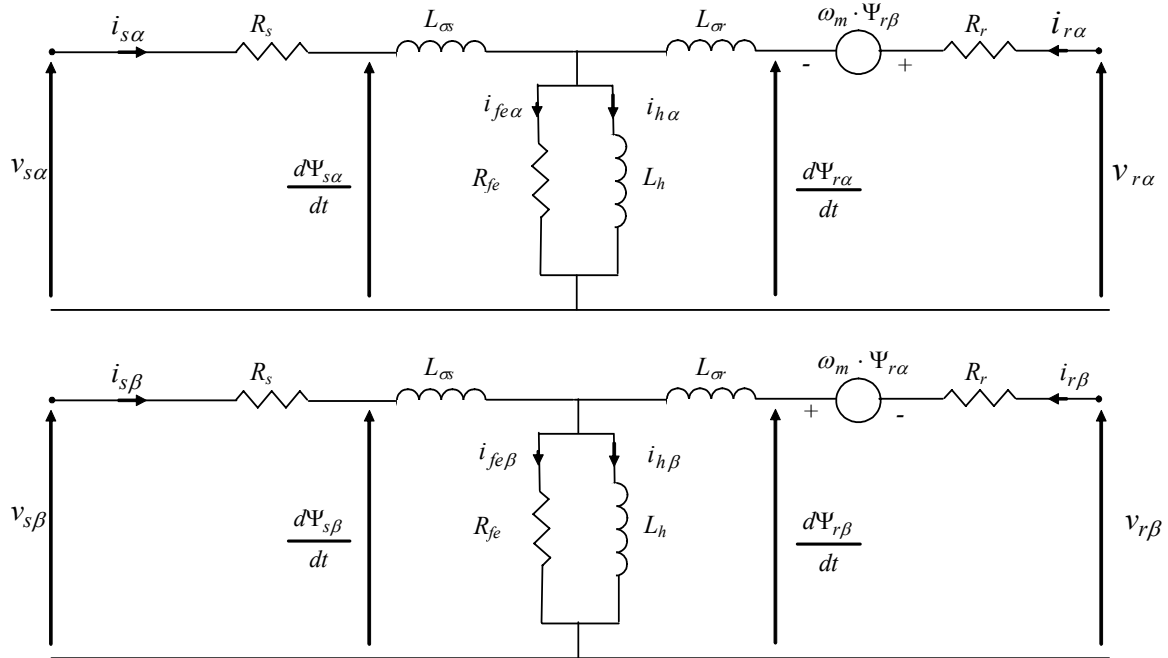


Fig. 3.7.  $\alpha\beta$  model of the DFIM in stator coordinates considering the iron loss.

On the other hand, the instantaneous power transmitted through the rotor and the stator is calculated as follows using the space vector notation:

$$\begin{aligned} p_s(t) &= v_{sa}(t) \cdot i_{sa}(t) + v_{sb}(t) \cdot i_{sb}(t) + v_{sc}(t) \cdot i_{sc}(t) = \\ &= \frac{3}{2} \cdot (v_{s\alpha} \cdot i_{s\alpha} + v_{s\beta} \cdot i_{s\beta}) = \frac{3}{2} \cdot \operatorname{Re}\left\{\vec{v}_s \cdot \vec{i}_s^*\right\} \end{aligned} \quad (3.46)$$

$$\begin{aligned} p_r(t) &= v_{ra}(t) \cdot i_{ra}(t) + v_{rb}(t) \cdot i_{rb}(t) + v_{rc}(t) \cdot i_{rc}(t) = \\ &= \frac{3}{2} \cdot (v_{r\alpha} \cdot i_{r\alpha} + v_{r\beta} \cdot i_{r\beta}) = \frac{3}{2} \cdot \operatorname{Re}\left\{\vec{v}_r \cdot \vec{i}_r^*\right\} \end{aligned} \quad (3.47)$$

Therefore, the total instantaneous power of the machine ( $p(t)$ ), is the sum of the stator and the rotor instantaneous powers. Note that in a balanced three phase system (with no zero sequence current component), the active power ( $P$ ) is equivalent to the instantaneous power ( $p(t)$ ).

$$\begin{aligned} p(t) &= \frac{3}{2} \cdot (v_{s\alpha} \cdot i_{s\alpha} + v_{s\beta} \cdot i_{s\beta}) + \frac{3}{2} \cdot (v_{r\alpha} \cdot i_{r\alpha} + v_{r\beta} \cdot i_{r\beta}) = \\ &= \frac{3}{2} \cdot \operatorname{Re}\left\{\vec{v}_s \cdot \vec{i}_s^*\right\} + \frac{3}{2} \cdot \operatorname{Re}\left\{\vec{v}_r \cdot \vec{i}_r^*\right\} \end{aligned} \quad (3.48)$$

By substituting expressions (3.40) and (3.41), the total power is given by:

$$\begin{aligned} p(t) &= \frac{3}{2} R_s |\vec{i}_s|^2 + \frac{3}{2} R_r |\vec{i}_r|^2 \\ &+ \frac{3}{2} \operatorname{Re} \left\{ \frac{d\vec{\Psi}_s}{dt} \cdot \vec{i}_s^* + \frac{d\vec{\Psi}_r}{dt} \cdot \vec{i}_r^* \right\} - \frac{3}{2} \operatorname{Re} \left\{ j \cdot \omega_m \cdot \vec{\Psi}_r \cdot \vec{i}_r^* \right\} \end{aligned} \quad (3.49)$$

Where for simplicity, the superscript “s” of the space vectors have been omitted. Again substituting equations (3.42)-(3.45) in order to remove the flux derivates from the last expression:

$$\begin{aligned} p(t) &= \frac{3}{2} R_s |\vec{i}_s|^2 + \frac{3}{2} R_r |\vec{i}_r|^2 + \frac{3}{2} R_{fe} |\vec{i}_{fe}|^2 \\ &+ \frac{3}{2} \operatorname{Re} \left\{ L_{\sigma s} \frac{d\vec{i}_s}{dt} \cdot \vec{i}_s^* + L_{\sigma r} \frac{d\vec{i}_r}{dt} \cdot \vec{i}_r^* + L_h \frac{d\vec{i}_h}{dt} \cdot \vec{i}_h^* \right\} \\ &- \frac{3}{2} \operatorname{Re} \left\{ j \cdot \omega_m \cdot \vec{\Psi}_r \cdot \vec{i}_r^* \right\} \end{aligned} \quad (3.50)$$

Hence, it is possible to distinguish three different terms:

$$P_{loss} = \frac{3}{2} \cdot R_s \cdot |\vec{i}_s|^2 + \frac{3}{2} \cdot R_r \cdot |\vec{i}_r|^2 + \frac{3}{2} \cdot R_{fe} \cdot |\vec{i}_{fe}|^2 \quad (3.51)$$

Where  $P_{loss}$  represent the resistive active power losses.

$$P_{mag} = \frac{3}{2} \cdot \text{Re} \left\{ L_{\alpha\alpha} \cdot \frac{d\vec{i}_s}{dt} \cdot \vec{i}_s^* + L_{\alpha r} \cdot \frac{d\vec{i}_r}{dt} \cdot \vec{i}_r^* + L_h \cdot \frac{d\vec{i}_h}{dt} \cdot \vec{i}_h^* \right\} \quad (3.52)$$

$P_{mag}$  is the stored magnetic power, i.e. the sum of the instantaneous phase reactive powers of a balanced three phase system, is equal to zero.

$$P_{mec} = -\frac{3}{2} \cdot \text{Re} \left\{ j \cdot \omega_m \cdot \vec{\Psi}_r \cdot \vec{i}_r^* \right\} \quad (3.53)$$

And  $P_{mec}$  is the mechanical power produced by the DFIM, i.e. the power stored in the equivalent voltage source  $j \cdot \omega_m \cdot \vec{\Psi}_r$ . So using this last result, the torque produced by the machine can be calculated from the mechanical power as follows:

$$\begin{aligned} T_{em} &= \frac{P_{mec}}{\omega_m / p} = -\frac{3}{2} p \cdot \text{Re} \left\{ j \cdot \vec{\Psi}_r \cdot \vec{i}_r^* \right\} \\ &= \frac{3}{2} p \cdot \text{Im} \left\{ \vec{\Psi}_r \cdot \vec{i}_r^* \right\} = \frac{3}{2} p \cdot (\Psi_{\beta r} \cdot i_{\alpha r} - \Psi_{\alpha r} \cdot i_{\beta r}) \end{aligned} \quad (3.54)$$

Note that the equivalent torque expressions from the model without considering the iron losses (3.28) and (3.37), in this case not remain.

### 3.3.2 dq Model

In this section, the model of the DFIM is developed using the space vector representation in the synchronous reference frame and considering the core loss. The voltage equations are equivalent to the voltage equations (3.29) and (3.30), from the “classic” model of the DFIM.

$$\vec{v}_s^a = R_s \cdot \vec{i}_s^a + \frac{d\vec{\Psi}_s^a}{dt} + j \cdot \omega_s \cdot \vec{\Psi}_s^a \quad (3.55)$$

$$\vec{v}_r^a = R_r \cdot \vec{i}_r^a + \frac{d\vec{\Psi}_r^a}{dt} + j \cdot (\omega_s - \omega_m) \cdot \vec{\Psi}_r^a \quad (3.56)$$

The rest of the flux and current equations are obtained from expressions (3.42) to (3.45), transforming them to the synchronous reference frame:

$$\vec{\Psi}_s^a = L_{\sigma s} \cdot \vec{i}_s^a + L_h \cdot \vec{i}_h^a \quad (3.57)$$

$$\vec{\Psi}_r^a = L_h \cdot \vec{i}_h^a + L_{\sigma r} \cdot \vec{i}_r^a \quad (3.58)$$

$$\vec{i}_s^a + \vec{i}_r^a = \vec{i}_{fe}^a + \vec{i}_h^a \quad (3.59)$$

$$R_{fe} \cdot \vec{i}_{fe}^a = L_h \cdot \frac{d\vec{i}_h^a}{dt} + j \cdot \omega_s \cdot \vec{i}_h^a \quad (3.60)$$

Fig. 3.8 shows the model of the DFIM in synchronous coordinates considering the iron loss.

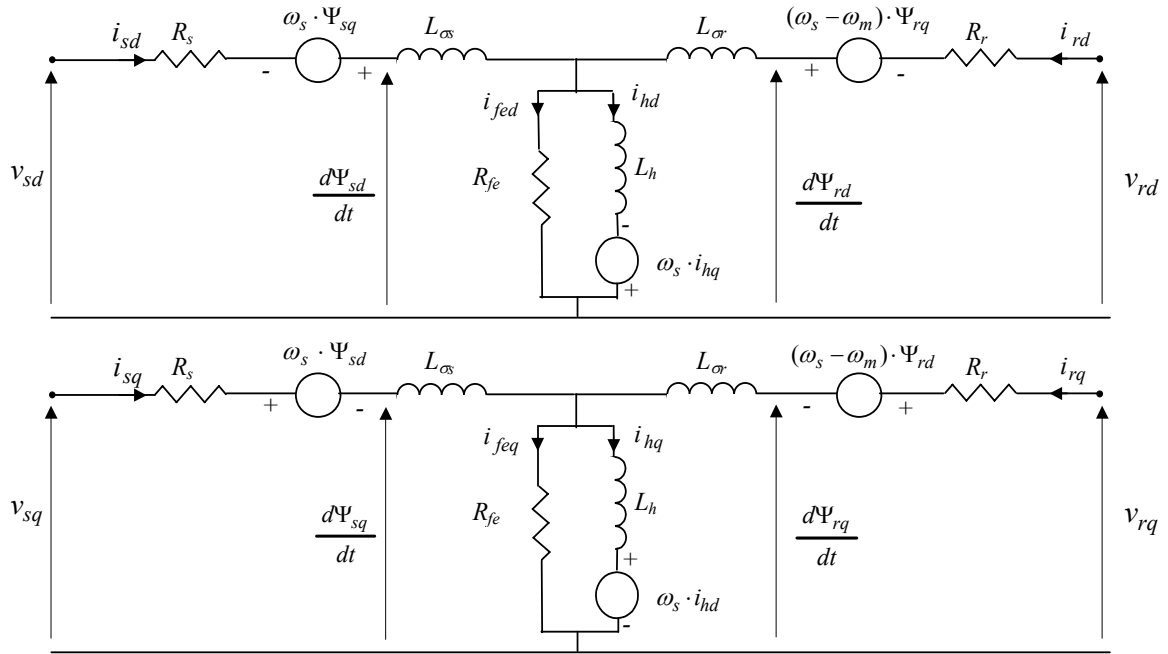


Fig. 3.8. dq model of the DFIM in synchronous coordinates, considering the iron loss.

Added to this, the instantaneous power transmitted through the rotor and the stator is calculated as follows, using the expression (3.48) in a synchronous reference frame:

$$\begin{aligned}
 p(t) &= \frac{3}{2} \cdot (v_{sd} \cdot i_{sd} + v_{sq} \cdot i_{sq}) + \frac{3}{2} \cdot (v_{rd} \cdot i_{rd} + v_{rq} \cdot i_{rq}) = \\
 &= \frac{3}{2} \cdot \text{Re} \left\{ \vec{v}_s \cdot \vec{i}_s^* \right\} + \frac{3}{2} \cdot \text{Re} \left\{ \vec{v}_r \cdot \vec{i}_r^* \right\}
 \end{aligned} \tag{3.61}$$

Substituting (3.55) and (3.56) in the last expression:

$$\begin{aligned}
 p(t) &= \frac{3}{2} \cdot R_s \cdot |\vec{i}_s|^2 + \frac{3}{2} \cdot R_r \cdot |\vec{i}_r|^2 + \frac{3}{2} \cdot \text{Re} \left\{ \frac{d\vec{\Psi}_s}{dt} \cdot \vec{i}_s^* + \frac{d\vec{\Psi}_r}{dt} \cdot \vec{i}_r^* \right\} \\
 &\quad - \frac{3}{2} \cdot \text{Re} \left\{ j \cdot \omega_s \cdot \vec{\Psi}_s \cdot \vec{i}_s^* \right\} - \frac{3}{2} \cdot \text{Re} \left\{ j \cdot (\omega_s - \omega_m) \cdot \vec{\Psi}_r \cdot \vec{i}_r^* \right\}
 \end{aligned} \tag{3.62}$$

As done in the  $\alpha\beta$  model, by substituting in this last equation the expressions (3.57)-(3.60), it leads to a equivalent expression of the power in dq coordinates (despite the fact that the original expression is slightly different):

$$\begin{aligned}
p(t) = & \frac{3}{2}R_s |\vec{i}_s|^2 + \frac{3}{2}R_r |\vec{i}_r|^2 + \frac{3}{2}R_{fe} |\vec{i}_{fe}|^2 \\
& + \frac{3}{2}\text{Re} \left\{ L_{os} \frac{d\vec{i}_s}{dt} \cdot \vec{i}_s^* + L_{or} \frac{d\vec{i}_r}{dt} \cdot \vec{i}_r^* + L_h \frac{d\vec{i}_h}{dt} \cdot \vec{i}_h^* \right\} \\
& - \frac{3}{2}\text{Re} \left\{ j\omega_m \vec{\Psi}_r \cdot \vec{i}_r^* \right\}
\end{aligned} \tag{3.63}$$

Consequently, the torque expression is calculated in the same manner:

$$\begin{aligned}
T_{em} = & \frac{P_{mec}}{\omega_m/p} = -\frac{3}{2}p \cdot \text{Re} \left\{ j\vec{\Psi}_r \cdot \vec{i}_r^* \right\} \\
= & \frac{3}{2}p \cdot \text{Im} \left\{ \vec{\Psi}_r \cdot \vec{i}_r^* \right\} = \frac{3}{2}p(\Psi_{qr} i_{dr} - \Psi_{dr} i_{qr})
\end{aligned} \tag{3.64}$$

### 3.3.3 State-Space Representation of $\alpha\beta$ Model

A representation of the  $\alpha\beta$  model in state space equations is very useful for simulation purposes. Next, one of the different state-space representation possibilities will be shown. It employs as state-space magnitudes:  $\vec{i}_s^s$ ,  $\vec{i}_r^s$  and  $\vec{i}_{fe}^s$ .

$$\frac{d}{dt} \begin{bmatrix} \vec{i}_s^s \\ \vec{i}_r^s \\ \vec{i}_{fe}^s \end{bmatrix} = \begin{bmatrix} -\frac{R_s}{L_{\sigma s}} & 0 & \left[ \begin{array}{c} -\frac{R_{fe}}{L_{\sigma s}} \\ \vec{i}_s^s \end{array} \right] \\ \left[ \begin{array}{c} j\omega_m \frac{L_h}{L_{\sigma r}} \\ -\frac{R_r}{L_{\sigma r}} + j\omega_m \frac{L_r}{L_{\sigma r}} \end{array} \right] & \left[ \begin{array}{c} -\frac{R_{fe}}{L_{\sigma r}} - j\omega_m \frac{L_h}{L_{\sigma r}} \\ \vec{i}_r^s \end{array} \right] \\ \left[ \begin{array}{c} -\frac{R_s}{L_{\sigma s}} + j\omega_m \frac{L_h}{L_{\sigma s}} \\ -\frac{R_r}{L_{\sigma r}} + j\omega_m \frac{L_r}{L_{\sigma r}} \end{array} \right] & \left[ \begin{array}{c} -R_{fe} \left( \frac{1}{L_{\sigma s}} + \frac{1}{L_{\sigma r}} + \frac{1}{L_h} \right) - j\omega_m \frac{L_h}{L_{\sigma r}} \\ \vec{i}_{fe}^s \end{array} \right] \end{bmatrix} \\ + \begin{bmatrix} \frac{1}{L_{\sigma s}} & 0 \\ 0 & \frac{1}{L_{\sigma r}} \\ \frac{1}{L_{\sigma s}} & \frac{1}{L_{\sigma r}} \end{bmatrix} \cdot \begin{bmatrix} \vec{v}_s^s \\ \vec{v}_r^s \end{bmatrix} \end{bmatrix} \quad (3.65)$$

If each space vector is replaced for its  $\alpha\beta$  components, the state-space representation yields:

$$\begin{aligned}
& \left[ \begin{array}{ccccc} \frac{R_s}{L_\infty} & 0 & 0 & 0 & 0 \\ 0 & \frac{R_s}{L_\infty} & 0 & 0 & 0 \\ 0 & -\omega_m \frac{L_h}{L_\sigma} & \frac{R_r}{L_\sigma} & -\omega_m \frac{L_r}{L_\sigma} & \frac{R_{fe}}{L_\sigma} \\ \omega_m \frac{L_h}{L_\sigma} & 0 & \omega_m \frac{L_r}{L_\sigma} & -R_r & -\omega_m \frac{L_h}{L_\sigma} \\ \frac{R_s}{L_\infty} & \omega_m \frac{L_h}{L_\sigma} & \frac{R_r}{L_\sigma} & -\omega_m \frac{L_r}{L_\sigma} & -R_{fe} \left( \frac{1}{L_\infty} + \frac{1}{L_\sigma} + \frac{1}{L_h} \right) \\ \omega_m \frac{L_h}{L_\sigma} & \frac{R_s}{L_\infty} & \omega_m \frac{L_r}{L_\sigma} & -R_r & -\omega_m \frac{L_h}{L_\sigma} \end{array} \right] \\
& = \left[ \begin{array}{ccccc} i_{\alpha s} & i_{\beta s} & i_{\alpha r} & i_{\beta r} & i_{\alpha e} \\ i_{\beta s} & i_{\alpha r} & i_{\beta r} & i_{\alpha e} & i_{\beta e} \\ i_{\alpha r} & i_{\beta r} & i_{\alpha e} & i_{\beta e} & i_{\alpha e} \\ \frac{d}{dt} & i_{\beta e} & i_{\alpha e} & i_{\beta e} & i_{\beta e} \end{array} \right] \left[ \begin{array}{c} 0 \\ \frac{R_{fe}}{L_\infty} \\ \omega_m \frac{L_h}{L_\sigma} \\ \frac{R_{fe}}{L_\sigma} \\ -R_{fe} \left( \frac{1}{L_\infty} + \frac{1}{L_\sigma} + \frac{1}{L_h} \right) \end{array} \right] \\
& + \left[ \begin{array}{ccccc} \frac{1}{L_\infty} & 0 & 0 & 0 & 0 \\ 0 & \frac{1}{L_\infty} & 0 & 0 & \begin{bmatrix} v_{\alpha s} \\ v_{\beta s} \\ v_{\alpha r} \\ v_{\beta r} \end{bmatrix} \\ 0 & 0 & \frac{1}{L_\sigma} & 0 & \begin{bmatrix} v_{\alpha s} \\ v_{\beta s} \\ v_{\alpha r} \\ v_{\beta r} \end{bmatrix} \\ \frac{1}{L_\infty} & 0 & \frac{1}{L_\sigma} & 0 & \begin{bmatrix} v_{\alpha s} \\ v_{\beta s} \\ v_{\alpha r} \\ v_{\beta r} \end{bmatrix} \\ 0 & \frac{1}{L_\infty} & 0 & \frac{1}{L_\sigma} & \begin{bmatrix} v_{\alpha s} \\ v_{\beta s} \\ v_{\alpha r} \\ v_{\beta r} \end{bmatrix} \end{array} \right]
\end{aligned} \tag{3.66}$$

### 3.4 DFIM at Steady State

In this subsection, the operation model of the DFIM will be studied at steady state, since depending on the speed of the machine and the torque that is producing, it can work in four different operation modes. This fact is presented in Fig. 3.9.

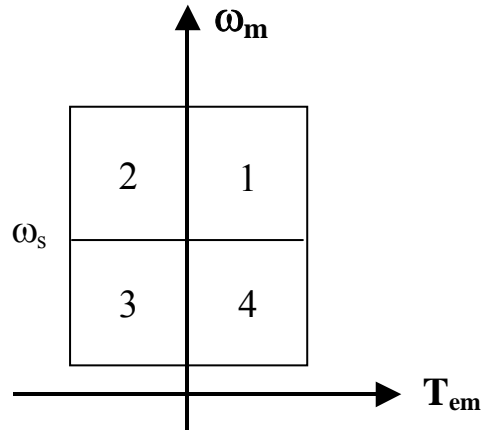


Fig. 3.9. Modes of operation of the DFIM.

On the other hand, considering the DFIM as a conservative system without electrical and mechanical losses, it is possible to use the following approximate expressions:

$$P_s + P_r = P_{mec} \quad (3.67)$$

Consequently, by taking into account the relation between the electromagnetic torque and the active powers:

$$\frac{T_{em} \cdot \omega_s}{p} - \frac{T_{em} \cdot \omega_r}{p} = \frac{T_{em} \cdot \omega_m}{p} \quad (3.68)$$

That means:

$$\omega_s = \omega_r + \omega_m \quad (3.69)$$

Hence, considering the slip ( $s$ ), the relation between the rotor and stator active power is:

$$-s \cdot P_s = P_r \quad (3.70)$$

With:

$$s = \frac{\omega_s - \omega_m}{\omega_s} \quad (3.71)$$

$$\omega_r = s \cdot \omega_s \quad (3.72)$$

Considering that the machine is operating in motor mode at constant torque but variable speed, Fig. 3.10 shows the relation between the active powers of the DFIM.

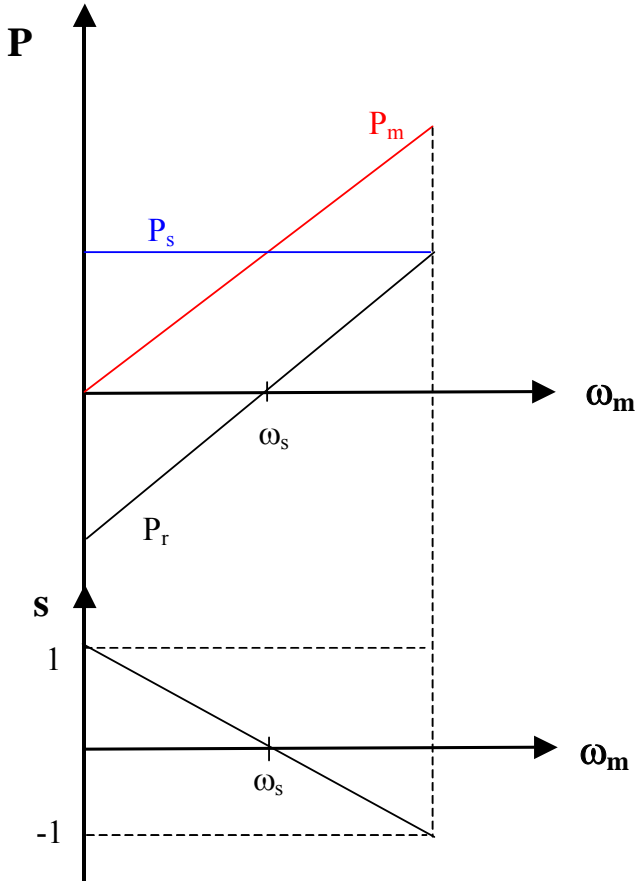


Fig. 3.10. DFIM power balance at constant electromagnetic torque.

So, taking as a reference the synchronous speed of the machine ( $\omega_s$ ), the machine can operate in four different state regions, of the speed-torque plane. More details about these operation modes are treated in the following subsections.

### 3.4.1 Mode 1. Motoring at Hypersynchronous Speed.

When the machine is operating in mode 1 at steady state, the active power flow of the machine is shown in Fig. 3.11.

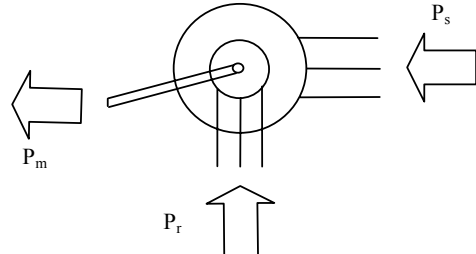


Fig. 3.11. Active power flow of the DFIM in mode 1.

On the other hand, depending on the stator reactive power consumption, two different space vector diagrams can be distinguished in mode 1, in the rotor reference frame:

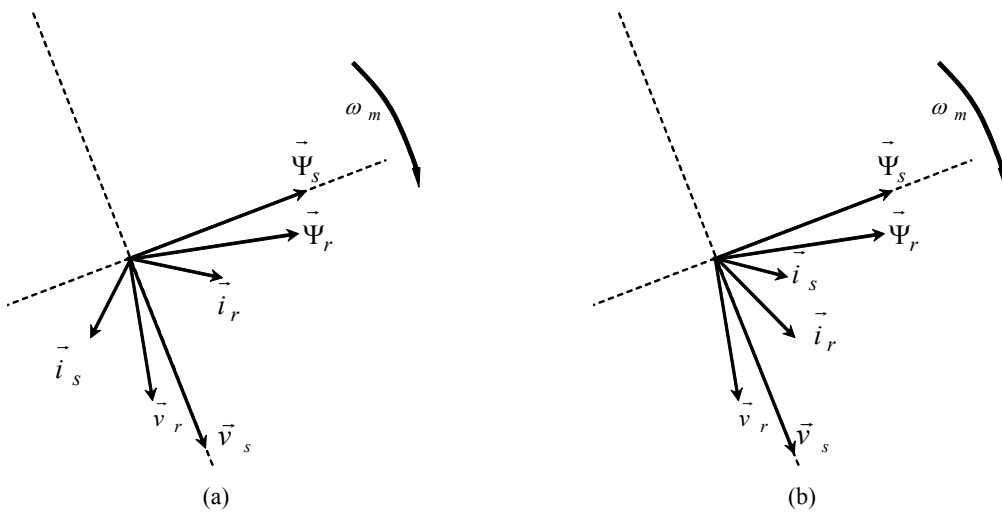


Fig. 3.12. Space Vector diagram of the DFIM in mode 1, in the rotor reference frame. (a)  $Q_s < 0$ , (b)  $Q_s > 0$ .

- The speed of the machine defines clockwise or anticlockwise rotation of the space vectors.
- The electromagnetic torque defines the relative position between the rotor flux and the stator flux, i.e. motoring or generating mode of operation on equation (3.68).
- The reactive power of the stator defines the relative position between the space vectors of the stator current and stator voltage.
- The rotor voltage space vector is always  $90^\circ$  shifted with the rotor flux vector.
- The rotor current space vector is calculated according to equations (3.21) and (3.22).

### 3.4.2 Mode 2. Generating at Hypersynchronous Speed.

When the machine is operating in mode 2 at steady state, the active power flow of the machine is shown in Fig. 3.13.

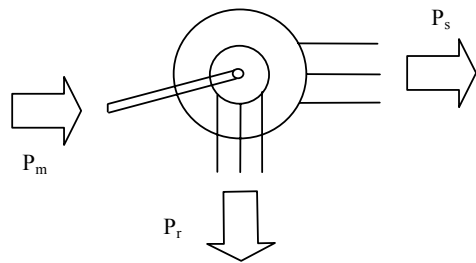


Fig. 3.13. Space Vector diagram and power flow in mode 2.

On the other hand, depending on the stator reactive power consumption, two different space vector diagrams can be distinguished in mode 2, in the rotor reference frame:

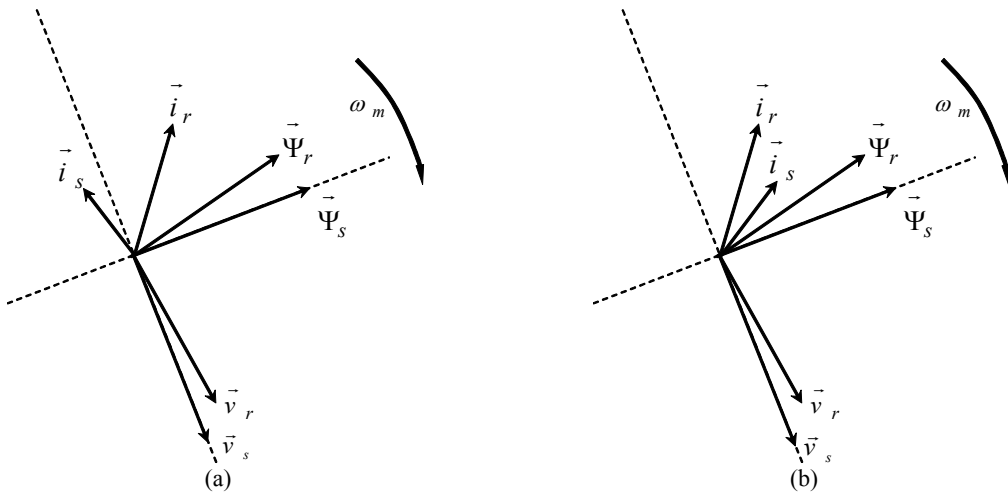


Fig. 3.14. Space Vector diagram of the DFIM in mode 2, in the rotor reference frame. (a)  $Q_s < 0$ , (b)  $Q_s > 0$ .

### 3.4.3 Mode 3. Generating at Subsynchronous Speed.

When the machine is operating in mode 3 at steady state, the active power flow of the machine is shown in Fig. 3.15.

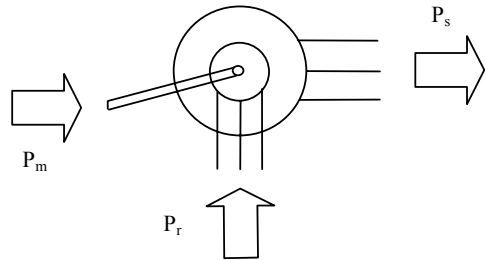


Fig. 3.15. Space Vector diagram and power flow in mode 3.

On the other hand, depending on the stator reactive power consumption, two different space vector diagrams can be distinguished in mode 3, in the rotor reference frame:

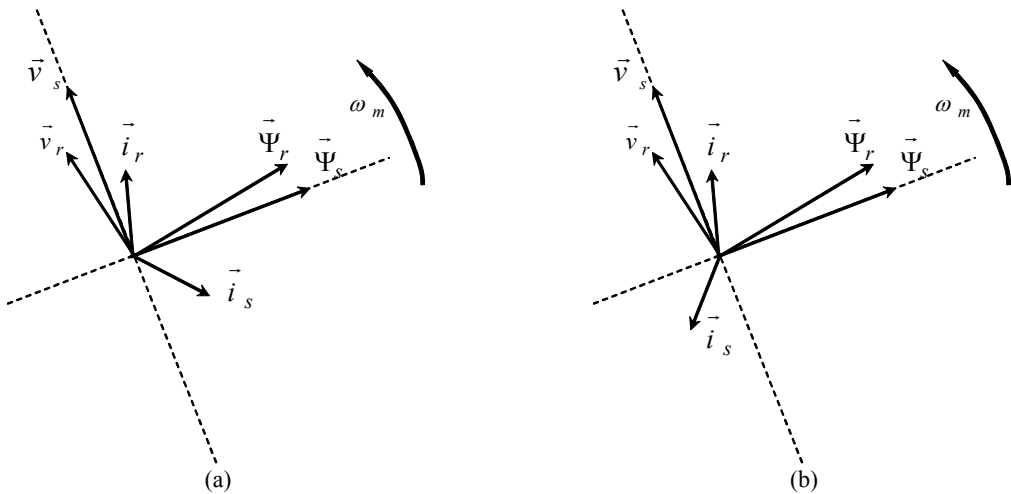


Fig. 3.16. Space Vector diagram of the DFIM in mode 3, in the rotor reference frame. (a)  $Q_s > 0$ , (b)  $Q_s < 0$ .

### 3.4.4 Mode 4. Motoring at Subsynchronous Speed.

When the machine is operating in mode 3 at steady state, the active power flow of the machine is shown in Fig. 3.17.

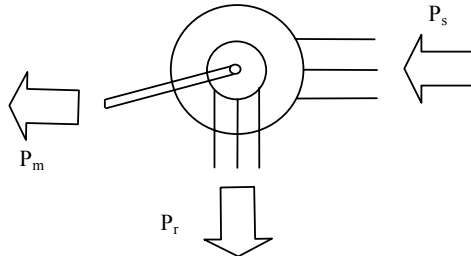


Fig. 3.17. Space Vector diagram and power flow in mode 4.

On the other hand, depending on the stator reactive power consumption, two different space vector diagrams can be distinguished in mode 4, in the rotor reference frame:

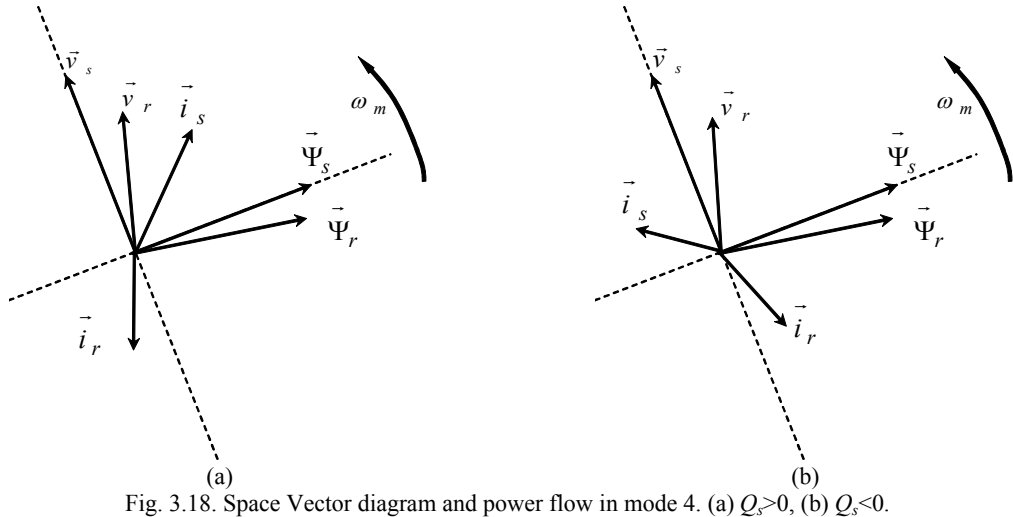


Fig. 3.18. Space Vector diagram and power flow in mode 4. (a)  $Q_s > 0$ , (b)  $Q_s < 0$ .

## 3.5 Conclusions of the Chapter

The dynamic models as well as the steady state studies described in this chapter, are one of the required background tools for the development of precedent control strategies.

*Once the model of the doubly fed induction machine is defined, in the following chapters, the control of the machine will be presented.*



## CONTENTS of Chapter 4

4 Two Level Converter Based Direct Torque Control of the Doubly Fed Induction Machine	68
4.1 Introduction.....	69
4.2 Study of Voltage Vectors Effect on the Doubly Fed Induction Machine .....	70
4.3 “Classic” Direct Torque Control (DTC) of the Doubly Fed Induction Machine (DFIM)	
74	
4.3.1 Control Block Diagram .....	74
4.3.2 Vector Selection Strategy .....	75
4.4 Predictive DTC Strategy with Reduced Torque Ripple and Constant Switching Frequency.....	78
4.4.1 Control Block Diagram .....	78
4.4.2 First Vector Selection Strategy.....	78
4.4.3 Torque Ripple Minimization Criteria at Constant Switching Frequency .....	81
4.4.4 Further Improvements Oriented to Low Switching Frequency .....	82
4.5 Predictive DTC Strategy with Reduced Torque and Flux Ripples and Constant Switching Frequency .....	83
4.5.1 Control Block Diagram .....	83
4.5.2 First vector Selection Strategy.....	84
4.5.3 Second and Third Vector Selection Strategy at Constant Switching Frequency.....	85
4.5.4 Torque and Flux Ripple Reduction Criteria at Constant Switching Frequency .....	87
4.5.5 Switching Power Losses Reduction .....	89
4.6 Simulation results .....	92
4.6.1 Overview of the Simulation Experiments .....	92
4.6.2 Transient and Steady-State Behavior for DTC Control Strategy. ....	93
4.6.3 Transient and Steady-State Behavior. Predictive DTC with Reduced Torque Ripple	
97	
4.6.4 Transient and Steady-State Behavior. Predictive DTC with Reduced Torque and Flux Ripples.....	102
4.6.5 Tracking behavior. Predictive DTC with Reduced Torque and Flux Ripples.....	108
4.7 Experimental Results .....	111
4.7.1 Overview of the Experimental Results.....	111
4.7.2 Experimental Rig.....	111
4.7.3 Steady state Operation Conditions .....	112
4.7.4 Transient Response.....	114

4.7.5	Tracking Behavior .....	116
4.7.6	Performance near Synchronism.....	118
4.8	Conclusions of the Chapter.....	120

## Chapter 4

### 4 Two Level Converter Based Direct Torque Control of the Doubly Fed Induction Machine

*In this chapter, three new different two level converter based Direct Torque Control (DTC) strategies of the Doubly Fed Induction Machine (DFIM) are presented. The first “Classic” DTC technique achieves good transient and steady-state performances but it presents non constant switching frequency behavior. Since this variable switching frequency behavior is problematic, specially in high power applications, the second DTC technique is developed, i.e. Predictive DTC strategy at constant switching frequency with reduced torque ripple. However, simulation results show that this technique presents an inefficient control of the rotor flux at low switching frequencies. This undesired fact, produces degradation in the stator and rotor currents as well, becoming this technique not useful for high power applications.*

*Consequently, to address these problems, the third control strategy is developed, i.e. Predictive DTC with reduced torque and flux ripples at constant switching frequency. It is especially designed to operate at a considerably low constant switching frequency, reducing the electromagnetic torque and rotor flux ripples, in order to provide good steady-state and fast dynamic performances. This control is convenient for high power drive and generator applications, with restricted switching frequencies. The DFIM is connected to the grid by the stator and the rotor is fed by a two level voltage source converter. In addition, this last control method allows to implement a technique that reduces the switching power losses of the converter.*

*Finally, simulation and experimental results show that the proposed predictive DTC method effectively reduces the torque and flux ripples at low switching frequency, even under variable speed operation conditions.*

## 4.1 Introduction

In this chapter, different DTC strategies for the DFIM will be presented, considering the recent developments in direct control techniques mentioned in the state of the art of the first Chapter. The DTC is based on a direct control of two magnitudes of the machine, i.e. the electromagnetic torque and the rotor flux of the machine. The background theory of DTC studied in this chapter, embraces the basic principles of the control strategies that will be developed and described in precedent chapters.

Hence, first of all the simplest version of DTC will be described, the “classic” DTC strategy. Simulation results will show that this technique provides with fast dynamic response and good quality of steady state in terms of stator current distortion. However it presents an important drawback: i.e. variable switching frequency behavior. For that reason, an improved version of DTC is developed then, namely, predictive DTC with reduced torque ripple. It operates at constant switching frequency by employing a sequence of one active vector and one zero vector at steady state, and it provides good steady and transient state performances. In contrast, simulation results at lower constant switching frequencies, uncovered a deterioration of the rotor flux control, that produces a degradation of the stator currents interchanged by the DFIM with the grid. This fact provokes that this control technique is not suitable for many high power applications that require to operate within the severity of low switching frequencies.

Consequently, in order to provide the capacity to operate at low switching frequencies, the third DTC strategy is developed, i.e. the predictive DTC with reduced torque and flux ripples. By employing a sequence of two active vectors and one zero vector per switching period, it is able to operate at low switching frequency with good steady state behavior and keeping the fast dynamic response capacity of direct control techniques. In addition, simulation and experimental results apart from corroborating these capacities at “low” and “high” switching frequencies, shows that this technique is also able to provide a good tracking behavior, making it suitable for several high power applications such as the wind energy generation.

Finally, it must be stressed that although the high power and medium voltage wind turbine designed in chapter 2, requires a rotor side filter in order to mitigate the current and torque ripples of the machine, for simplicity in the exposition, it will not be considered neither in this chapter nor in the next chapter. Thus, the performance of the proposed control strategies will be analyzed, under severe power and torque ripples scenario.

Afterwards, once the basic principles of the predictive direct control techniques are presented in chapter 4 and 5, the wind turbine scenario defined in chapter 2 will be considered in chapter 6.

## 4.2 Study of Voltage Vectors Effect on the Doubly Fed Induction Machine

The DTC strategy as it was initially developed, determines rotor voltage vectors in order to control directly the rotor flux and the electromagnetic torque of the machine [31]. Depending on the operation conditions of the machine and the position of the rotor and stator flux space vectors expressed in the rotor reference frame, the rotor voltage vectors affect the torque in a different manner. For that reason, in this first section before defining the control technique, the study of the voltage vector effect will be carried out.

From expression (3.28), the torque can be represented as a function of the angle  $\delta$  between the stator and the rotor fluxes space vectors as follows:

$$T_{em} = \frac{3}{2} p \frac{L_h}{\sigma L_s L_r} |\vec{\Psi}_r \parallel \vec{\Psi}_s| \sin \delta \quad (4.1)$$

When the speed of the machine is higher than the synchronous speed, as the space vectors rotate clockwise, the effect of the zero vectors on the electromagnetic torque for example, is the opposite at lower speeds than the synchronous speed. The corresponding space vector representation of the fluxes in the rotor reference frame [48] is illustrated in Fig. 4.1.

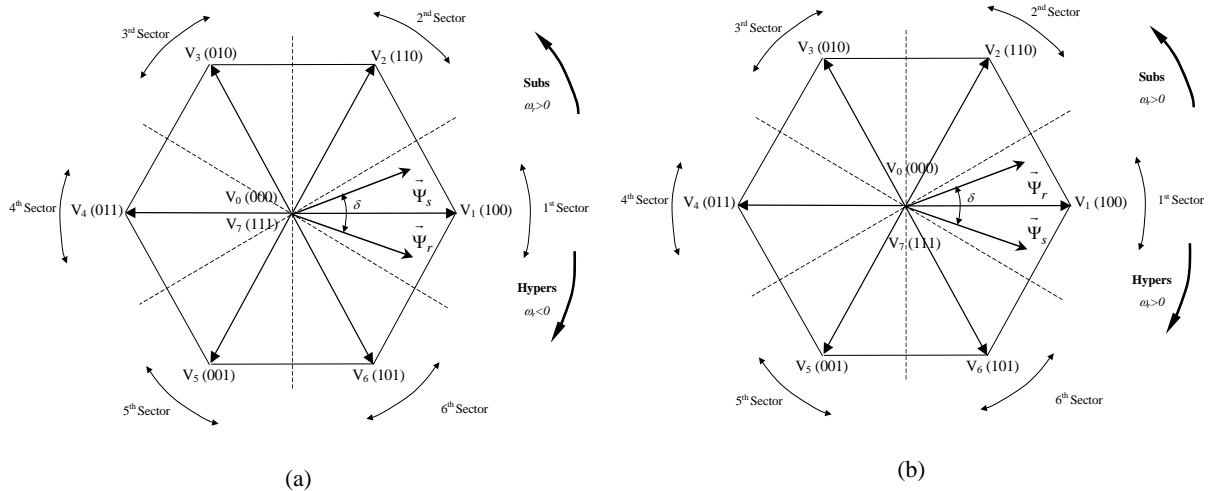


Fig. 4.1 Flux space vectors in the rotor reference frame, in motor and generator modes. (a) Motor mode, (b) Generator mode.

For predictive purposes, the torque and the flux derivative expressions are presented next, deduced from equations (3.19)-(3.22) in the stator reference frame.

$$\frac{d|\vec{\Psi}_r|}{dt} = \frac{1}{|\vec{\Psi}_r|} \left[ \left( \frac{R_r L_h}{\sigma L_s L_r} \right) \operatorname{Re} \left\{ \vec{\Psi}_r \cdot \vec{\Psi}_s^* \right\} - \left( \frac{R_r}{\sigma L_r} \right) |\vec{\Psi}_r|^2 + \operatorname{Re} \left\{ \vec{\Psi}_r \cdot \vec{v}_r^* \right\} \right] \quad (4.2)$$

$$\begin{aligned} \frac{dT_{em}}{dt} = & \frac{3}{2} p \frac{L_h}{\sigma L_s L_r} \left[ \left( \frac{R_s}{\sigma L_s} + \frac{R_r}{\sigma L_r} \right) \operatorname{Im} \left\{ \vec{\Psi}_r \cdot \vec{\Psi}_s^* \right\} \right. \\ & \left. - \omega_m \operatorname{Re} \left\{ \vec{\Psi}_r \cdot \vec{\Psi}_s^* \right\} + \operatorname{Im} \left\{ \vec{v}_s \cdot \vec{\Psi}_r^* \right\} + \operatorname{Im} \left\{ \vec{\Psi}_s \cdot \vec{v}_r^* \right\} \right] \end{aligned} \quad (4.3)$$

In order to analyze these expressions, it is necessary to consider the following space vector representations, in the stator reference frame:

$$\vec{\Psi}_r = |\vec{\Psi}_r| e^{j\omega_s t} \quad (4.4)$$

$$\vec{\Psi}_s = |\vec{\Psi}_s| e^{j(\omega_s t + \delta)} \quad (4.5)$$

$$\vec{v}_s = |\vec{v}_s| e^{j(\omega_s t + \delta + \frac{\pi}{2})} \quad (4.6)$$

$$\vec{v}_r = \frac{2}{3} V_{bus} e^{j(\omega_m t + \frac{\pi}{3}(n-1))} \quad (4.7)$$

Where the relation between the synchronous speed and the mechanical speed is:

$$\omega_r = \omega_s - \omega_m \quad (4.8)$$

and with n sub-index of the rotor voltage vector from 1 to 6. For vectors  $\vec{V}_0$  and  $\vec{V}_7$ ,  $\vec{v}_r = 0$ . By substituting the expressions (4.4)-(4.8) into equation (4.2), the rotor flux derivative yields:

$$\frac{d|\vec{\Psi}_r|}{dt} = \left( \frac{R_r L_h}{\sigma L_s L_r} \right) / \vec{\Psi}_s / \cos \delta - \left( \frac{R_r}{\sigma L_r} \right) / \vec{\Psi}_r / + \frac{2}{3} V_{bus} \cos(\omega_r t - \frac{\pi}{3}(n-1)) \quad (4.9)$$

The rotor flux derivative is composed by two constant terms and a cosine term, with  $\omega_r$  pulsation and amplitude only dependent on the DC bus voltage. The zero vector, produces constant rotor flux variation, what means that the cosine term is only valid for the active vectors. Similarly, the torque derivative expression (4.3) at steady state, may be simplified considering

$$|\vec{\Psi}_s| \equiv \frac{|\vec{v}_s|}{\omega_s}$$

that the stator flux vector module is nearly constant :

$$\frac{dT_{em}}{dt} = T_{em} \left( \frac{\omega_r}{\tan \delta} - \left( \frac{R_s}{\sigma L_s} + \frac{R_r}{\sigma L_r} \right) \right) + p \frac{L_h}{\sigma L_s L_r} V_{bus} |\vec{\Psi}_s| \sin(\omega_r t + \delta - \frac{\pi}{3}(n-1)) \quad (4.10)$$

As similarly occurs with the rotor flux, in this case again the torque derivative expression is composed by one constant term and one sine term with  $\omega_r$  pulsation. Its amplitude is only dependent on the bus voltage, since the stator flux module is considered constant. Again, the zero vectors produce constant torque variation. Fig. 4.2 graphically shows the torque and flux derivative evolutions of a specific DFIM, at steady-state and for each rotor voltage vector.

In general, the constant terms of the rotor flux derivative expression (4.9) are nearly eliminated, so the zero vectors almost do not produce rotor flux variation. On the other hand, the constant term of expression (4.10) is dependent on the electromagnetic torque and the speed of the machine. So depending on the machine's operation conditions it can be positive or negative as shown in Fig. 4.2. For the same reason, the phase shift order of each active vector varies from subsynchronous to hypersynchronous operation, since  $\omega_r$  varies from positive to negative values.

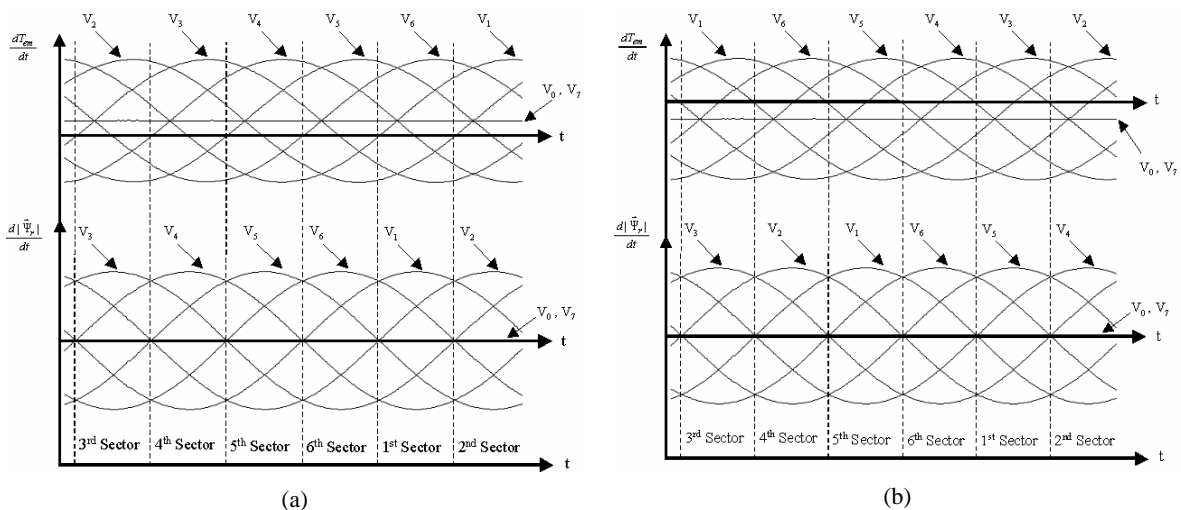


Fig. 4.2 Torque and flux slopes as a function of the time in motor or generator mode at hypersynchronism and subsynchronism, for each rotor voltage vector. (a) Subsynchronism, (b) Hypersynchronism.

The final expressions (4.9) and (4.10) are more suitable to be employed for real time implementation purposes, rather than equations (4.2) and (4.3). Considering the DC bus voltage, the stator voltage and the stator flux as constant magnitudes, the torque and rotor flux derivatives will only depend on four magnitudes as shown in the simplified block diagram of Fig. 4.3.

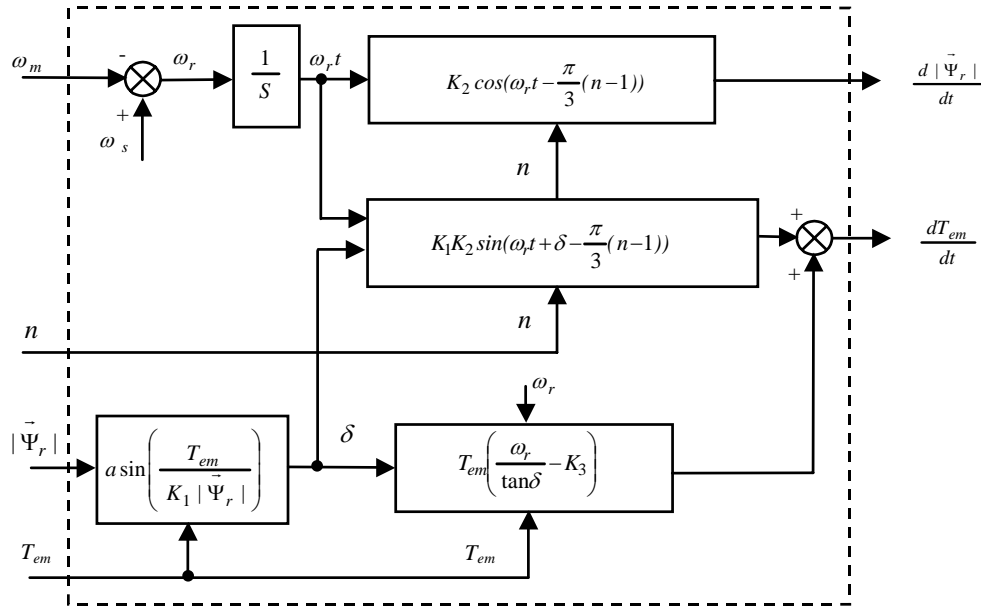


Fig. 4.3 Simplified prediction schema. Torque and flux derivative expressions calculation.

With;

$$K_1 = \frac{3}{2} p \frac{L_h}{\sigma L_s L_r} |\vec{\Psi}_s| \quad (4.11)$$

$$K_2 = \frac{2}{3} V_{bus} \quad (4.12)$$

$$K_3 = \frac{R_s}{\sigma L_s} + \frac{R_r}{\sigma L_r} \quad (4.13)$$

Added to this, from Fig. 4.2, it can be considered that for small switching sample periods, the torque and flux evolutions can be approximated to straight lines. From the numerical value of the slopes, it can be seen that the zero voltage vector is the vector which will produce the smallest torque variation, since at steady-state in each sector k, only k and k+3 vectors produce smaller slopes, and in general, they are not allowed to be used in DTC control strategies.

Further analysis of the torque variation produced by the zero vectors can be deduced by considering the first term of equation (4.10). At fixed torque and rotor flux operation conditions, the slope varies proportionally to the slip speed. More specifically, as shown in Fig. 4.4, at speeds near to the synchronous speed, the slope of the zero vectors becomes smaller. This fact implies that as at speeds near the synchronism, the required rotor voltage vector amplitude is very small, the torque ripple will be also small since the most demanded vector will be the zero vector. Finally, note that the transition from positive to negative torque slope, in general is different to the synchronous speed.

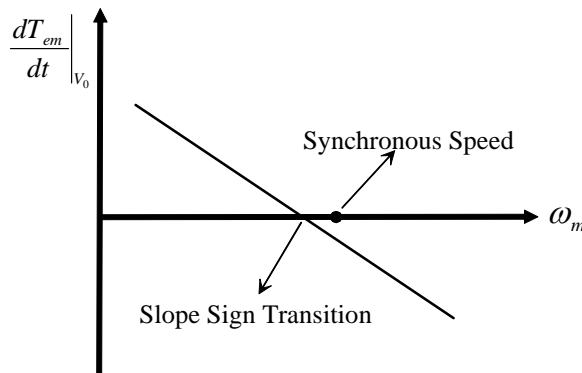


Fig. 4.4 Torque variation produced by the zero vector, at constant torque and rotor flux.

### 4.3 “Classic” Direct Torque Control (DTC) of the Doubly Fed Induction Machine (DFIM)

#### 4.3.1 Control Block Diagram

The control block diagram of the proposed strategy is shown in Fig. 4.5. As mentioned before, the directly controlled variables are the electromagnetic torque and the rotor flux amplitude. From the torque and flux references, the control strategy calculates the pulses ( $S_a$ ,  $S_b$ ,  $S_c$ ) for the IGBTs of the two level voltage converter. As depicted in Fig. 4.5, the control strategy is divided into five different tasks represented in five different blocks.

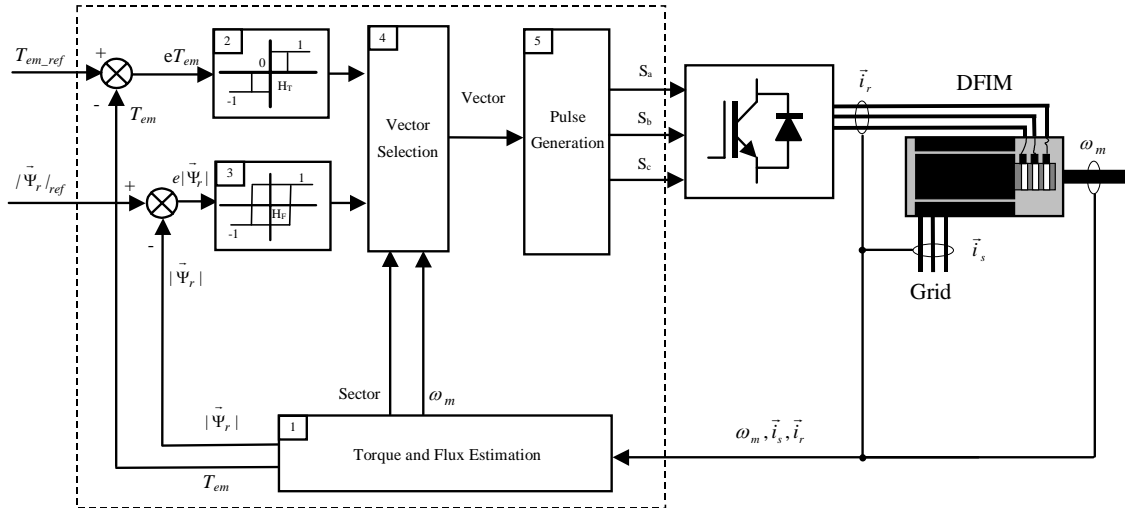


Fig. 4.5 Classic DTC block diagram.

### 4.3.2 Vector Selection Strategy

The DTC technique selects the required rotor vector directly from the rotor flux and electromagnetic torque errors, using hysteresis ON-OFF controllers (block 2 and 3 from Fig. 4.5). The flux controller is based on a two level hysteresis comparator with  $H_F$  hysteresis band, while the torque controller uses a three level hysteresis comparator with  $H_T$  hysteresis band. At the zero level of this controller, the zero voltage vector is selected in order reduce the torque ripple. Therefore, the voltage vector selection is carried out according to the following table, deduced from Fig. 4.2:

TABLE 4.I  
VECTOR SELECTION AS A FUNCTION OF THE TORQUE AND FLUX ON-OFF CONTROLLER OUTPUTS (K = SECTOR)

		$eT_{em}$		
		1	0	-1
$e \vec{\Psi}_r $	1	$V_{(k-1)}$	$V_0, V_7$	$V_{(k+1)}$
	-1	$V_{(k-2)}$	$V_0, V_7$	$V_{(k+2)}$

From (4.10) it can be noticed that the effect of the zero vector to the electromagnetic torque is different depending on a subsynchronous or hypersynchronous operation mode of the machine. Hence, the zero vector will be only permitted when the torque has reached the reference within the hysteresis bands.

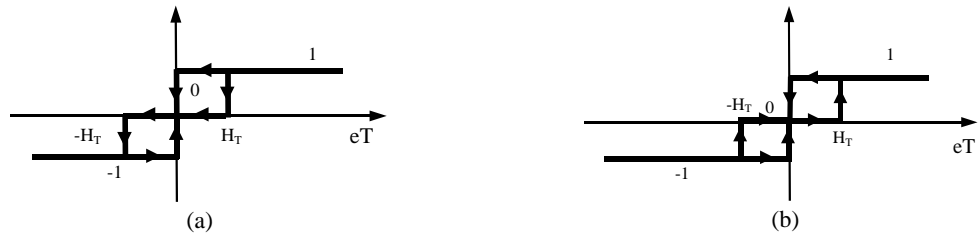


Fig. 4.6. ON-OFF Electromagnetic torque controller with hysteresis band. (a) Subsynchronous, (b) Hypersynchronous

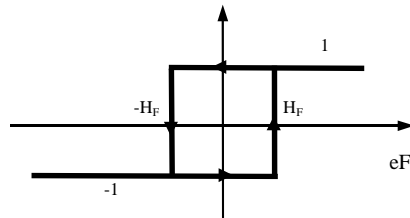


Fig. 4.7 ON-OFF Rotor flux controller with hysteresis band.

When the output of the controller is set to 1, it means a positive variation requirement. On the contrary, when the output is set to  $-1$ , a negative variation is required. Alternatively, when the output of the torque controller is set to zero, the torque and the flux are within the hysteresis band limits, and in order to minimize the torque and the flux ripples, the zero vector is introduced. In Fig. 4.8, an example of torque and flux waveforms at steady-state conditions, of a digitally implemented DTC control strategy is illustrated.

The choice of the zero vector is suitable to reduce torque and flux ripples since it produces smaller torque and flux variations compared with the active vectors. In order to reduce torque and flux ripples, the hysteresis bands width of both controllers ( $H_T$  and  $H_F$ ) should be set to small values. Unfortunately it exists a limit for those values, related to the minimum switching sample period ( $h$ ) of the hardware used for the implementation. Hence, an overshoot in torque or flux beyond the hysteresis bands is unavoidable. Under these circumstances, added to the fact that according to (4.9) and (4.10), the slopes of the electromagnetic torque and the rotor flux variations due to an active vector selection, take different values depending on the operating conditions and the time, the converter presents variable switching frequency behavior.

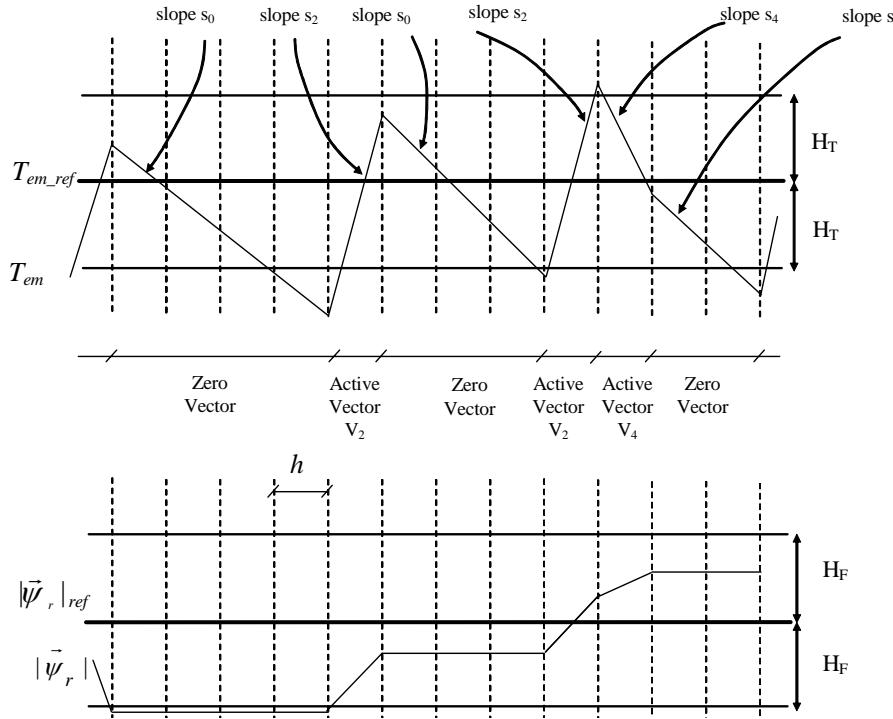


Fig. 4.8. Steady state Torque and Flux waveforms at motor and generator modes at hypersynchronism.

Fig. 4.8 serves a short period of time at the beginning of the third sector. Torque overshoot occurs 3 times, while the flux goes beyond the hysteresis band limit once producing inevitable torque and flux ripples. On the other hand, after the second zero vector is applied, since the required active vector ( $V_2$ ) at that moment produces a fast torque variation, the reverse active vector is applied then instead the zero vector, yielding to a variable frequency switching frequency behavior.

In any case, if a reduced torque and flux ripples are required, in general a small hysteresis band should be used together with a small switching sample period. Nevertheless, the choice of the hysteresis bands is not so obvious even for a given sample time ( $h$ ), since they will produce different torque and flux ripples depending on the operation conditions of the machine.

Added to this, based on the DTC control strategy presented in this section and altering some specific aspects of this strategy, constant switching frequency behavior with “reduced” ripples can be achieved. For example, some authors have focused their efforts in a modification of the hysteresis bands of the controllers [51], while others, in a prediction of the commutation instants based on the machine model [34], [37]. In the next section, a predictive DTC control technique will be presented, achieving constant switching frequency and reduced torque and flux ripples.

## 4.4 Predictive DTC Strategy with Reduced Torque Ripple and Constant Switching Frequency

### 4.4.1 Control Block Diagram

The control block diagram of the proposed strategy is depicted in Fig. 4.9. As in the previous case, the directly controlled variables are the electromagnetic torque and the rotor flux amplitude. From the torque and flux references, the control strategy calculates the pulses ( $S_a, S_b, S_c$ ) for the IGBTs of the two level voltage source converter. As shown in Fig. 4.9, the control strategy is divided into seven different tasks represented in seven different blocks. The tasks carried out in blocks 1-4, are the basic Direct Torque Control principles formulated by authors such as [31] and [48]. On the contrary, the tasks performed in blocks 5-7, are introduced in order to achieve the improvements mentioned above, i.e. reduced torque ripple and constant switching frequency behavior.

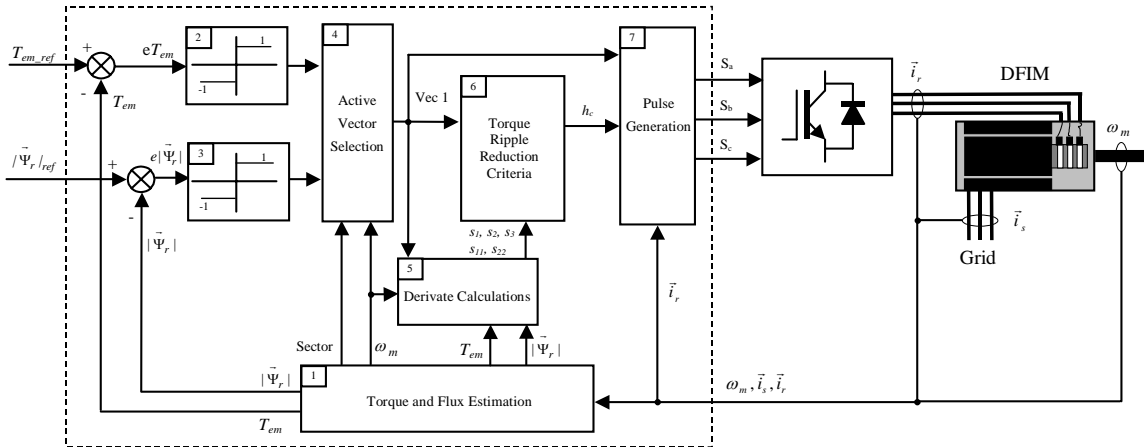


Fig. 4.9. Predictive DTC block diagram with reduced torque ripple and constant switching frequency.

### 4.4.2 First Vector Selection Strategy

In the first block, the estimated flux and torque values are calculated with the equations of the DFIM model presented in Chapter 3. Added to this, the sector in which the rotor flux space vector is located is estimated too. After that, the torque and flux references are compared with their estimated values, so the torque and flux errors are obtained.

The basic principle of the Direct Control techniques determines the choice of one specific active voltage vector of the converter, in order to correct the torque and flux errors. The choice of this vector is directly calculated from the torque and flux errors themselves and the sector where the rotor flux lies.

This predictive DTC control technique achieves constant switching frequency behavior. It is defined a constant switching period  $h$ , in which only one or two vectors are permitted. From those two vectors, there will always be an active vector, and in general, the second permitted vector will be a zero vector. The choice of the zero vector is due to the fact that it is very suitable for steady-state operation conditions, since it produce “small” torque variations and almost zero flux variations. At the beginning of each switching period, the control strategy calculates the active vector required to keep the rotor flux and the electromagnetic torque controlled [34], [37]. Hence, the first active voltage vector selection is based on a look-up table mapped by the output of two ON-OFF comparators without hysteresis bands. In this case, the ON-OFF controllers do not present hysteresis bands, since they are only in charge to select the active vector.

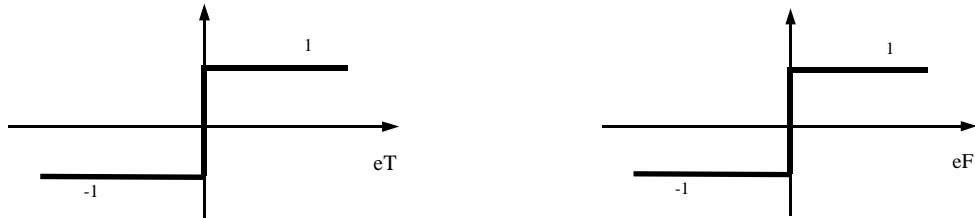


Figure 4.10. Electromagnetic torque and rotor flux ON-OFF controllers for the predictive DTC control strategy for reduced torque ripple.

These tasks are accomplished in blocks 2, 3 and 4 of Fig. 4.9. One comparator is dedicated to the torque control and the other to the flux control. The look-up table is made up according to TABLE 4.II.

TABLE 4.II

FIRST ACTIVE VECTOR SELECTION AS A FUNCTION OF THE TORQUE AND FLUX ON-OFF CONTROLLERS' OUTPUTS (K = SECTOR)

	$eT_{em}$	
	1	-1
$e  \vec{\Psi}_r $	$V_{(k-1)}$	$V_{(k+1)}$
	$V_{(k-2)}$	$V_{(k+2)}$

When the output of the comparator is set to 1, i.e. positive error, it means a positive slope variation requirement. On the contrary, when the output is set to -1, i.e. negative error, a negative slope variation is required.

The portion of time in the sample period  $h_c$ , dedicated to the active vector respect to the zero vector is calculated with a torque ripple minimization criteria. The typical torque and flux waveforms, for this control strategy are represented in Fig. 4.11 and Fig. 4.12.

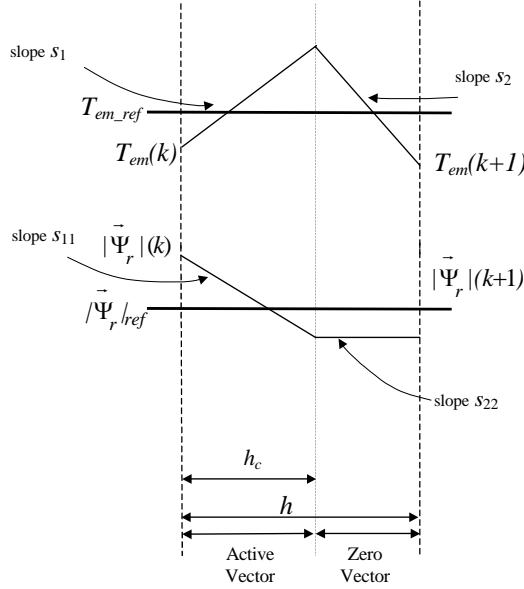


Fig. 4.11. Steady state Torque and Flux waveforms at motor and generator modes at hypersynchronism.

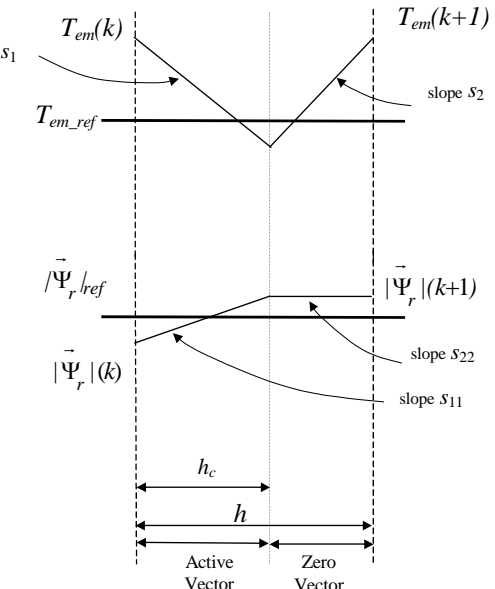


Fig. 4.12 Steady state Torque and Flux waveforms at motor and generator modes at subsynchronousism.

Thus, at steady-state operation conditions, at each switching period, when two vectors are introduced, only one leg of the two level converter will switch at the time instant  $h_c$  (from active vector to zero vector) for the transition of the active to the zero vector. On the other hand, at the transition from one switching period to its consecutive, more than one leg may switch (from zero vector to active vector).

#### 4.4.3 Torque Ripple Minimization Criteria at Constant Switching Frequency

Depending on the applied vector and the initial conditions at the current switching period, the slopes of the torque and flux variations can be calculated using the expressions (4.9) and (4.10). The adopted notation names  $s_1$  and  $s_2$  to the slopes of the torque, for the active and zero vectors at each sample period. Similarly,  $s_{11}$  and  $s_{22}$  are the slopes of the flux, for the active and the zero vectors.

It has to be pointed out that the slope of the torque  $s_2$  at hypersynchronous speed is negative, while at subsynchronous speed is positive. During one sample period, the square of the rms torque ripple is calculated as follows:

$$\begin{aligned} T_{em\_ripple}^2 = & \frac{1}{h} \int_0^{h_c} (s_1 \cdot t + T_{em}(k) - T_{em\_ref})^2 \cdot dt \\ & + \frac{1}{h} \int_{h_c}^h (s_2 \cdot t - s_2 \cdot h_c + s_1 \cdot h_c + T_{em}(k) - T_{em\_ref})^2 \cdot dt \end{aligned} \quad (4.14)$$

The expression that achieves the minimum torque ripple is calculated derivating the last expression respect to the vector change instant  $h_c$ , and equaling to zero.

$$\frac{dT_{em\_ripple}}{dh_c} = 0 \quad (4.15)$$

Solving this equation, the optimal switching instant  $h_c$  is obtained as:

$$h_c = \frac{2 \cdot (T_{em\_ref} - T_{em}(k)) - s_2 \cdot h_c}{2 \cdot s_1 - s_2} \quad (4.16)$$

Taking into account the above proposed switching criteria, the control block diagram presented in Fig. 4.9. can be described as follows:

1.- Torque and flux references are compared with their estimated values. The estimated flux and torque are calculated with the equations of the DFIM model presented in Chapter 3.

2.- From the torque and the flux errors, the ON-OFF controllers allows to select the active vector, according to TABLE 4.II.

3.- Using expression (4.16), the vector change instant  $h_c$  is calculated. If the computed value is greater than  $h$  or smaller than zero, the torque is not in the steady state yet, hence the active vector is maintained during the whole switching period  $h$ . Thus, at transient conditions quick dynamic responses are guaranteed.

4.- After computing the switching instant and the corresponding active vector, they are transformed into pulses for the IGBTs of the two level converter.

By this predictive DTC control technique, compared with the “classic” DTC control strategy, two interesting advantages are achieved, i.e. constant switching behavior and reduced torque ripple. Unfortunately, when the application demands small switching frequencies, this control technique present some drawbacks because the more the switching period is reduced, the more the quality of the stator and rotor current waveforms are degraded . This problem occurs basically because this technique only is focused on reducing the torque ripple, while during the whole switching instant, the flux is varying as well but without supervision. Added to the fact that there are some instants at steady-state where the flux slope is very high, when a long switching period is used, yields to a very high flux variation from the reference value, which consequently produces, a very high stator and rotor current variations, degrading finally their quality.

#### 4.4.4 Further Improvements Oriented to Low Switching Frequency

Although several authors [34], [37] have used only one active vector together with the zero vector at every switching period, in the next subsection two active vectors together with the zero vector will be used. This choice is justified for example at high power applications, when “small” switching frequency are required. Thus, reduced torque and flux ripples are guaranteed at every switching instant, and consequently minimum stator and rotor current ripple waveforms are achieved.

This fact can be understood studying Fig. 4.13, focusing the analysis on one specific sector, if the zero vector produces a positive torque slope because the machine is rotating at subsynchronous speed, there are always only two vectors that produce uniform negative torque slope. Consequently this two vectors are suitable to minimize the torque ripple. At the same time, using those two specific active vectors, positive and negative slopes can be achieved for the flux variation, since they produce opposite sign slopes. Therefore, both active vectors are useful to control the flux as well.

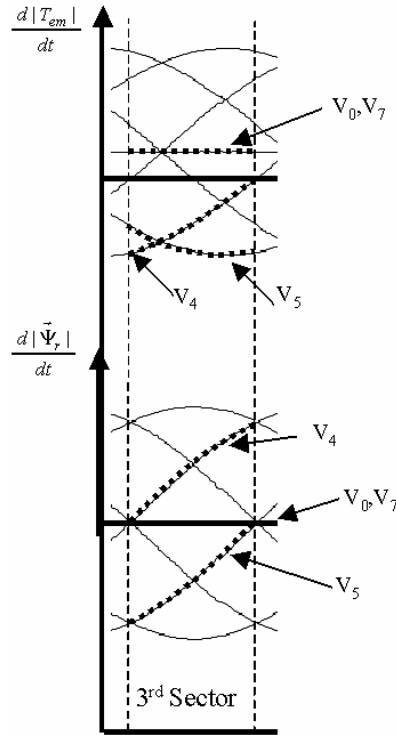


Fig. 4.13. Torque and Flux slopes.

This means that for example in the third sector, in steady-state operation conditions, using the vectors 4 and 5 the torque and the flux can be controlled, and furthermore combining their effect with the zero vector, the torque and the flux can be controlled at the same time minimizing their variations from the reference point.

## 4.5 Predictive DTC Strategy with Reduced Torque and Flux Ripples and Constant Switching Frequency

### 4.5.1 Control Block Diagram

The control block diagram of the proposed strategy is depicted in Fig. 4.14. As mentioned before, the directly controlled variables are the electromagnetic torque and the rotor flux amplitude. From the torque and flux references, the control strategy calculates the pulses ( $S_a, S_b, S_c$ ) for the IGBTs of the two level voltage source converter, in order to meet the following two objectives: reduced torque and flux ripples and constant switching frequency behavior. As shown in Fig. 4.14, the control strategy is divided into seven different tasks represented in seven different blocks. The tasks carried out in blocks 1-4, are the basic Direct Torque Control principles formulated by authors such as [31] and [48]. On the contrary, the tasks performed in

blocks 5-7, are introduced in order to achieve the improvements mentioned above, i.e. reduced ripples and constant switching frequency behavior.

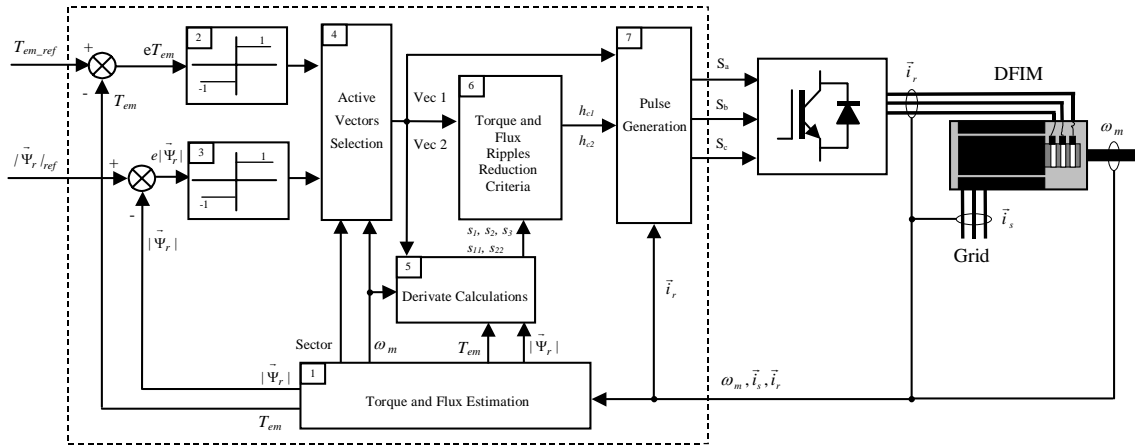


Fig. 4.14. Predictive DTC block diagram with reduced torque and flux ripples and constant switching frequency.

#### 4.5.2 First vector Selection Strategy

In the first block, the estimated flux and torque values are calculated with the equations of the DFIM model presented in Chapter 3. Added to this, the sector in which the rotor flux space vector is located is estimated too. After that, the torque and flux references are compared with their estimated values, so the torque and flux errors are obtained.

The basic principle of the Direct Control techniques again determines the choice of one specific active voltage vector of the converter, in order to correct the torque and flux errors. The choice of this vector is directly calculated from the torque and flux errors themselves and the sector where the rotor flux lies.

The proposed predictive DTC strategy, adopts this principle to select the first active voltage vector of the three vectors sequence employed to minimize the torque and flux ripples, as will be justified in the next sub-section. Hence, the first active voltage vector selection is based on a look-up table mapped by the output of two ON-OFF comparators without hysteresis bands. These tasks are accomplished in blocks 2, 3 and 4 of Fig. 4.14. One comparator is dedicated to the torque control and the other to the flux control. The look-up table is made up according to TABLE 4.III.

TABLE 4.III

FIRST ACTIVE VECTOR SELECTION AS A FUNCTION OF THE TORQUE AND FLUX ON-OFF CONTROLLERS' OUTPUTS (K = SECTOR)

	$eT_{em}$	
	1	-1
$e   \vec{\Psi}_r  $	$V_{(k-1)}$	$V_{(k+1)}$
	$V_{(k-2)}$	$V_{(k+2)}$

When the output of the comparator is set to 1, i.e. positive error, it means a positive slope variation requirement. On the contrary, when the output is set to -1, i.e. negative error, a negative slope variation is required. Note that this table is equal to TABLE 4.II.

#### 4.5.3 Second and Third Vector Selection Strategy at Constant Switching Frequency

Once the first active vector is selected from the classical DTC switching table in order to correct the electromagnetic torque and the rotor flux errors, the predictive DTC control strategy employs a sequence of three different voltage vectors in a constant switching period  $h$ , under steady-state operation conditions. Hence, a second active vector is introduced followed always by a zero vector with the objective of minimizing the torque and the rotor flux ripples, from their reference values. The typical torque and flux waveforms for this control strategy are illustrated in Fig. 4.15.

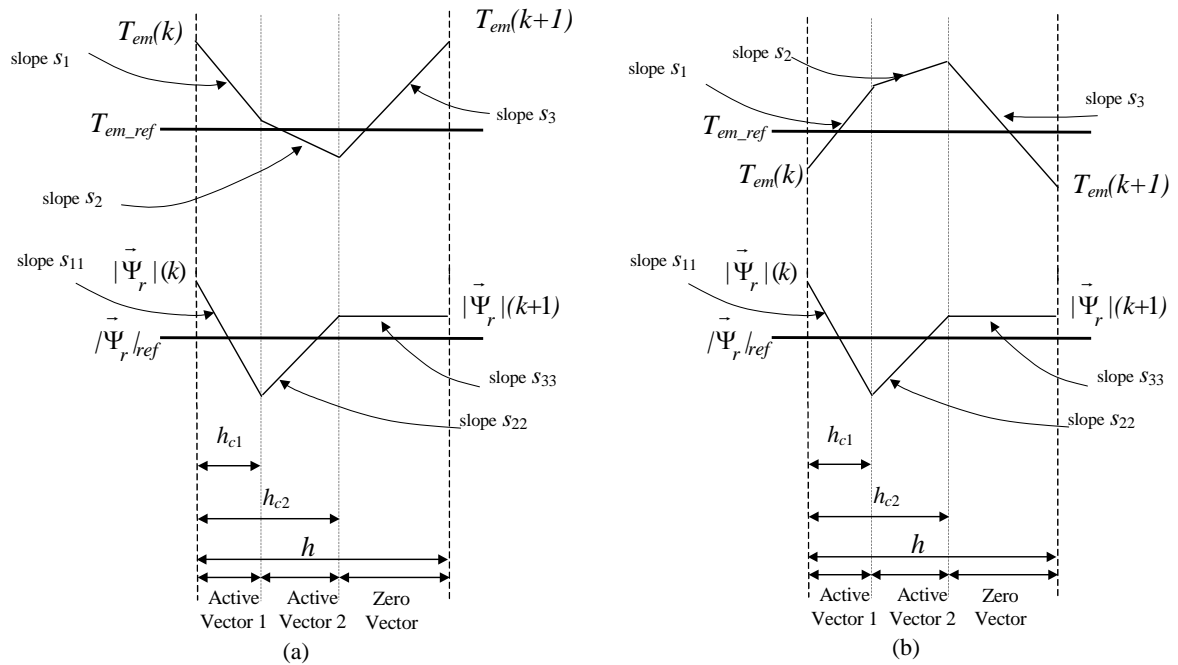


Fig. 4.15 Steady state Torque and Flux waveforms at subsynchronous and hypersynchronous speeds with three vector based DTC strategy. (a) Subsynchronous, (b) Hypersynchronous

In the adopted notation, the slopes of the torque are called  $s_1$ ,  $s_2$  and  $s_3$  for the active and zero vectors at each switching sample period. Similarly,  $s_{11}$ ,  $s_{22}$  and  $s_{33}$  are the slopes of the rotor flux, for the active and the zero vectors. The slope of the torque  $s_3$  at hypersynchronous speed is negative, while at subsynchronous speed is positive.  $h_{c1}$  and  $h_{c2}$  are the time intervals dedicated for the first and the second active vectors. The second active vector produces the same sign variation as the first active vector in the torque, while it produces the opposite sign variation in the rotor flux. On the other hand, the zero vector produces opposite sign torque variation to the first two active vectors, while the rotor flux is nearly maintained constant, as can be inferred from equations (4.9) and (4.10). These slopes are calculated in block 5 of Fig. 4.14. The presence of the zero vector in the three vectors sequence is very useful at steady-state operation conditions, since it provides “small” torque variations and almost zero flux variations, yielding to a reduction in the torque and flux ripples.

So, once the first active vector is chosen, if the torque and the flux ripples can be reduced, the choice of the second active vector is made according to TABLE 4.IV. It defines the correct choice of the active vectors, depending on the speed of the machine and the sector in which the rotor flux is located.

TABLE 4.IV  
ACTIVE VECTORS SELECTION AT STEADY-STATE (K = SECTOR)

Active Vectors	
<b>Subsynchronism</b>	$V_{(k+1)}, V_{(k+2)}$
<b>Hypersynchronism</b>	$V_{(k-1)}, V_{(k-2)}$

For instance, when the machine is rotating at subsynchronous speed, the rotor flux is in the first sector, and the actual torque and flux values are close enough to their references, the combination of the active vectors 2 and 3 produces the torque and flux waveforms according to Fig. 4.15.

Finally, the necessity of two active vectors at each switching period is justified, especially at the beginning and at the end of the sector since the slope of the flux that they produce is either very big or very small. So if only one active vector was used in an attempt to minimize only the torque ripple, the flux would experiment a very big or a very small variation, depending on the vector that has been used, leading to a poor flux control and consequently a poor current quality.

#### 4.5.4 Torque and Flux Ripple Reduction Criteria at Constant Switching Frequency

The switching instants  $h_{c1}$  and  $h_{c2}$  shown in Fig. 4.15, as mentioned before, are calculated in order to obtain two objectives, i.e. reduce the rotor flux and the torque ripple. So, once the active vectors are identified by using TABLE 4.III and TABLE 4.IV, their corresponding time intervals are calculated based on a prediction of the torque and the rotor flux. This task is graphically represented in block 6 of Fig. 4.14.

Firstly, taking advantage of the fact that the slope of the flux when the zero vector is applied is nearly zero ( $s_{33}=0$ ), the expression that relates  $h_{c1}$  and  $h_{c2}$  is derived by minimizing the flux ripple. Hence, the square of the rms flux ripple is calculated as follows:

$$\begin{aligned} |\vec{\Psi}_r|_{\text{ripple}}^2 &= \frac{1}{h_{c2}} \int_0^{h_{c1}} (s_{11}t + |\vec{\Psi}_r|(k) - |\vec{\Psi}_r|_{\text{ref}})^2 dt \\ &\quad + \frac{1}{h_{c2}} \int_{h_{c1}}^{h_{c2}} (s_{22}t - s_{22}h_{c1} + s_{11}h_{c1} + |\vec{\Psi}_r|(k) - |\vec{\Psi}_r|_{\text{ref}})^2 dt \end{aligned} \quad (4.17)$$

Differentiating this expression with respect to the switching instant of the first active vector  $h_{c1}$ :

$$\frac{d|\vec{\Psi}_r|_{\text{ripple}}^2}{dh_{c1}} = 0 \quad (4.18)$$

and solving this equation, the optimal switching instant  $h_{c1}$  is obtained:

$$h_{c1} = \frac{2(|\vec{\Psi}_r|_{\text{ref}} - |\vec{\Psi}_r|(k)) - s_{22}h_{c2}}{2s_{11} - s_{22}} \quad (4.19)$$

Secondly, once the relation  $h_{c1} = f(h_{c2})$  is obtained, it is possible to calculate the equivalent slope  $s_{12}$  of the first two active vectors for the torque. As illustrated in Fig. 4.16, the equivalent slope is calculated by means of the expression:

$$s_{12} = \frac{s_1 h_{c1} + s_2 (h_{c2} - h_{c1})}{h_{c2}} \quad (4.20)$$

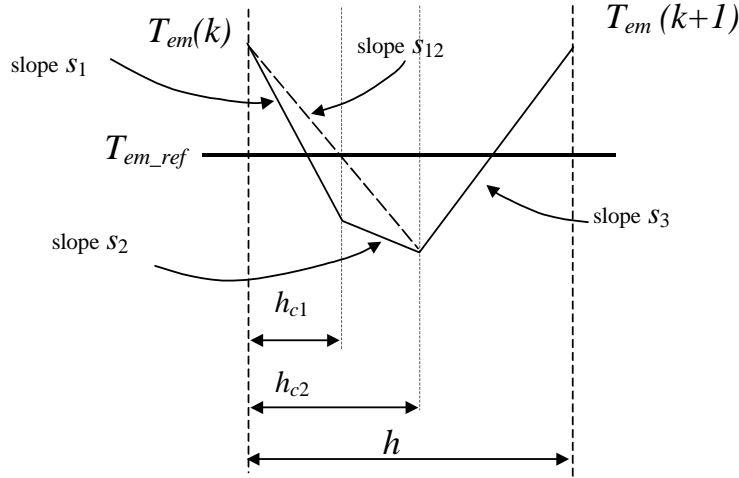


Fig. 4.16. Equivalent slope  $s_{12}$  for the torque, of the first two active vectors.

After that, as done with the flux ripple, the square of the rms torque ripple is calculated with the integral:

$$T_{em\_ripple}^2 = \frac{1}{h} \int_0^{h_{c2}} (s_{12}t + T_{em}(k) - T_{em\_ref})^2 dt + \frac{1}{h} \int_{h_{c2}}^h (s_3t - s_3h_{c2} + s_{12}h_{c2} + T_{em}(k) - T_{em\_ref})^2 dt \quad (4.21)$$

Considering that the equivalent slope  $s_{12}$  is constant, the rms square ripple of the torque can be minimized by the expression:

$$\frac{dT_{em\_ripple}^2}{dh_{c2}} = 0 \quad (4.22)$$

That leads to an equivalent expression to (4.19):

$$h_{c2} = \frac{2(T_{em\_ref} - T_{em}(k)) - s_3h}{2s_{12} - s_3} \quad (4.23)$$

Finally, combining this last expression and the expressions (4.19) and (4.20), both switching instants are calculated by means of the following expressions:

$$h_{c1} = \frac{2s_{22}T_{em\_ref} - 2s_{22}T_{em}(k) - s_{22}s_3h + (2s_3 - 4s_2)/\vec{\Psi}_r|_{ref} + (4s_2 - 2s_3)/\vec{\Psi}_r|(k)}{2s_{22}s_1 - 4s_{11}s_2 + 2s_{11}s_3 - s_{22}s_3} \quad (4.24)$$

$$h_{c2} = \frac{(2s_{22}-4s_{11})T_{em\_ref} + (4s_{11}-2s_{22})T_{em}(k)}{2s_{22}s_1-4s_{11}s_2+2s_{11}s_3-s_{22}s_3} + \frac{(2s_{11}-s_{22})s_3h + (4s_1-4s_2)\bar{\Psi}_r|_{ref} + (4s_2-4s_1)\bar{\Psi}_r|(k)}{2s_{22}s_1-4s_{11}s_2+2s_{11}s_3-s_{22}s_3} \quad (4.25)$$

If the computed values for  $h_{c1}$  and  $h_{c2}$  are greater than  $h$  or smaller than zero, or either  $h_{c2}$  is smaller than  $h_{c1}$ , it means that the torque and the flux cannot reach their references yet, hence, the first active vector is maintained during the whole switching period  $h$ .

It is necessary to point out that, alternatively to these approximated expressions, more complex torque reduction criteria could be adopted, but in general, it would lead to very complex and computationally expensive expressions. For simplicity, and because further torque reduction would be almost insignificant, the proposed solution has been considered as the simplest solution.

#### 4.5.5 Switching Power Losses Reduction

Added to this, focusing the analysis on steady-state operation conditions within the switching period  $h$ , if three vectors are used only two legs of the 2 level converter are switched at different instants. This is due to the fact that the sequence of vectors will be always composed of two consecutive active vectors and one zero vector. The right choice of the zero vector between  $V_0$  and  $V_7$  provides another degree of freedom, i.e. the reduction of the switching power losses of the converter.

For each pair of required active vectors, two different sequences exist that allow the commutations of the converter to be reduced. Analyzing both candidate sequences, the sequence that requires commutation of the legs that are transmitting the smallest currents will be employed, in order to reduce the switching power losses. TABLE 4.V summarizes the information necessary to select the correct sequence of vectors, guaranteeing only 4 commutations per switching period  $h$ .

So for instance, when the machine is operating at steady-state, if active vectors  $V_2$  and  $V_3$  are going to be used, leg a will always switch and the decision of choosing one sequence from the two candidates will be carried out by checking the highest current between  $i_b$  and  $i_c$ .

TABLE 4.V  
VECTOR SEQUENCE SELECTION FOR SWITCHING POWER LOSSES REDUCTION AT STEADY-STATE.

<b>Active vectors</b>	<b>Sector</b>	<b>Candidate sequences</b>	<b>Zero vector</b>	<b>Inevitable switching leg</b>	<b>Switching legs</b>
$V_1 - V_2$	6 (subs)	100-110-111	$V_7$	b	b, c ( $i_a > i_c$ )
	3 (hypers)	110-100-000	$V_0$		a, b ( $i_a < i_c$ )
$V_2 - V_3$	1 (subs)	110-010-000	$V_0$	a	a, b ( $i_b < i_c$ )
	4 (hypers)	010-110-111	$V_7$		a, c ( $i_b > i_c$ )
$V_3 - V_4$	2 (subs)	010-011-111	$V_7$	c	a, c ( $i_a < i_b$ )
	5 (hypers)	011-010-000	$V_0$		b, c ( $i_a > i_b$ )
$V_4 - V_5$	3 (subs)	011-001-000	$V_0$	b	b, c ( $i_c < i_a$ )
	6 (hypers)	001-011-111	$V_7$		b, a ( $i_c > i_a$ )
$V_5 - V_6$	4 (subs)	001-101-111	$V_7$	a	a, b ( $i_b < i_c$ )
	1 (hypers)	101-001-000	$V_0$		a, c ( $i_b > i_c$ )
$V_6 - V_1$	5 (subs)	101-100-000	$V_0$	c	a, c ( $i_a < i_b$ )
	2 (hypers)	100-101-111	$V_7$		b, c ( $i_a > i_b$ )

To conclude with the predictive DTC strategy description, this last task is represented in block 7 of the whole control block diagram of Fig.4.14. Using this predictive DTC control technique, it is possible to reduce the switching frequency considerably without loss of current quality due to control degradation, since the torque and the flux ripples are both reduced. This fact is shown in the next figure:

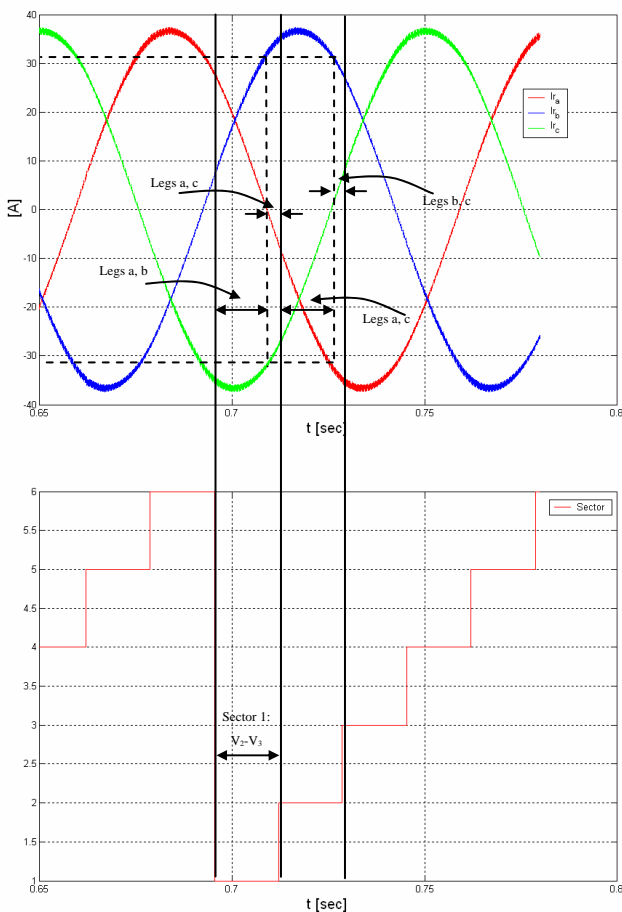


Fig. 4.17. Sequence candidate selection, reducing switching power losses.

## 4.6 Simulation results

### 4.6.1 Overview of the Simulation Experiments

In this section, simulation results of the previously presented control strategies will be served. Thus, the behavior of a specific DFIM will be shown, controlled by three different DTC control techniques. The main characteristics of the simulated system are shown in the following table.

TABLE 4.VI  
NOMINAL RATINGS OF THE SYSTEM

<b>Doubly fed induction machine</b>	
Rated power	15kW
Torque	95 Nm
Rated stator phase voltage	220 V
Rated rotor standstill phase voltage	220 V
Rated stator current	32 A
Rated rotor current	32 A
Synchronous speed	1500 rev/min
$R_s$	0.168 $\Omega$
$R_r$	0.199 $\Omega$
$L_s$	0.050 H
$L_r$	0.050 H
$L_h$	0.045 H
<b>Two level converter</b>	
DC link voltage	1000 V
Switching device	IGBTs

All the simulations have been carried out by Matlab-Simulink. The speed of the machine is controlled externally. The references for the machine are the electromagnetic torque and the rotor flux. By means of the DTC control strategy, the references will be followed by their actual values as close as possible. Since the capacity to operate at different switching frequencies is different for each proposed control strategy, several simulation results at “low” and “high” switching frequencies will be carried out. The simulation results are divided in two different groups.

1.- Transient and steady-state behaviour. In sections 4.6.2, 4.6.3 and 4.6.4, the analysis will be focused on the transient and the steady-state performance of the presented three control strategies, at different operation conditions. Section 4.6.2 is dedicated for the “classic” DTC control strategy, section 4.6.3 for the predictive DTC with reduced torque ripple control strategy and finally section 4.6.4, for the predictive DTC with reduced torque and flux ripples control strategy. The response of the machine when it is driven by each control strategy will be shown under sudden changes in the torque demand, and at the same time, the behavior of the machine’s magnitudes at steady-state will be presented. The quality of the steady-state behavior produced in the machine by each control strategy, will be measured in terms of the torque spectrum and the stator and rotor current spectrum.

Added to this, the capacity to work at different switching frequencies will be explored too for both predictive control strategies in sections 4.6.3 and 4.6.4. Especially at “low” switching frequencies.

2.-Tracking behavior: In section 4.6.5, the tracking problem is presented for the predictive DTC with minimum torque and flux ripple control strategy. Under variable speed operation conditions, variable electromagnetic torque will be demanded. The torque and flux references will be followed by the actual values closely, guarantying reduced torque and flux ripples.

#### **4.6.2 Transient and Steady-State Behavior for DTC Control Strategy.**

In this section, the behavior of the DFIM at steady-state and the transient response to a torque step reference is studied, under constant speed operation conditions. In this case, the “classic” DTC control technique will be in charge to do it. The most interesting characteristics are summarized next.

- Sample period  $50\mu\text{s}$  (20 kHz)
- Hysteresis bands of the ON-OFF controllers:  $H_T = 1$  and  $H_F = 0.0075$ .
- $V_{\text{bus}} = 500 \text{ V}$ . Speed : 750 rev/min ( $s = 0.5$ )
- Torque step: From -100 Nm (generator mode), to 100 Nm (motor mode).

The results are shown in the next figures:

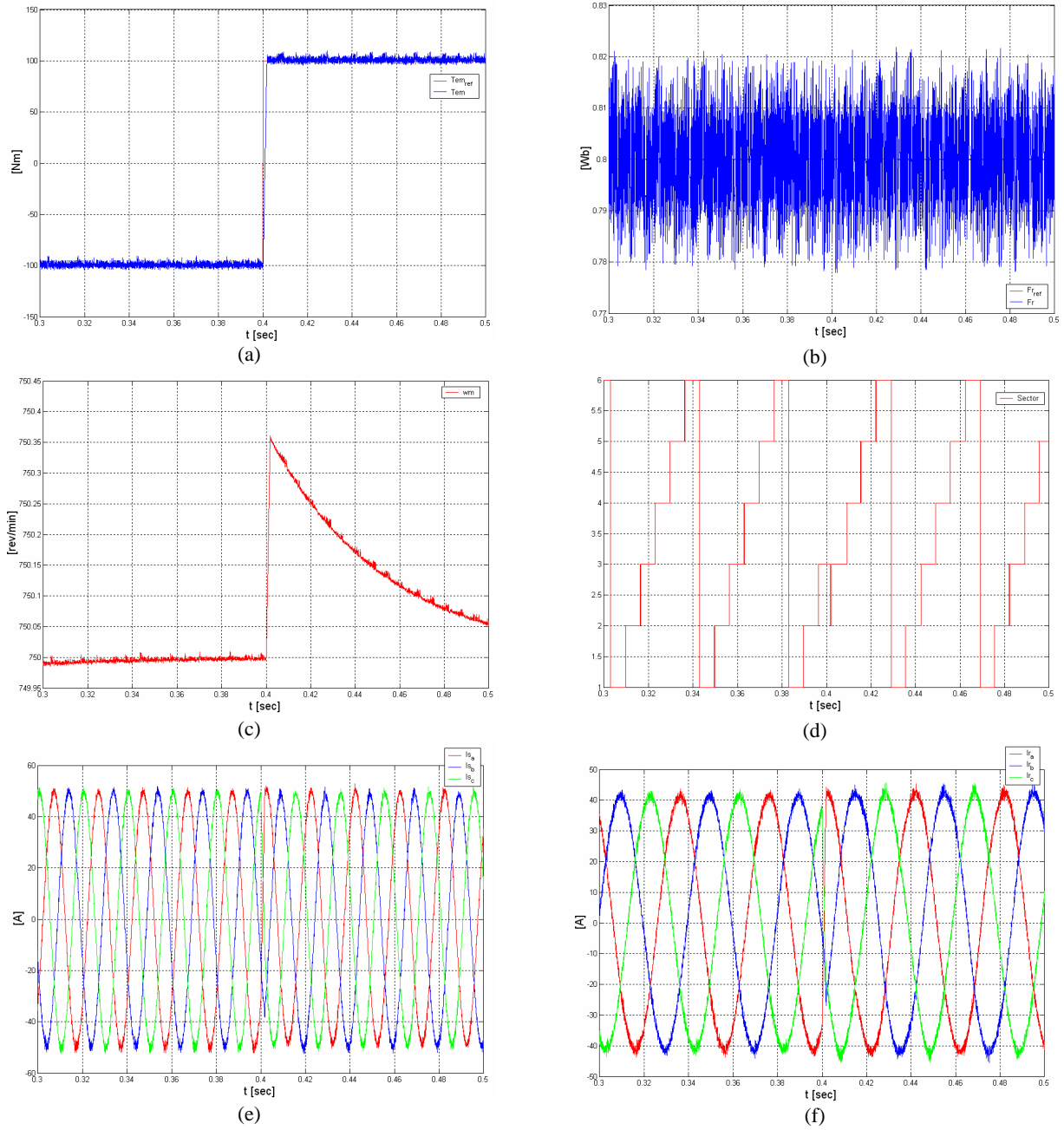


Fig. 4.18. “Classic” DTC control strategy simulation results at 20 kHz. Transient and steady-state behavior I. (a) Electromagnetic torque, (b) Rotor flux, (c) Mechanical speed, (d) Sector, (e) Stator currents, (f) Rotor currents.

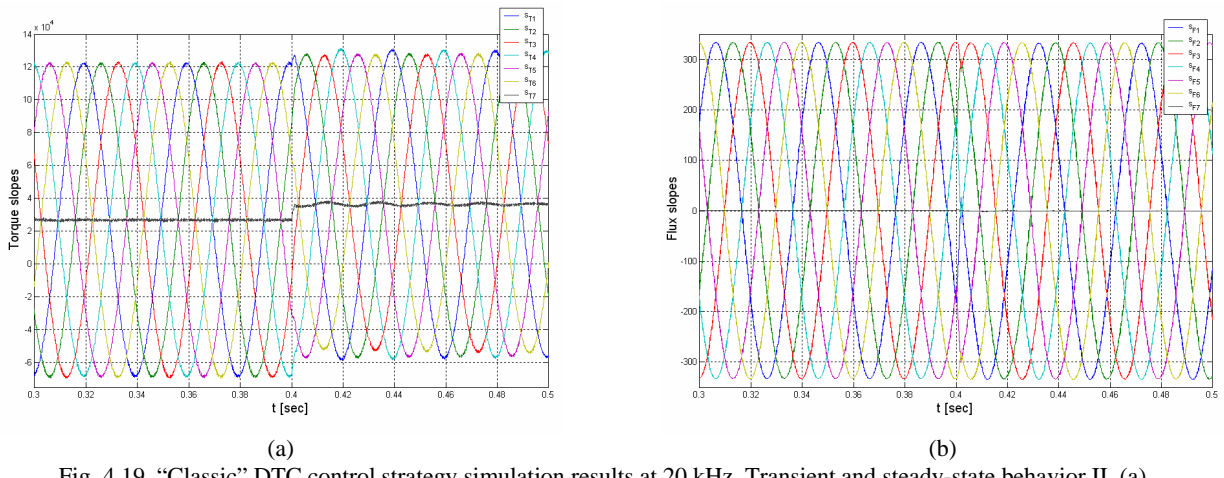


Fig. 4.19. ‘Classic’ DTC control strategy simulation results at 20 kHz. Transient and steady-state behavior II. (a) Torque Slopes, (b) Flux Slopes.

When the machine is driven at constant mechanical speed, the rotor flux reference is maintained constant. The electromagnetic torque reference is suddenly changed from its negative (generator mode) nominal value to its positive (motor mode) nominal value. Hence, it is possible to observe the transient and the steady-state behavior of the magnitudes of the machine under the mentioned operation conditions.

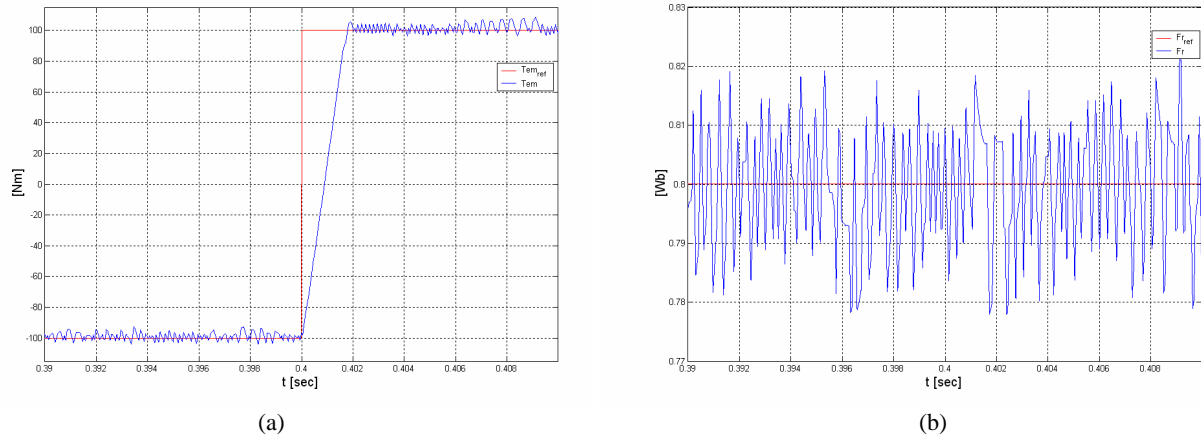


Fig. 4.20. ‘Classic’ DTC control strategy simulation results at 20 kHz. Transient and steady-state behavior III. Zoom of the torque reference step. (a) Electromagnetic torque zoom, (b) Rotor flux zoom.

In Fig. 4.18, (e) and (f), the rotor and the stator currents can be appreciated. The severe change in the torque demand, do not produce any over current in the machine. In Fig. 4.20, the fast dynamic torque response is shown. Approximately after 200  $\mu$ s from the torque step, the DFIM reaches the steady-state again. Although this time depends on the available bus voltage level of the converter, the DTC control technique, allows to take maximum advantage of this

voltage. On the other hand, the rotor flux is kept controlled during the whole experiment as can be noticed from Fig. 4.20 (b) and Fig. 4.18 (b).

Finally, in Fig. 4.19 (a) and (b), the torque and the flux slopes are shown for each rotor voltage vector. They are sinusoidal magnitudes, and their amplitude, phase and frequency depends on the operation condition of the machine, as can be deduced from equations (4.9) and (4.10). Analyzing the steady-state behavior produced by this control technique in terms of quality, looking at the electromagnetic torque and the rotor flux variations from the reference point, it can be inferred that the typical DTC controlled steady-state characteristics are noticed. The torque overshoot predicted in theory, produce a non-constant ripple, due to the practical physical limitation in the sample period  $h$ . Consequently, variable switching frequency behavior is achieved. According to this, the electromagnetic torque spectrum shown in Fig. 4.21, presents different frequency harmonic components. Their amplitude and the frequency where they appear, depends on the operation conditions of the machine, such as the velocity, the torque and the flux references, etc... , as well as, on the programmed hysteresis bands of the ON – OFF controllers together with the sample period  $h$ .

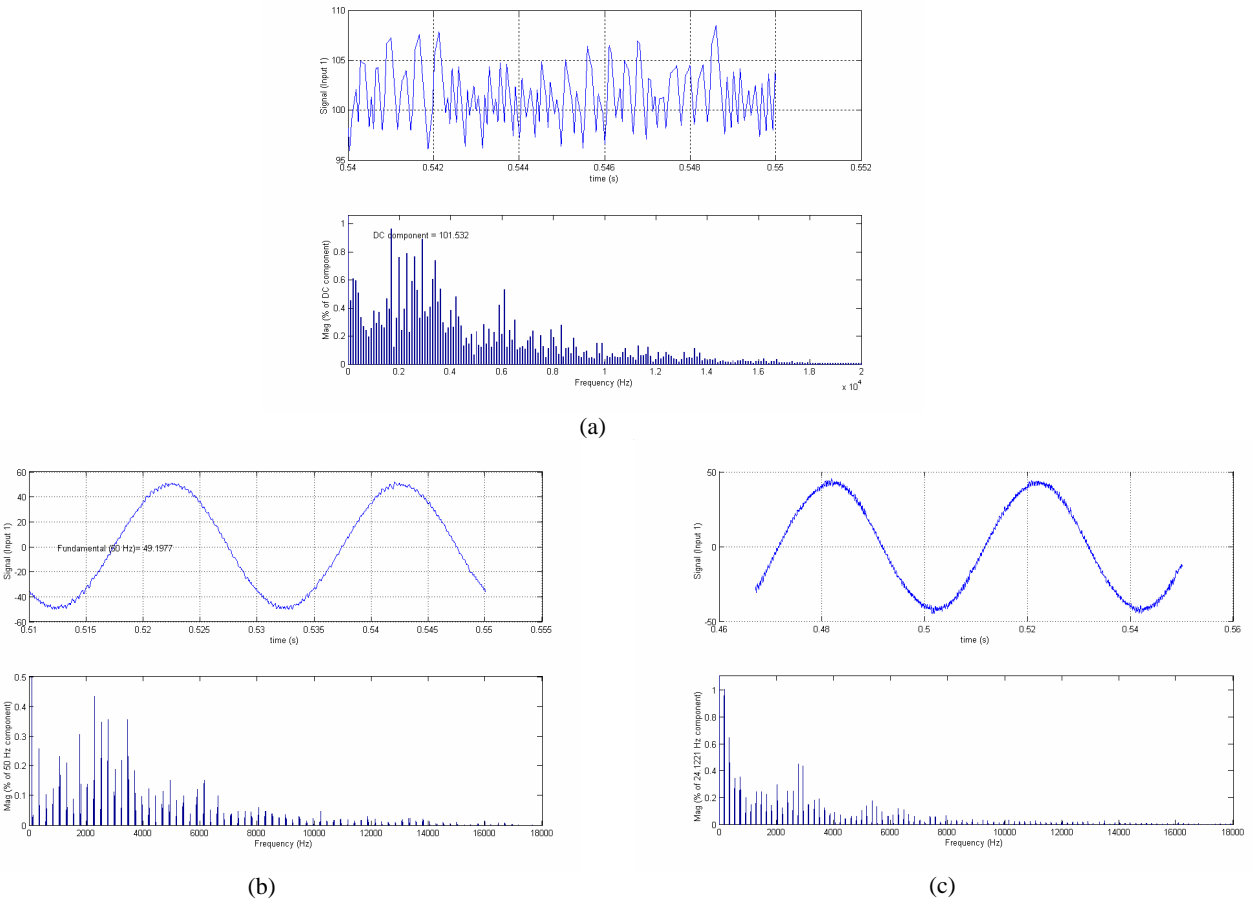


Fig. 4.21. “Classic” DTC control strategy simulation results at 20 kHz. Transient and steady-state behavior IV. Currents and torque Spectrums. (a) Electromagnetic torque spectrum, (b) Stator current Spectrum, (c) Rotor current Spectrum.

To conclude, analyzing the steady-state behavior's quality in terms of the currents interchanged with the grid and with the converter by the stator and the rotor respectively. It is highly remarkable that the more accurately that torque and flux are controlled, the more the quality of the currents is improved. Hence, when very small ripples are achieved, in general, good current qualities are expected. Thus, concerned with the simulation experiments, the stator and the rotor spectrums present high number of harmonic components due to the variable switching frequency behavior, but of quite "acceptable" small amplitude due to reduced torque and flux ripples. In both cases, there is not harmonic component higher than 1 % of the fundamental component.

#### **4.6.3 Transient and Steady-State Behavior. Predictive DTC with Reduced Torque Ripple**

In this section, the same simulation experiments of the previous section are carried out, for the predictive DTC for minimum torque ripple control strategy. The characteristics of the experiment are summarized as follows:

- Switching frequency: 8kHz and 4kHz
- Speed : 1350 rev/min ( $s = 0.9$ ).  $V_{bus} = 500$  V
- Torque step: From -100 Nm (generator mode), to 100 Nm (motor mode).

The results are shown in the next figures:

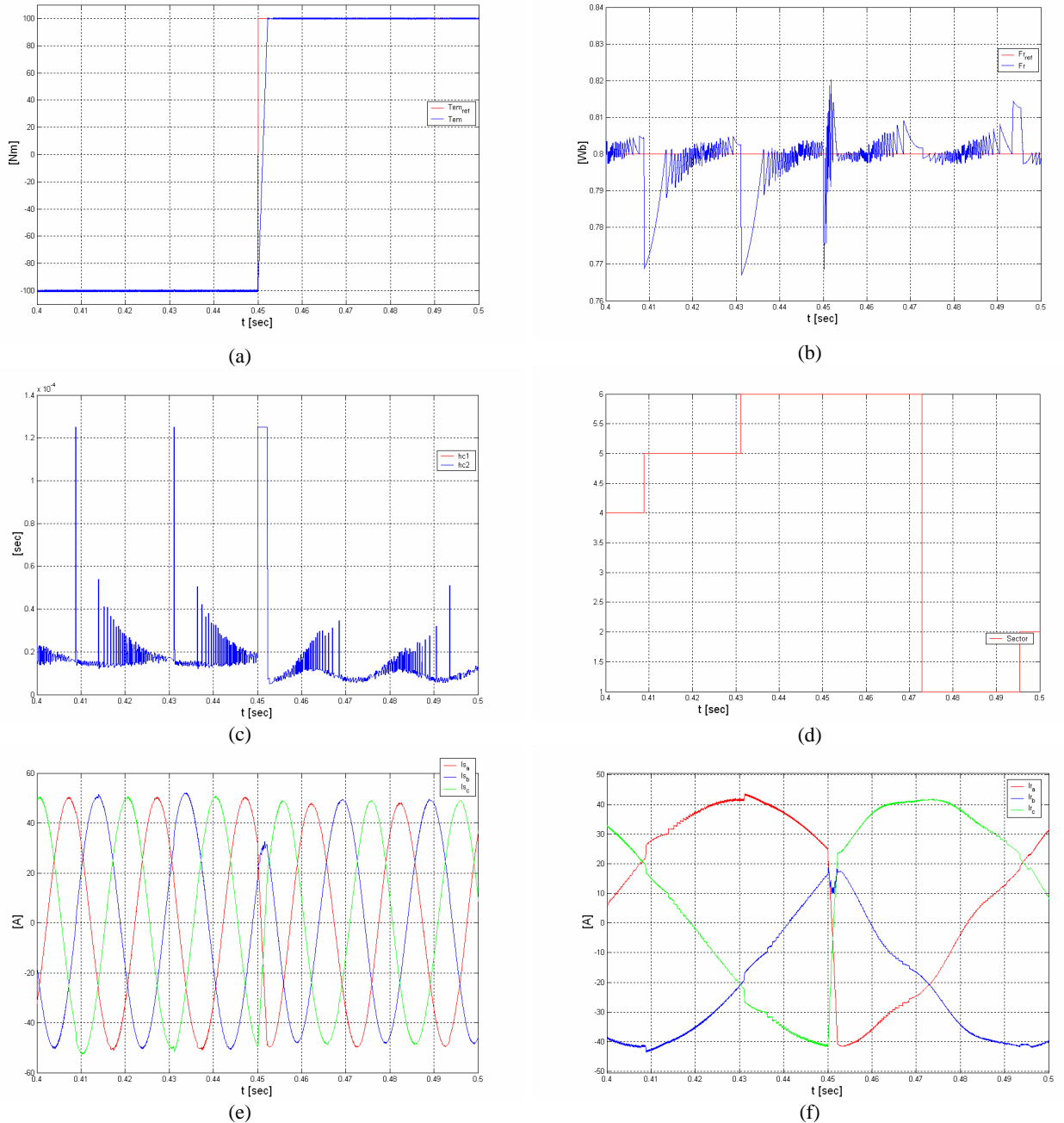


Fig. 4.22. Predictive DTC for minimum torque ripple control strategy (2 vectors per switching period) simulation results at 8kHz. Transient and steady-state behavior I. (a) Electromagnetic torque, (b) Rotor flux, (c) Mechanical speed, (d) Sector, (e) Stator currents, (f) Rotor currents.

Despite the similar appearance of these results compared with the results of the previous control strategy, there exists some remarkable differences. From Fig. 4.22 (a) and (b), by this predictive control technique, the flux and torque ripples are considerably reduced. From the point of view of the transient response, in this case similar results are achieved in terms of velocity of the response (200  $\mu$ s approximately) and absence of overcurrent.

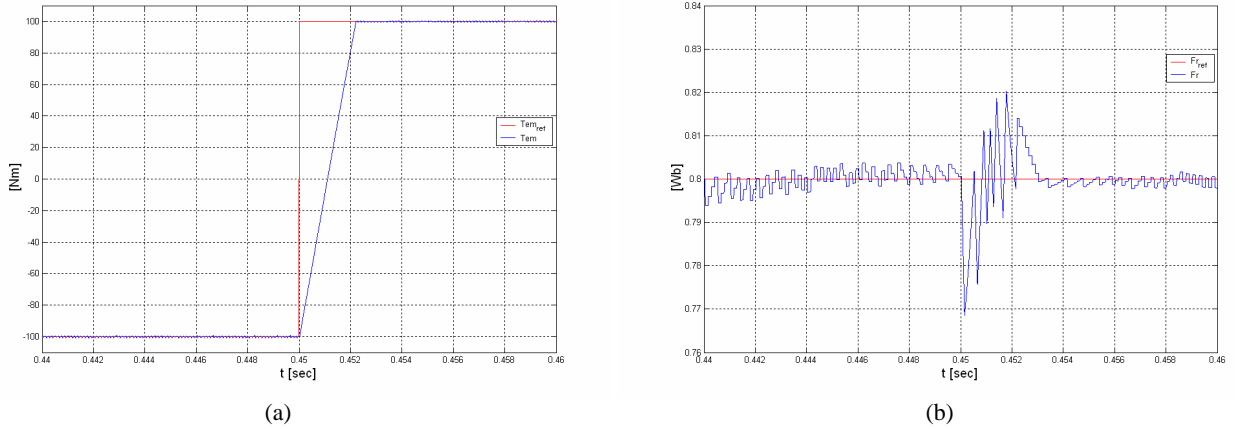


Fig. 4.23. Predictive DTC for minimum torque ripple control strategy (2 vectors per switching period) simulation results at 8kHz. Transient and steady-state behavior II. Zoom of the torque reference step. (a) Electromagnetic torque zoom, (b) Rotor flux zoom.

Unfortunately, although the torque ripple is reduced to nearly constant 1 Nm, the flux presents non continuous variation behavior. In Fig. 4.22 (b) and (d), it is shown that in the sector transitions, a strong flux peak occurs. As mentioned previously, this flux overshoot is due to the fact that this predictive control strategy, only actuates correcting the flux error at the beginning of the switching period, during the rest of the switching period the flux is not supervised again. Taking into account that near to the limits of the sectors, there exist some vectors that produce very high flux variations, and when it comes the time to be used, they therefore produce these high flux variations from the reference value. This effect produces unavoidable non uniform flux ripple, that also produces rotor currents and stator currents sudden variations, finally provoking a degradation in the quality of those currents.

This undesired, but inevitable behavior will provoke higher flux overshoots at lower switching periods. Depending on the application where this control strategy is going to be performed and its requirements, this effect may be insignificant and it may not suppose a problem. Thus, for example in Fig. 4.24, analyzing the quality of the torque and the currents in terms of their spectrum, the amplitudes of the current harmonics are considerably reduced compared with the previously presented results. Furthermore, the constant switching behavior produced by this control strategy, produce torque and current dominant harmonic components to the switching frequency and their multiples. This fact is very useful for some specific applications, and it also reduces and distributes simetrically the stresses among the switching devices of the converter. These advantages have been obtained, reducing the switching frequency of the system to 8 kHz.

Finally, in Fig. 4.22 (c), the on-line computed switching instant ( $h_c$ ) is shown. It seems that it tends to follow a sinusoidal trajectory, but it presents some discontinuities due to the fact that this control strategy does not take into account the flux ripple supervision within the

switching period. The average of the switching instant ( $h_c$ ), is near to 20  $\mu$ s and the switching period ( $h$ ) is 125  $\mu$ s for 8 kHz, this means that for this operation conditions, i.e. the torque and the flux references and the speed of the machine, the bus voltage available is more than required. For instance, if the speed of the machine varies further away from the synchronous speed, there will be a necessity of higher rotor voltage.

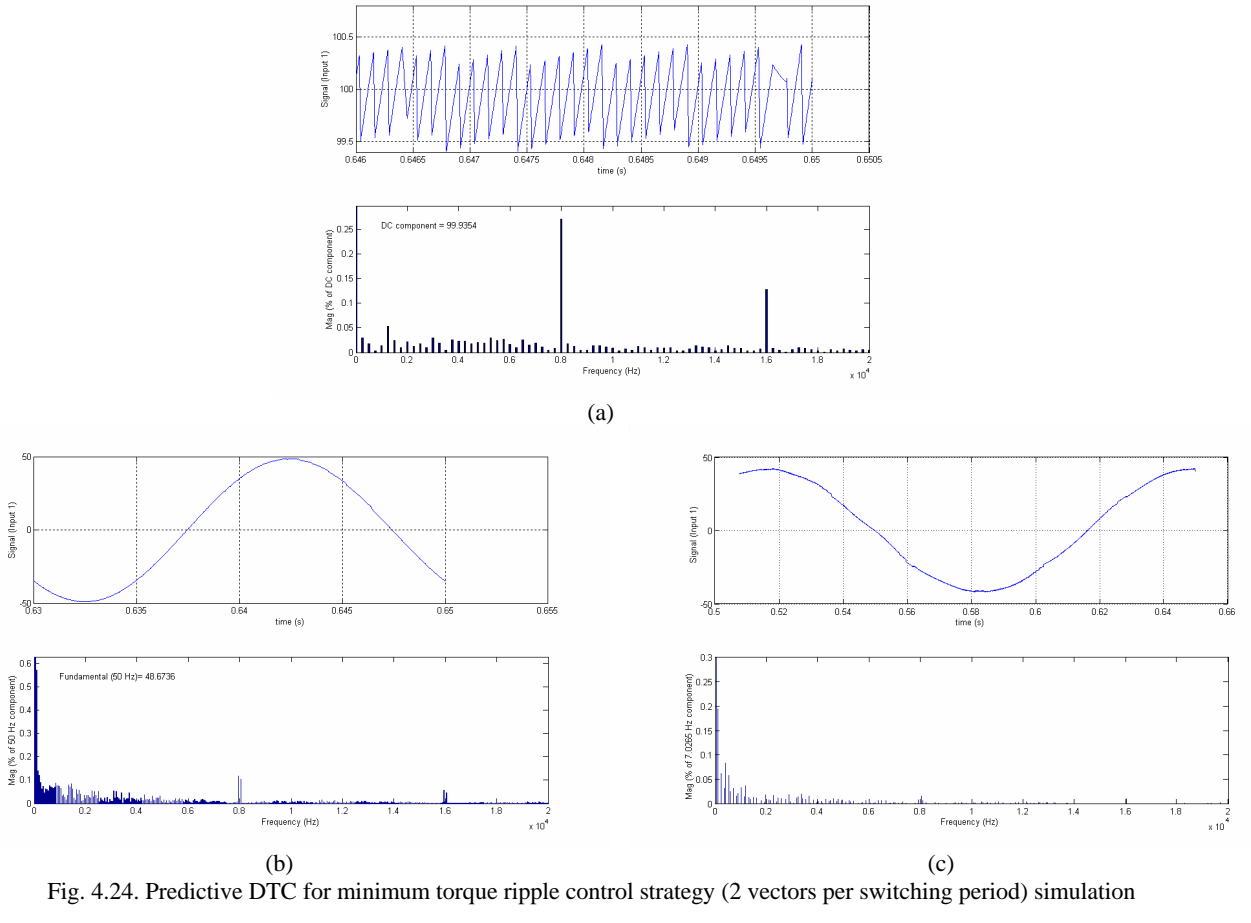


Fig. 4.24. Predictive DTC for minimum torque ripple control strategy (2 vectors per switching period) simulation results at 8kHz. Transient and steady-state behavior III. Currents and torque Spectrums. (a) Electromagnetic torque spectrum, (b) Stator current Spectrum, (c) Rotor current Spectrum.

In the following simulation results, the same experiment is carried out at different switching frequency. In this case, it is reduced to 4 kHz. The steady-state and transient behavior is shown in the next figures.

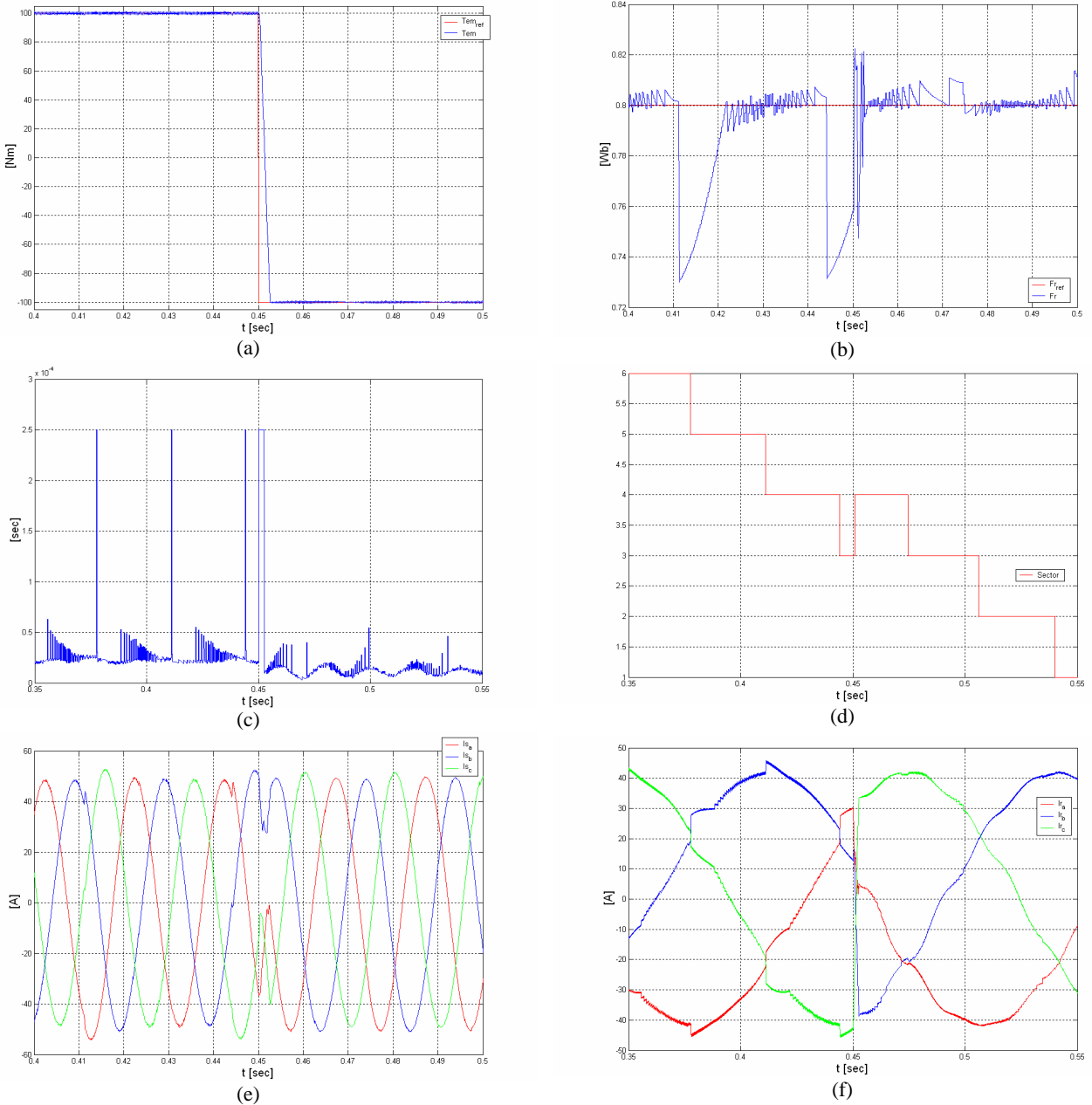


Fig. 4.25 Predictive DTC for reduced torque ripple control strategy (2 vectors per switching period) simulation results at 4kHz. Transient and steady-state behavior IV. (a) Electromagnetic torque, (b) Rotor flux, (c) Mechanical speed, (d) Sector, (e) Stator currents, (f) Rotor currents.

In this case again, as expected, the same good quality of transient response is achieved. On the other hand, due to the reduction in the switching frequency, the torque ripple in steady-state is increased 0.5 Nm approximately. The rotor flux overshoots are more severe, because the time where the flux is not supervised is bigger. This effect, yields to a degradation in the steady-state behavior. This fact is clearly seen in Fig. 4.25 (f), the rotor flux overshoots affect directly to the rotor currents degrading still more their quality. This degradation is considerably reduced in the stator currents because the stator of the machine actuates as a filter.

Depending on the requirements of the application where the control strategy will be used, this behavior can be still acceptable, otherwise, in the following simulation experiments the presented control strategy will eliminate the strong flux variations.

#### **4.6.4 Transient and Steady-State Behavior. Predictive DTC with Reduced Torque and Flux Ripples**

In this section, the same simulation experiments of the previous sections are carried out, for the predictive DTC for reduced torque and flux ripple control strategy. The main characteristics of the experiment are summarized as follows:

- Switching frequency: 4kHz
- Speed : 1350 rev/min ( $s = 0.9$ ).  $V_{bus} = 500$  V.
- Torque step: From 100 Nm (motor mode), to -100 Nm (generator mode).

The results are shown in the next figures:

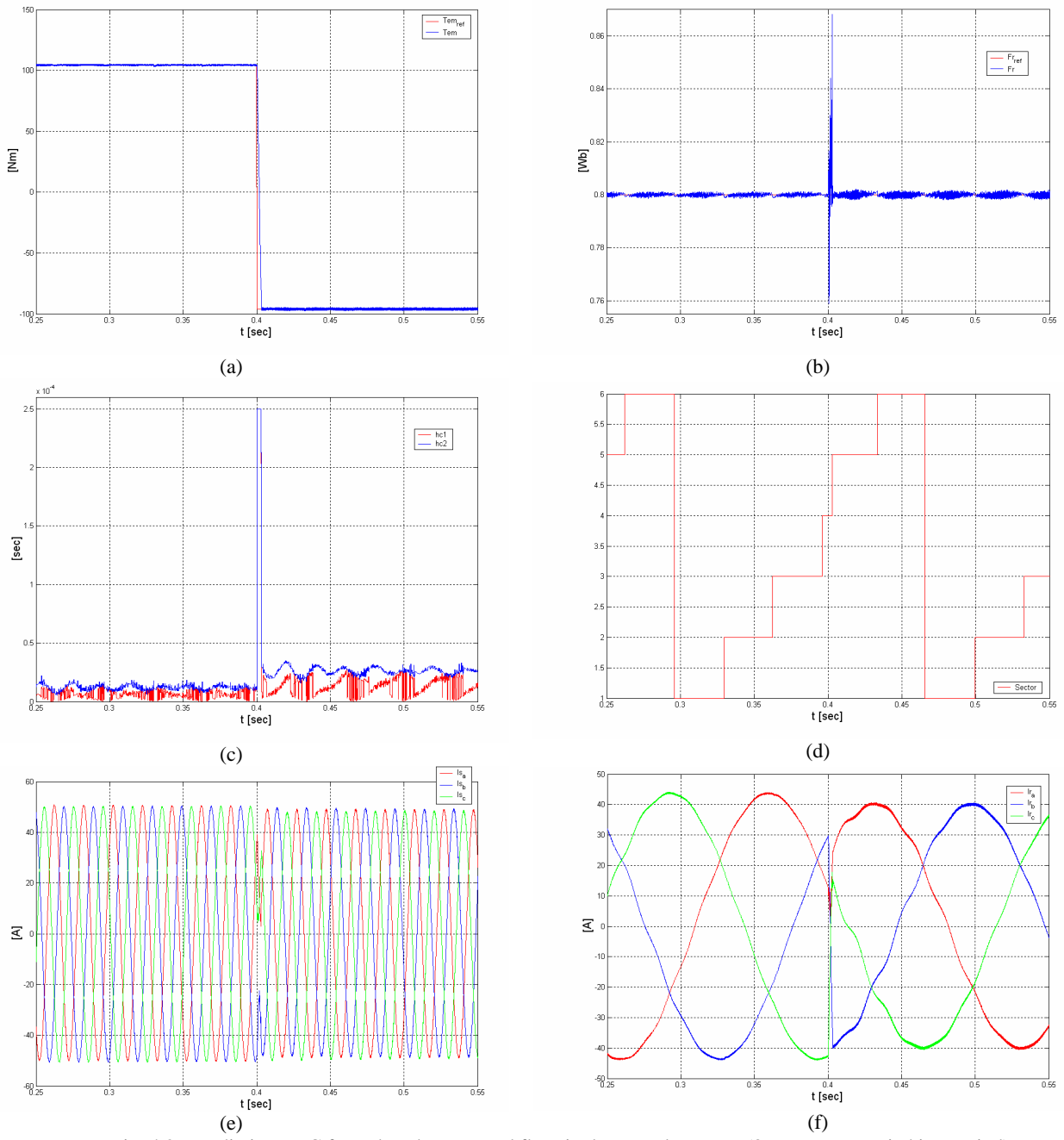
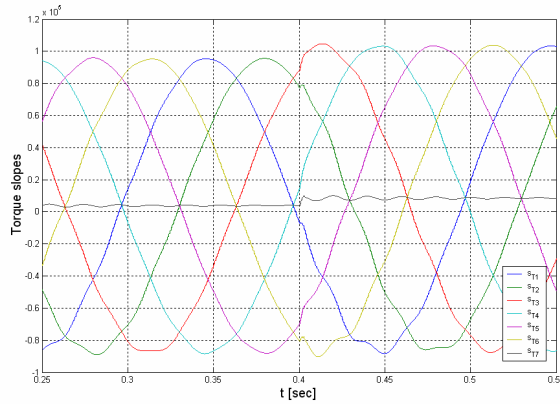
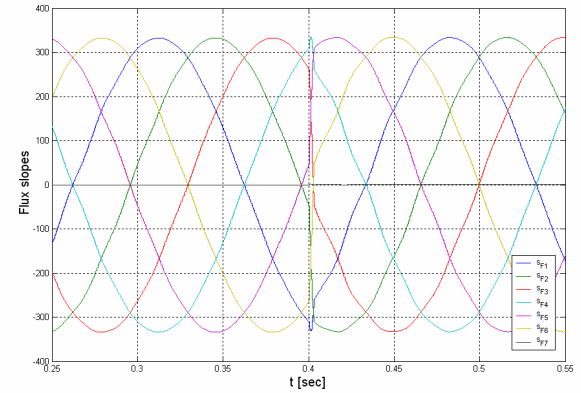


Fig. 4.26 Predictive DTC for reduced torque and flux ripple control strategy (3 vectors per switching period) simulation results at 4kHz. Transient and steady-state behavior I. (a) Electromagnetic torque, (b) Rotor flux, (c)  $h_{c1}$ ,  $h_{c2}$ , (d) Sector, (e) Stator currents, (f) Rotor currents.

In this case, better steady-state behavior is obtained than in the previous two control strategies. Basically, analyzing the torque and the flux magnitudes in Fig. 4.26 (a) and (b), very reduced and uniform ripple is observed. It is very interesting to remark the absence of rotor flux overshoot. This implies very uniform current waveform, improving their quality from the two previous control strategies.



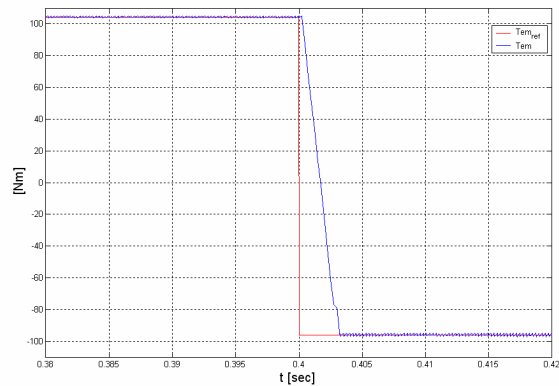
(a)



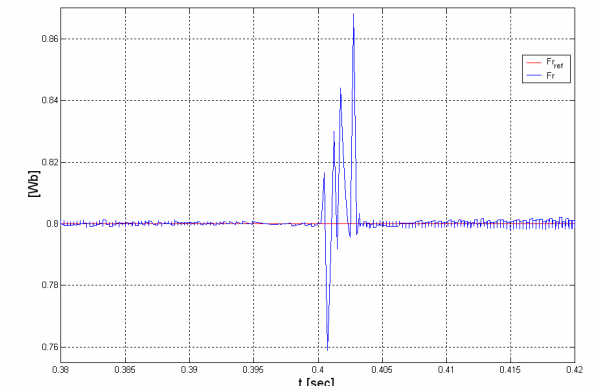
(b)

Fig. 4.27 Predictive DTC for reduced torque and flux ripple control strategy (3 vectors per switching period) simulation results at 4kHz. Transient and steady-state behavior II. (a) Torque slopes, (b) Rotor flux slopes.

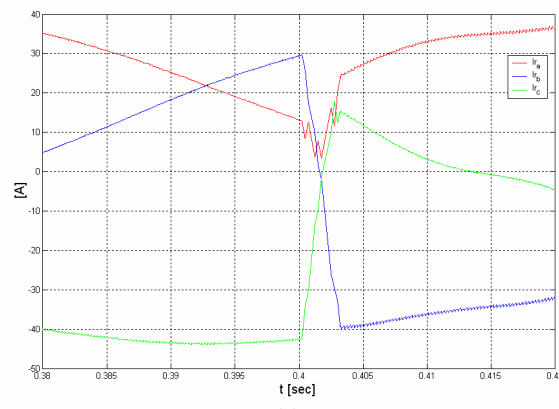
Added to this, the same quality of transient response is achieved by this control technique, i.e. quick and keeping controlled the currents within their safety limits, Fig. 4.29 (c) and (d).



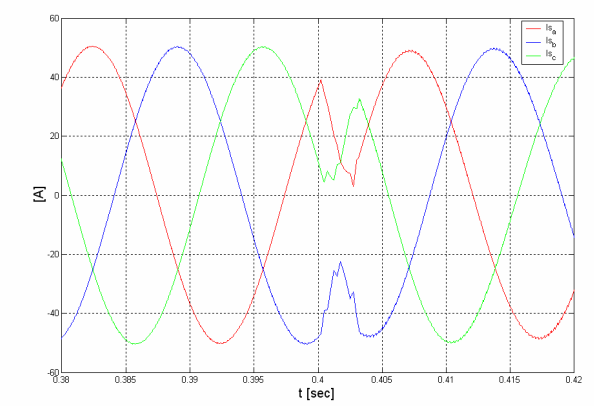
(a)



(b)



(c)



(d)

Fig. 4.28 Predictive DTC for reduced torque and flux ripple control strategy (3 vectors per switching period) simulation results at 4kHz. Transient and steady-state behavior III. Zoom of the torque reference step. (a) Electromagnetic torque zoom, (b) Rotor flux zoom, (c) Rotor currents zoom, (d) Stator currents zoom.

There exist a small drawback for the predictive DTC control strategy with minimum torque and flux ripple in terms of the steady-state torque ripple, compared with the previously presented predictive control strategy. In this case, as shown in Fig. 4.29 (a), the torque presents a 2 Nm ripple approximately, while in the previous simulation results, for the same operation conditions, the torque ripple was slightly smaller. The reason is because this control strategy, at the same switching period as the previous control technique, fulfills two requirements at the same time, i.e. torque and flux ripple reduction.

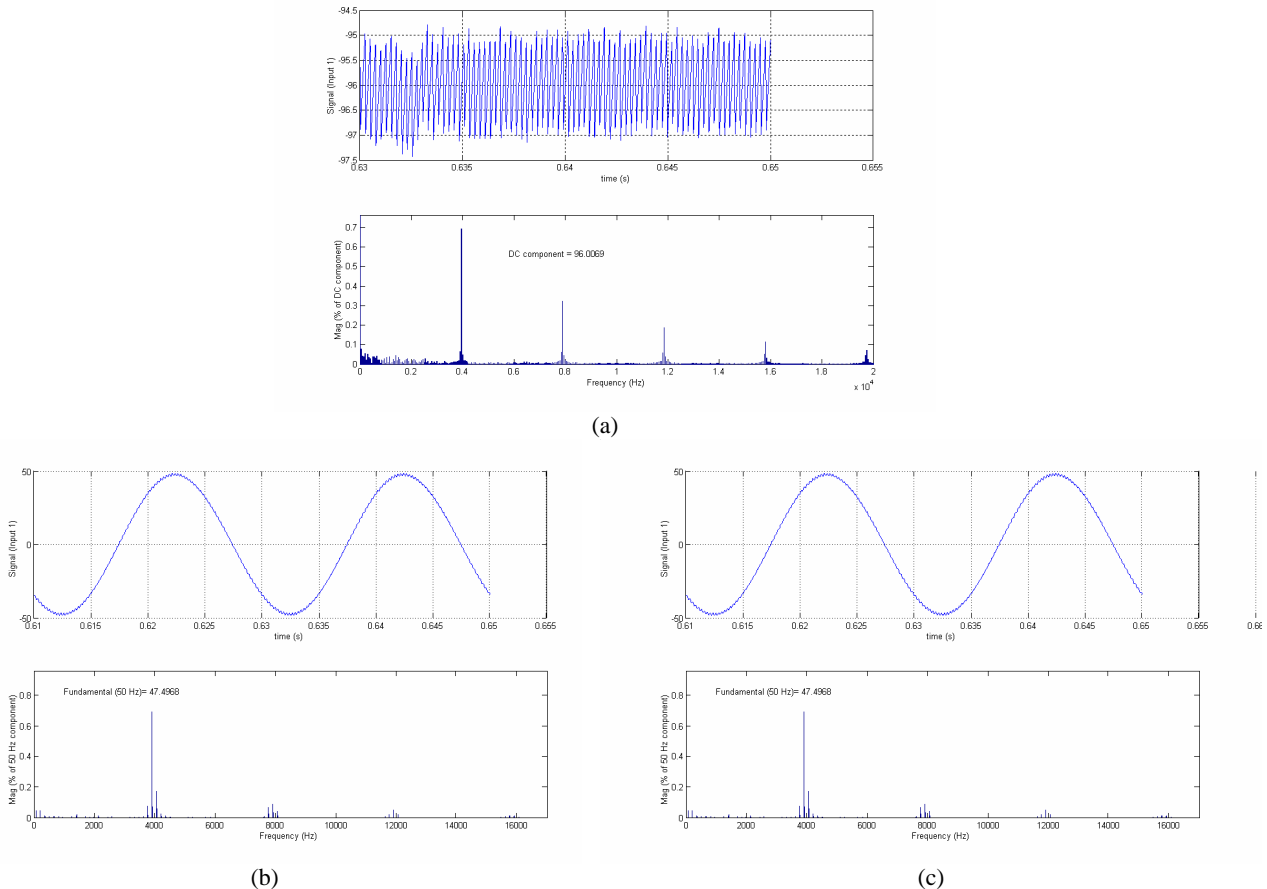


Fig. 4.29 Predictive DTC for reduced torque and flux ripple control strategy (3 vectors per switching period) simulation results at 4kHz. Transient and steady-state behavior III. (a) Electromagnetic torque spectrum, (b) Stator current Spectrum, (c) Rotor current Spectrum.

Finally, from the point of view of the quality of the currents obtained by this control technique at this switching frequency, it is possible to state a considerably high improvement, because now, since the flux overshoot has disappeared, the currents are mainly only “polluted” by the “high” frequency ripple, i.e. the ripple that appears due to the harmonic components multiple to the switching frequency.

In the next simulation experiment, the capacity of this DTC control technique to operate at “low” switching frequencies is explored. Hence, the machine will be driven by this control

strategy with a considerably low switching frequency of 800 Hz. The experiment will be carried out in the same way as the previous experiments, according to the following operation conditions:

- Switching frequency: 800 Hz
- Speed : 1000 rev/min ( $s = 0.66$ )
- $V_{bus} = 500$  V
- Torque step: From -100 Nm (generator mode), to 100 Nm (motor mode).

The results are shown in the next figure:

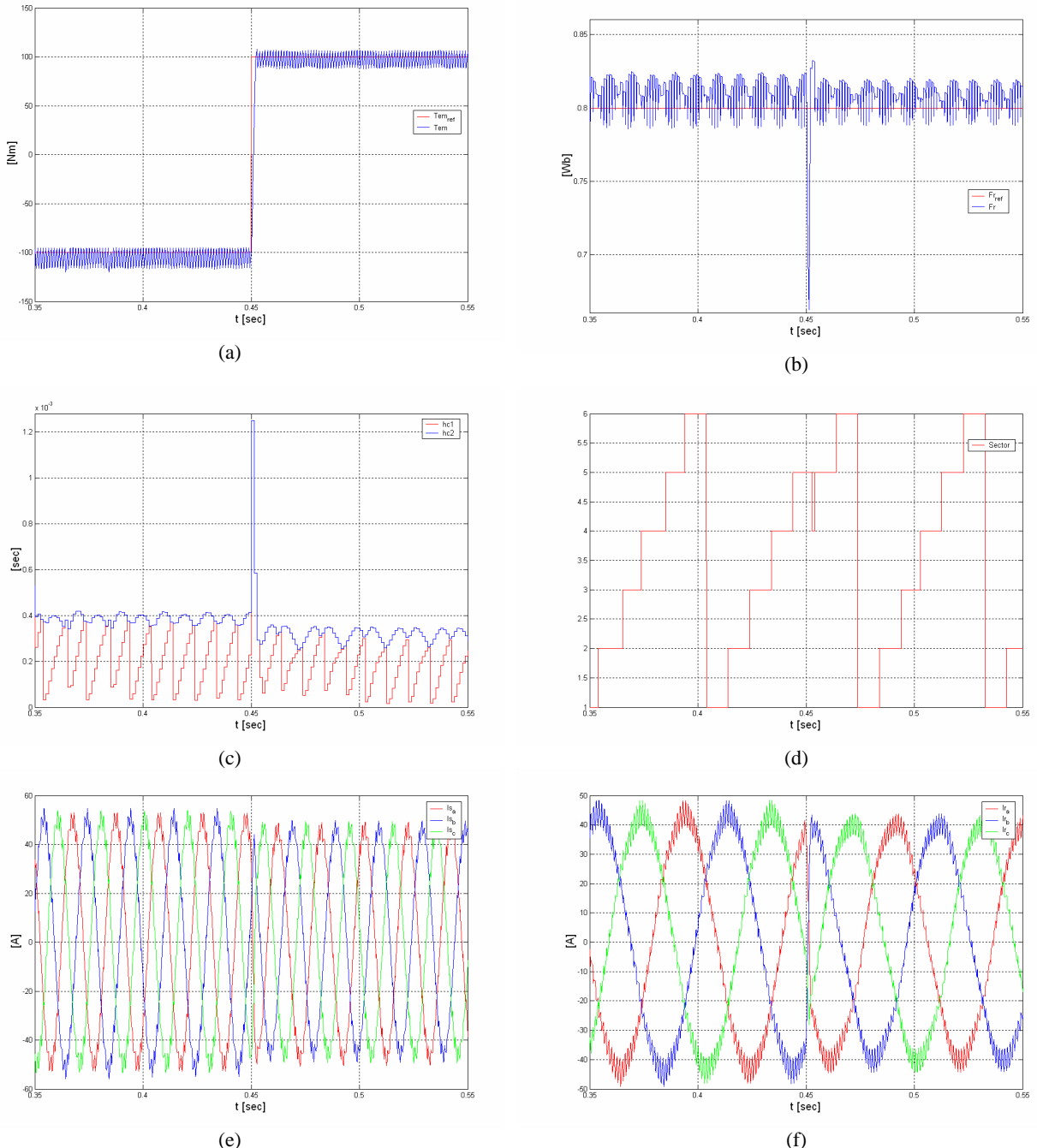


Fig. 4.30 Predictive DTC for reduced torque and flux ripple control strategy (3 vectors per switching period) simulation results at 800 Hz. Transient and steady-state behavior IV. (a) Electromagnetic torque, (b) Rotor flux, (c)  $h_{c1}, h_{c2}$ , (d) Sector, (e) Stator currents, (f) Rotor currents.

By this simulation experiment, it is observed how the quality of the steady state behavior is reduced due to the reduction in the switching frequency, but not due a degradation of the control strategy performance. The DTC control technique, still is able to reduce the torque and flux ripples, but at the imposed switching frequency. Comparing with previously presented simulation results, the ripples are increased considerably both in the torque and in the flux as in the currents.

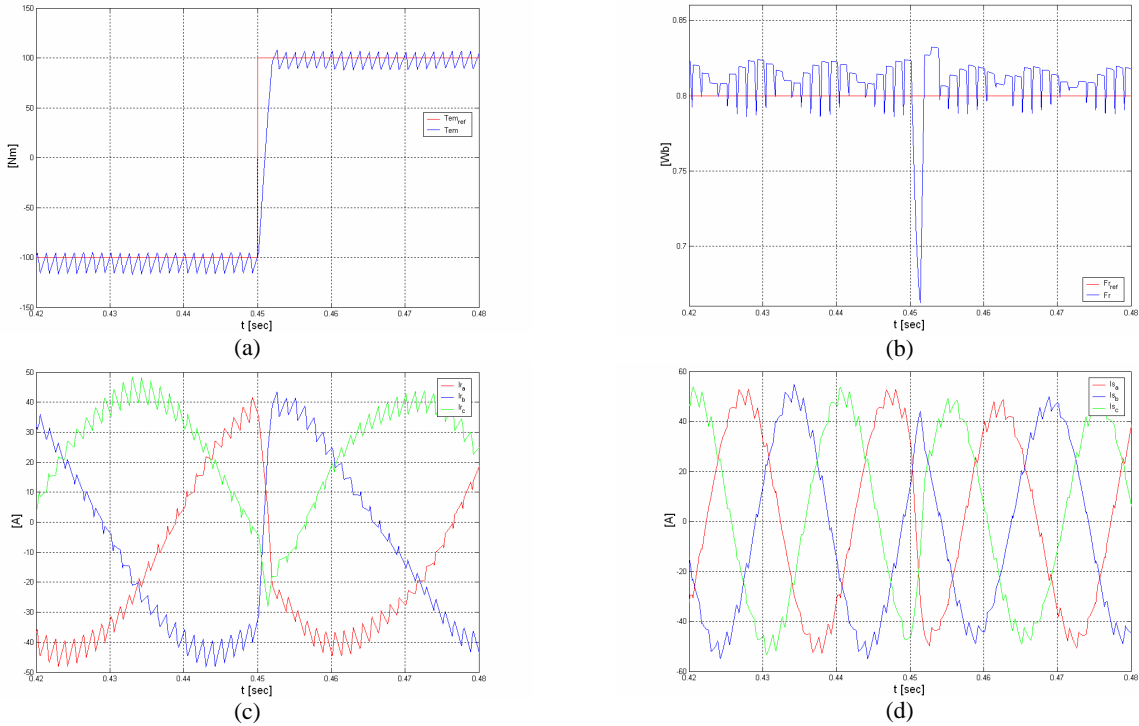


Figure 4.31. Predictive DTC for reduced torque and flux ripple control strategy (3 vectors per switching period) simulation results at 800 Hz. Transient and steady-state behavior V. Zoom of the torque reference step. (a) Electromagnetic torque zoom, (b) Rotor flux zoom, (c) Rotor currents zoom, (d) Stator currents zoom.

Nevertheless, an acceptable transient response is obtained, it presents very similar characteristics to the previous simulation results. Thus, thanks to this simulation experiment, it is shown how this control strategy may be useful for high power applications where the switching frequencies are limited, since it ensures quick and smooth transient responses and reduced ripples at steady-state.

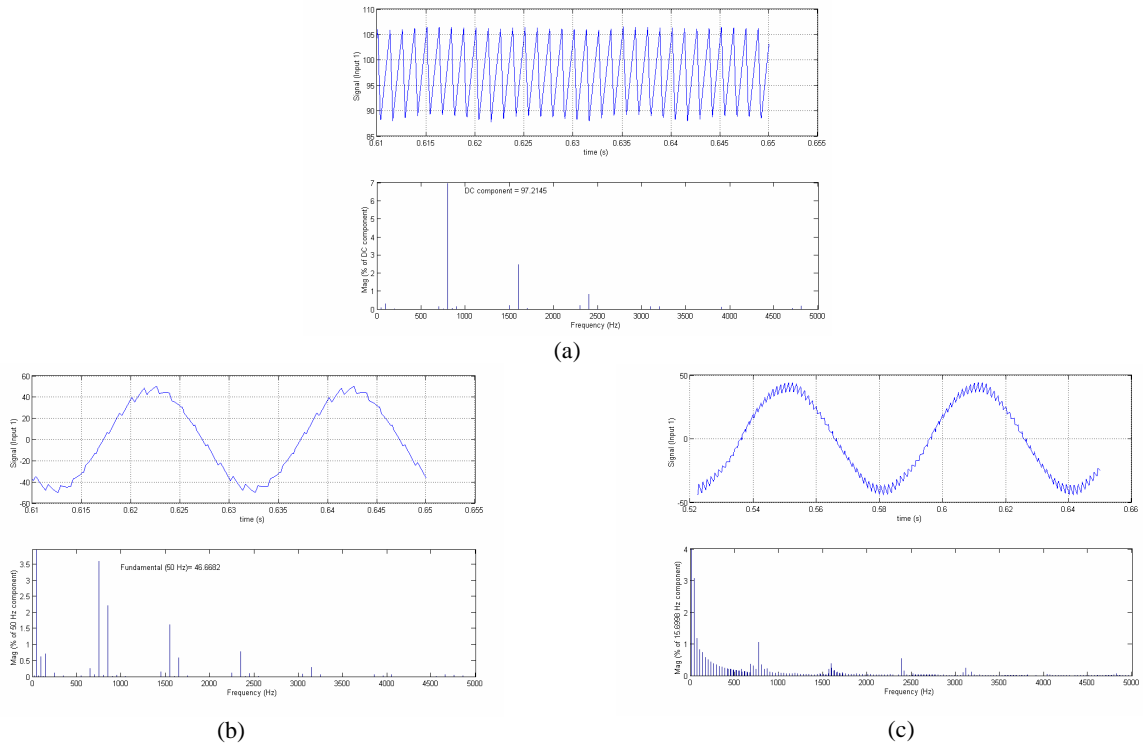


Figure 4.32 Predictive DTC for reduced torque and flux ripple control strategy (3 vectors per switching period) simulation results at 800 Hz. Transient and steady-state behavior VI. Currents and torque Spectrums. (a) Electromagnetic torque spectrum, (b) Stator current Spectrum, (c) Rotor current Spectrum.

#### 4.6.5 Tracking behavior. Predictive DTC with Reduced Torque and Flux Ripples

In the following simulation experiment, the behavior of the system is shown when the torque reference and the speed of the machine are varying during the time. Compared with the previous experiments, it is wanted to explore another capacity of the proposed DTC control strategies, i.e. the tracking behavior.

There are some applications where the DFIM is required to operate at variable speed and at the same time, the demanded torque may also be variable. Under these circumstances the control strategy should guarantee that the references will be followed by their actual values as close as possible. The next experiment has been developed, in order to show this ability for the predictive DTC for minimum torque and flux ripple. The most interesting characteristics of the experiment are summarized as:

- Switching frequency: 4 kHz
- Vbus = 500 V
- Torque reference: 4 Hz frequency and 100 Nm sinusoidal reference (generator mode and motor mode).
- Constant rotor flux reference.
- Variable speed at subsynchronous and hypersynchronous modes, crossing the synchronous speed (1500 rev/min) either increasing and decreasing.

The three vector predictive DTC control technique has been used for this experiment, because at steady-state, it provides the best results from the presented three DTC control techniques.

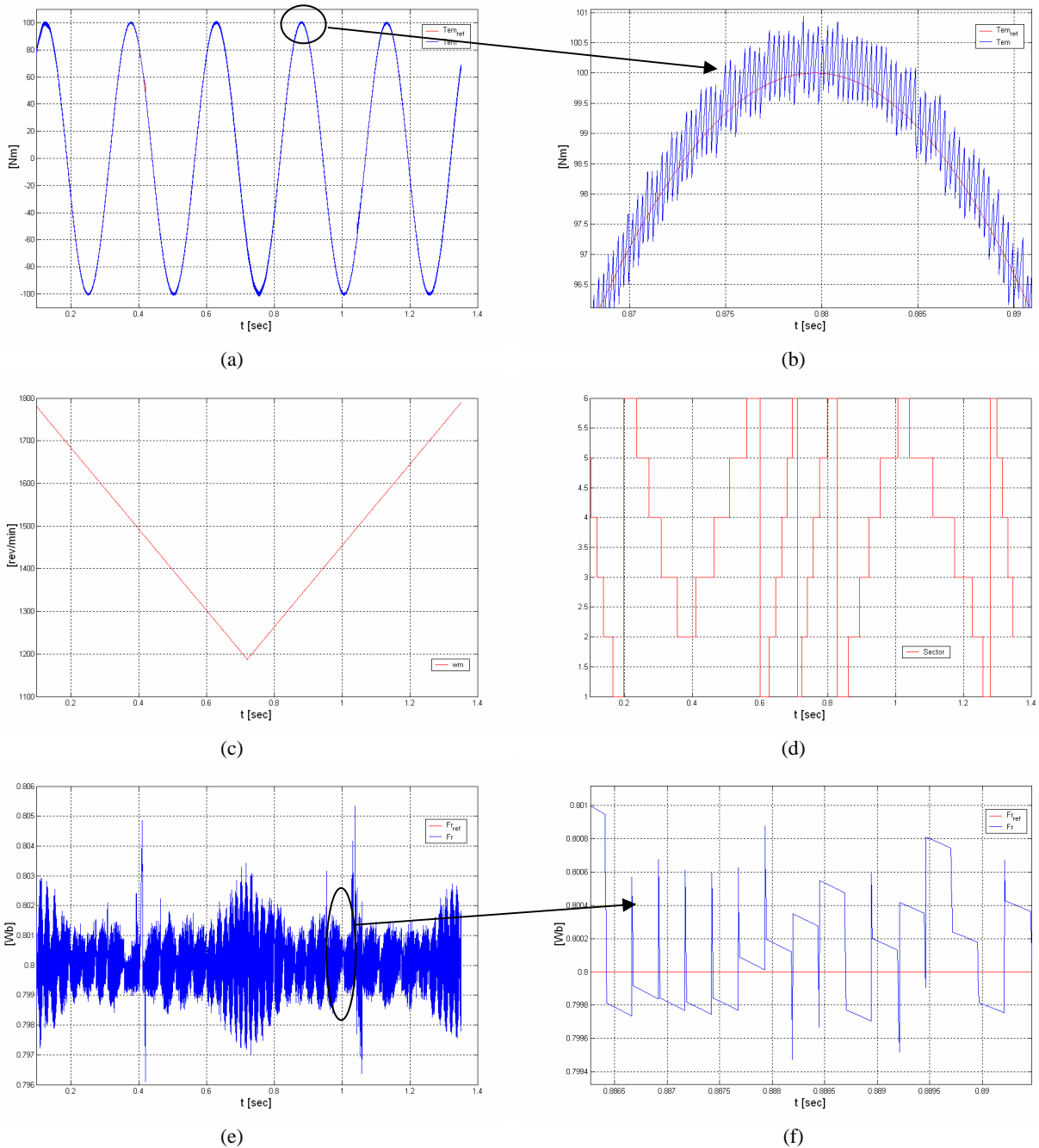


Fig. 4.33 Predictive DTC for minimum torque and flux ripple control strategy simulation results. 4kHz. System tracking for variable speed and torque reference. (a) Electromagnetic torque, (b) Electromagnetic torque zoom, (c) Speed, (d) Sector, (e) Rotor flux, (f) Rotor flux zoom.

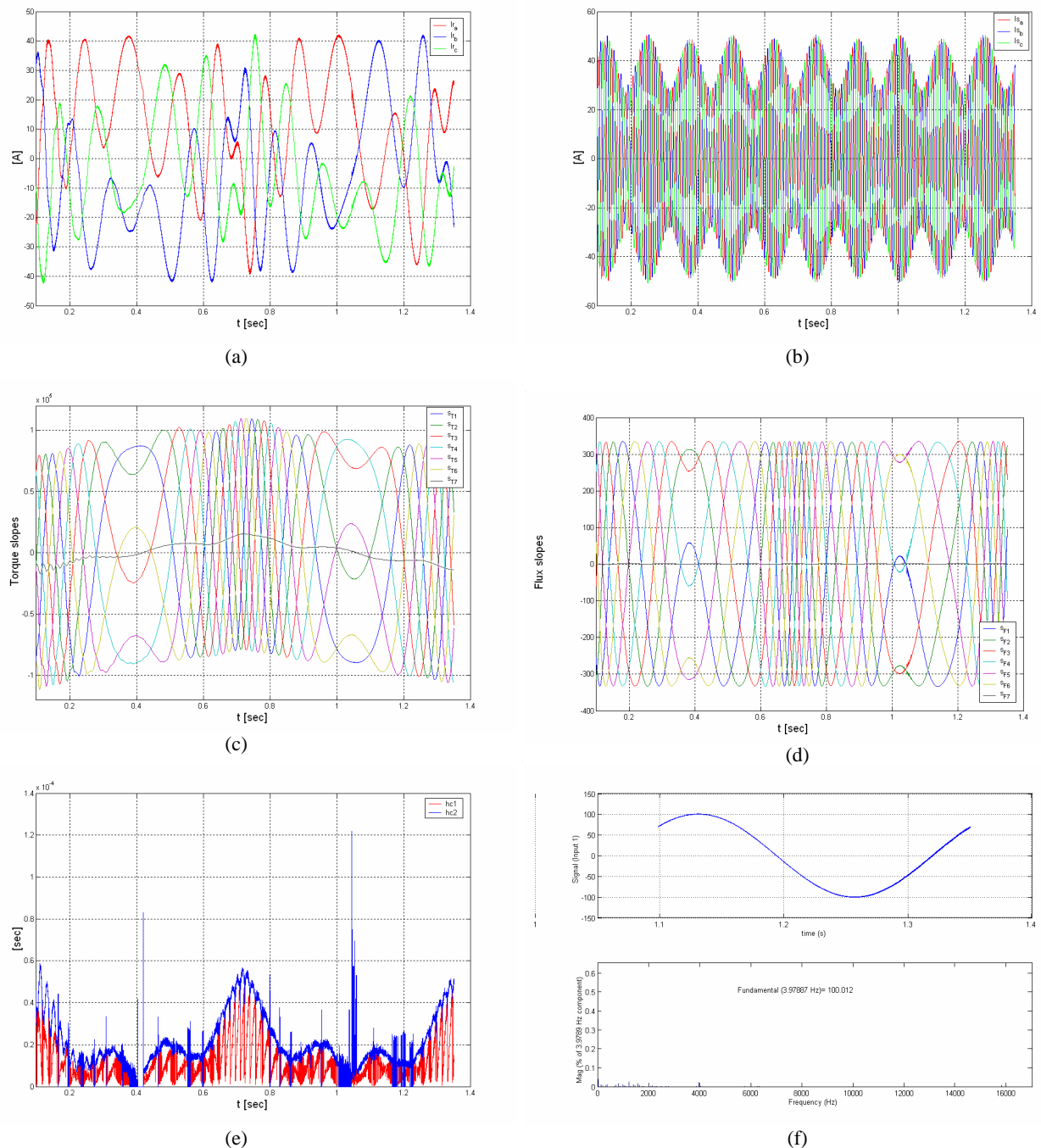


Fig. 4.34 Predictive DTC for minimum torque and flux ripple control strategy simulation results. 4kHz. System tracking for variable speed and torque reference. (a) Rotor currents, (b) Stator currents, (c) Torque slopes, (d) Rotor flux slopes. (e)  $h_{c1}$ ,  $h_{c2}$ , (f) Torque spectrum.

It is noticed that despite the severe conditions of the experiment, the control strategy is able to keep the torque and the rotor flux controlled all the time, leading to a acceptable system tracking behavior. This means, that this control strategy might be suitable for variable speed and variable torque applications.

## 4.7 Experimental Results

### 4.7.1 Overview of the Experimental Results

In this section, experimental results of the predictive DTC strategy with reduced torque and flux ripples, presented in the previous sections will be carried out. All the experiments have been focused on this control technique, since the other two control techniques developed and presented in this chapter, are not useful at low switching frequency operation.

Despite the fact that this control technique is oriented to high power applications, the test bench in which the results have been obtained is of lower scale. Thus, the behavior of a specific 15kW DFIM is studied, controlled by the predictive DTC control technique with reduced torque and flux ripples. Hence, the experimental trials will be divided into three different categories, showing the performance of the control under three different operation conditions: the steady state, the transient response and the tracking behavior. Since the control strategy has been specially designed to operate at low constant switching frequencies, the working scenario will be focused on the severity of the low switching frequency, nevertheless, at higher switching frequencies equivalent performance is achieved.

### 4.7.2 Experimental Rig

The most relevant characteristics of the DFIM are summarized in TABLE 4.VI. It is coupled to a DC machine supplied by a controlled reversible rectifier. By this DC machine, the speed of both machines is controlled, while in the DFIM, the torque and the rotor flux are directly controlled. The rotor of the DFIM is supplied by a reversible two level converter and the stator is directly connected to the grid. The DC side of the two level converter is supplied by a programmable constant reversible voltage source.

The predictive DTC technique is implemented on a DSP-FPGA based platform, composed by a dSPACE 1103 board and a Spartan 3 from XILINX. It allows to perform constant and different switching frequency pulse patterns in real time, for the two level converter. For estimation and visualization purposes, there is an acquisition task running on the board, which operates at 100 $\mu$ sec constant sample period.

In other words, the simulations carried out in the previous section are oriented to reproduce the experimental conditions of this experimental rig.

#### 4.7.3 Steady state Operation Conditions

In this subsection, the steady state performance of the system is presented under different constant switching frequencies. The speed of the machine is controlled externally at 1100 rev/min, the DC bus voltage of the two level converter is 300V, while the torque reference is set to the nominal torque of the machine. Fig. 4.35 shows the most interesting magnitudes of the machine, when the control strategy is operating at 0.5kHz switching frequency. Thus, Fig. 4.35 (a) and (b), show the reduced torque and rotor flux ripple behavior. Then, in Fig. 4.35 (c) and (d), the uniform stator and rotor current evolutions are observed due to a proper simultaneous torque and flux control, as stated previously. Finally, Fig. 4.35 (e) and (f), present the sector in which the rotor flux is located and the duty cycle variations to achieve this state.

On the other hand, in order to quantify the quality of the steady state behavior achieved with the proposed control strategy, the torque and the stator current spectrums are shown in Fig. 4.36, at three different switching frequencies: 0.5kHz, 1kHz and 2.5kHz. The comparison is carried out, under the same torque, rotor flux, speed and DC bus voltage conditions as the previous experiment.

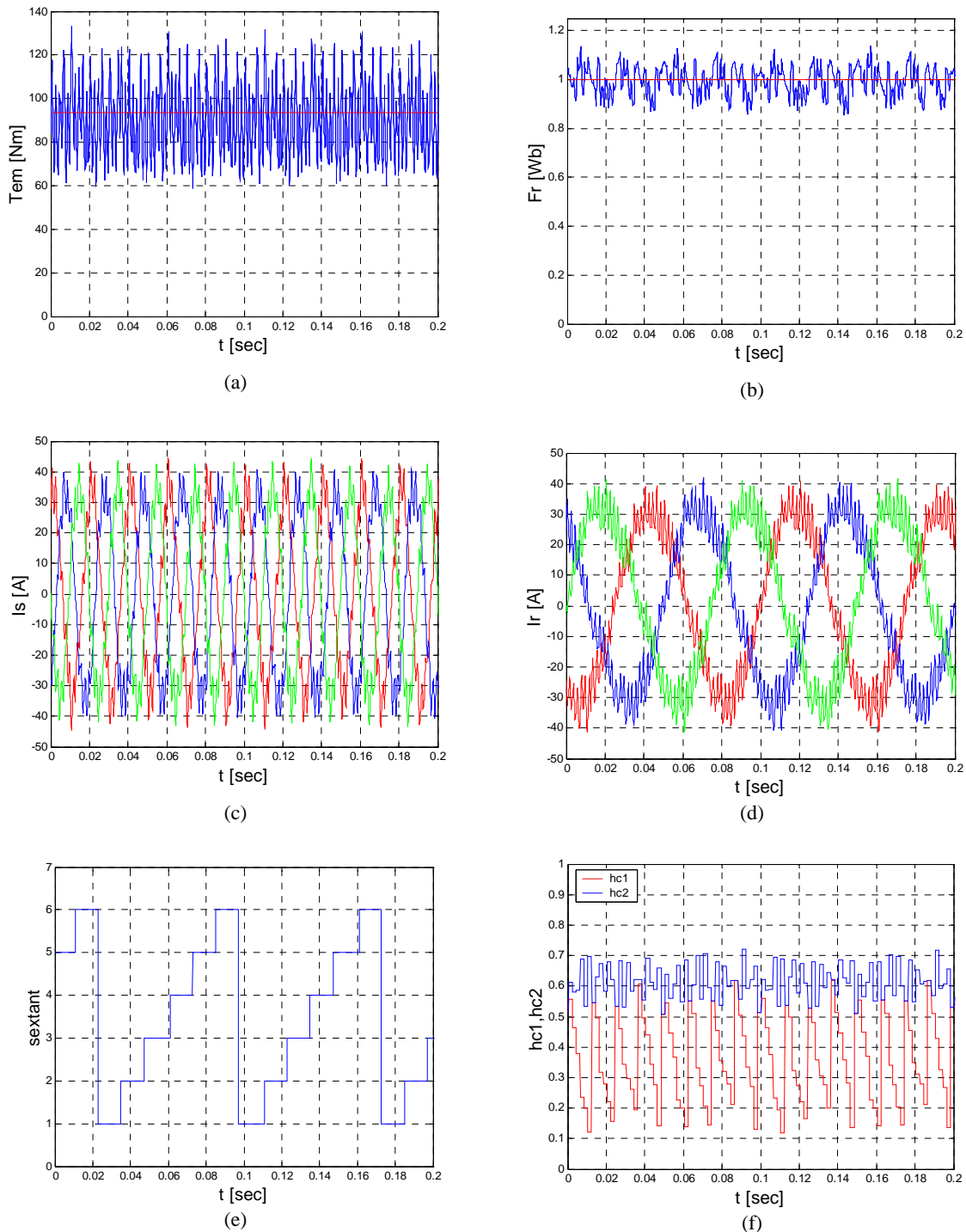


Fig. 4.35. Experimental results. Steady state behavior of the predictive DTC control strategy at 0.5kHz switching frequency. (a) Electromagnetic Torque, (b) Rotor Flux, (c) Stator Current, (d) Rotor Current, (e) Sector, (f)  $hc1, hc2$ .

In the torque spectrums, the constant switching frequency behavior of the system may be observed. The higher magnitude harmonics are present at 0.5kHz, 1kHz and 2.5kHz in each case. In addition, the stator current spectrum is a consequence of both torque and rotor flux behavior. Obviously, the higher the switching frequency it is, the better spectrum quality that can be obtained.

When a specific application requires better current or torque spectrum qualities, but without increasing the switching frequency, it is possible to adopt a multilevel converter topology or to employ active or passive filters. In this research work, focusing on the two level converter topology analysis, no further developments have been carried out.

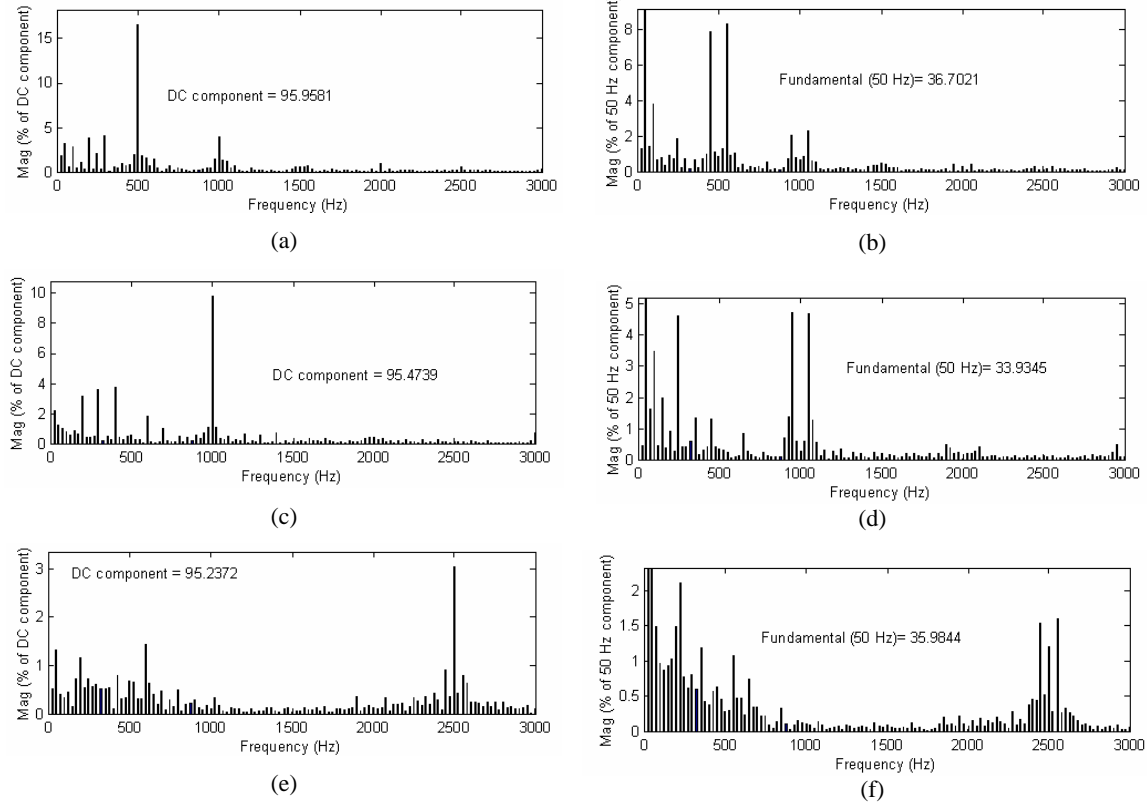


Fig. 4.36. Experimental results. Torque and stator current spectra of the predictive DTC control strategy at different switching frequencies. (a)  $T_{em}$  spectrum (0.5kHz), (b)  $i_{sa}$  spectrum (0.5kHz, THD=13.4%), (c)  $T_{em}$  spectrum (1kHz), (d)  $i_{sa}$  spectrum (1kHz, THD=9.9%), (e)  $T_{em}$  spectrum (2.5kHz), (f)  $i_{sa}$  spectrum (2.5kHz, THD=6.1%).

#### 4.7.4 Transient Response

In this subsection, the dynamic response of the system will be shown when a torque step reference is demanded. The switching frequency is set to 1 kHz. The torque reference variation is 95Nm (the nominal torque), and it will provoke a sudden change of the machine operation from motoring mode to generating mode. This fact can be observed in Fig. 4.37 (a). The torque reference is reached in approximately 2.5msec, and at this switching frequency, this time only depends on the DC bus voltage. This severe torque variation demand, is accomplished in a reliable and safe way by the control strategy, as can be inferred from Fig. 4.37 (b), (c) and (d). There is an absolute absence of overcurrent in both stator and rotor phase currents, and it is achieved by introducing the appropriate vector sequence, the required time intervals, as shown in Fig. 4.38 (b).

Finally, this fast and strong torque variation produces a small variation in the speed (Fig. 4.37 (e)), since it is controlled externally by a system that does not present the same dynamic response capacity as the predictive DTC technique presented in this paper. It is also responsible of the rotor current frequency increase, produced after the torque step. This fact, can also be understood by looking at Fig. 4.37 (e), after the torque step, the time intervals in which the rotor flux lies in a specific sector are reduced. Fig. 4.38 shows with more detail the transient response.

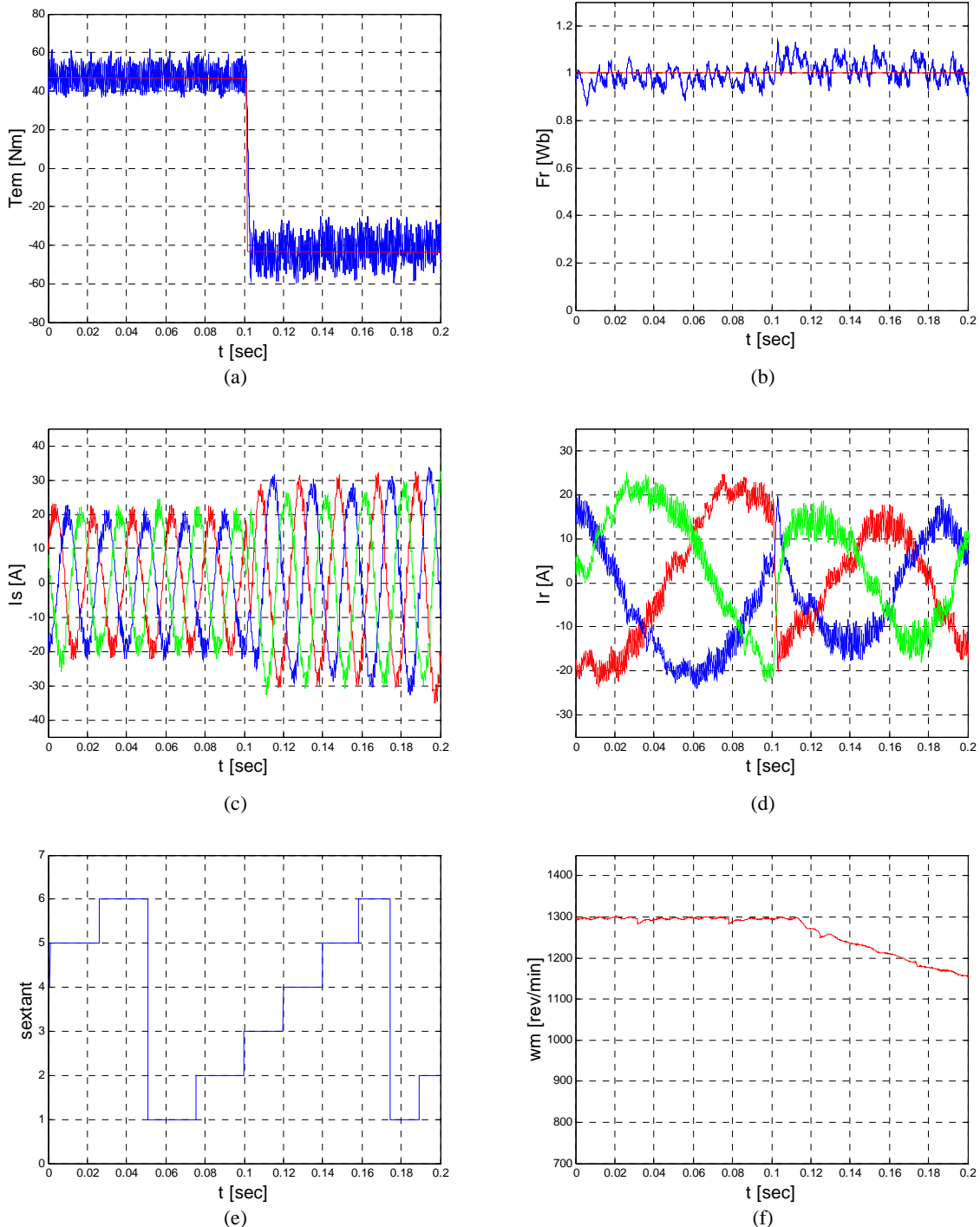


Fig. 4.37 Experimental transient response of the predictive DTC control strategy at 1kHz switching frequency. (a) Electromagnetic Torque, (b) Rotor Flux, (c) Stator Current, (d) Rotor Current, (e) Sector, (f) speed.

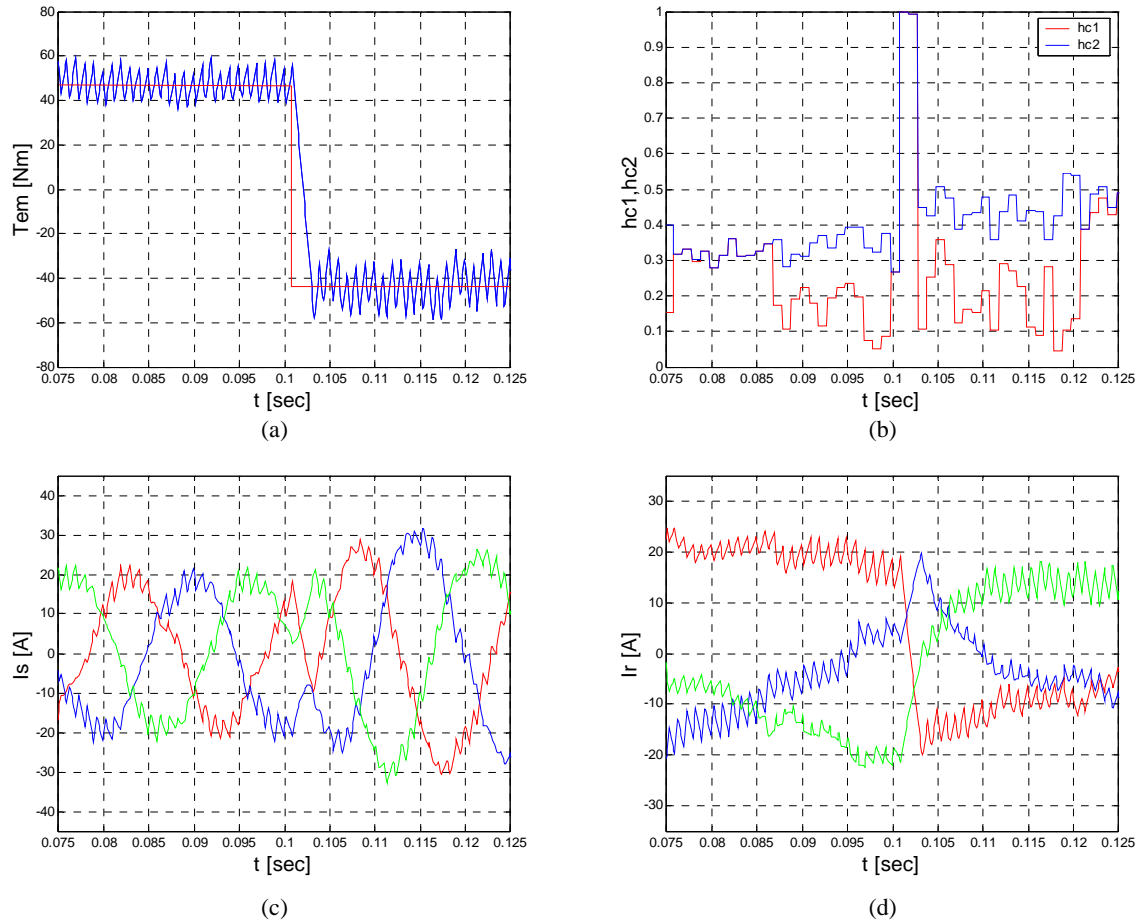


Fig. 4.38 Experimental transient response (zoom) of the predictive DTC control strategy at 1kHz switching frequency. (a) Electromagnetic Torque, (b) Rotor Flux, (c) Stator Current, (d) Rotor Current.

#### 4.7.5 Tracking Behavior

In this next experiment, the behavior of the system is shown when the torque reference and the speed of the machine are varying during the time. Compared with the previous experiments, it is wanted to explore another capacity of the proposed DTC control strategy, i.e. the tracking behavior.

There are some applications where the DFIM is required to operate at variable speed and at the same time, the demanded torque may also be variable. Under these circumstances, the control strategy should guarantee that the references will be followed by their actual values as close as possible. The next experiment has been developed, in order to show this ability for the predictive DTC technique. The system again operates at 1kHz switching frequency, and the sinusoidally varying torque reference (3Hz and 60Nm amplitude) makes it operate at motor and generator modes.

Fig. 4.39 shows the captured most important magnitudes of the experiment. Thus, in Fig. 4.39 (a) and (b), the torque and flux tracking behavior can be observed. Under these conditions, the stator and rotor currents experiment the evolution shown in Fig. 4.39 (c) and (d), while in Fig. 4.39 (f), the externally controlled speed variation is presented.

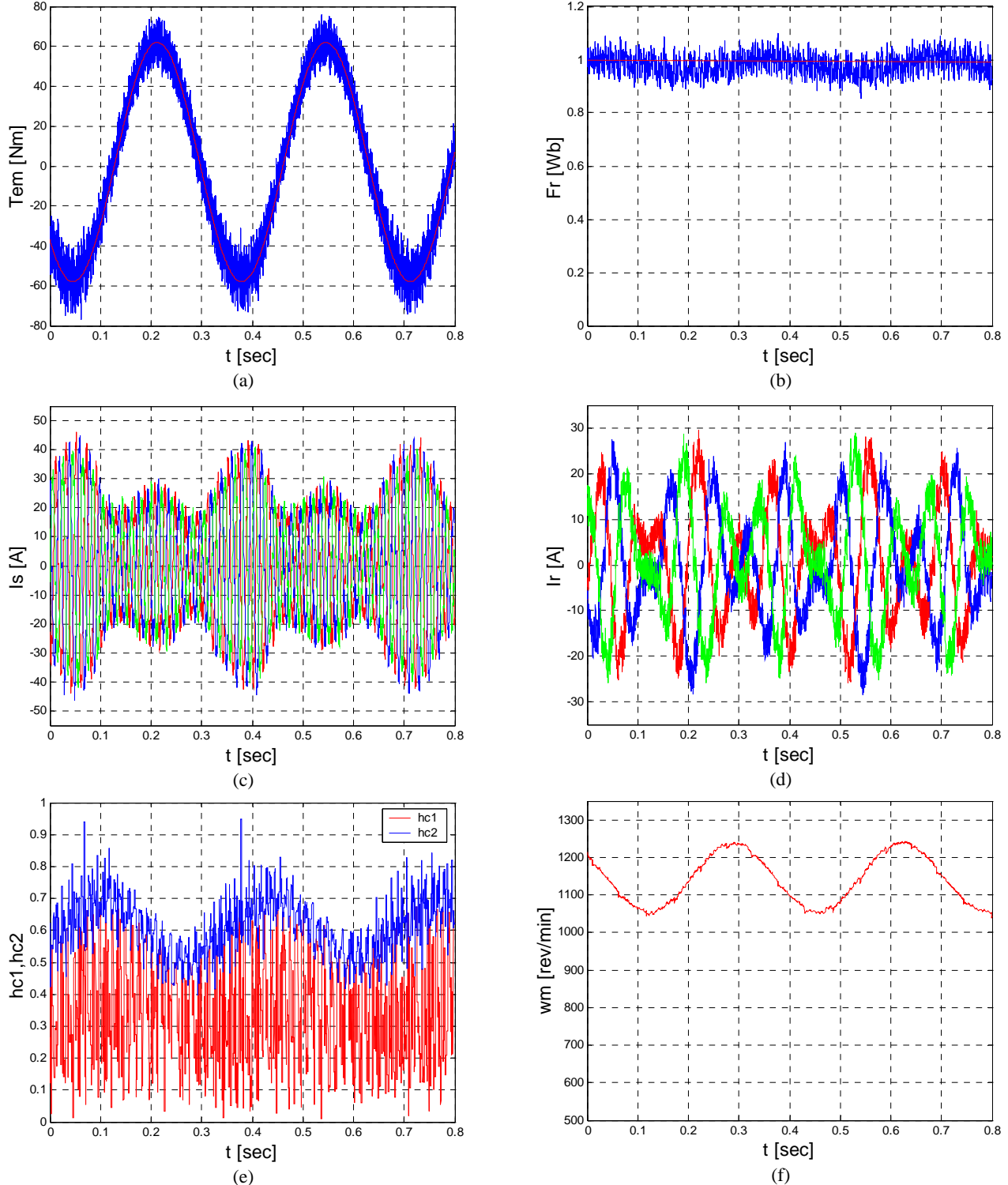


Fig. 4.39 Experimental results. Tracking behavior of the predictive DTC control strategy at 1kHz switching frequency.

(a) Electromagnetic Torque, (b) Rotor Flux, (c) Stator Current, (d) Rotor Current, (e)  $h_{c1}, h_{c2}$ , (f) speed.

Finally in Fig. 4.40, 40 msec of the experiment is shown under detail. It can be inferred that the reduced torque and flux ripples are achieved, producing reduced current ripples as well.

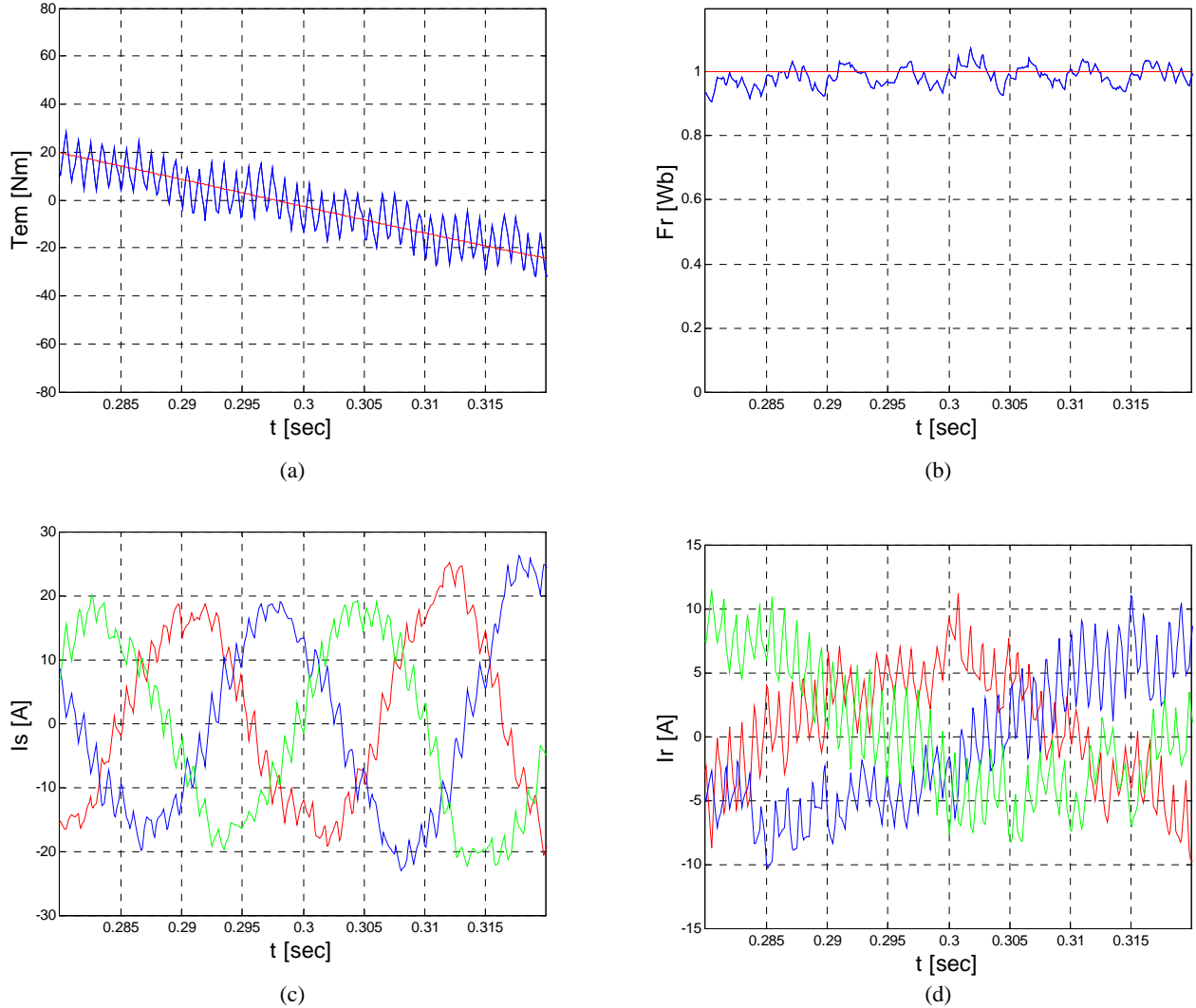


Fig. 4.40 Experimental results. Tracking behavior (zoom) of the predictive DTC control strategy at 1kHz switching frequency. (a) Electromagnetic Torque, (b) Rotor Flux, (c) Stator Current, (d) Rotor Current,

#### 4.7.6 Performance near Synchronism

In this last experiment, the performance near the synchronous speed of the proposed predictive control strategy is studied. For that purpose, the speed of the machine is varied from hypersynchronous to subsynchronous speed as shown in Fig. 4.41 (a). The electromagnetic torque reference is kept to a half of the nominal torque (47.5Nm) and the rotor flux reference to 0.9 Wb, as shown in Fig. 4.41 (b) and (c). During the whole experiment, the control strategy ensures that

the torque and the flux actual values are kept as close as possible to the reference values, with a total absence of no desired overcurrents in both stator and rotor currents, as can be observed in Fig. 4.41 (d) and (e).

In addition, the closer it is the speed of the machine to the synchronism, smaller it is the required rotor voltage vector amplitude, as illustrated in the duty cycles of Fig. 4.41 (f). Fig. 4.41 (b) shows that this fact produces a variable torque ripple, depending on the speed of the machine according to the study of subsection 4.2. On the contrary, the rotor flux ripple amplitude is not affected by the speed of the machine.

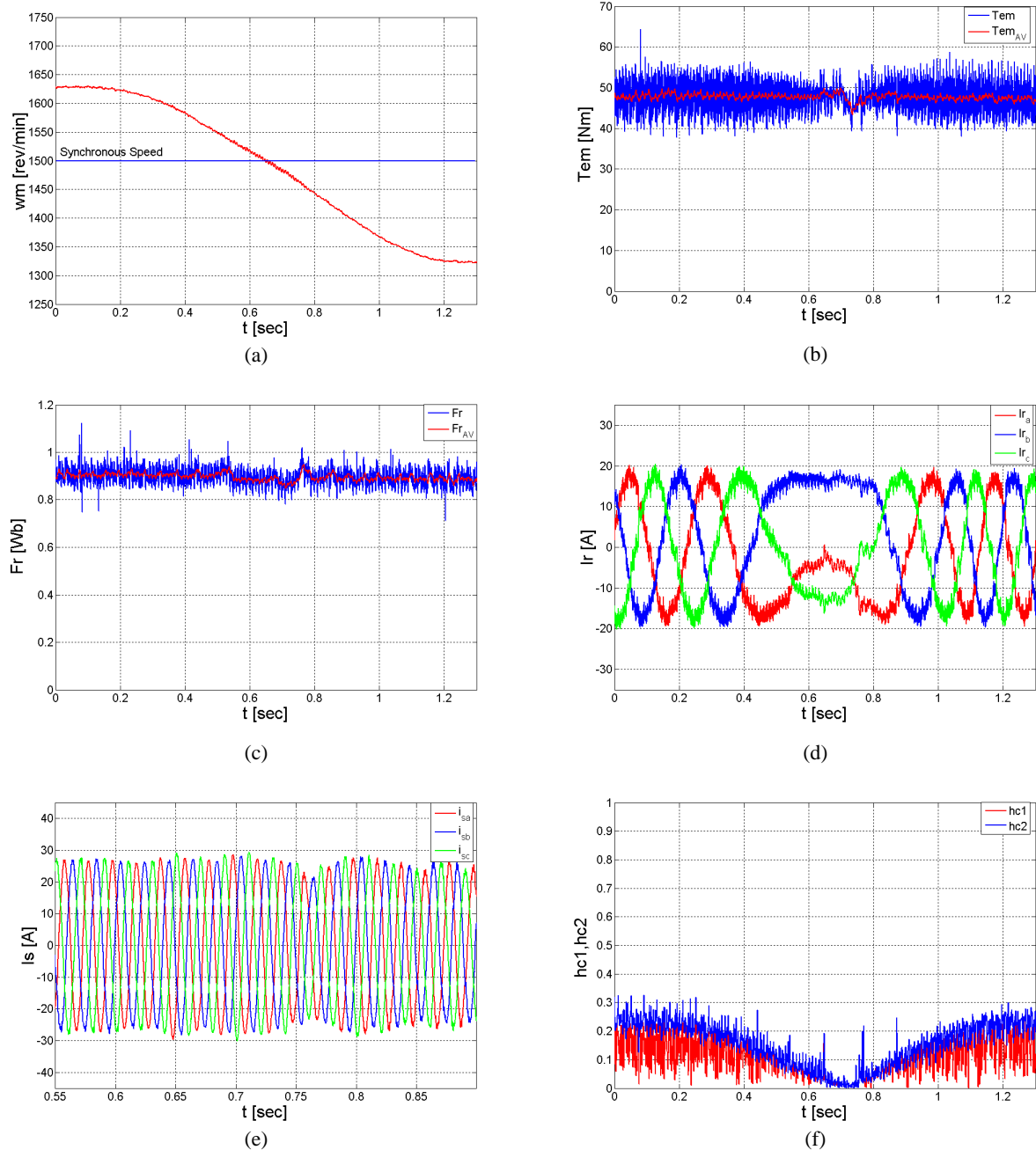


Fig. 4.41 Experimental transient response of the predictive DTC control strategy at 1kHz switching frequency. (a) Speed (b) Electromagnetic Torque, (c) Rotor Flux, (d) Rotor Current, (e) Stator Current, (f)  $h_{c1}, h_{c2}$ .

However, it is very important to emphasize the fact that the quality of the control is partially degraded in the very close proximity to the synchronous speed, appearing low frequency oscillations. When the required voltage vector is near to zero, torque control deterioration is particularly common in direct control techniques [59] for induction machines, since the prediction becomes more sensible to non linearities such as, model uncertainties, electromagnetic noises, dead time of the converter and so on.

## 4.8 Conclusions of the Chapter

Simulation and experimental results show the capacity of this new predictive DTC technique with reduced torque and flux ripples, to control the torque and the flux of the DFIM at considerably low constant switching frequency. It allows to obtain quick dynamic responses, with absolute absence of non-desired overcurrents in the machine. It ensures reduced torque and flux ripples, due to the control effect. In addition to this, it also presents good tracking behavior, capable of working at variable speed operation conditions, for both motoring and generating modes, making this control suitable for applications such as wind power generation. The implementation of the control algorithm does not require powerful digital processors, thanks to its computational simplicity.

To conclude, by means of the proposed control method, it is possible to reduce the stress of the switching devices of the voltage source converter, in terms of low constant switching frequency behavior and switching power losses reduction, often demanded requirements in high power applications.

Finally, this chapter makes two general contributions to the predictive control techniques. Firstly, it shows that using three appropriate vectors instead of two, allows to operate at low constant switching frequency. Secondly, reducing the ripples of both directly controlled variables instead of only one, is crucial to achieve the whole good performance of the machine, in terms of torque and current ripples.

*However, depending on the application's requirements, it could be also interesting the possibility to perform this predictive control strategy directly controlling some other magnitudes such as the stator active and reactive powers. In the next chapter, the predictive control strategy defined in this chapter is adapted to the direct control of these two stator powers. It will be demonstrated that apart from satisfy the necessities of different control applications, it is possible to further improve the quality of the steady state performance.*



## **CONTENTS of Chapter 5**

5	Two Level Converter Based Direct Power Control of the Doubly Fed Induction Machine .....	123
5.1	Introduction .....	123
5.2	Conceptual Analysis of the Direct Power Control Technique.....	124
5.2.1	Stator Active and Reactive Power Dependence on the Fluxes .....	124
5.2.2	Study of the Voltage Effect on the Fluxes.....	125
5.2.3	Geometrical Study of the Rotor Voltage Vectors Effect on the Stator Active and Reactive Power	126
5.2.4	Analytical Study of the Rotor Voltage Vectors Effect on the Stator Active and Reactive Power	128
5.3	Predictive DPC Strategy with Reduced Power Ripple at Low Constant Switching Frequency	
		130
5.3.1	Control Block Diagram .....	130
5.3.2	First Vector Selection Strategy .....	131
5.3.3	Second and Third Vector Selection Strategy at Constant Switching Frequency .....	132
5.3.4	Power Ripple Reduction Criteria at Constant Switching Frequency .....	134
5.4	Experimental Results.....	135
5.4.1	Steady State Operation Conditions at 250Hz Switching Frequency.....	136
5.4.2	Comparison of the Steady State Behavior between Different Control Strategies.....	137
5.4.3	Comparison of the Transient Response Behavior Between the Vector Control and the Predictive DPC .....	140
5.5	Conclusions of the Chapter .....	142

# Chapter 5

## 5 Two Level Converter Based Direct Power Control of the Doubly Fed Induction Machine

*In this chapter, a new two level converter based predictive Direct Power Control (DPC) technique is presented for the Doubly Fed Induction Machine (DFIM). Based on this predictive control, the strategy is able to operate at considerably low constant switching frequencies and allows it to perform a power ripple minimization technique, in order to improve the steady state and transient response behaviors of the machine. In addition to the control technique definition, this chapter includes a conceptual analysis of the Direct Power Control. On the other hand, to validate the control strategy, it will be experimentally compared to the well known Voltage Frequency Control, to the Vector Control, to the non predictive DPC strategy and to the Predictive DTC strategy with reduced torque and flux ripples presented in the previous chapter. The comparison will be carried out in terms of steady state behavior and transient response capacity, and it will be shown that the proposed predictive DPC technique allows to obtain the combination of the quick dynamic response of direct control techniques, and the benefits of constant switching frequency based control techniques.*

### 5.1 Introduction

In this chapter, a new predictive DPC for the DFIM will be presented, considering the recent developments in predictive direct control techniques mentioned in the state of the art of the first Chapter. The Direct Power Control is based on the same control principles as the Direct Torque Control technique. The unique difference is the directly controlled variables. In the case of the DTC, the electromagnetic torque and the rotor flux are directly controlled while in the DPC, the stator active and reactive power. Hence, first a conceptual study of the DPC technique will be carried out. This conceptual analysis is essential to understand the fundaments of the DPC strategy and provides the necessary clearance to understand the parallelism between the DTC and the DPC control principles.

After that, the predictive DPC control technique will be presented. This control technique has been developed taking into account the analysis and conclusions of the previous chapter. For that reason, from the beginning all the efforts have been oriented to develop the most complete control strategy, i.e. the one that achieves best results at low switching frequency by reducing the ripples of both controlled variables, the stator active and reactive power.

Finally, an experimental comparison with other four different control techniques, will evaluate the steady state and the transient response behavior of the proposed predictive DPC algorithm. For simplicity, always required simulation results have been omitted from this chapter, due to the fact that they are very similar to the experimental results. Once again, the experiments have been focused on the severity of the low switching frequency. Consequently, by these experimental tests the advantages and disadvantages of the proposed DPC are explored and compared to the most common control techniques and to the equivalent predictive DTC strategy presented in the previous chapter.

## 5.2 Conceptual Analysis of the Direct Power Control Technique

As mentioned before, the DPC technique is based on a direct control of the stator active and reactive power of the DFIM. The stator active and the reactive power of the machine can be calculated directly from the stator voltage and currents as follows:

$$P_s = \frac{3}{2} \operatorname{Re} \left\{ \vec{v}_s^s \cdot \vec{i}_s^{s*} \right\} \quad (5.1)$$

$$Q_s = \frac{3}{2} \operatorname{Im} \left\{ \vec{v}_s^s \cdot \vec{i}_s^{s*} \right\} \quad (5.2)$$

These last two expressions do not provide the required information to analyse the Direct Power Control, so in the following subsections equivalent modified expressions will be derived.

### 5.2.1 Stator Active and Reactive Power Dependence on the Fluxes

First of all, the relation of the stator active and reactive power on the stator and rotor fluxes is deduced [49]. By substituting into (5.1) and (5.2), the equations (3.19), (3.21) and (3.22) yields:

$$Q_s = \frac{3}{2} \frac{\omega_s}{\sigma L_s} / \vec{\Psi}_s / \left[ \frac{L_h}{L_r} / \vec{\Psi}_s / - / \vec{\Psi}_r / \cos \delta \right] \quad (5.3)$$

$$P_s = \frac{3}{2} \frac{L_h}{\sigma L_s L_r} \omega_s / \vec{\Psi}_s // \vec{\Psi}_r / \sin \delta \quad (5.4)$$

being  $\delta$  the angle between the stator and the rotor flux space vectors. The voltage dropped in the stator resistance has been neglected.

Hence, these last two expressions show that the stator active and reactive power can be controlled by modifying the relative angle between the rotor and stator flux space vectors and their amplitudes. In the following two subsections, the effect of the stator and rotor voltages on the fluxes will be analysed.

### 5.2.2 Study of the Voltage Effect on the Fluxes

Neglecting the dropping voltage due to the rotor resistance in equation (3.14), the rotor flux space vector time evolution in the rotor reference frame, can be calculated by means of the following expression:

$$\vec{\Psi}_{r \text{ fin}} = \vec{\Psi}_{r \text{ ini}} + \int_0^T \vec{v}_r dt \quad (5.5)$$

Considering the voltage vector constant during the application time  $T$ :

$$\vec{\Psi}_{r \text{ fin}} = \vec{\Psi}_{r \text{ ini}} + \vec{v}_r T \quad (5.6)$$

Consequently, by knowing the initial rotor flux space vector and the rotor voltage space vector that it is going to be introduced, it is possible to predict the rotor flux space vector time evolution.

The fact that the stator is directly connected to the grid, produces a stator flux vector with constant amplitude and constant speed of  $\omega_s$  in the stator reference frame, and  $\omega_r$  speed in the rotor reference frame.

These facts are graphically shown in Fig. 5.1. The application of a sufficiently large constant voltage vector in the rotor, produces simultaneously an increase of  $\delta$  and the rotor flux space vector amplitudes.

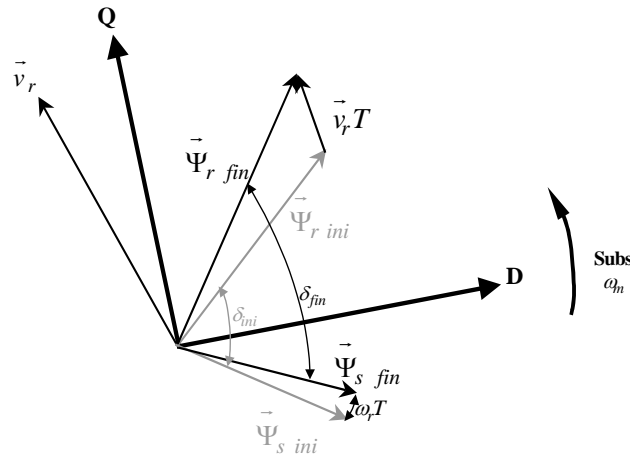


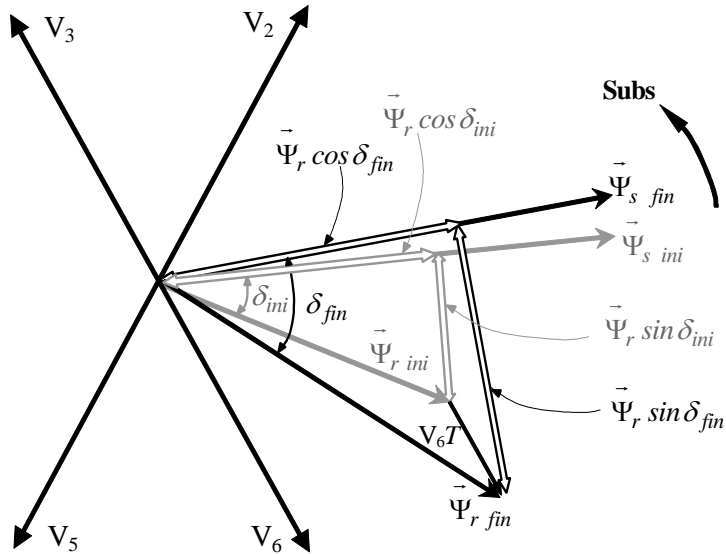
Fig. 5.1. Stator and rotor voltage vector effect on the stator and rotor fluxes.

So, depending on the relative position of the stator and rotor fluxes, and the rotor voltage vector introduced, it is possible to modify the relative angle  $\delta$  between both fluxes and the amplitude of the rotor flux.

### 5.2.3 Geometrical Study of the Rotor Voltage Vectors Effect on the Stator Active and Reactive Power

Once it is shown the rotor voltage vector effect on the rotor flux, the expressions (5.3) and (5.4) provide enough information to analyze the rotor voltage vector effect on the stator active and reactive power. Considering that the stator flux space vector amplitude is constant, the stator active and reactive powers only depend on the relative angle between the fluxes  $\delta$  and the rotor flux space vector amplitude. Since the stator flux space vector rotates at constant speed, any of the eight voltage vectors of the two level converter will produce a  $\delta$  angle variation. Consequently, by checking the terms  $|\vec{\Psi}_r| \cos \delta$  and  $|\vec{\Psi}_r| \sin \delta$  it is possible to deduce the stator active and reactive power variation.

Fig. 5.2 shows an increase of the terms  $|\vec{\Psi}_r| \cos \delta$  and  $|\vec{\Psi}_r| \sin \delta$ , due to the effect of the active voltage vector  $V_6$ . These increases produce an active power increase and a reactive power decrease, when the machine is operating at subsynchronous speed in motor mode.

Fig. 5.2. Effect of  $V_6$  voltage vector, on the active and reactive power.

It can be noticed that depending on the position of the rotor flux space vector in the plane, the same voltage vector will produce different effect on the stator active and reactive power.

Therefore, with this geometrical analysis, the parallelism between the Direct Power Control and the Direct Torque Control basic principle can be inferred. Both methods are based on a direct control of a pair of magnitudes, torque and rotor flux in the DTC and stator active and reactive power in the DPC. These magnitudes are controlled by introducing rotor voltage vectors that produce variations in the rotor flux space vector amplitude and its relative distance with the stator flux space vector.

In addition, although the Direct Power Control technique does not impose a direct rotor flux control, indirectly by controlling the stator active and reactive power, it is imposing an amplitude for the rotor flux space vector and its rotation to a distance  $\delta$  from the stator flux space vector (equations (5.3) and (5.4)). This is a necessary condition to ensure that the DFIM reaches a stable steady state operation point, because as shown before, the proper creation and rotation of the stator flux space vector is already guaranteed by feeding the stator of the DFIM from the grid.

In the next subsection, an alternative analysis to this graphical study will be carried out. Mathematical expressions will be derived in order to analyze the rotor voltage vector effect on the stator active and reactive power.

### 5.2.4 Analytical Study of the Rotor Voltage Vectors Effect on the Stator Active and Reactive Power

In this subsection, the mathematical expressions that relates the stator active and reactive power variation with the rotor voltage vectors will be derived. For that purpose, it is necessary to consider the following space vectors represented in the rotor reference frame (see Chapter 4).

$$\vec{\Psi}_r^r = |\vec{\Psi}_r| e^{j\omega_r t} \quad (5.7)$$

$$\vec{\Psi}_s^r = |\vec{\Psi}_s| e^{j(\omega_r t + \delta)} \quad (5.8)$$

$$\vec{v}_s^r = |\vec{v}_s| e^{j(\omega_r t + \delta + \frac{\pi}{2})} \quad (5.9)$$

$$\vec{v}_r^r = \frac{2}{3} V_{bus} e^{j\frac{\pi}{3}(n-1)} \quad (5.10)$$

In addition, from equations (5.1) and (5.2), the stator active and reactive power variations can be calculated in coordinates referenced to the rotor reference frame:

$$\frac{dP_s}{dt} = \frac{3}{2} \left( \frac{dv_{Ds}}{dt} i_{Ds} + \frac{di_{Qs}}{dt} v_{Qs} + \frac{dv_{Qs}}{dt} i_{Qs} + v_{Ds} \frac{di_{Ds}}{dt} \right) \quad (5.11)$$

$$\frac{dQ_s}{dt} = \frac{3}{2} \left( \frac{dv_{Qs}}{dt} i_{Ds} + \frac{di_{Ds}}{dt} v_{Qs} - \frac{dv_{Ds}}{dt} i_{Qs} - v_{Ds} \frac{di_{Qs}}{dt} \right) \quad (5.12)$$

By substituting the expressions (3.19) to (3.22) and (5.7) to (5.10) into equation (5.11) and (5.12), and considering that the amplitude of the stator flux space vector is constant, the stator active and reactive power variations yield:

$$\begin{aligned} \frac{dP_s}{dt} = & -P_s \left( \frac{R_s}{\sigma L_s} + \frac{R_r}{\sigma L_r} \right) - \omega_r Q_s + \frac{3}{2} \omega_r \frac{|\vec{v}_s|^2}{\sigma L_s \omega_s} \\ & + \frac{L_h}{\sigma L_s L_r} V_{bus} |\vec{v}_s| \sin(\omega_r t + \delta - \frac{\pi}{3}(n-1)) \end{aligned} \quad (5.13)$$

$$\begin{aligned} \frac{dQ_s}{dt} = & -Q_s \left( \frac{R_s}{\sigma L_s} + \frac{R_r}{\sigma L_r} \right) + \omega_r P_s + \frac{3 R_r |\vec{v}_s|^2}{2 L_r \sigma L_s \omega_s} \\ & - \frac{L_h}{\sigma L_s L_r} V_{bus} |\vec{v}_s| \cos(\omega_r t + \delta - \frac{\pi}{3}(n-1)) \end{aligned} \quad (5.14)$$

The power derivatives are composed by three constant terms and a cosine or a sine term, with  $\omega_r$  pulsation and amplitude dependant of the DC bus voltage. The zero vector, produces constant active and reactive power variation, since the cosine and the sine term of the expressions (5.13) and (5.14) are only valid for the active vectors.

On the other hand, by combining the expressions (5.3) and (5.4), the angle  $\delta$  between the rotor and the stator flux space vectors can be expressed as a function of the active and reactive power:

$$\delta = \arctan \left( \frac{L_r}{L_h} \frac{P_s}{\frac{3}{2} \frac{L_h}{\sigma L_s L_r} \frac{|\vec{v}_s|^2}{\omega_s} - Q_s} \right) \quad (5.15)$$

Fig. 5.3 graphically serves the stator active and reactive power derivative evolutions of a specific DFIM at steady-state and for each rotor voltage vector.

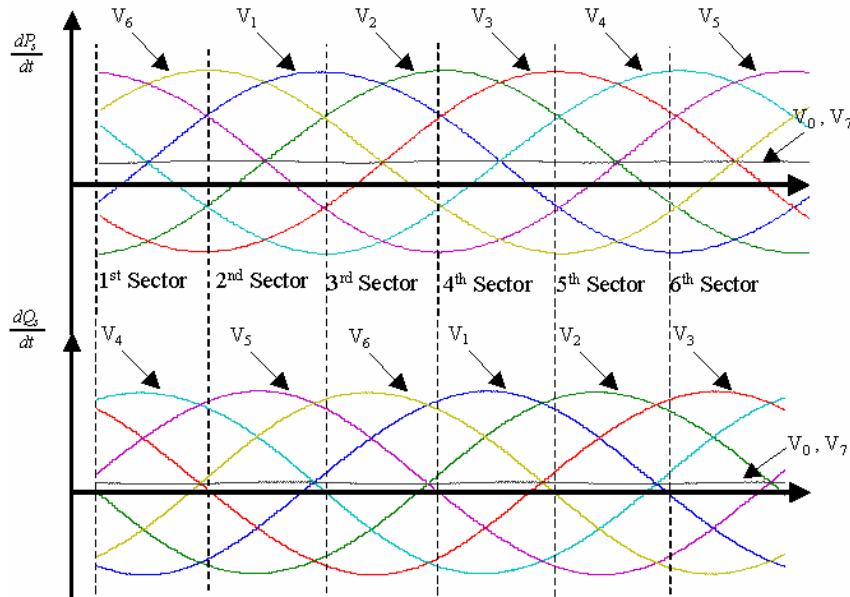


Fig. 5.3. Active and reactive power slopes as a function of the rotor flux angle in motor or generator mode and subsynchronous, for each rotor voltage vector.

The whole period of the power derivative waveforms can be divided into six different sectors, being the limit between sectors the zero crossing of the reactive power derivatives. In that way, the reactive power derivatives will present uniform sign in every sector. Considering the DC bus voltage and the stator voltage as constant magnitudes, the stator active and reactive power

derivatives will only depend on four magnitudes as shown in the simplified block diagram of Fig. 5.4.

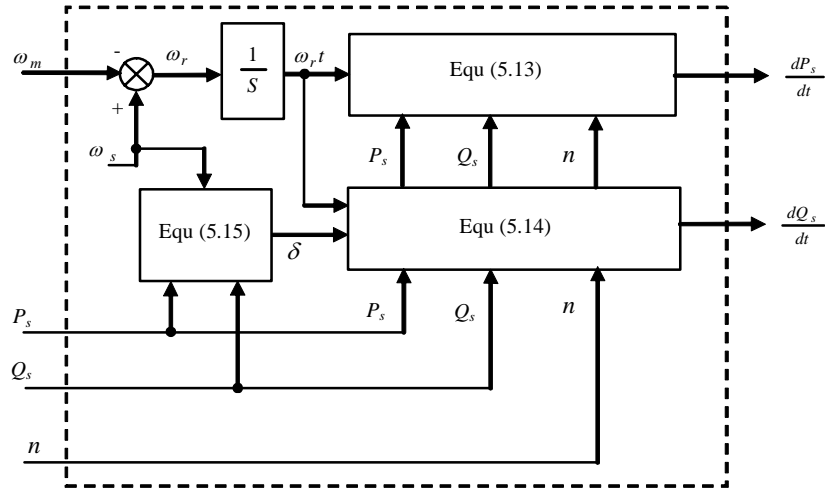


Fig. 5.4. Simplified prediction schema. Power derivative expression calculation.

### 5.3 Predictive DPC Strategy with Reduced Power Ripple at Low Constant Switching Frequency

#### 5.3.1 Control Block Diagram

The block diagram of the proposed control strategy is depicted in Fig. 5.5. As mentioned before, the directly controlled variables are the stator active and reactive powers. From the stator power references, the control strategy calculates the pulses ( $S_a, S_b, S_c$ ) for the IGBTs of the two level voltage source converter, in order to meet the following two objectives: reduced power ripples and constant switching frequency behavior. Fig. 5.5 shows that the control strategy is divided into seven different tasks represented in seven different blocks. The tasks carried out in blocks 1-4, are the basic Direct Power Control principles formulated by authors such as [31] and [48]. On the contrary, the tasks performed in blocks 5-7, are introduced in order to achieve the improvements mentioned above.

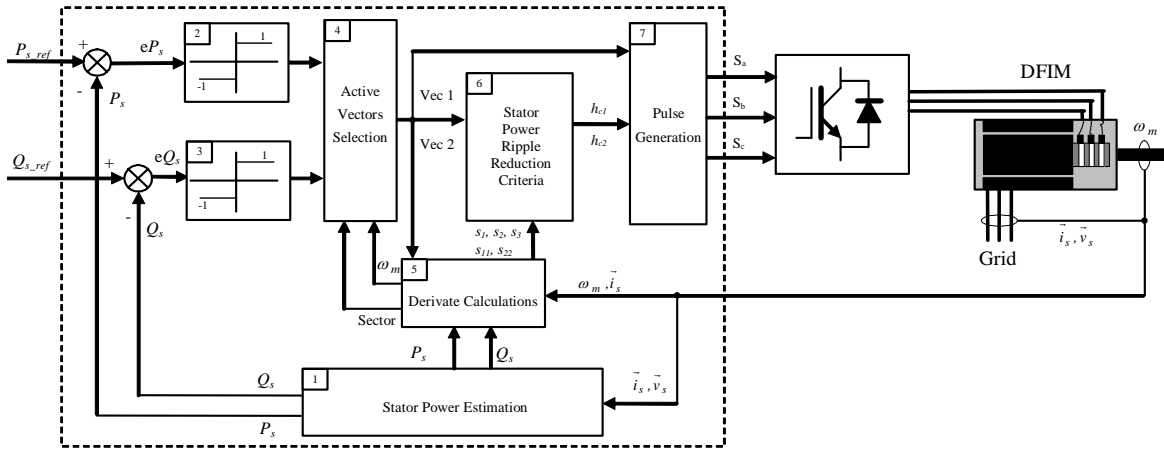


Fig. 5.5. Predictive DPC block diagram.

### 5.3.2 First Vector Selection Strategy

In the first block, the stator active and reactive power values are calculated with the equations (5.1) and (5.2). After that, the stator active and reactive power references are compared with their estimated values, so the stator power errors are obtained.

The basic principle of the Direct Control techniques determines the choice of one specific active voltage vector of the converter, in order to correct the stator power errors. The choice of this vector is directly calculated from the stator active and reactive power errors themselves and the sector where the rotor flux lies.

The proposed predictive DPC strategy, adopts this principle to select the first active voltage vector of the three vectors sequence employed to minimize the stator power ripple, as will be justified in the next sub-section. In Fig. 5.6, the voltage vectors and their effect on the stator active and reactive power as a function of the sector is graphically illustrated.

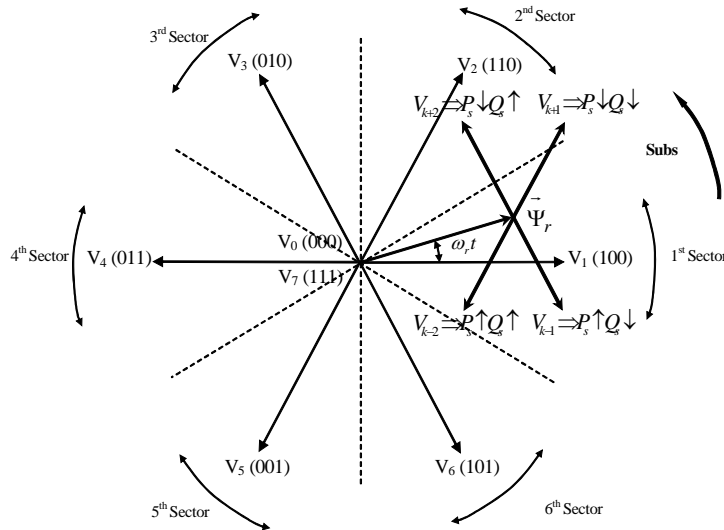


Fig. 5.6. Voltage vectors and their effect on the stator active and reactive power at subsynchronous speed in motor mode.

Hence, the first active voltage vector selection is based on a look-up table mapped by the output of two ON-OFF comparators without hysteresis bands. These tasks are accomplished in blocks 2, 3 and 4 of Fig. 5.5. The look-up table is made up according to TABLE 5.I.

TABLE 5.I  
FIRST ACTIVE VECTOR SELECTION AS A FUNCTION OF THE STATOR ACTIVE AND REACTIVE POWER  
ON-OFF CONTROLLERS' OUTPUTS (K = SECTOR)

		$eP_s$	
		1	-1
$eQ_s$	1	$V_{(k-2)}$	$V_{(k+2)}$
	-1	$V_{(k-1)}$	$V_{(k+1)}$

### 5.3.3 Second and Third Vector Selection Strategy at Constant Switching Frequency

Once the first active vector is chosen from the classical DPC switching table, the predictive DPC control strategy employs a sequence of three different voltage vectors in a constant switching period  $h$ , under steady-state operation conditions. Hence, a second active vector is introduced followed always by a zero vector with the objective of minimising the stator active and reactive power ripples. The typical power waveforms for this control strategy are shown in Fig. 5.7.

The time intervals dedicated to each active vector:  $h_{cl}$  and  $h_{c2}-h_{cl}$ , are calculated according to the minimization criteria that will be presented in the next section.

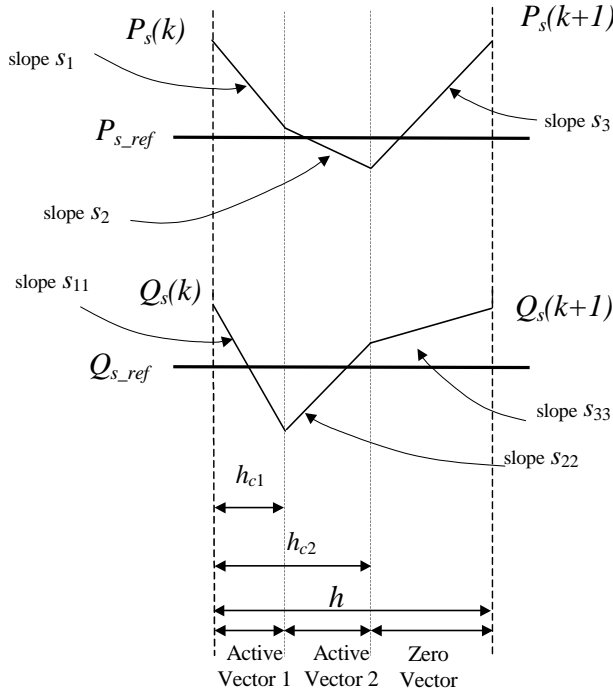


Fig. 5.7 Steady state active and reactive power waveforms at motor and generator modes in subsynchronousism.

So, after selecting the first active vector, if the stator power ripples can be reduced, the choice of the second active vector is made according to TABLE 5.II. It defines the correct choice of the active vectors, depending on the speed of the machine and the sector in which the rotor flux is located.

TABLE 5.II  
SECOND ACTIVE VECTORS SELECTION AT STEADY-STATE (K = SECTOR)

Active Vectors	
Subsynchronism	$V_{(k+1)}, V_{(k+2)}$
Hypersynchronism	$V_{(k-1)}, V_{(k-2)}$

On the other hand, taking into account the equation (3.14), it is deduced that the rotor space flux vector and the rotor voltage space vector at steady state always are going to be shifted  $90^\circ$  approximately. So from a different point of view, the proposed choice of the three vectors guarantees the generation of the rotor voltage space vector  $\vec{v}_r$ , using the nearest three voltage vectors provided by the converter, as can be observed in Fig. 5.8.

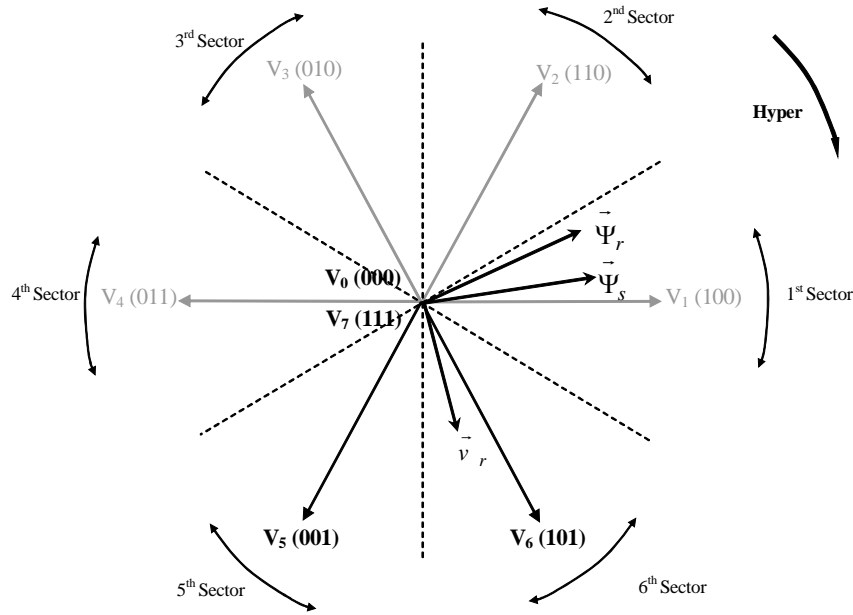


Fig. 5.8. Choice of the nearest three voltage vectors at steady state in hypersynchronism.

### 5.3.4 Power Ripple Reduction Criteria at Constant Switching Frequency

The switching instants  $h_{c1}$  and  $h_{c2}$  defined in Fig. 5.7, as mentioned before, are calculated in order to reduce the active power ripple and the reactive power ripple. So, once the active vectors are identified by using TABLE 5.I and TABLE 5.II, their corresponding time intervals are calculated based on a prediction of the stator active and reactive power. This task is graphically represented in block 6 of Fig. 5.5.

Hence, taking advantage of the fact that the slope of the reactive power when the zero vector is applied is nearly zero ( $s_{33}=0$ ), and considering the equivalent slope  $s_{12}$  of the first two active vectors for the stator active power, that can be calculated by means of the expression:

$$s_{12} = \frac{s_1 h_{c1} + s_2 (h_{c2} - h_{c1})}{h_{c2}} \quad (5.16)$$

the expression for  $h_{c1}$  and  $h_{c2}$  is derived by minimizing the ripples:

$$\begin{aligned} Q_{s\_ripple}^2 &= \frac{1}{h_{c2}} \int_0^{h_{c1}} (s_{11}t + Q_s(k) - Q_{s\_ref})^2 dt \\ &\quad + \frac{1}{h_{c2}} \int_{h_{c1}}^{h_{c2}} (s_{22}t - s_{22}h_{c1} + s_{11}h_{c1} + Q_s(k) - Q_{s\_ref})^2 dt \end{aligned} \quad (5.17)$$

$$\begin{aligned} P_{s\_ripple}^2 &= \frac{1}{h} \int_0^{h_{c2}} (s_{12}t + P_s(k) - P_{s\_ref})^2 dt \\ &\quad + \frac{1}{h} \int_{h_{c2}}^h (s_3t - s_3h_{c2} + s_{12}h_{c2} + P_s(k) - P_{s\_ref})^2 dt \end{aligned} \quad (5.18)$$

The switching time instants yield:

$$\begin{aligned} h_{c1} &= \frac{2s_{22}P_{s\_ref} - 2s_{22}P_s(k) - s_{22}s_3h}{2s_{22}s_1 - 4s_{11}s_2 + 2s_{11}s_3 - s_{22}s_3} \\ &\quad + \frac{(2s_3 - 4s_2)Q_{s\_ref} + (4s_2 - 2s_3)Q_s(k)}{2s_{22}s_1 - 4s_{11}s_2 + 2s_{11}s_3 - s_{22}s_3} \end{aligned} \quad (5.19)$$

$$\begin{aligned} h_{c2} &= \frac{(2s_{22} - 4s_{11})P_{s\_ref} + (4s_{11} - 2s_{22})P_s(k) + (2s_{11} - s_{22})s_3h}{2s_{22}s_1 - 4s_{11}s_2 + 2s_{11}s_3 - s_{22}s_3} \\ &\quad + \frac{(4s_1 - 4s_2)Q_{s\_ref} + (4s_2 - 4s_1)Q_s(k)}{2s_{22}s_1 - 4s_{11}s_2 + 2s_{11}s_3 - s_{22}s_3} \end{aligned} \quad (5.20)$$

## 5.4 Experimental Results

In this section, experimental results of the control strategy presented in the previous section will be carried out. Despite the fact that this control technique is oriented to high power applications, for practical reasons the results have been obtained in a 15kW test bench. This test bench is equal to the one presented in the previous chapter.

Firstly, the behavior of a specific 15kW DFIM is studied, controlled by the predictive DPC control technique, with reduced power ripples at the considerably low 250 Hz constant switching frequency.

Secondly, the quality of the steady state behaviour achieved with the predictive DPC strategy will be compared to four different control techniques: the Vector Control, the non predictive DPC, the Voltage Frequency Control (Open Loop) and the predictive DTC presented in the previous chapter.

Finally, a second comparison will be carried out, evaluating the transient response capacities of the predictive DPC and the Vector Control technique.

### 5.4.1 Steady State Operation Conditions at 250Hz Switching Frequency

In this first experiment, the steady state behavior of the presented DPC strategy will be shown. The switching frequency is set to the considerably low value of 250Hz. The speed of the machine is controlled externally to 1250rev/m, the stator active power reference is 15kW, what means that the machine will be operating in motor mode at nominal power. The machine is magnetized by the stator, setting a stator reactive power reference of 11kVAR. Since the selected low switching frequency will produce in this system high current and power ripples, in order to palliate this effect, the DC bus voltage of the two level converter has been reduced to 200V.

In Fig. 5.9, the most interesting magnitudes captured in the experiment are shown. Fig. 5.9 (a) and (b), illustrate the reduced ripple behavior of the stator active and reactive power, under these operation conditions. These ripple behavior is due to the stator and rotor phase currents shown in Fig. 5.9 (c) and (d). Finally, in Fig. 5.9 (e) and (f), the duty cycles of the vectors introduced by the DPC strategy, added to the sector where rotor flux is located are presented.

Although the quality of the steady state achieved in this experiment would not be probably accepted at any real application, what it is wanted to explore is the capacity of the presented DPC strategy to operate under low switching frequencies, addressing the high power and high current ripples associated to these working conditions.

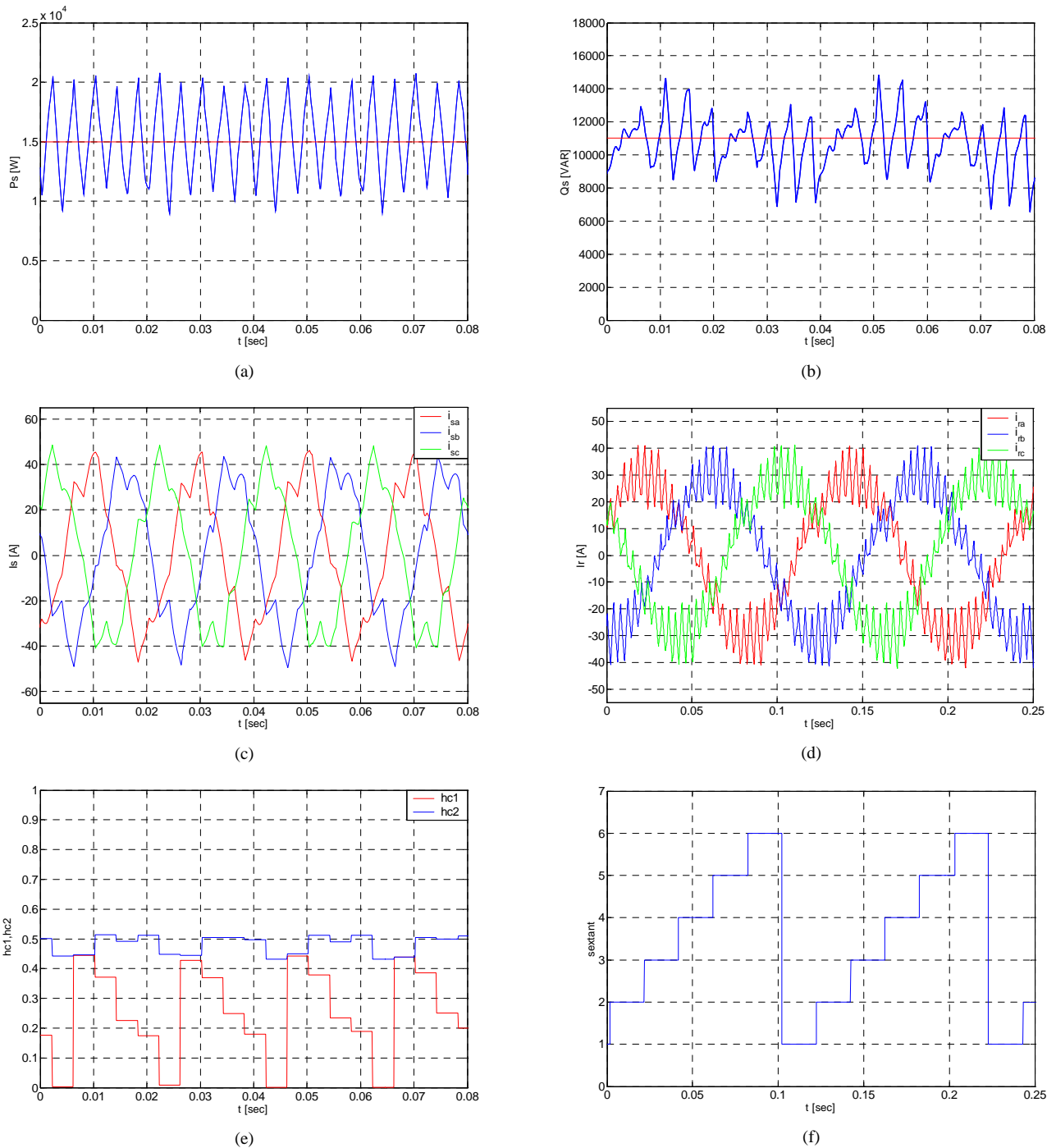


Fig. 5.9. Experimental results. Steady state behavior of the predictive DPC control strategy at 250Hz switching frequency. (a) Stator Active Power, (b) Stator Reactive Power, (c) Stator Current, (d) Rotor Current, (e)  $h_{c1}, h_{c2}$ , (f) Sector.

#### 5.4.2 Comparison of the Steady State Behavior between Different Control Strategies

In this subsection, the predictive DPC technique will be compared with four different control strategies. The objective of this experiment is to quantify the quality of the steady state

behavior achieved with the DPC strategy, in terms of the torque and stator current spectrums qualities. After that, it will be compared with the “classic” non predictive DPC technique [48], the Vector Control technique first presented by [6], the Open Loop feeding of the DFIM that is also known as the Voltage Frequency Control and the predictive DTC control technique described in the previous chapter. Hence, the predictive DPC technique will be compared with the two most widely extended control strategies in the industry and in the research field for the DFIM, i.e the non predictive DPC technique and the VC technique. In addition, although feeding the DFIM in Open Loop, does not allow reaching the dynamic performances achieved in closed loop, it will be considered as a reference to quantify the quality of the steady state behavior, since it does not present the “distortion” that often produce the closed loop control strategies.

Finally, the compared magnitudes will be first the electromagnetic torque, because it provides information related to the mechanical issues of the machine and it is a direct image of the stator active power. The second compared variable will be the stator current, since most of the applications for this machine make them work as a generator, interchanging energy with the network through the stator.

Consequently, a set of experiments have been carried out with the above mentioned control strategies. In all the cases, the operation conditions of the machine are equal:  $P_s=15$  kW,  $Q_s=11$  kVAR, the speed is controlled to 1250 rev/min while the DC bus voltage is 320V. The switching frequency is fixed to 1kHz. In Fig. 5.10, the spectrum comparison is presented. In the torque spectrums, the constant switching frequency behavior of the control strategy can be observed since the higher amplitude harmonics appears at multiples of the switching frequency, except for the non predictive DPC technique, that works at variable switching frequency. It can be noticed that spectrums from Fig. 5.10 (a), (e), (g) and (i) present very similar characteristics. As mentioned before, as these torque spectrums are a direct consequence of the stator power spectrums, they also provide with the information of the stator power control capacity.

Similarly, the current spectrums shown in Fig. 5.10 (b), (f), (h) and (j), present constant switching frequency. The higher order harmonics appear at 1 kHz frequency and its multiplies, due to the switching nature of the rotor voltage. Then, some inevitable other low order harmonics of lower amplitude are also present due to closed loop control effects, quantifications, etc ... On the other hand, the spectrum of Fig. 5.10 (d) is much more dense than the other four ones, but the amplitude of the harmonic is lower.

As similarly occurs with the torque spectrums, the stator current spectrums are a consequence of both controlled magnitudes, the stator active and reactive powers. Consequently, the stator current spectrum includes information of the whole control performance, showing the importance of achieving good quality control of both directly controlled variables. The presented results can be considered that represent the performance of each control strategy in the whole operation range, since not significant changes are expected under different operation conditions.

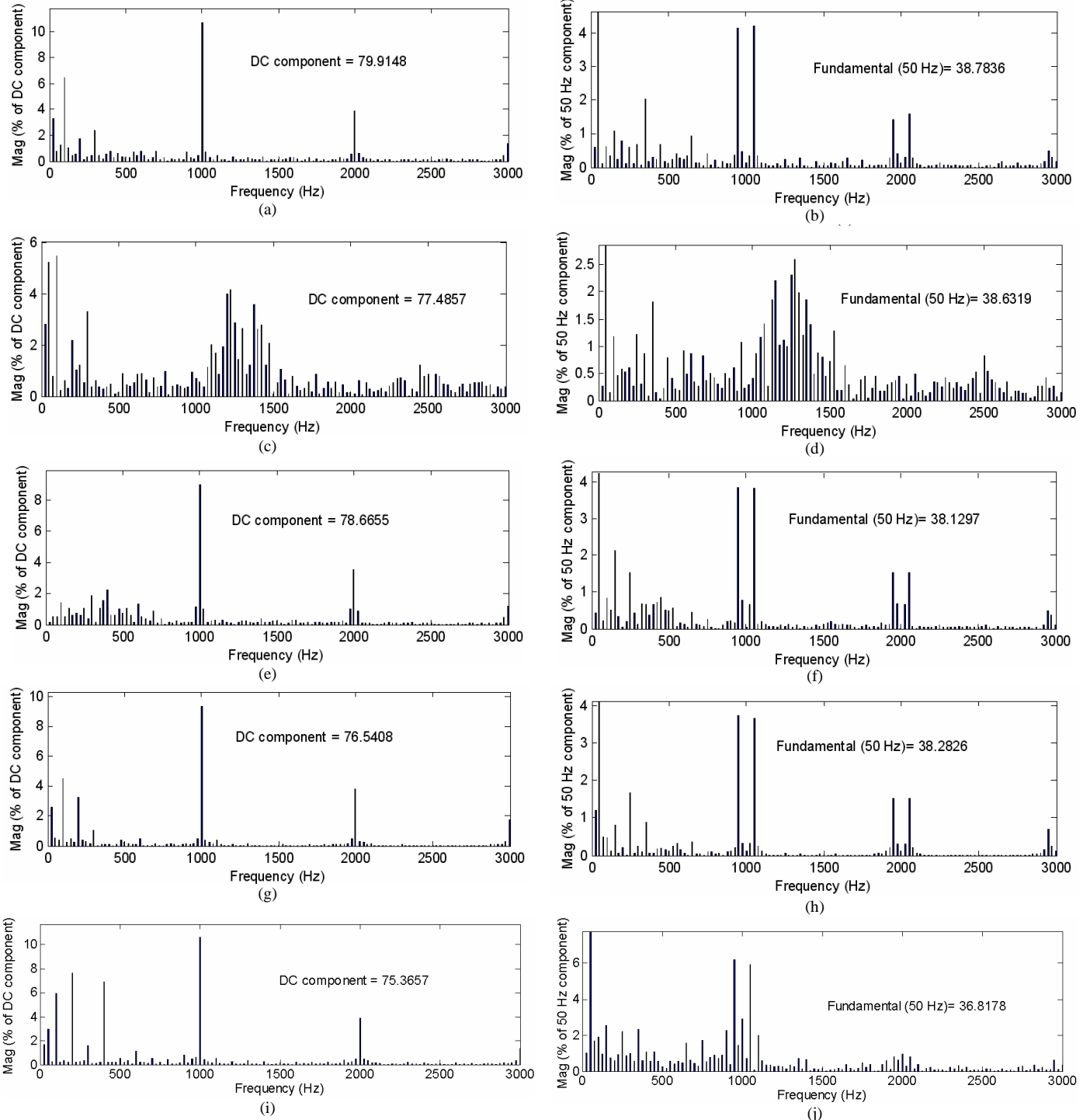


Fig. 5.10. Experimental results. Torque and stator current spectra of different control techniques. (a)  $T_{em}$  Spectrum (Predictive DPC 1kHz), (b)  $i_{sa}$  Spectrum (Predictive DPC 1kHz) (THD=7.22%), (c)  $T_{em}$  Spectrum (Non Predictive DPC), (d)  $i_{sa}$  Spectrum (Non Predictive DPC) (THD=7.1%), (e)  $T_{em}$  Spectrum (VC 1kHz), (f)  $i_{sa}$  Spectrum (VC 1kHz) (THD=7.04%), (g)  $T_{em}$  Spectrum (VF 1kHz), (h)  $i_{sa}$  Spectrum (VF 1kHz) (THD=6.35%), (i)  $T_{em}$  Spectrum (Predictive DTC 1kHz), (j)  $i_{sa}$  Spectrum (Predictive DTC 1kHz) (THD=8.85%).

After that, the total harmonic distortion of the stator currents is calculated. It can be inferred that apart from the Voltage-Frequency control, the other four control strategies present very similar distortions, and as it was expected, the Open Loop achieves the best results.

Nevertheless, the distortion deterioration achieved with the closed loop control strategies is not so important, and in general it is accepted for many applications because they do not have the opportunity to work in Open Loop requirements.

On the contrary, the predictive DTC control achieves poorer steady state results than the other closed loop techniques, in terms of spectrum quality and stator current distortion. The reason for that is because the DTC control is based on a prediction of the electromagnetic torque and the rotor flux, and these magnitudes are more difficultly estimated rather than the stator active and reactive power, that can be simply measured from the stator current and voltages.

To conclude, after quantifying the quality of the steady state performances, it is deduced that all closed loop control strategies present very similar results, and not very distant to the optimal Open Loop case. However, it has to be taken into account that the non predictive DPC technique presents non constant switching frequency behavior.

#### **5.4.3 Comparison of the Transient Response Behavior Between the Vector Control and the Predictive DPC**

In this last experimental trial, the dynamic response of the predictive DPC strategy will be studied and compared to the Vector Control dynamic response. In this case, the Open Loop behaviour have been excluded from the experiment for obvious reasons, and the non predictive DPC strategy and the predictive DTC has been excluded too, due to the fact that it is the same control principle as the predictive DPC technique under the transient states. Consequently, since equal dynamic response capacity is achieved with both DPC strategies, the experiment has been focused on comparing the predictive DPC technique and the Vector Control.

So for that purpose, a severe active power variation will be demanded, and the control strategies will provoke that the machine responds to that demand in a quick and safe manner. The selected active power variation is a step of 15 kW, i.e. the nominal stator active power of the machine. Thus, Fig. 5.11 shows the transient response of both control strategies when they operate at 1250 rev/min, 11kVAR reactive power and 320V of DC bus voltage.

From Fig. 5.11 (a) and (b), the stator active power steady state is reached much faster by the predictive DPC technique (10msec against 2 msec approximately). Fig. 5.11 (c), (d), (e) and (f) show that both techniques permit a safe transient response with an absolute absence of over currents in both stator and rotor currents. But it has to be pointed out that much stronger tuning efforts require the Vector Control technique, rather the DPC technique. So, it has been observed that for very quick dynamic response demanding applications, the predictive DPC technique is more suitable rather than the Vector Control technique.

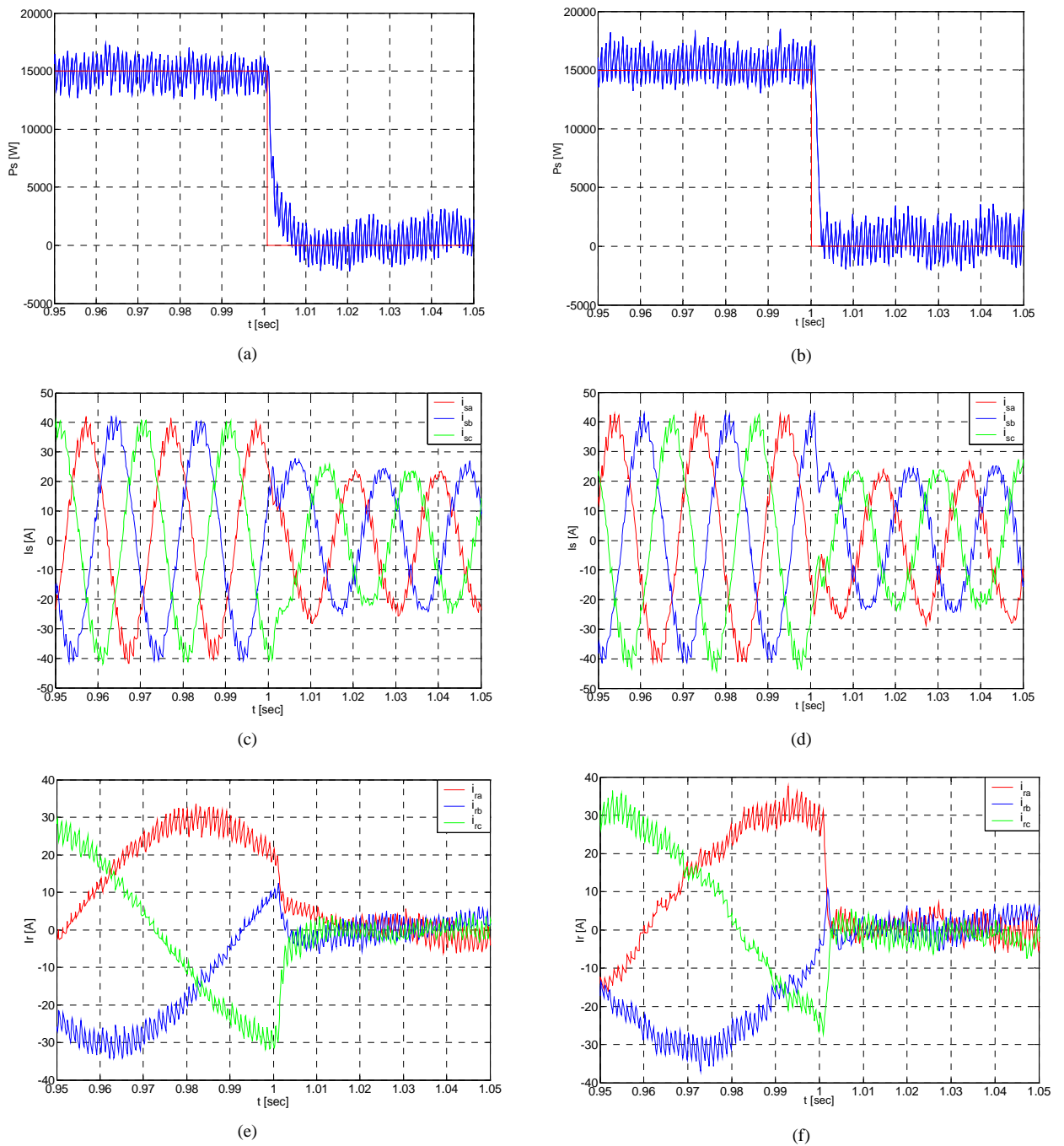


Fig. 5.11 Experimental transient response of the predictive DPC control strategy and the Vector Control strategy at 1kHz switching frequency. (a) Stator Active Power (V.C.), (b) Stator Active Power (DPC), (c) Stator Current (V.C.), (d) Stator Current (DPC), (e) Rotor Current (V.C.), (f) Rotor Current (DPC).

## 5.5 Conclusions of the Chapter

The conceptual analysis of the DPC technique presented in this chapter, demonstrates that by directly controlling the stator active and reactive powers, it is possible to control the rotor flux space vector amplitude and its relative distance to the stator flux space vector, i.e. a necessary condition for the control of the DFIM.

On the other hand, the experimental results obtained show the capacity of the proposed predictive DPC technique, to control the stator active and reactive power of the DFIM at considerably low constant switching frequency. It allows obtaining quick dynamic responses, with absolute absence of non-desired overcurrents in the machine. It also ensures reduced power ripples, due to the control effect.

Added to this, the experimental comparison between different control techniques shows that the steady state performance achieved with the proposed predictive DPC, is very similar to the already developed closed loop control techniques such as, the Vector Control and the non predictive DPC. As it was expected, the open loop steady state behavior (Voltage-Frequency Control) shortly improves the quantified closed loop behavior.

In contrast, although the predictive DTC and DPC techniques are designed under the same control principles, the DPC achieves slightly better quality steady state behavior rather than the DTC, in terms of current and electromagnetic torque distortion. Basically, this is due to the fact that these control strategies are based on predictions, and it has been proved that the prediction of the stator active and reactive powers are much more easy than magnitudes such as the electromagnetic torque and the rotor flux. For that reason, the predictive control techniques are more suitable to easy predictable magnitudes, non dependant to model uncertainties. Nevertheless, for obvious reasons the transient capacity of both control techniques are equivalent.

Finally, the experimental transient response comparison between the proposed predictive DPC and the Vector Control technique, shows that the DPC provides faster dynamic response and without the necessity of a special controller tuning effort as requires the Vector Control.

To conclude, since the implementation of the proposed predictive DPC algorithm does not require powerful digital processors, thanks to its computational simplicity, added to the fact that it combines the advantages and the benefits of direct control techniques and the constant switching frequency based control techniques such as the Vector Control, makes this control strategy suitable for a wide range of high power applications.

*However, the predictive direct control techniques enunciated in this chapter and in the previous chapter, are based on the two level voltage source converter (VSC). As stated in Chapter 2, the tendency of high power drives for industry applications is to use multilevel converter topologies, in order to operate at higher voltage levels. For that reason, in the next Chapter, the predictive direct control techniques studied in these last two chapters, will be adapted to the most widely extended multilevel converter topology, i.e. the three level NPC converter, together to the wind turbine scenario designed in Chapter 2.*



# CONTENTS of Chapter 6

6 Three Level NPC Converter Based Direct Power Control and Direct Torque Control of the Doubly Fed Induction Machine.....	146
6.1 Introduction .....	147
6.2 Predictive Direct Power Control Strategy (DPC) at Low Constant Switching Frequency ....	147
6.2.1 Model of the Doubly Fed Induction Machine and the Rotor Side Filter .....	148
6.2.2 Control Block Diagram .....	149
6.2.3 Sector and Region Calculation .....	150
6.2.4 First Vector Selection Strategy .....	152
6.2.5 Second and Third Vector Selection Strategy at Constant Switching Frequency .....	155
6.2.6 Derivative Expressions Calculation.....	157
6.2.7 Power Error Reduction Criteria at Constant Switching Frequency .....	159
6.2.8 Balancing of DC Bus Capacitors Voltages.....	160
6.2.9 Vector Sequence Definition. Reduction of the Commutations.....	161
6.2.10 Real Vector Definition.....	162
6.3 Experimental Results of Predictive DPC Strategy .....	163
6.3.1 Steady State Operation Conditions at 0.5kHz Constant Switching Frequency with and without Inductive Rotor Filter.....	164
6.3.2 Transient Response Capacity at 0.5kHz Constant Switching Frequency with Inductive Rotor Filter	165
6.3.3 Tracking behavior at 0.5kHz Constant Switching Frequency with Inductive Rotor Filter..	166
6.3.4 Variable speed performance at 0.5kHz Constant Switching Frequency with Inductive Rotor Filter	167
6.3.5 Performance near the Synchronous Speed at 0.5kHz Constant Switching Frequency with Inductive Rotor Filter.....	169
6.4 Predictive Direct Torque Control Strategy (DTC) at Low Constant Switching Frequency ..	171
6.4.1 Control Block Diagram .....	171
6.4.2 First Vector Selection Strategy .....	172
6.4.3 Derivative Expressions Calculation.....	173
6.4.4 Power Error Reduction Criteria at Constant Switching Frequency .....	174
6.5 Experimental Results of Predictive DTC Strategy .....	175
6.5.1 Steady State Operation Conditions at 1kHz Constant Switching Frequency without Inductive Rotor Filter.....	175
6.6 Conclusions of the Chapter .....	178

## Chapter 6

# 6 Three Level NPC Converter Based Direct Power Control and Direct Torque Control of the Doubly Fed Induction Machine

*In this chapter, two new three level NPC converter based predictive Direct Torque Control (DTC) and Direct Power Control (DPC) techniques are presented for the Doubly Fed Induction Machine (DFIM). Based on these predictive controls, the machine is able to operate at considerably low constant switching frequency, making them suitable for high power drive and generator applications, with restricted switching frequencies, where total harmonic distortion of the generated power is relevant. A three level NPC converter feeds the rotor by means of an intermediate inductive filter. The developed control techniques takes into account the inductive filter in the prediction stage as a part of the plant model, deals with the different sectors and regions of converter available voltage vectors and the balancing of the bus capacitors voltages*

*In addition, they are specially designed to keep the implementation structure and simplicity of the “classical” direct control strategies, as well as to be robust to model uncertainties. In order to facilitate the understanding, first the DPC control technique is presented and analyzed under deep detail. After that, the DTC technique is briefly described.*

*On the other hand, to validate the control strategies, experimental results will serve the performance of the predictive DPC strategy for the overall speed and power range, including synchronous speed and transient response behavior. Finally, a second set of experimental results will compare both predictive DTC and DPC control techniques in terms of the steady state behavior, concluding that although both predictive controls show very similar performances, the predictive DPC control achieves slightly better steady state behavior than the DTC control. This is due to the fact that the estimation of the electromagnetic torque and the rotor flux (DTC) is more difficult than a simple measurement of the stator active and reactive powers (DPC).*

## 6.1 Introduction

In this chapter, two new predictive DTC and DPC techniques based on the three level NPC converter for the DFIM will be presented, taking into account the recent developments on predictive direct control techniques, mentioned in the state of the art of the first Thesis. Considering the control theories developed in Chapters 4 and 5 for the two level converter, in this chapter, the DTC and the DPC strategies are developed at the same time for the tree level NPC converter. Hence, it will be shown that with a common control structure, it will be possible to directly control different magnitudes such as, the torque and rotor flux (DTC) or the stator active and reactive powers (DPC). Compared to the two level based converter based direct control strategies developed in the previous two chapters, this control technique maintains the same control principles, i.e. a sequence of three vectors per constant switching period is defined, in which the first vector is selected from a look up table in order to correct the directly controlled magnitude errors. The other two vectors are introduced with the objective of minimize the directly controlled magnitudes evolution from the references.

In addition, this control technique includes a DC bus capacitors voltage balancing algorithm since the three level NPC converter requires it.

On the other hand, as it will be demonstrated at the end of the chapter, the predictive DPC strategy provides with better steady state results rather than the predictive DTC. For that reason, the theoretical exposition of the control strategy will focus only on the predictive DPC. After deep analysis of DPC, the most significant characteristics and features of predictive DTC strategy will be briefly presented at the end of the chapter.

## 6.2 Predictive Direct Power Control Strategy (DPC) at Low Constant Switching Frequency

In this section, the predictive DPC strategy is presented and analyzed under detail. The directly controlled variables will be the stator active and reactive powers ( $P_s$  and  $Q_s$ ). Since in order to improve the quality of the generated power, the presence of a rotor side inductive filter is considered, the model equations of the DFIM and the inductive rotor filter will be analyzed first, before the control strategy is presented.

### 6.2.1 Model of the Doubly Fed Induction Machine and the Rotor Side Filter

As mentioned in previous chapters, although there exist different supplying combinations for the doubly fed induction machine based wind turbines, the configuration adopted in this chapter connects the stator directly to the grid, and the rotor is fed by a reversible three level NPC voltage source converter.

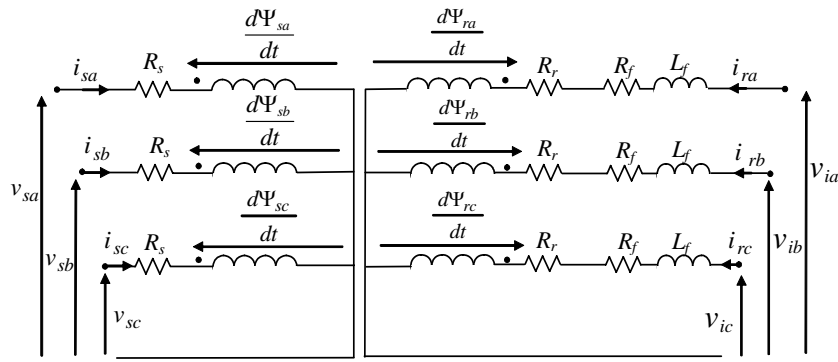


Fig. 6.1. Electrical model of the DFIM and the filter.

The stator side is supplied at constant frequency and constant three phase amplitude, since it is directly connected to the grid. The speed and the flow of active and reactive power through the rotor and the stator, is controlled by adjusting the amplitude, phase and frequency of the voltage introduced in the rotor.

The simplified equivalent electrical circuit [47] of the doubly fed induction machine and the considered inductive filter can be represented as depicted in Fig. 6.1. Thus, considering the rotor side inductive filter, the rotor voltage equation (3.14) is transformed into the following inverter voltage equation:

$$\vec{v}_i^r = R_r \vec{i}_r^r + \frac{d\vec{\Psi}_r^r}{dt} + R_f \vec{i}_r^r + L_f \frac{d\vec{i}_r^r}{dt} \quad (6.1)$$

From this equation and equations (3.19), (3.21) and (3.22), the state space equations of the machine and the filter model, selecting the stator and rotor currents as state variables yields:

$$\frac{d}{dt} \begin{bmatrix} \vec{i}_s^r \\ \vec{i}_r^r \end{bmatrix} = \frac{1}{\sigma_f L_s L_{rf}} \begin{pmatrix} -R_s L_{rf} - j\omega_m L_s L_{rf} & R_{rf} L_h - j\omega_m L_h L_{rf} \\ R_s L_h + j\omega_m L_s L_h & -R_{rf} L_s + j\omega_m L_h^2 \end{pmatrix} \begin{bmatrix} \vec{i}_s^r \\ \vec{i}_r^r \end{bmatrix} + \begin{bmatrix} L_{rf} & -L_h \\ -L_h & L_s \end{bmatrix} \begin{bmatrix} \vec{v}_s^r \\ \vec{v}_i^r \end{bmatrix} \quad (6.2)$$

with:  $L_{rf} = L_r + L_f$ ,  $R_{rf} = R_r + R_f$  and  $\sigma_f = 1 - L_h/L_s L_{rf}$ .

On the other hand, the stator active and reactive power of the machine, i.e. the directly controlled variables, can be calculated from the stator voltage and currents in the rotor reference frame as follows:

$$P_s = \frac{3}{2} \operatorname{Re} \left\{ \vec{v}_s^r \cdot \vec{i}_s^{r*} \right\} = \frac{3}{2} (v_{sD} i_{sD} + v_{sQ} i_{sQ}) \quad (6.3)$$

$$Q_s = \frac{3}{2} \operatorname{Im} \left\{ \vec{v}_s^r \cdot \vec{i}_s^{r*} \right\} = \frac{3}{2} (v_{sQ} i_{sD} - v_{sD} i_{sQ}) \quad (6.4)$$

### 6.2.2 Control Block Diagram

The block diagram of the proposed control strategy is illustrated in Fig. 6.2. As mentioned before, the directly controlled magnitudes are  $P_s$  and  $Q_s$ . From the references, the control strategy calculates the pulses ( $S_{1a}, S_{2a}, S_{1b}, S_{2b}, S_{1c}, S_{2c}$ ) for the IGBTs of the three level NPC voltage source converter (VSC), in order to meet the following two objectives: reduced power ripples and constant switching frequency behavior. Fig. 6.2 shows that the control strategy is divided into eight different tasks represented in eight different blocks.

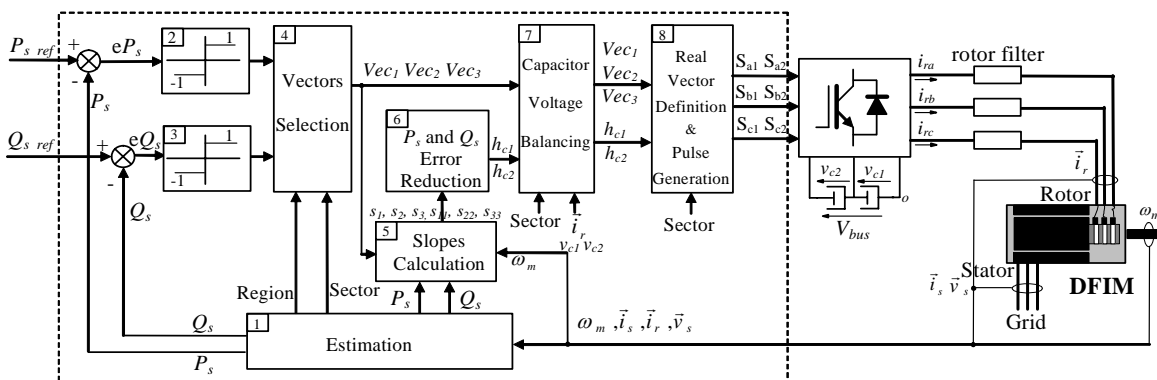


Fig. 6.2. Predictive DPC block diagram.

### 6.2.3 Sector and Region Calculation

The selection of the vectors of the three level NPC converter is made according to the nearest three vector choice principle [60]. As can be derived from equation (6.1), the relation between the rotor magnitudes space vectors at steady-state is:

$$\vec{v}_i^r = R_{rf} \vec{i}_r^r + j\omega_r (\vec{\Psi}_r^r + L_f \vec{i}_r^r) \quad (6.5)$$

Hence, modifying this last expression, it is possible to define a new space vector  $\vec{x}^r$  as follows:

$$\vec{x}^r = -j\vec{v}_i^r = -jR_{rf} \vec{i}_r^r + \omega_r (\vec{\Psi}_r^r + L_f \vec{i}_r^r) \quad (6.6)$$

As graphically shown in Fig. 6.3, the inverter voltage space vector will be always  $90^\circ$  shifted to the  $\vec{x}^r$  space vector.

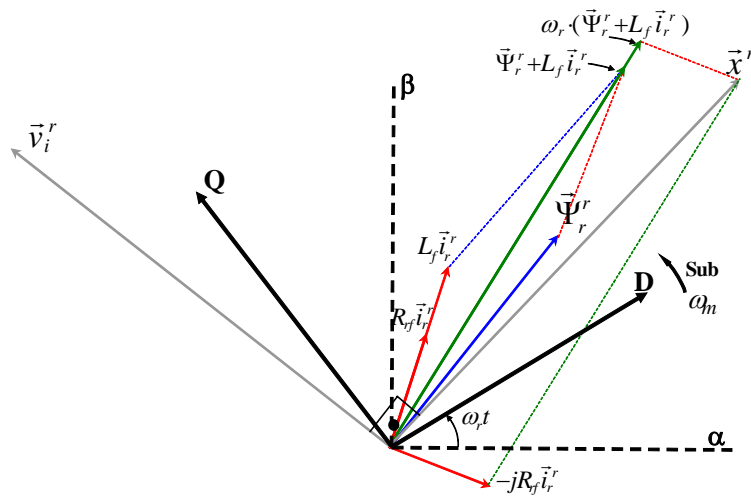


Fig. 6.3. Relation between the inverter voltage, the rotor flux and the rotor current space vectors at steady-state.

Added to this, the three level vector diagram may be divided into 12 different sectors, as shown in Fig. 6.4. In the example represented, the space vector  $\vec{x}^r$  is lying in the 4th sector. At steady state operation conditions, the converter voltage space vector lies in the 7th sector and can be generated by using the following nearest vectors: 021, 022, 122 and 011, guarantying that this choice of vectors produces reduced  $P_s$  and  $Q_s$  variations from the reference values.

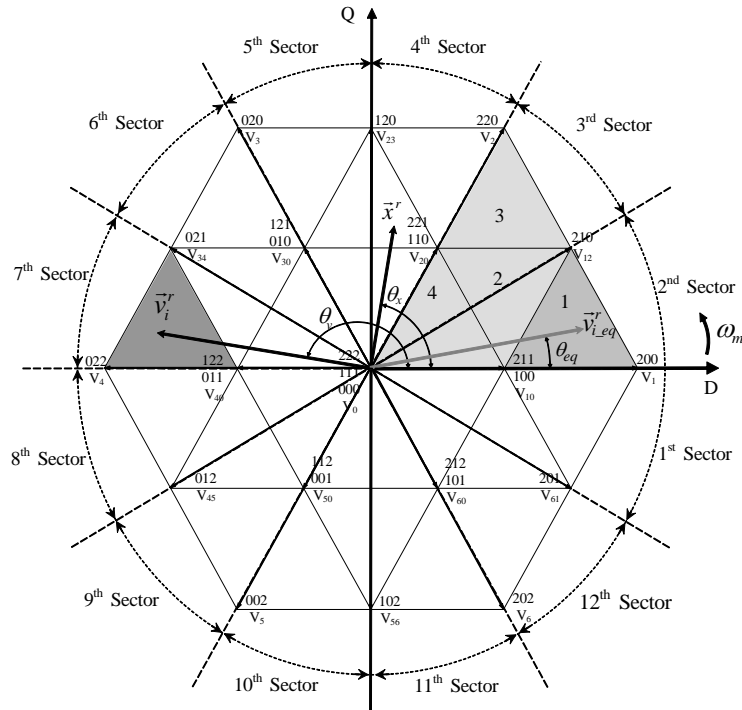


Fig. 6.4. Three level space vector diagram at subsynchronousism.

In addition, taking advantage of the symmetry present in the three level NPC converter and in order to reduce the implementation complexity of the proposed control strategy, the task of knowing which are the nearest vectors, for a given inverter voltage space vector position will be carried out by generating an equivalent voltage space vector  $\vec{v}_{i\_eq}$  in sectors 2 and 3 of the vector diagram. Thus, by dividing the sectors 2 and 3 into four different regions, the equivalent voltage vector of the example illustrated in Fig. 6.4 lies in region 1. The sufficient information to calculate the angle  $\theta_{eq}$  of the equivalent inverter voltage space vector is provided in TABLE 6.I.

TABLE 6.I  
ANGLE OF THE EQUIVALENT VOLTAGE SPACE VECTOR AS A FUNCTION OF THE SECTOR WHERE THE X SPACE VECTOR LIES AT SUBSYNCHRONISM.

$\theta_x$	$\theta_v$	Sector	$\theta_{eq}$
[330°, 30°]	[60°, 120°]	1, 2	- $\theta_v + 120^\circ$
[30°, 90°]	[120°, 180°]	3, 4	$\theta_v - 120^\circ$
[90°, 150°]	[180°, 240°]	5, 6	- $\theta_v - 120^\circ$
[150°, 210°]	[240°, 300°]	7, 8	$\theta_v + 120^\circ$
[210°, 270°]	[300°, 0°]	9, 10	- $\theta_v$
[270°, 330°]	[0°, 60°]	11, 12	$\theta_v$

Once  $\theta_{eq}$  has been calculated, the region may be deduced by normalizing the voltage vector to its maximum value ( $V_{bus}/\sqrt{3}$  not considering overmodulation), and checking the  $DQ$

components of the normalized voltage vector according to the information provided in Table 6.II. Finally, the selection of the region and the sector is made in block 1 of Fig. 6.2.

TABLE 6.II  
REGION CALCULATION AS A FUNCTION OF  $V_D$  AND  $V_Q$ .

Case	Region
$v_D > 1, v_Q < \sqrt{3}(v_D - 1)$	1
$v_Q < \frac{\sqrt{3}}{2}, v_D > 1 - \frac{v_Q}{\sqrt{3}}, v_D < 1 + \frac{v_Q}{\sqrt{3}}$	2
$v_Q > \frac{\sqrt{3}}{2}$	3
$v_D < 1 - \frac{v_Q}{\sqrt{3}}, v_Q < \frac{\sqrt{3}}{2}$	4

All the required calculations performed in block 1, of Fig. 6.2 for the sector and region estimations are represented in the simplified block diagram of Fig. 6.5.

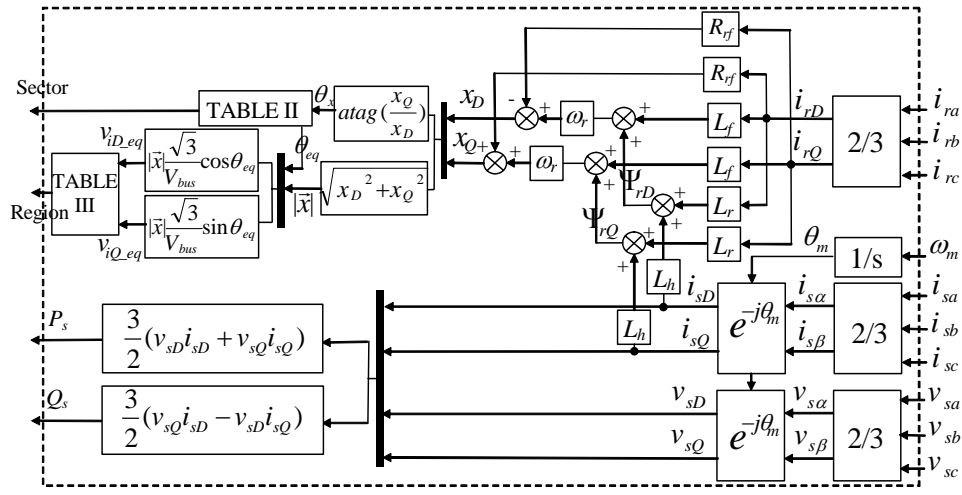


Fig. 6.5. Stator powers, sector and region estimations.

#### 6.2.4 First Vector Selection Strategy

The basic principle of the Direct Control techniques determines the choice of one specific voltage vectors of the converter, in order to correct the directly controlled magnitude's errors. The choice of this vector is directly made from the  $P_s$  and  $Q_s$  errors themselves, the sector where  $\vec{x}^r$  lies and the region of the equivalent voltage vector  $\vec{v}_{i\_eq}$ .

The proposed predictive DPC strategy adopts this principle to select the first voltage vector of the three vectors sequence employed to minimize the  $P_s$  and  $Q_s$  errors, as will be justified in the next sub-section. Hence, the first voltage vector selection is based on a look-up table mapped by the output of two ON-OFF comparators without hysteresis bands. These tasks

are accomplished in blocks 2, 3 and 4 of Fig. 6.2. One comparator is dedicated to the  $P_s$  control and the other to the  $Q_s$  control.

Depending on the sector and the region, there are permitted only four vectors in order to apply the four different combinations to the  $P_s$  and  $Q_s$  variation, as shown in Fig. 6.6 (note that only one of the two double vectors will be used).

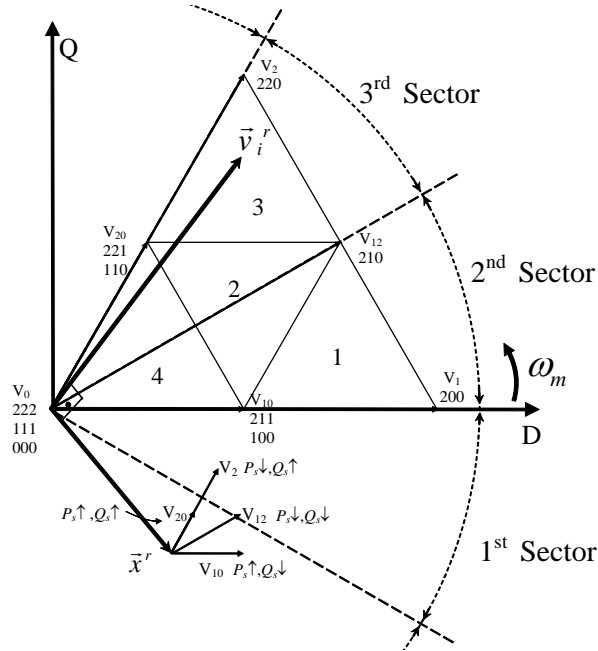


Fig. 6.6. Vector selection for regions 1, 2 and 3 at subsynchronousism.

Hence, if the voltage vector lies in regions 1, 2 or 3, the four permitted vectors can be calculated from the four equivalent vectors  $V_{10}$ ,  $V_1$ ,  $V_{20}$ ,  $V_2$  and  $V_{12}$  of sectors 2 and 3. As shown in Fig. 6.6, these permitted vectors are the closest vectors to the voltage reference vector when it lies in regions 1, 2 or 3. The look-up table is made up according to Table 6.III that is deduced from expressions (6.11) and (6.12) as will be shown in subsection 6.2.6. It defines the first vector as a function of the sector and the stator power errors.

TABLE 6.III  
FIRST VECTOR SELECTION FOR REGIONS 1, 2 AND 3 AT SUBSYNCHRONISM.

	$eP_s, eQ_s$			
Sectors	(1,1)	(1,-1)	(-1,1)	(-1,-1)
<b>4, 8, 12</b>	$V_{20}$	$V_{10}$	$V_2$	$V_{12}$
<b>3, 7, 11</b>	$V_{20}$	$V_{10}$	$V_{12}$	$V_1$
<b>2, 6, 10</b>	$V_{10}$	$V_{20}$	$V_1$	$V_{12}$
<b>1, 5, 9</b>	$V_{10}$	$V_{20}$	$V_{12}$	$V_2$

Three of the permitted vectors belong to the region where the equivalent inverter voltage vector is located, these vectors are the closest vectors that provides the three level NPC converter to the predicted required inverter voltage vector. In contrast, the fourth permitted vector requires a jump to the subsequent region and in general it is only used in dynamic operation requirements.

It is necessary to highlight that there is not difference of using different redundant vectors, since they produce the same line to line voltage at the output of the converter, what means that they produce the same directly controlled magnitudes variation. However, they will be used to balance the DC bus capacitor voltages according to the criteria shown in subsection 6.2.8.

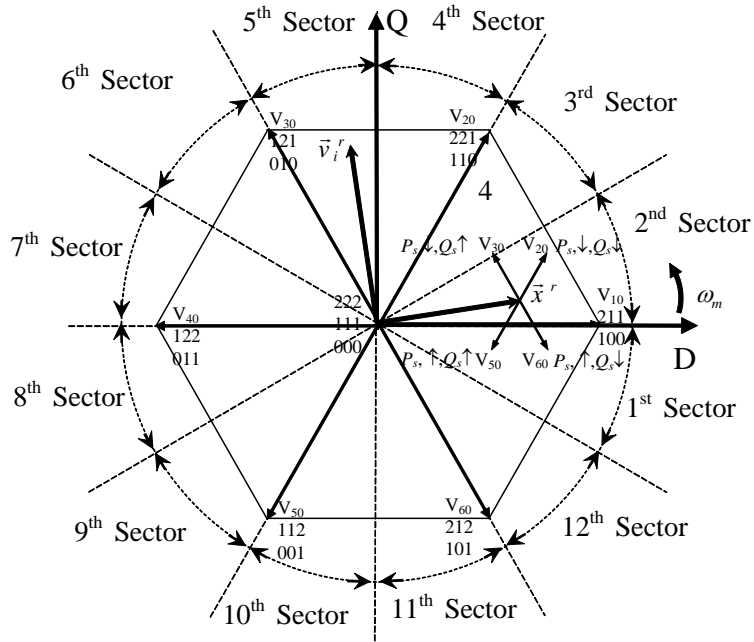


Fig. 6.7. Three level space vector diagram omitting regions 1, 2 and 3.

On the other hand, if the rotor voltage vector lies in region 4, the first vector selection is made according a slightly different procedure. Since in this region 4, the closest four vectors to the inverter voltage vector does not produce equal stator power variations along one sector, the choice is made equivalently to the two level converter based DTC or DPC strategies [31], [48]. Omitting regions 1, 2 and 3 from the three level space vector diagram as structured in Fig. 6.7, the four permitted vectors are selected from six vectors candidates  $V_{10}$ ,  $V_{20}$ ,  $V_{30}$ ,  $V_{40}$ ,  $V_{50}$  and  $V_{60}$  according to the information given in Table 6.IV.

In both cases, the permitted vectors are selected assuming that the variation of the inverter voltage vector is not high, what means that not strong speed variation is required. Otherwise, in applications where the speed of the machine varies rapidly, the transient response could be improved selecting the four permitted vectors from any region.

TABLE 6.IV  
FIRST VECTOR SELECTION FOR ALL THE SECTORS AND REGION 4, AT SUBSYNCHRONISM.

<b>Sectors</b>	<b><math>eP_s, eQ_s</math></b>			
	<b>(1,-1)</b>	<b>(1,1)</b>	<b>(-1,-1)</b>	<b>(-1,1)</b>
<b>1, 2</b>	V <sub>60</sub>	V <sub>50</sub>	V <sub>20</sub>	V <sub>30</sub>
<b>3, 4</b>	V <sub>10</sub>	V <sub>60</sub>	V <sub>30</sub>	V <sub>40</sub>
<b>5, 6</b>	V <sub>20</sub>	V <sub>10</sub>	V <sub>40</sub>	V <sub>50</sub>
<b>7,8</b>	V <sub>30</sub>	V <sub>20</sub>	V <sub>50</sub>	V <sub>60</sub>
<b>9, 10</b>	V <sub>40</sub>	V <sub>30</sub>	V <sub>60</sub>	V <sub>10</sub>
<b>11, 12</b>	V <sub>50</sub>	V <sub>40</sub>	V <sub>10</sub>	V <sub>20</sub>

It must be stressed, that this TABLE 6.IV is equivalent to TABLE 5.I defined for DPC based on the two level VSC.

### 6.2.5 Second and Third Vector Selection Strategy at Constant Switching Frequency

Once the first active vector is selected from TABLES 6.III or 6.IV, in order to correct the controlled  $P_s$  and  $Q_s$  errors, the predictive DPC control strategy employs a sequence of three different voltage vectors in a constant switching period  $h$ , under steady-state operation conditions.

Hence, a second and a third vector is introduced, with the objective of minimizing the  $P_s$  and  $Q_s$  errors, from their reference values. One example of the typical waveform evolutions for this control strategy is served in Fig. 6.8.

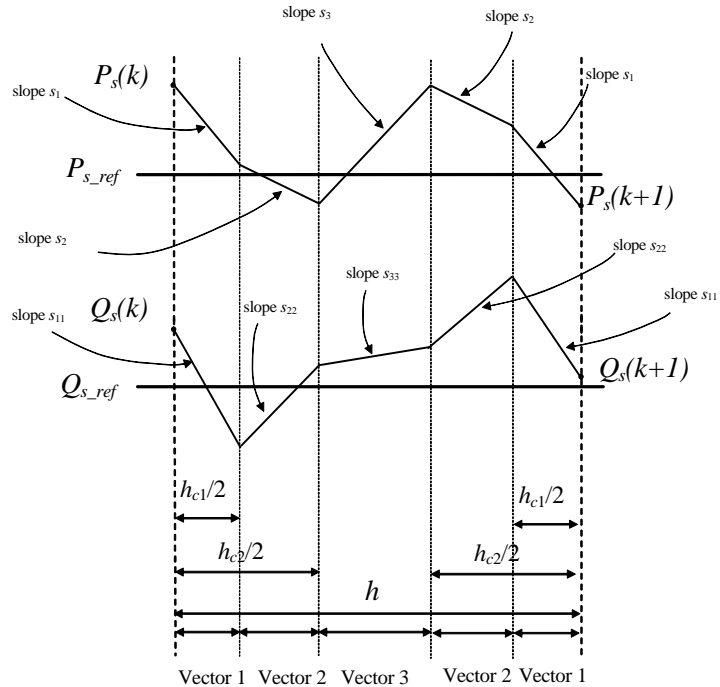


Fig. 6.8. Steady state active and reactive power waveforms at motor and generator modes in subsynchronousism.

In the adopted notation the slopes of  $P_s$  are called  $s_1$ ,  $s_2$  and  $s_3$ , while  $s_{11}$ ,  $s_{22}$  and  $s_{33}$  are the slopes of  $Q_s$ . Depending on the sector where the  $\vec{x}^r$  vector lies, different voltage vectors will produce different  $P_s$  and  $Q_s$  variations. These slopes are calculated in block 5 of Fig. 6.2 and the calculation procedure is described in the next section.

The first vector choice defines the second and the third vectors as mapped in TABLE 6.V. The three vectors introduced during one sample period  $h$ , under steady state operation conditions are the nearest three vectors to the inverter voltage reference vector. Thus, it is ensured that these vectors produce the smallest  $P_s$  and  $Q_s$  variation.

TABLE 6.V  
SECOND AND THIRD VECTOR SELECTION ACCORDING TO THE  
NEAREST THREE VECTORS CRITERIA IN EQUIVALENT SECTORS 2 AND 3

Region	Vectors
1	$V_{10}, V_1, V_{12}$
2	$V_{10}, V_{12}, V_{20}$
3	$V_{20}, V_2, V_{12}$
4	$V_{20}, V_{10}, V_0$

It could occur that the selected first vector (Fig. 6.6, Fig. 6.7 and TABLE 6.III and 6.IV), is not one of the nearest three vectors to the required voltage vector, so there is a region jump requirement. For instance, vector  $V_{20}$  for region 1. In general, this situation is due to a change in the demanded steady state, provoking a transient response. Under these circumstances, only the

first vector will be introduced during the whole sample period  $h$ , in order to achieve fast dynamic operation capacity. Finally, the selection of the second and third vector as well as the first vector is accomplished in block 4 of Fig. 6.2.

### 6.2.6 Derivative Expressions Calculation

In this subsection, the mathematical expressions that relate the stator active and reactive power variation with the inverter voltage vectors will be derived. It is necessary to consider the stator power derivative expressions from equations (6.3) and (6.4):

$$\frac{dP_s}{dt} = \frac{3}{2} \left( \frac{dv_{Ds}}{dt} i_{Ds} + \frac{di_{Qs}}{dt} v_{Qs} + \frac{dv_{Qs}}{dt} i_{Qs} + v_{Ds} \frac{di_{Ds}}{dt} \right) \quad (6.7)$$

$$\frac{dQ_s}{dt} = \frac{3}{2} \left( \frac{dv_{Qs}}{dt} i_{Ds} + \frac{di_{Ds}}{dt} v_{Qs} - \frac{dv_{Ds}}{dt} i_{Qs} - v_{Ds} \frac{di_{Qs}}{dt} \right) \quad (6.8)$$

Consequently, by substituting the state space representation of the machine and the filter (6.2) into expressions (6.7) and (6.8), it is possible to deduce the derivative expressions of the stator active and reactive powers, for each voltage vector of the three level NPC converter. Hence, the slopes produced by the zero vectors are calculated as:

$$\left. \frac{dP_s}{dt} \right|_{V_0} = K_{Lf} \left( -P_s K_1 - \omega_r Q_s / K_{Lf} + \omega_r K_2 \right) \quad (6.9)$$

$$\left. \frac{dQ_s}{dt} \right|_{V_0} = K_{Lf} \left( -Q_s K_1 + \omega_r P_s / K_{Lf} + K_3 \right) \quad (6.10)$$

After that, the slopes produced by the rest of the vectors can be calculated according to the following equations:

$$\left. \frac{dP_s}{dt} \right|_V = \left. \frac{dP_s}{dt} \right|_{V_0} + K_v K_4 \sin(\omega_r t + \delta + \theta) \quad (6.11)$$

$$\left. \frac{dQ_s}{dt} \right|_V = \left. \frac{dQ_s}{dt} \right|_{V_0} - K_v K_4 \cos(\omega_r t + \delta + \theta) \quad (6.12)$$

with  $\delta$  the phase shift between the rotor and stator fluxes space vectors, and the constant values:

TABLE 6.VI  
AMPLITUDE AND PHASE SHIFT CONSTANTS FOR VECTORS OF THE THREE LEVEL NPC CONVERTER WITH (N=1..6)

	$V$	$K_v$	$\theta$
Large Vectors	$V_N \Rightarrow V_1, V_2, V_3, V_4, V_5, V_6$	1	$-\frac{\pi}{3}(N-1)$
Medium Vectors	$V_{N,N+1} \Rightarrow V_{12}, V_{23}, V_{34}, V_{45}, V_{56}, V_{61}$	$\frac{\sqrt{3}}{2}$	$-\frac{\pi}{3}(N-1) - \frac{\pi}{6}$
Short Vectors	$V_{N0} \Rightarrow V_{10}, V_{20}, V_{30}, V_{40}, V_{50}, V_{60}$	$\frac{1}{2}$	$-\frac{\pi}{3}(N-1)$

$$K_{Lf} = \frac{1}{\sigma_f L_s L_{rf}} \quad (6.13)$$

$$K_1 = R_s L_{rf} + R_{rf} L_s \quad (6.14)$$

$$K_2 = \frac{3}{2} L_{rf} \frac{|\vec{v}_s|^2}{\omega_s} \quad (6.15)$$

$$K_3 = \frac{3}{2} R_{rf} \frac{|\vec{v}_s|^2}{\omega_s} \quad (6.16)$$

$$K_4 = K_{Lf} L_h V_{bus} |\vec{v}_s| \quad (6.17)$$

Therefore, in Fig. 6.9, the stator active power and reactive power derivative expressions are graphically represented, when the machine operates at subsynchronous speed with an inverter voltage vector that lies in regions 1, 2 and 3. Analyzing the resulting sinusoidal waveforms, for instance in sector 12, under these operation conditions regions 2 and 3 are required. In that sector, according to TABLE 6.III, vectors  $V_{20}$ ,  $V_{10}$ ,  $V_2$  and  $V_{12}$  are the corresponding voltage vectors. As can be noticed from Fig. 6.9, these four vectors produce the four required combinations of  $P_s$  and  $Q_s$  variations (1,1), (1,-1), (-1,1) and (-1,-1), with the smallest slope magnitude. Consequently, by using these four vectors choice procedure, it is ensured the possibility to control the stator active reactive power, with reduced errors.

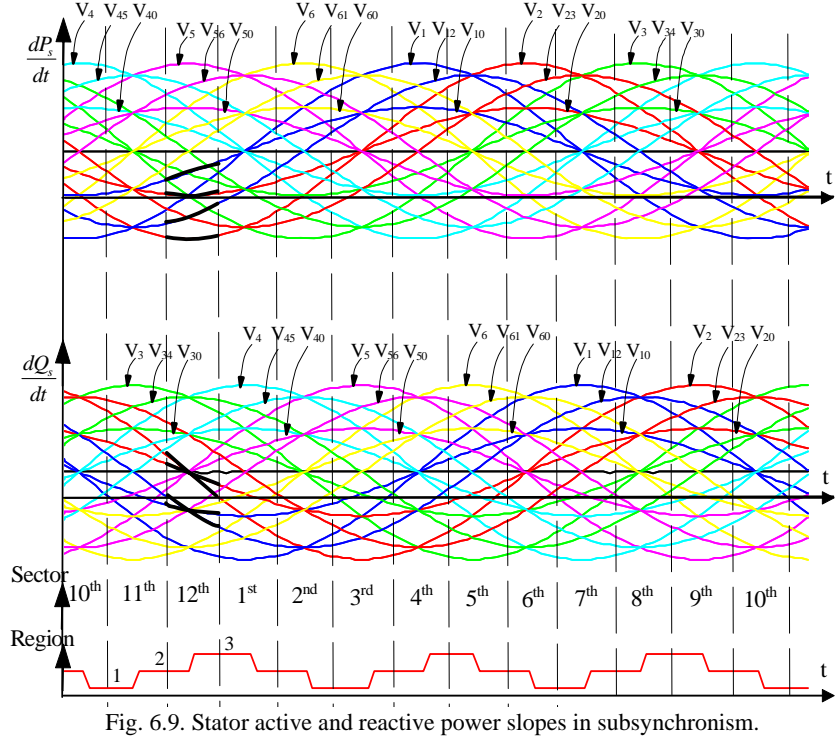


Fig. 6.9. Stator active and reactive power slopes in subsynchronous.

### 6.2.7 Power Error Reduction Criteria at Constant Switching Frequency

The switching instants  $h_{c1}$  and  $h_{c2}$  shown in Fig. 6.8, are calculated in order to obtain the objective of reducing the squared  $P_s$  and  $Q_s$  errors at the end of the sample period. So, once the three vectors are chosen, their corresponding time intervals are calculated based on a prediction of the  $P_s$  and  $Q_s$ . This task is graphically represented in block 6 of Fig. 6.2.

Thus, since the objective is to minimize the sum of the squared  $P_s$  and  $Q_s$  errors at the end of the switching period  $h$ , it can be mathematically expressed as:

$$f = e_{P_s}^2 + e_{Q_s}^2 \quad (6.18)$$

being:

$$e_{P_s}^2 = (h_{c1}(s_1 - s_2) + h_{c2}(s_2 - s_3) + s_3 h - P_{s\_ref} + P_s(k))^2 \quad (6.19)$$

$$e_{Q_s}^2 = (h_{c1}(s_{11} - s_{22}) + h_{c2}(s_{22} - s_{33}) + s_{33} h - Q_{s\_ref} + Q_s(k))^2 \quad (6.20)$$

Hence, it is well known that the minimum of the expression (6.18) can be derived by calculating the derivative expressions:

$$\frac{\partial f(h_{c1}, h_{c2})}{\partial h_{c1}} = 0 \quad \frac{\partial f(h_{c1}, h_{c2})}{\partial h_{c2}} = 0 \quad (6.21)$$

and solving the system of two equations and two unknowns, that yields the following switching instants:

$$h_{c1} = -\frac{(s_{22} - s_{11})\bar{P}_s + (s_1 - s_2)\bar{Q}_s + (s_{22}s_3 - s_2s_{33} + s_{33}s_1 - s_{11}s_3)h}{s_{22}s_1 - s_{33}s_1 - s_{22}s_3 + s_3s_{11} - s_2s_{11} + s_{33}s_2} \quad (6.22)$$

$$h_{c2} = -\frac{(s_{22} - s_{33})\bar{P}_s + (s_3 - s_2)\bar{Q}_s + (s_{22}s_3 - s_2s_{33})h}{s_{22}s_1 - s_{33}s_1 - s_{22}s_3 + s_3s_{11} - s_2s_{11} + s_{33}s_2} \quad (6.23)$$

with:

$$\bar{P}_s = -P_{s\_ref} + P_s(k) \quad \text{and} \quad \bar{Q}_s = -Q_{s\_ref} + Q_s(k)$$

The pair of equations (6.22) and (6.23) will minimize the  $P_s$  and  $Q_s$  errors in the same proportion. These expressions are valid for magnitudes of different scales, not requiring a special weighting treatment.

### 6.2.8 Balancing of DC Bus Capacitors Voltages

The medium vectors of the three level NPC converter must be appropriately selected to ensure the DC bus capacitor voltage balancing. That choice is simply made by only considering the medium vectors  $V_{10}$  and  $V_{20}$  of equivalent sectors 2 and 3 and the output currents of the converter. This task is accomplished in block 7 of Fig. 6.2.

Hence, from the equivalent sectors 2 and 3 TABLES 6.VII and 6.VIII provide the sufficient information to perform the voltage balancing [60].

TABLE 6.VII  
MEDIUM VECTORS ( $V_{10}$  AND  $V_{20}$ ) SELECTION TO PERFORM THE CAPACITOR VOLTAGE BALANCING

$v_{c1} > v_{c2}$	$i_{ra\_eq} > 0$	Vector $V_{10}$	$v_{c1} > v_{c2}$	$i_{rc\_eq} > 0$	Vector $V_{20}$
0	0	100	0	0	221
0	1	211	0	1	110
1	0	211	1	0	110
1	1	100	1	1	221

TABLE 6.VIII  
EQUIVALENCE OF THE CURRENTS TO PERFORM THE CAPACITOR VOLTAGE BALANCING

<b>Equivalent Current</b>	<b>Sectors 2, 3</b>	<b>Sectors 4, 5</b>	<b>Sectors 6, 7</b>	<b>Sectors 8, 9</b>	<b>Sectors 10, 11</b>	<b>Sectors 12, 1</b>
$i_{ra\_eq}$	$i_{ra}$	$i_{rb}$	$i_{rb}$	$i_{rc}$	$i_{rc}$	$i_{ra}$
$i_{rc\_eq}$	$i_{rc}$	$i_{rc}$	$i_{ra}$	$i_{ra}$	$i_{rb}$	$i_{rb}$

### 6.2.9 Vector Sequence Definition. Reduction of the Commutations

Once are selected the three vectors and their duty cycles ( $h_{c1}$  and  $h_{c2}$ ) from the equivalent sectors 2 and 3, the next task is to define the right implementation sequence, in order to reduce the commutations of the semiconductors. As can be noticed from Fig. 6.8, the vectors are generated by a triangular based comparison, since the first and the second vector of the sequence are split into two different application time intervals. This strategy is different from the one employed in Chapters 4 and 5, for two level converter based DTC and DPC strategies. In this case, for an equal sample period  $h$ , the switching frequency of the devices is increased compared to the two level converter based control strategies. On the contrary, the  $P_s$  and  $Q_s$  errors are decreased for the triangular based vector sequence implementation. In addition, many authors adopt this implementation procedure for three level NPC converter applications, since in general it produces more symmetric commutations of the switching devices especially considering the transition to subsequent sample periods [60] among others.

TABLE 6.IX  
VECTOR SEQUENCE OF VECTORS FROM SECTORS 2 AND 3 THAT REDUCES  
THE COMMUTATIONS OF THE SEMICONDUCTORS.

<b>Region</b>	<b>Double Vector</b>	<b>Sequence</b>
1	100	100-200-210---210-200-100
	211	200-210-211---211-210-200
2	100 - 110	100-110-210---210-110-100
	100-221	100-210-221---221-210-100
	211-110	110-210-211---211-210-110
	211-221	210-211-221---221-211-210
3	110	110-210-220---220-210-110
	221	210-220-221---221-220-210
4	100-110	100-110-111---111-110-100
	100-221	100-111-221---221-111-100
	211-110	110-111-211---211-111-110
	211-221	111-211-221---221-211-111

Hence, depending on the medium vector choice, defined by the DC bus capacitor voltage balancing algorithm that has been described in the previous section, TABLE 6.IX provides the vector sequence order that reduces the switching frequency. According to that, the zero vector employed will be always 111 since it produces the lowest switching frequency.

### 6.2.10 Real Vector Definition

The last task of the proposed algorithm is to generate the real voltage vectors, from the calculated equivalent vectors in sectors 2 and 3. In [60] is shown that the real vector definition can be performed by simply interchanging the phases according to TABLE 6.X considering the sector where the  $\vec{x}^r$  space vector lies. Finally, these two last tasks are accomplished in block 8 of Fig. 6.2.

TABLE 6.X  
CHANGE OF PHASES FOR REAL VECTOR GENERATION.

Sectors 11, 12	Sectors 1, 2	Sectors 3, 4	Sectors 5, 6	Sectors 7, 8	Sectors 9, 10
a	$a \rightarrow b$	$a \rightarrow b$	$a \rightarrow c$	$a \rightarrow c$	a
b	$b \rightarrow a$	$b \rightarrow c$	b	$b \rightarrow a$	$b \rightarrow c$
c	c	$c \rightarrow a$	$c \rightarrow a$	$c \rightarrow b$	$c \rightarrow b$

### 6.3 Experimental Results of Predictive DPC Strategy

In this section, experimental results of the control strategy presented in the previous section will be carried out. Despite the fact that this control technique is oriented to high power applications, for practical reasons and as made in previous chapters, the results have been obtained in a 15kW test bench, composed by a 380V-15kW-1500rev/min doubly fed induction machine, coupled to a DC machine. The DC machine controls the speed of both machines, while the proposed predictive DPC technique is implemented for the DFIM.

The selection of the rotor side inductive filter is made according to a simulation and experimental comparison procedure. TABLE 6.XI shows the obtained stator current THD with several inductance values, at nominal power conditions.

TABLE 6.XI  
GENERATED STATOR CURRENT QUALITY FOR DIFFERENT ROTOR SIDE FILTER  
VALUES (15kW,11kVAR, 1250REV/MIN AND 500HZ SWITCHING FREQUENCY )

$L_f$ [mH]	Stator currents THD	
	Simulation	Experimental
0	7.1%	7.8%
4	4%	4.7%
10	2.6%	3.1%
14	2.5%	2.8%

In order to produce stator currents THD that meets the IEEE Std. 519-1992 recommendation, the selected inductive filter will be 14mH, for subsequent experimental trials.

Therefore, firstly the quality of the steady state behavior achieved with the predictive DPC strategy will be presented at 0.5kHz constant switching frequency. After that, the quality of the steady state performance will be compared at different constant switching frequencies, in terms of total harmonic distortion of the generated stator currents and their spectrums.

Secondly, in a second set of experimental results, the transient response capacities of the predictive DPC strategy will be evaluated. After that, in a third experiment, the behavior of the system is shown, when the stator power references and the speed of the machine are varying during the time. i.e. the tracking behavior.

Then, a ramp speed response is analyzed, showing the performance at hypersynchronous and subsynchronous speeds, when the converter operates in all the possible regions. Finally, in the last experiment, the behavior of the system is shown in the neighborhood of the synchronous speed.

### 6.3.1 Steady State Operation Conditions at 0.5kHz Constant Switching Frequency with and without Inductive Rotor Filter

In this first experiment, the steady state behavior of the presented predictive DPC strategy will be shown in two different scenarios, i.e. with a 14mH inductive rotor filter and without rotor filter. It is obvious that with filter, the achieved current and power qualities will be better rather than without filter.

Hence, the machine is magnetized by the stator, interchanging a stator reactive power of 11kVAR with the grid. The DC bus voltage of the three level NPC converter has been set to 320V. The switching frequency is imposed to the considerably low value of 0.5kHz. In both cases, the stator active power reference is set to the nominal power of 15kW, implying that the machine will operate at the nominal torque. The speed of the machine is controlled externally to 1250rev/m firstly and secondly to 750rev/min. Under these operation conditions, the three level NPC converter will operate in the fourth region (1250rev/m) and in the first, second and third regions (750rev/min) of the space vector diagram.

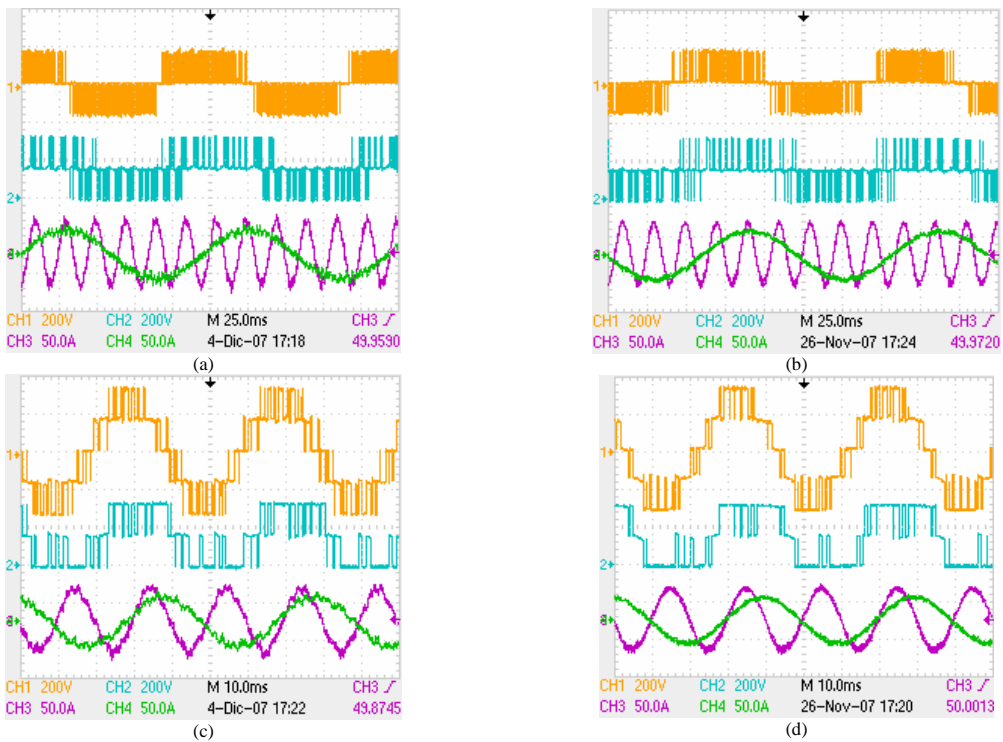


Fig. 6.10. Voltage (CH1- $V_{ab}$  and CH2- $V_{ao}$ ) and current (CH3- $i_{as}$  and CH4- $i_{ar}$ ) waveforms of predictive DPC control strategy, with and without rotor side inductive filter, at steady state with  $P_s=15\text{kW}$ ,  $Q_s=11\text{kVAR}$  and 0.5kHz switching frequency. (a) 1250 rev/min without filter. (b) 1250 rev/min with 14mH inductive filter. (c) 750 rev/min without filter. (d) 750 rev/min with 14mH inductive filter.

As noticed in Fig. 6.10, the quality of the generated stator and rotor currents are better when the machine is fed with the rotor filter, on the other hand, while only at higher modulation indexes (Fig. 6.10 (c) and (d)), all the voltage levels of the three level NPC converter are used.

In addition, this subsection analysis concludes with a spectrum comparison of the generated stator currents at different constant switching frequencies, with and without inductive rotor filter. Fig. 6.11 shows the constant switching frequency behavior achieved by the machine when it is controlled by the proposed predictive DPC strategy. In both cases, the selected switching frequencies are 0.5kHz and 2.5kHz and the operation conditions are the same as in the previous experiment. It can be noticed that at “low” switching frequency (Fig. 6.11 (a) and (b)), the high amplitude group of harmonics appear around the constant switching frequency. On the other hand, at “high” switching frequency (Fig. 6.11 (c) and (d)), the group of harmonics at 2.5kHz becomes smaller than the low frequency harmonics. Moreover, at higher switching frequency, the quality of the spectrums is improved. As expected once again, the quality of the steady state behavior is improved with the rotor side inductive filter.

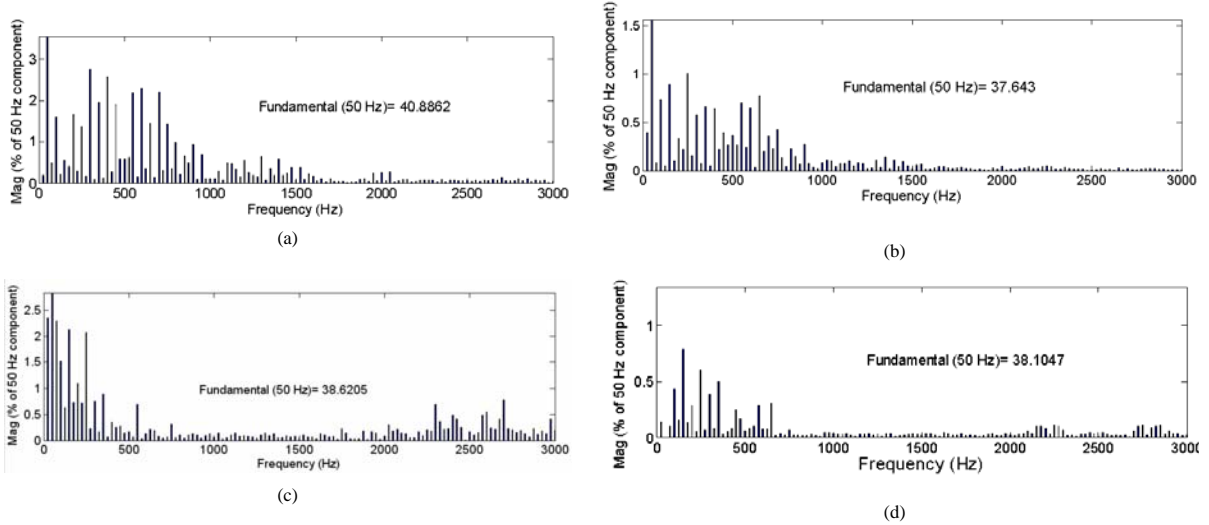


Fig. 6.11. Stator current spectrums of predictive DPC control strategy at different switching frequencies, with and without rotor side inductive filter at 1250rev/min, with  $P_s=15\text{kW}$ ,  $Q_s=11\text{kVAR}$ . (a) 0.5kHz without filter, THD=7.8%.  
(b) 0.5kHz with 14mH inductive filter, THD=2.8%. (c) 2.5kHz without filter, THD=4.7%, (d) 2.5kHz with 14mH inductive filter, THD= 1.75%.

### 6.3.2 Transient Response Capacity at 0.5kHz Constant Switching Frequency with Inductive Rotor Filter

In this experimental trial, the dynamic response of the predictive DPC strategy will be studied and compared. For that purpose, severe stator active and reactive power variations will be demanded, and the control strategies will provoke that the machine responds to that demand in a quick and safe manner. The selected power variations are 5kW and 5kVAR, and they will be accomplished at different instants. The first and the second power variations will affect to only

one of the power references, while the third variation will demand a simultaneous active and reactive power variation.

Thus, Fig. 6.12 shows the transient response of the control strategy when they operate at 1250rev/min, 0.5kHz switching frequency and 320V of DC bus voltage. The severity of the step power variations is successfully addressed by the DPC strategy, with an absolute absence of overcurrents.

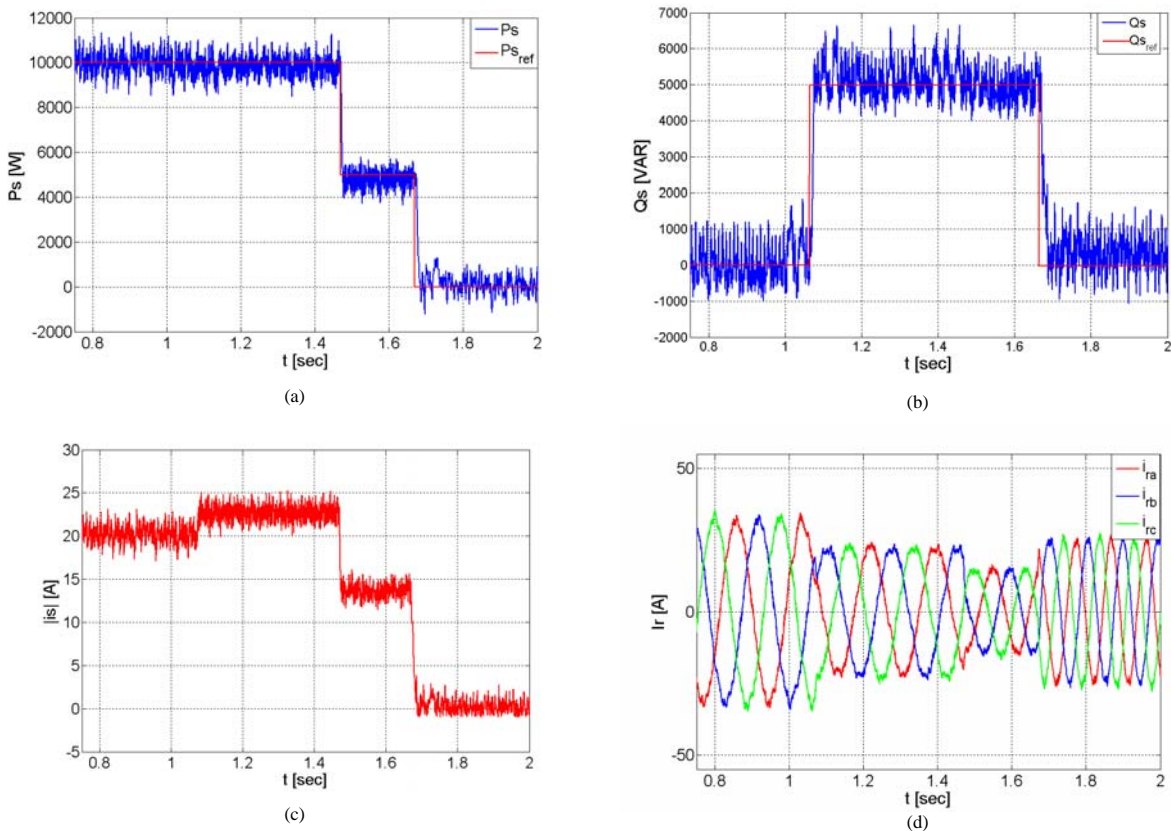


Fig. 6.12. Transient response of the predictive DPC control strategy at 0.5kHz switching frequency. (a) Stator active power, (b) Stator reactive power, (c) Stator currents module, (d) Rotor currents.

### 6.3.3 Tracking behavior at 0.5kHz Constant Switching Frequency with Inductive Rotor Filter

In this experiment, the behavior of the system is analyzed when the stator active and reactive power together with the speed of the machine are varying over the time. Compared with the previous experiments, it is wanted to explore another capacity of the proposed DPC control strategy, i.e. the tracking behavior. Hence, with equal operation conditions as in the previous

experiments, the sinusoidally varying stator active and reactive power references will make the stator of the machine operate in four possible states, i.e. inductive generating, inductive motoring, capacitive generating and capacitive motoring.

Fig. 6.13 shows the captured most important magnitudes of the experiment. Thus, in Fig. 6.13 (a) and (b), the stator active and reactive power tracking behavior can be observed. Under these conditions, the stator and rotor currents experiment the evolution shown in Fig. 6.13 (d), while in Fig. 6.13 (c), the externally controlled speed variation is presented.

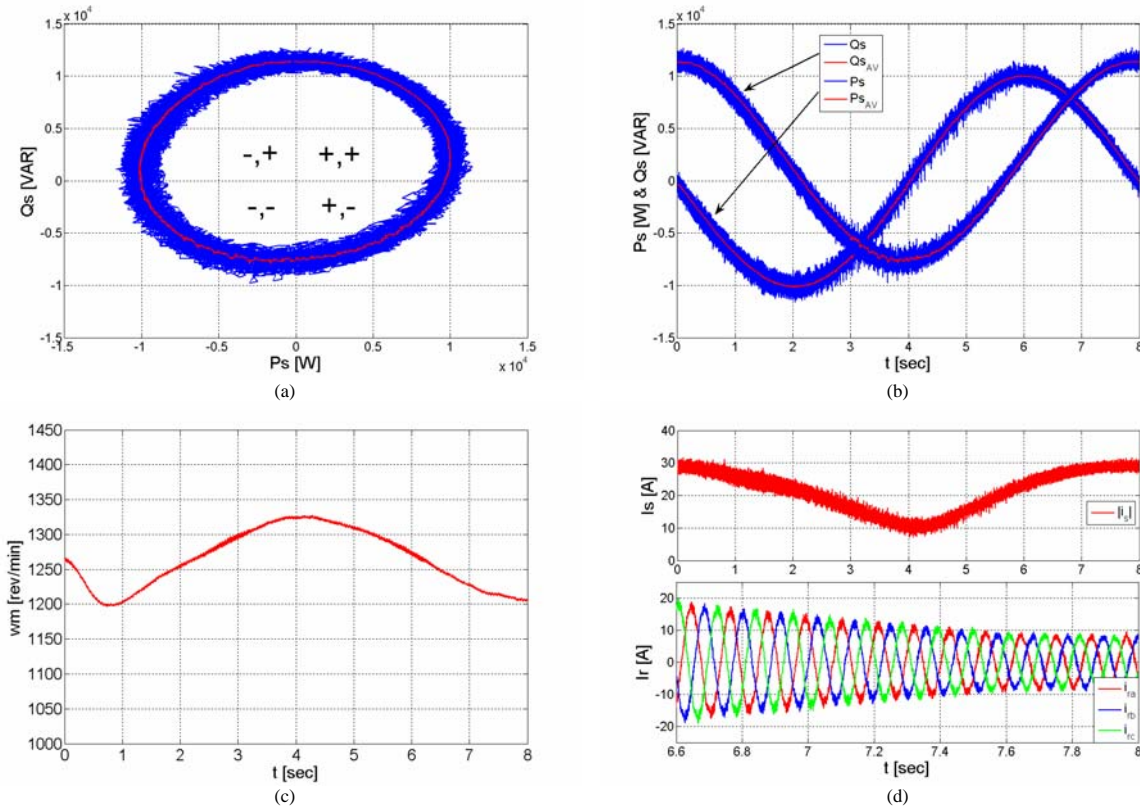


Fig. 6.13. Tracking behavior of the predictive DPC control strategy at 0.5kHz switching frequency. (a)  $Q_s$  vs.  $P_s$ , (b) Stator active and reactive power, (c) Speed, (d) Stator current module and rotor currents (Enlarged).

### 6.3.4 Variable speed performance at 0.5kHz Constant Switching Frequency with Inductive Rotor Filter

In this subsection, the performance of the control strategy at variable speed is analyzed. The experiment performs a speed ramp from 1750rev/min to 650rev/min (Fig. 6.14 (a)) that will make the rotor currents operate from -8.3Hz to 28.3Hz range of frequencies. The DPC strategy is required to maintain the references at constant 5kW and 11kVAR stator active and reactive powers.

As illustrated in Fig. 6.14 (b), during the 8 seconds of the experiment, the stator active and reactive powers are controlled to their reference values. Due to the maximum mechanical speed limitation of the test bench, a non symmetric speed ramp has been performed. The DFIM is used typically at  $\pm 30\%$  of the synchronous speed in wind energy applications, requiring 1/3 of nominal rotor voltage (with  $|V_s|/|V_r| \leq 1$  as in the test bench), in order to increase the rotor voltage amplitude and frequency, the speed has been taken further away (up to 650rev/min) from the synchronous speed. Hence, with a constant switching frequency of 500Hz, the experiment shows that the system is able to operate with rotor currents of higher frequency than 25Hz.

In Fig. 6.14 (d), the sector and the region are represented in two transition moments, firstly at the synchronous speed (1.8sec). Secondly, at the limit between operating region 4, and operating regions 1, 2 and 3 of the three level NPC converter. Finally Fig. 6.14 (c) shows the stator currents in the vicinity of the transition between the hypersynchronous and subsynchronous speed.

It can be noticed, that the quality of the currents is not affected in the transitions. However, a smooth deterioration of the averaged stator active power is observed in both transitions, as deduced from Fig. 6.14 (b).

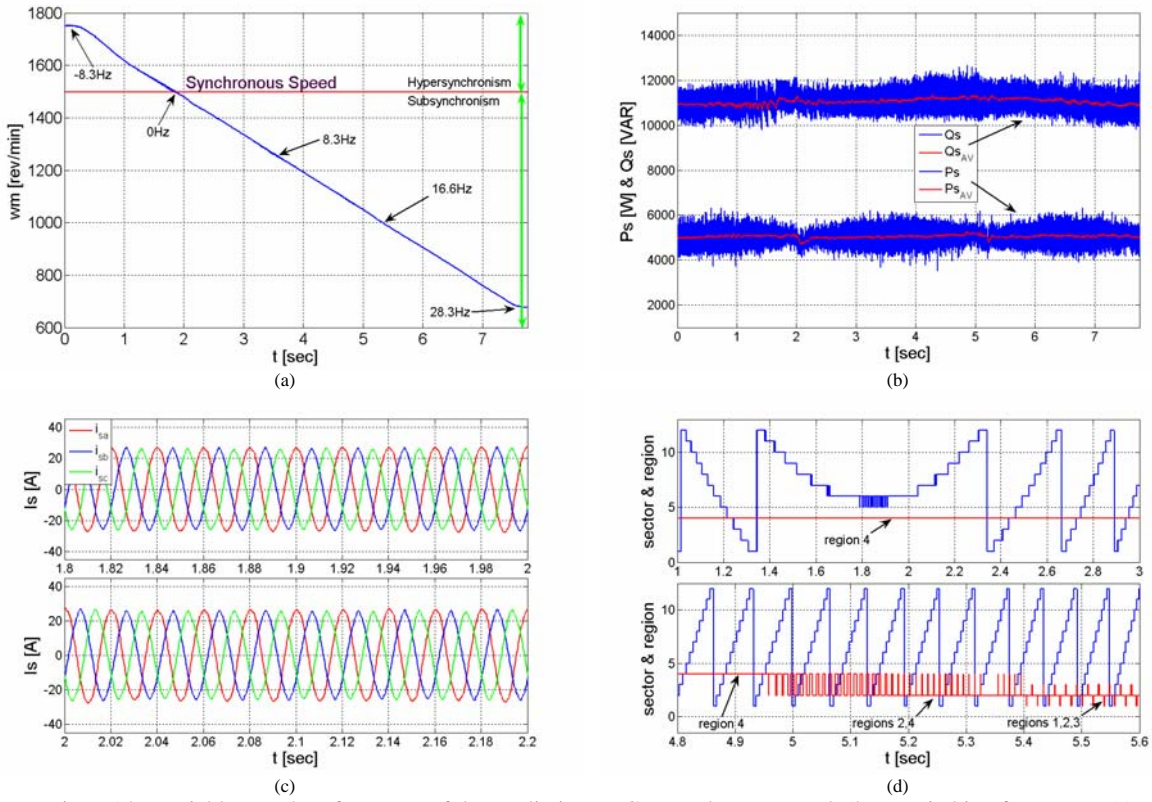


Fig. 6.14. Variable speed performance of the predictive DPC control strategy at 0.5kHz switching frequency. (a) Speed, (b) Stator active and reactive power, (c) Stator currents (Enlarged), (d) Sector and region (Enlarged).

### 6.3.5 Performance near the Synchronous Speed at 0.5kHz Constant Switching Frequency with Inductive Rotor Filter

In this last experiment, the behavior of the system is studied, when the machine operates in the vicinity of the synchronous speed. Under these conditions, the required rotor voltage space vector has small amplitude and a frequency close to 0Hz.

In Fig. 6.15 (a), the speed of the machine is presented. At the beginning and at the end of the experiment, the speed is maintained in the synchronism, while in the middle, several transitions from hypersynchronous to subsynchronous speeds are performed.

Fig. 6.15 (b) shows the stator active and reactive power performances. The machine is magnetized by the stator with 11kVAR reactive power and the active power reference is 5kW. Analyzing the averaged  $P_s$  and  $Q_s$  values during the experiment, smooth control deterioration is observed. At synchronous speed, approximately 5% amplitude low frequency reactive power oscillations are experimented.

In addition, under dynamic speed operation, during the transitions through the synchronous speed, the stator active and reactive powers experiment further low frequency oscillations.

However, as shown in Fig. 6.15 (c) and (d), the quality of the stator and rotor currents is not affected by this stator power control deterioration. Mainly, it only produces a smooth deviation of the demanded stator power.

Finally, it is necessary to highlight that one important reason of this control degradation is the performance of the three level NPC converter at very low modulation indexes. Improvements in nonlinearities, dead times effect and inaccuracies in general, of the experimental rig [59], will contribute to a better performance near the synchronism.

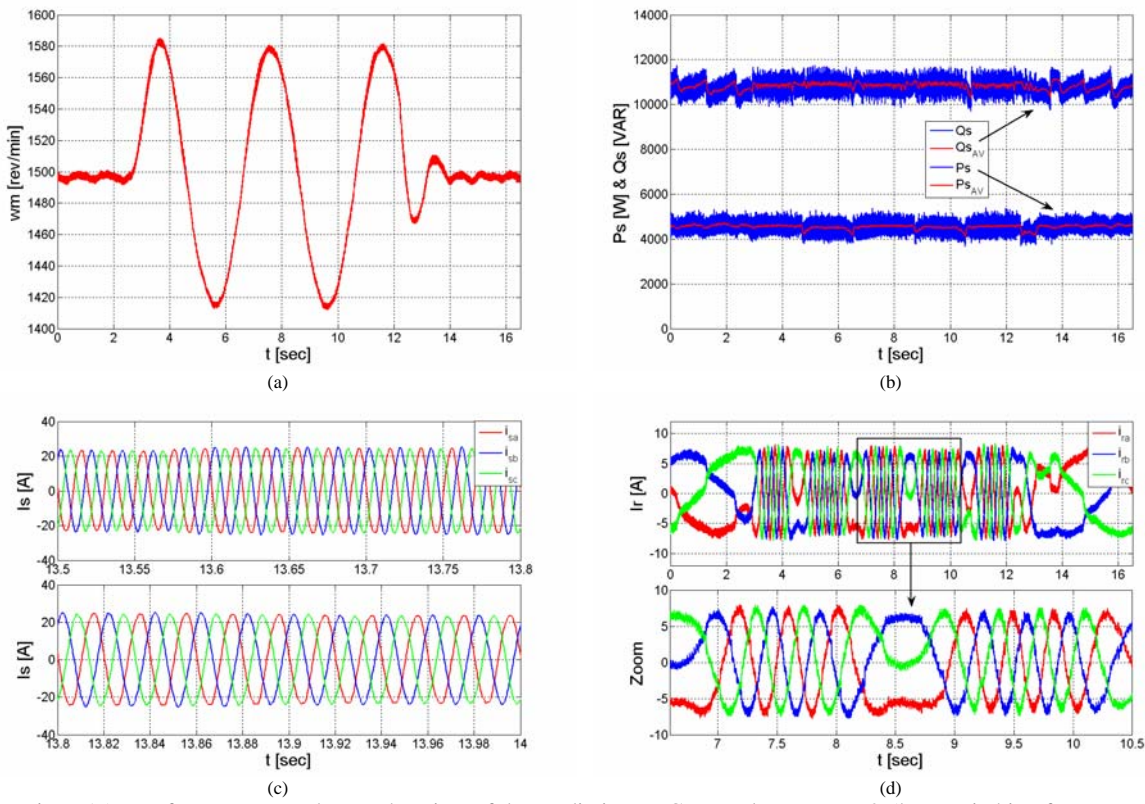


Fig. 6.15. Performance near the synchronism of the predictive DPC control strategy at 0.5kHz switching frequency.  
 (a) Speed, (b)  $P_s$  and  $Q_s$ , (c) Stator currents (Enlarged), (d) Rotor currents.

## 6.4 Predictive Direct Torque Control Strategy (DTC) at Low Constant Switching Frequency

In this next section, the predictive DTC strategy is depicted for the three level NPC converter. Since this control strategy is equivalent to the DPC strategy presented in this chapter, only the most significant features of the predictive DTC will be analyzed. First of all, the control block diagram will be presented, after that, only the new different blocks will be analyzed, i.e. the first vector selection blocks, the slopes calculation block and the error reduction block.

### 6.4.1 Control Block Diagram

The block diagram of the proposed control strategy is shown in Fig. 6.16. The directly controlled magnitudes are the electromagnetic torque and the rotor flux amplitude. From the references, the control strategy calculates the pulses ( $S_{1a}, S_{2a}, S_{1b}, S_{2b}, S_{1c}, S_{2c}$ ) for the IGBTs of the three level NPC voltage source converter (VSC), in order to meet the following two objectives: reduced ripples and constant switching frequency behavior. Fig. 6.16 shows that the control strategy is divided into eight different tasks represented in eight different blocks. Note that this control block diagram is equivalent to block diagram of Fig. 6.2 for predictive DPC strategy. In fact, blocks 1, 2, 3, 7 and 8 are exactly the same, so for simplicity they will not be analyzed again in this section. On the other hand, blocks 4, 5 and 6 present some differences that will be analyzed in subsequent subsections.

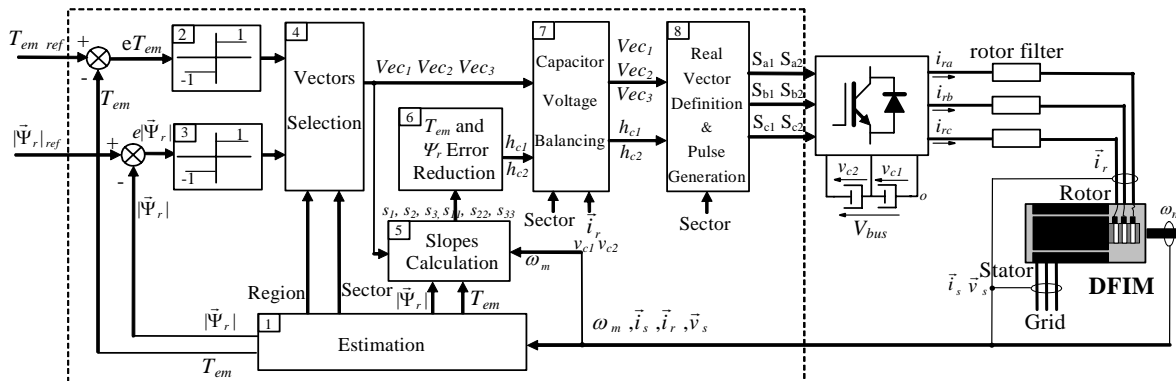


Fig. 6.16. Predictive DTC block diagram.

### 6.4.2 First Vector Selection Strategy

The basic principle of the Direct Control techniques determines the choice of one specific voltage vectors of the converter, in order to correct the directly controlled magnitude's errors. Equivalently as occurred with the predictive DPC, the choice of this vector is directly calculated from the electromagnetic torque and the rotor flux amplitude errors themselves, the sector where the  $\vec{x}^r$  lies and the region of the equivalent voltage vector  $\vec{v}_{i\_eq}$ .

Once again, the proposed predictive DTC strategy adopts this principle to select the first voltage vector of the three vectors sequence employed to minimize the  $T_{em}$  and  $|\vec{\Psi}_r|$  errors. Hence, the first voltage vector selection is based on a look-up table mapped by the output of two ON-OFF comparators without hysteresis bands. These tasks are accomplished in blocks 2, 3 and 4 of Fig. 6.16. When the estimated inverter voltage vector lies in regions 1, 2 or 3, the look-up table is made according to Table 6.XII.

TABLE 6.XII  
FIRST VECTOR SELECTION FOR REGIONS 1, 2 AND 3 AT SUBSYNCHRONISM.

Sectors		$(eT_{em}, e  \vec{\Psi}_r ) \text{ or } (eP_s, eQ_s)$			
DTC	DPC	(1,1)	(1,-1)	(-1,1)	(-1,-1)
<b>1, 5, 9</b>	<b>4, 8, 12</b>	$V_{20}$	$V_{10}$	$V_2$	$V_{12}$
<b>2, 6, 10</b>	<b>3, 7, 11</b>	$V_{20}$	$V_{10}$	$V_{12}$	$V_1$
<b>3, 7, 11</b>	<b>2, 6, 10</b>	$V_{10}$	$V_{20}$	$V_1$	$V_{12}$
<b>4, 8, 12</b>	<b>1, 5, 9</b>	$V_{10}$	$V_{20}$	$V_{12}$	$V_2$

On the contrary, when the inverter space vector is located in region 4, the look-up table is made according to Table 6.XIII. Note that in both cases, the required information to select the first vector for the predictive DTC and DPC strategies has been included.

After that, the second and third vector selection procedure of DTC strategy employs the same table of DPC strategy (Table 6.V).

TABLE 6.XIII  
FIRST VECTOR SELECTION FOR ALL THE SECTORS AND REGION 4 AT SUBSYNCHRONISM.

Sector	DTC ( $\mathbf{e}T_{em}, e \mid \vec{\Psi}_r \mid$ )			
	(1,1)	(1,-1)	(-1,1)	(-1,-1)
<b>1, 2</b>	V <sub>60</sub>	V <sub>50</sub>	V <sub>20</sub>	V <sub>30</sub>
<b>3, 4</b>	V <sub>10</sub>	V <sub>60</sub>	V <sub>30</sub>	V <sub>40</sub>
<b>5, 6</b>	V <sub>20</sub>	V <sub>10</sub>	V <sub>40</sub>	V <sub>50</sub>
<b>7,8</b>	V <sub>30</sub>	V <sub>20</sub>	V <sub>50</sub>	V <sub>60</sub>
<b>9, 10</b>	V <sub>40</sub>	V <sub>30</sub>	V <sub>60</sub>	V <sub>10</sub>
<b>11, 12</b>	V <sub>50</sub>	V <sub>40</sub>	V <sub>10</sub>	V <sub>20</sub>
Sector	(1,-1)	(1,1)	(-1,-1)	(-1,1)
	DPC ( $eP_s, eQ_s$ )			

#### 6.4.3 Derivative Expressions Calculation

In this subsection, the mathematical expressions that relate the electromagnetic torque and the rotor flux amplitude variations with the inverter voltage vectors are presented. Substituting the equation (6.2) into the torque and rotor flux amplitude derivative expressions ((4.2) and (4.3)), the derivative expressions yields:

$$\frac{d|\vec{\Psi}_r|}{dt} = \left( \frac{R_{rf} L_h}{\sigma L_s L_r} \right) |\vec{\Psi}_s| \cos \delta - \left( \frac{R_{rf}}{\sigma L_r} \right) |\vec{\Psi}_r| \\ - \left( \frac{L_f L_h}{\sigma L_s L_r} \right) \omega_r |\vec{\Psi}_s| \sin \delta + \frac{2}{3} V_{bus} \cos(\omega_r t - \frac{\pi}{3}(n-1)) \quad (6.24)$$

$$\frac{dT_{em}}{dt} = T_{em} \left( \left( \frac{L_f}{\sigma L_r} + 1 \right) \frac{\omega_r}{\tan \delta} - \left( \frac{R_s}{\sigma L_s} + \frac{R_r}{\sigma L_r} \right) \right) - \frac{3}{2} p L_f \left( \frac{L_h}{\sigma L_s L_r} \right)^2 \omega_r |\vec{\Psi}_s|^2 \\ + p \frac{L_h}{\sigma L_s L_r} V_{bus} |\vec{\Psi}_s| \sin(\omega_r t + \delta - \frac{\pi}{3}(n-1)) \quad (6.25)$$

#### 6.4.4 Power Error Reduction Criteria at Constant Switching Frequency

The expected electromagnetic torque and rotor flux evolutions in one switching period are shown in Fig 6.17. Since the same error reduction procedure as predictive DPC is followed, the expressions for the duty cycles are:

$$h_{c1} = \frac{(s_{22} - s_{11})\bar{T}_{em} + (s_1 - s_2)\bar{F}_r + (s_{22}s_3 - s_2s_{33} + s_{33}s_1 - s_{11}s_3)h}{s_{22}s_1 - s_{33}s_1 - s_{22}s_3 + s_3s_{11} - s_2s_{11} + s_{33}s_2} \quad (6.26)$$

$$h_{c2} = \frac{(s_{22} - s_{33})\bar{T}_{em} + (s_3 - s_2)\bar{F}_r + (s_{22}s_3 - s_2s_{33})h}{s_{22}s_1 - s_{33}s_1 - s_{22}s_3 + s_3s_{11} - s_2s_{11} + s_{33}s_2} \quad (6.27)$$

with:

$$\bar{T}_{em} = T_{em\_ref} + T_{em}(k) \quad \text{and} \quad \bar{F}_r = |\vec{\Psi}_r|_{ref} + |\vec{\Psi}_r|(k)$$

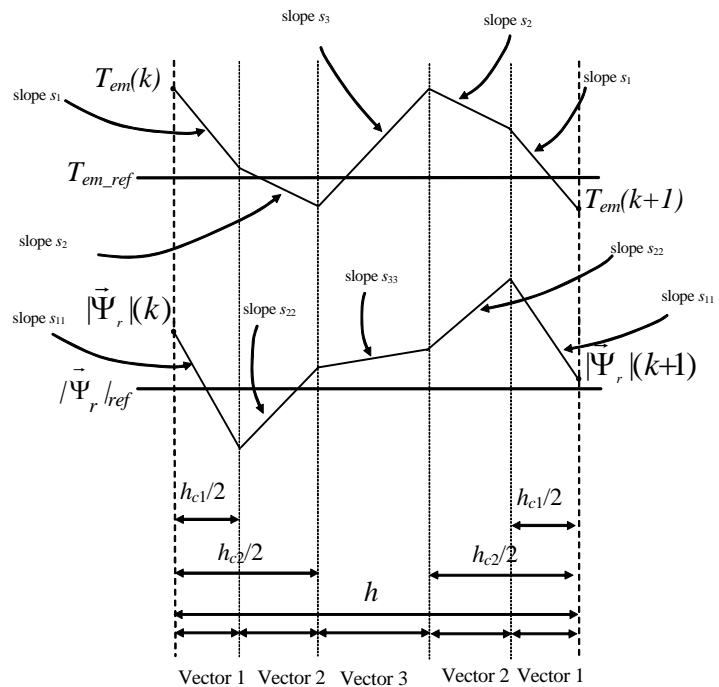


Fig. 6.17. Steady state electromagnetic torque and rotor flux amplitude waveforms at motor and generator modes in subsynchronousism.

## 6.5 Experimental Results of Predictive DTC Strategy

In order to improve in simplicity, not as many experimental results as in the predictive DPC will be presented. The same experimental platform as in experiments of previous sections and chapters has been used. First of all, the steady state performance of the predictive DTC will be presented and compared with the predictive DPC. After that, a steady state quality comparison between predictive DTC and DPC is carried out.

Since both control strategies share the same control structure and principles, very similar transient response capacity and tracking behavior are achieved. For that reason, they have not been included in the document.

### 6.5.1 Steady State Operation Conditions at 1kHz Constant Switching Frequency without Inductive Rotor Filter

In this first experiment, the steady state behavior of the presented DTC and DPC strategies will be shown. Equal operation conditions are set for both control strategies. Hence, the machine is magnetized by the stator, interchanging a stator reactive power of 11kVAR with the grid. The DC bus voltage of the three level NPC converter has been set to 320V. The switching frequency is set to the considerably low value of 1kHz. The speed of the machine is controlled externally. In both cases too, the machine will operate at the nominal torque (nominal stator active power).

The experiment has been carried out without rotor side inductive filter. Fig. 6.18 shows voltage and current captures of both predictive DTC and DPC control strategies at nominal torque (nominal stator active power) at two different constant speeds. Thus, in Fig. 6.18 (a) and (b), the rotor voltage space vector rotates in the fourth region, requiring low voltage fundamental amplitude, while in Fig. 6.18 (c) and (d), the space vector rotates in regions 1, 2 and 3, demanding higher fundamental component of voltage amplitude.

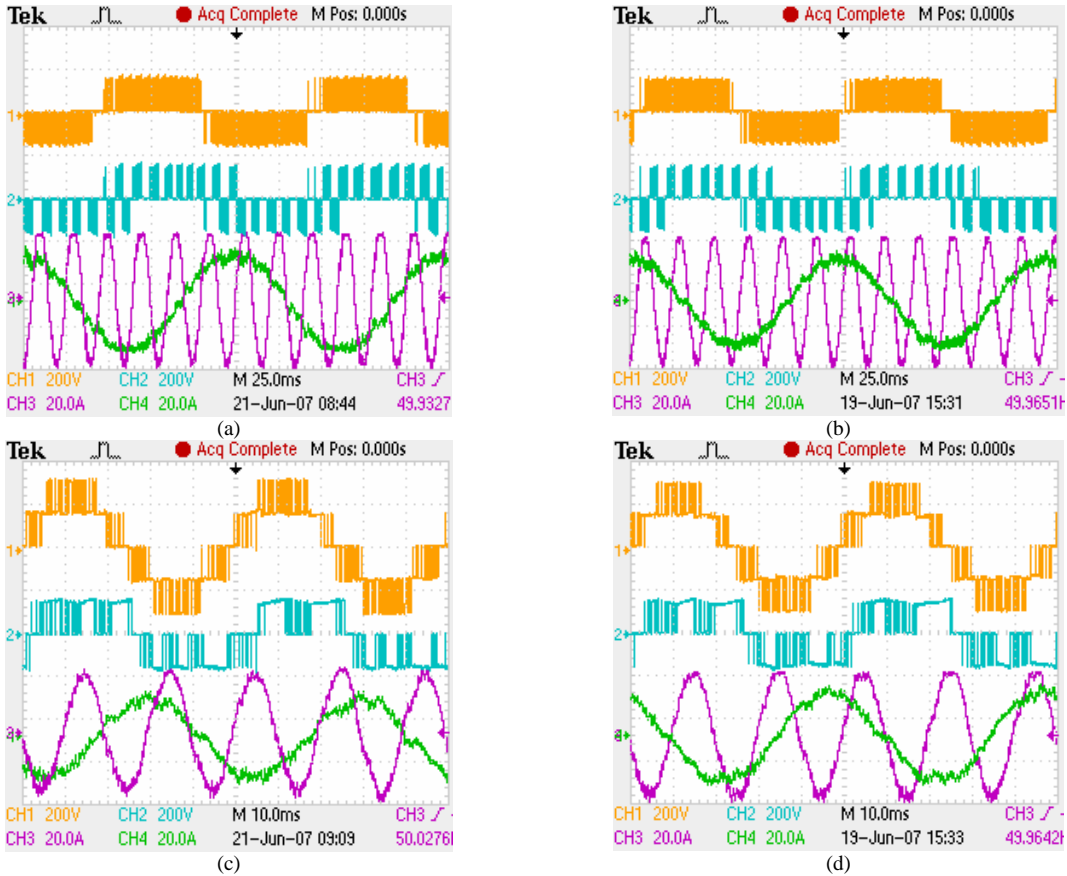


Fig. 6.18. Voltage (CH1- $V_{ab}$  and CH2- $V_{ao}$ ) and current (CH3- $i_{as}$  and CH4- $i_{ar}$ ) waveforms of predictive DTC and DPC control strategies at steady state and 1kHz switching frequency, without inductive rotor filter. (a) DTC at 1250rev/min, (b) DPC at 1250rev/min, (c) DTC at 950rev/min, (d) DPC at 950rev/min.

Finally, this subsection analysis concludes with a spectrum comparison of the generated stator currents and the electromagnetic torque, at different constant switching frequencies. Fig. 6.19 and Fig. 6.20 present the constant switching frequency behavior achieved by the machine when it is controlled by the proposed predictive DTC and DPC strategies. In both cases, the selected switching frequencies are 0.5kHz, 1kHz and 2.5kHz and the operation conditions are the same as in the first experiment. It can be noticed that at a specific switching frequency, the highest amplitude harmonics appear around the employed constant switching frequency. Similarly, at higher switching frequency, the quality of the spectrums is improved. In Fig. 6.20 (a), (c) and (e), since the directly controlled variable is the stator active power, the electromagnetic torque presents some considerably high amplitude low frequency harmonics.

To conclude, it can be noticed that the quality of the achieved steady state is better for the DPC strategy rather than the DTC strategy due to the nature of the directly controlled variables. The DPC technique requires a “simple” measurement of the stator active and reactive power, while the DTC technique requires an estimation of the electromagnetic torque and the rotor flux. In addition, this estimation depends on both stator and rotor currents (see equations (3.22) and (3.28)), that are magnitudes to be controlled indirectly by the control strategy. This fact yields to a

more difficult estimation procedure, since for the case of the DPC technique, the measurement of the stator powers depends on the stator currents and a externally fixed stator voltage (see equations (3.24) and (3.26)). These estimation issues, added to the fact that we are dealing with a prediction based control strategy, makes the DPC strategy more robust to model uncertainties and noise perturbations rather than the DTC, achieving better steady state performance results.

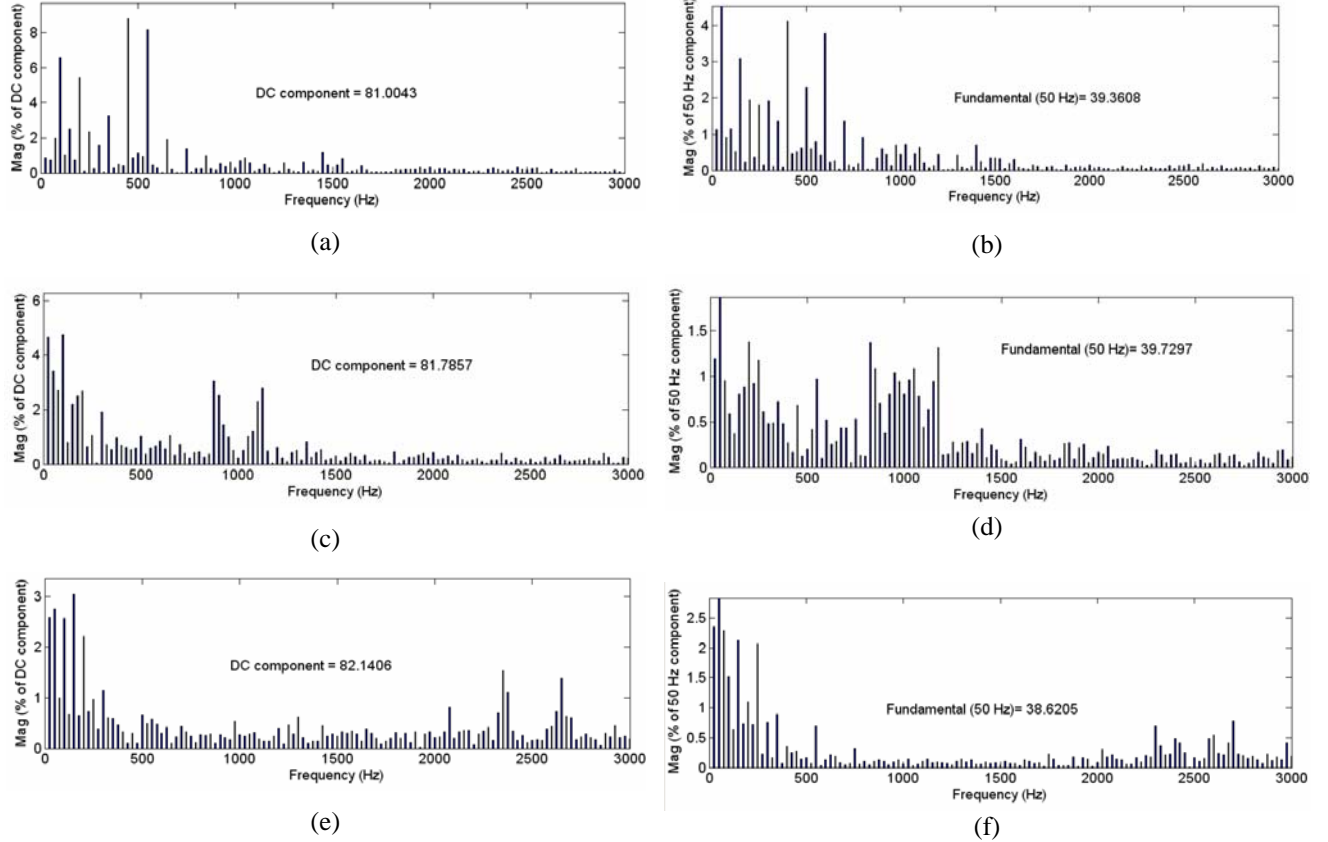


Fig. 6.19. Torque and stator current spectra of predictive DTC control strategy at different switching frequencies, without rotor side inductive filter at 1250rev/min, with  $P_s=15\text{kW}$ ,  $Q_s=11\text{kVAR}$ . (a)  $T_{em}$  at 0.5kHz. (b)  $i_{sa}$  at 0.5kHz, THD=8.5%. (c)  $T_{em}$  at 1kHz. (d)  $i_{sa}$  at 1kHz, THD=5.4%. (e)  $T_{em}$  at 2.5kHz. (f)  $i_{sa}$  at 2.5kHz, THD=4.7%.

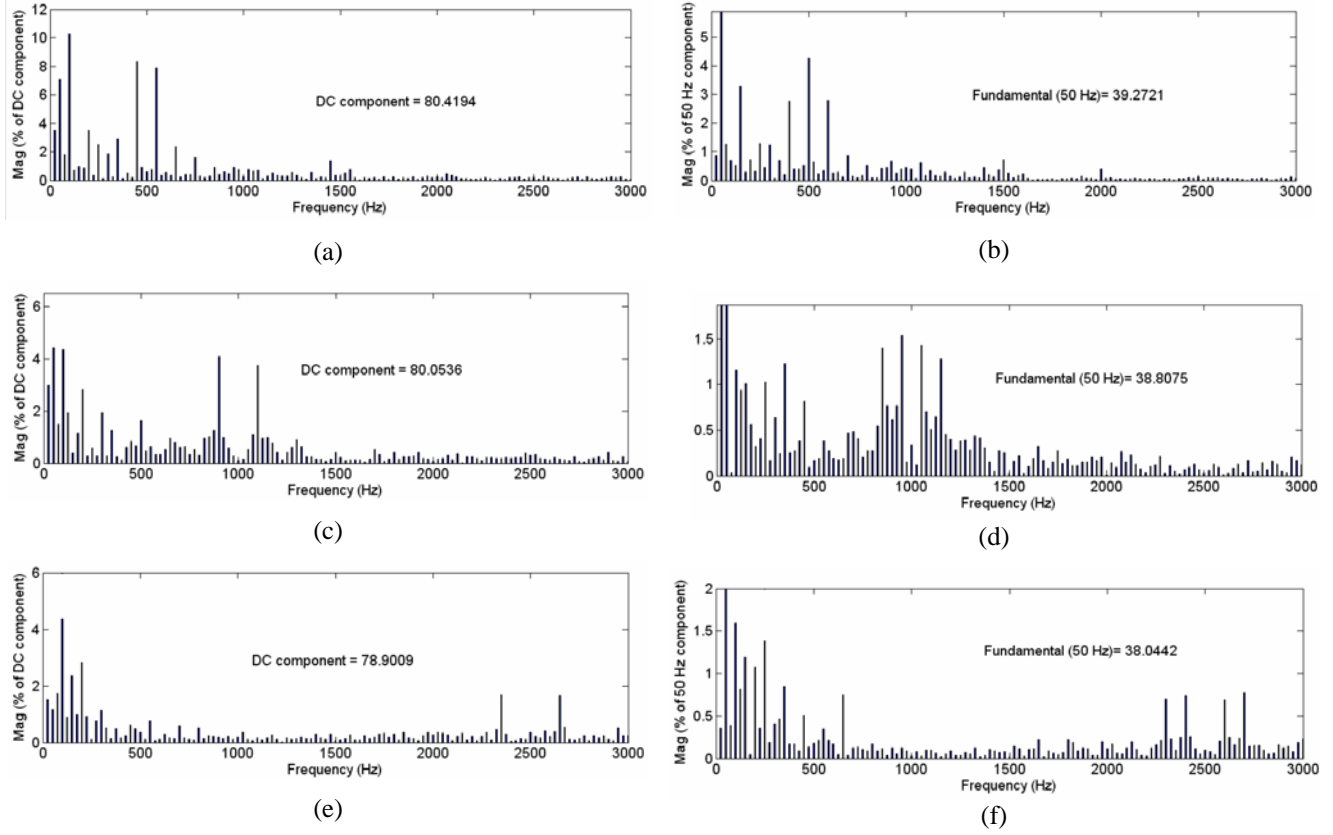


Fig. 6.20. Torque and stator current spectra of predictive DPC control strategy at different switching frequencies, without rotor side inductive filter at 1250rev/min, with  $P_s=15\text{kW}$ ,  $Q_s=11\text{kVAR}$ . (a)  $T_{em}$  at 0.5kHz. (b)  $i_{sa}$  at 0.5kHz, THD=8%. (c)  $T_{em}$  at 1kHz. (d)  $i_{sa}$  at 1kHz, THD=5.1%. (e)  $T_{em}$  at 2.5kHz. (f)  $i_{sa}$  at 2.5kHz, THD=4.3%.

## 6.6 Conclusions of the Chapter

In this chapter, it has been demonstrated that by using the theory developed in chapters 4 and 5, it is possible to design predictive DTC and DPC strategies, supplied by a three level NPC inverter using an inductive rotor side filter. These control strategies have been specially designed to keep the on-line implementation simplicity of the “classical” direct control techniques.

The controlled system presents fast active and reactive power response, constant switching frequency, a good THD, and keeps the DC bus capacitors voltages balanced in any situation.

The proposed theoretical approach combines the nearest three vectors selection principle proposed for the space vector modulations in three level NPC inverters and the classical DTC-DPC technique, taking into account the inductive filter.

In order to validate these control strategies, a set of experimental tests have been carried out concluding that they provide the capacity to operate at considerably low constant switching

frequency, with acceptable steady state, dynamic response capacity and tracking behavior, making them convenient for high power drive and generator applications with restricted switching frequencies.

In contrast, as occurred with the two level based control strategies, although the predictive DTC and DPC techniques are designed under the same control principles, the DPC achieves slightly better quality steady state behavior rather than the DTC, in terms of current and electromagnetic torque distortion. Basically, this is due to the fact that these control strategies are based on predictions, and it has been proved that the prediction of the stator active and reactive powers are much more easy than magnitudes such as the electromagnetic torque and the rotor flux. For that reason, the predictive control techniques are more suitable to easy predictable magnitudes, non dependant to model uncertainties. Nevertheless, for obvious reasons the transient capacity and the tracking behavior of both control techniques are equivalent.

Finally, the achieved results show that these predictive direct control techniques could become an alternative solution to classical control methods in the field of high power applications.

*However, once reached to the point that these proposed predictive direct control techniques are successfully validated under a low switching frequency and multilevel converter scenario, the next challenge is to show the behavior of these predictive direct control methods under faulty operation conditions.*

*Since the stator of the doubly fed induction machine is directly connected to the grid, undesired but sometimes common faulty operation conditions of the grid, such as, unbalanced voltages, harmonic pollution, voltage dips, flicker, etc... will lead to an undesired performance degradation of the machine, if not special control efforts are considered.*

*Consequently, in the next chapter, further improvements to the already proposed and validated predictive direct control techniques will be developed, focusing on the following faulty operation conditions: grid voltage unbalance polluted by voltage harmonics.*



## CONTENTS of Chapter 7

7	Control of Doubly Fed Induction Machine based Wind Turbine under Distorted Grid Voltage Operation Conditions .....	182
7.1	Introduction .....	182
7.2	Wind Power Energy Generation System under Unbalanced Voltage Grid .....	184
7.2.1	Model of the Unbalanced Grid .....	185
7.3	Model of the Doubly Fed Induction Machine under Unbalanced Voltage Grid Conditions .	187
7.4	Control of the Doubly Fed Induction Machine under Unbalanced Voltage Grid Conditions	191
7.4.1	Direct Power Control (DPC) .....	191
7.4.2	Stator Current Negative Sequence Cancellation Strategy.....	193
7.4.3	Torque Oscillations Cancellation Strategy .....	195
7.5	Control of the Grid Side Converter under Unbalanced Voltage Grid Conditions .....	197
7.5.1	Direct Power Control (DPC) of the Grid Side Converter .....	198
7.5.2	Power References Generation Strategy. Negative Sequence Cancellation.....	199
7.6	Contribution to Balance the Grid Voltage Unbalance .....	201
7.7	Simulation Results.....	203
7.7.1	Unbalanced Voltage Situation .....	203
7.7.2	Unbalanced Voltage Situation under Presence of Harmonics .....	208
7.8	Conclusions of the Chapter .....	211

# Chapter 7

## 7 Control of Doubly Fed Induction Machine based Wind Turbine under Distorted Grid Voltage Operation Conditions

*In this chapter, the behavior of the wind turbine generation system will be studied under abnormal grid voltage situations. Mainly an unbalanced grid voltage scenario will be studied, but the presence of voltage harmonics in the grid will be also shortly considered. It will be shown that if no special control efforts are employed, the wind turbine system behavior will be deteriorated, basically due to two reasons, i.e. electromagnetic torque oscillations and non-sinusoidal current exchange with the grid.*

*Therefore, in order to tackle these problems, different control strategies will be provided, for both rotor side and grid side converters control of the wind turbine. Finally, simulation results will successfully validate the proposed control strategies under the distorted grid voltage operation conditions considered.*

### 7.1 Introduction

In this chapter, both grid side and rotor side converter control strategies will be developed, under distorted voltage operation conditions of the wind turbine. Two different grid disturbances will be analyzed, unbalanced voltage and the presence of voltage harmonics in the grid. For easier understanding, and in order on the control solutions for these two disturbances, simple DPC techniques will be employed, and the easy back to back converter will be used as VSC.

The control solutions proposed for this faulty scenario, will be based on the appropriate active and reactive power reference generation strategy. Therefore, with the combination of an simple but efficient DPC technique, together with the required power generation strategy, the wind turbine system will be able to tackle with two main challenges, i.e. avoid electromagnetic torque oscillations, exchanging sinusoidal currents with the grid.

Hence, first of all, different control solutions will be proposed to address the disturbances provoked by the grid voltage unbalance. The behavior of the DFIM and the grid side converter system will be deeply analyzed, under the provided control solutions. Simulation results will validate the theoretical study, showing that it is possible to achieve the two main objectives under unbalanced voltage grid conditions, i.e. avoid the necessity to disconnect the wind turbine generation system due to electromagnetic torque oscillations, ensuring sinusoidal current exchange with the grid.

On the other hand, the proposed control strategy for an unbalanced voltage scenario, will be also tested including the presence of voltage harmonics in the grid at the end of the chapter. Therefore, by means of simulation results, it will be concluded that the behavior of the systems still is able to eliminate the torque oscillations, but the exchanged currents with the grid will be polluted by the same harmonics present in the grid voltage.

## 7.2 Wind Power Energy Generation System under Unbalanced Voltage Grid

First of all, as mentioned above, the system under analysis will consider the unbalance created in the grid voltage by the presence of an unbalanced load as illustrated in Fig 7.1. In a general situation, not all the impedances ( $R_a$ ,  $R_b$ ,  $R_c$ ) of the load are equal. The unbalanced consumption of currents of the load ( $i_{L_a}$ ,  $i_{L_b}$ ,  $i_{L_c}$ ) together with the impedance of the grid ( $Z_{N1}$ ,  $Z_{N2}$ ), will provoke an unbalanced voltage in the wind turbine ( $v_s$ ).

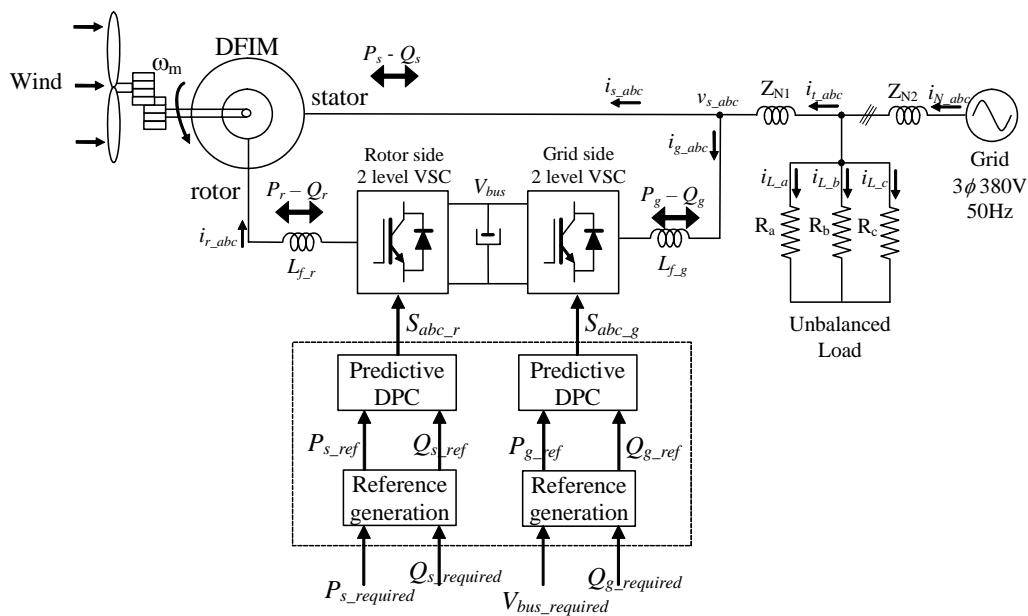


Fig. 7.1. Wind energy generation system under unbalanced grid conditions.

As will be later shown in this article, this unbalanced voltage will affect to the grid side converter and to the stator of the DFIM. If a standard version of control is employed in both side of the converters, a non-efficient performance of the system is achieved. Several authors [61]-[63] and [28] already have shown that this requires additional control efforts in order to avoid electromagnetic torque oscillations and non-sinusoidal currents, in both grid side converter currents and stator currents.

The adopted control strategies for both sides of the converter will be the Direct Power Control (DPC). In the rotor side converter, the stator active and reactive powers ( $P_s$  and  $Q_s$ ) exchanged with the grid will be directly controlled. Similarly, the grid side converter active and reactive powers ( $P_g$  and  $Q_g$ ) will be also directly controlled. Hence, the pulses for the controlled semiconductors of the two level back to back converter will be generated from the stator active and reactive power references, together with the grid side converter active and reactive power.

In the following two sections, a special reference generation strategy will be justified under unbalanced voltage operations conditions, as schematically represented in Fig. 7.1.

### 7.2.1 Model of the Unbalanced Grid

As introduced in the previous section, it is necessary to consider the grid voltage unbalance due to asymmetrical loads connected to the grid. In this section, this fact will be analyzed with the mathematical symmetric decomposition theory. An unbalanced three phase system can be discomposed in three balanced symmetric three phase systems [64]. These three phase systems are called the zero sequence, the positive sequence and the negative sequence components, and can be calculated according to the following expression [63]:

$$\begin{bmatrix} x^o \\ x^+ \\ x^- \end{bmatrix} = \frac{1}{3} \begin{bmatrix} 1 & 1 & 1 \\ 1 & a & a^2 \\ 1 & a^2 & a \end{bmatrix} \begin{bmatrix} x_a \\ x_b \\ x_c \end{bmatrix} \quad (7.1)$$

being the time operator  $a = e^{j\frac{2\pi}{3}}$ ,  $x_a$ ,  $x_b$  and  $x_c$  the three phase unbalanced system,  $x^o$  the zero sequence component,  $x^+$  the positive sequence component and  $x^-$  the negative sequence component. This decomposition can be graphically represented as shown in Fig. 7.2.

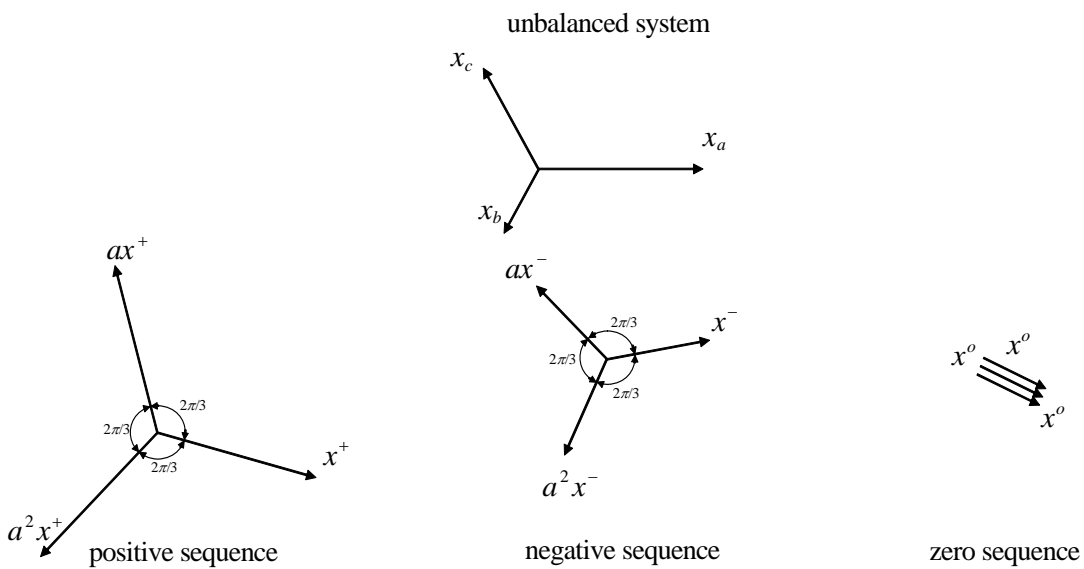


Fig. 7.2. Three phase unbalanced system decomposition.

It must be stressed that all sequences and the system considered above, are expressed in the theory of complexors used for steady state analysis of sinusoidal voltages and currents, as was initially enunciated by [64].

The three phase systems considered in this analysis assume a three wire connection system, i.e. not neutral point connection. This fact means that the sum of the currents will always be zero  $i_a + i_b + i_c = 0$ , consequently the zero sequence of the current will be zero as well. For this reason, the zero sequence of the voltages will be also zero ( $v_a + v_b + v_c = 0$ ).

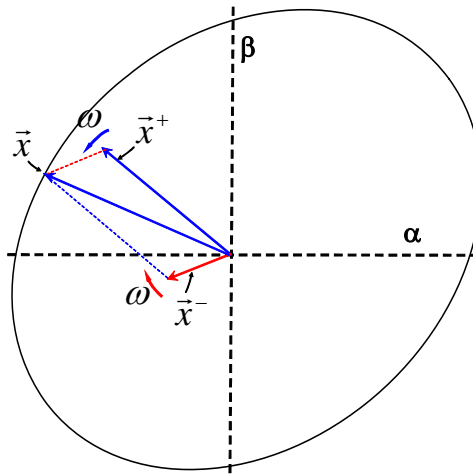


Fig. 7.3. Positive and negative space vector decomposition of the space vector representing an unbalanced system.

Related to this, by using the Clarke transformation given by the space vector theory introduced in Chapter 3:

$$\vec{x} = x_\alpha + j \cdot x_\beta = \frac{2}{3} (x_a + a \cdot x_b + a^2 \cdot x_c) \quad (7.2)$$

The unbalanced three phase system can be represented by a space vector  $\vec{x}$ , calculated from the addition of two space vectors  $\vec{x}^+$  and  $\vec{x}^-$ , rotating in opposite direction and same pulsation as depicted in Fig. 7.3.

$$\vec{x} = |\vec{x}^+| e^{j\omega t} + |\vec{x}^-| e^{-j\omega t} \quad (7.3)$$

Hence, the positive and the negative sequence space vectors describe circular trajectories, while the  $\vec{x}$  space vector will describe in general an ellipsoid trajectory. This analysis will be applied to the voltages and currents affecting to the system.

Once again, it must be emphasized that  $1, a, a^2$ , from equation (7.2) are spatial operators. Although these spatial operators are formally the same as the time operators from equation (7.1),

they should not be confused. From this point of view, it would be justifiable to use a different notation for these operators, but historically they have been introduced by using the same notation, which is therefore used throughout this chapter.

### 7.3 Model of the Doubly Fed Induction Machine under Unbalanced Voltage Grid Conditions

The doubly fed induction machine can be modeled with the following voltage and flux equations in the stator reference frame (section 3.2.2):

$$\vec{v}_s = R_s \vec{i}_s + \frac{d\vec{\Psi}_s}{dt} \quad (7.4)$$

$$\vec{v}_r = R_r \vec{i}_r + \frac{d\vec{\Psi}_r}{dt} - j\omega_m \vec{\Psi}_r \quad (7.5)$$

$$\vec{\Psi}_s = L_s \vec{i}_s + L_h \vec{i}_r \quad (7.6)$$

$$\vec{\Psi}_r = L_r \vec{i}_r + L_h \vec{i}_s \quad (7.7)$$

On the other hand, the electromagnetic torque and the stator active and reactive powers, can be calculated using the following equations:

$$T_{em} = \frac{3}{2} p \text{Im} \left\{ \vec{\Psi}_s^* \cdot \vec{i}_s \right\} = \frac{3}{2} p (\Psi_{s\alpha} i_{s\beta} - \Psi_{s\beta} i_{s\alpha}) \quad (7.8)$$

$$P_s = \frac{3}{2} \text{Re} \left\{ \vec{v}_s^* \cdot \vec{i}_s^* \right\} = \frac{3}{2} (v_{s\alpha} i_{s\alpha} + v_{s\beta} i_{s\beta}) \quad (7.9)$$

$$Q_s = \frac{3}{2} \text{Im} \left\{ \vec{v}_s^* \cdot \vec{i}_s^* \right\} = \frac{3}{2} (v_{s\beta} i_{s\alpha} - v_{s\alpha} i_{s\beta}) \quad (7.10)$$

Note that only three wires have been considered to feed the machine, implying that no zero current component will exist, as equivalently occurs with the grid model.

Note that since the stator voltage is unbalanced, all the space vectors represented in equations (7.4)-(7.10), could have positive and negative sequences. Hence, considering the positive and negative sequences, the following space vectors yields:

$$\vec{v}_s = v_{s\alpha} + j v_{s\beta} = (v_{s\alpha}^+ + v_{s\alpha}^-) + j(v_{s\beta}^+ + v_{s\beta}^-) \quad (7.11)$$

$$\vec{i}_s = i_{s\alpha} + j i_{s\beta} = (i_{s\alpha}^+ + i_{s\alpha}^-) + j(i_{s\beta}^+ + i_{s\beta}^-) \quad (7.12)$$

$$\vec{\Psi}_s = \Psi_{s\alpha} + j \Psi_{s\beta} = (\Psi_{s\alpha}^+ + \Psi_{s\alpha}^-) + j(\Psi_{s\beta}^+ + \Psi_{s\beta}^-) \quad (7.13)$$

Substituting expressions (7.11) and (7.12) in equations (7.9) and (7.10), the stator active and reactive power expressions as a function of the positive and negative sequences of the voltage and currents, yields:

$$P_s = \frac{3}{2}(A_{s\_P} + B_{s\_P} + C_{s\_P} + D_{s\_P}) \quad (7.14)$$

$$Q_s = \frac{3}{2}(A_{s\_Q} + B_{s\_Q} + C_{s\_Q} + D_{s\_Q}) \quad (7.15)$$

$$A_{s\_P} = v_{s\alpha}^+ i_{s\alpha}^+ + v_{s\beta}^+ i_{s\beta}^+ \quad (7.16)$$

$$B_{s\_P} = v_{s\alpha}^- i_{s\alpha}^- + v_{s\beta}^- i_{s\beta}^- \quad (7.17)$$

$$C_{s\_P} = v_{s\alpha}^+ i_{s\alpha}^- + v_{s\beta}^+ i_{s\beta}^- \quad (7.18)$$

$$D_{s\_P} = v_{s\alpha}^- i_{s\alpha}^+ + v_{s\beta}^- i_{s\beta}^+ \quad (7.19)$$

$$A_{s\_Q} = v_{s\beta}^+ i_{s\alpha}^+ - v_{s\alpha}^+ i_{s\beta}^+ \quad (7.20)$$

$$B_{s_Q} = v_{s\beta}^- i_{s\alpha}^- - v_{s\alpha}^- i_{s\beta}^- \quad (7.21)$$

$$C_{s_Q} = v_{s\beta}^+ i_{s\alpha}^- - v_{s\alpha}^+ i_{s\beta}^- \quad (7.22)$$

$$D_{s_Q} = v_{s\beta}^- i_{s\alpha}^+ - v_{s\alpha}^- i_{s\beta}^+ \quad (7.23)$$

Terms,  $A_{s_P}$ ,  $B_{s_P}$ ,  $A_{s_Q}$  and  $B_{s_Q}$  are constant terms at steady state, since they are composed by the same sequence product. However, terms  $C_{s_P}$ ,  $D_{s_P}$ ,  $C_{s_Q}$  and  $D_{s_Q}$  oscillate at  $2\omega_s$  pulsation, since they are composed by positive and negative sequence products.

Similarly, substituting the positive and negative sequence components of the stator current and flux, from expression (7.8) the torque yields:

$$\begin{aligned} T_{em} = & \frac{3}{2} p \left[ (\Psi_{s\alpha}^+ i_{s\beta}^+ - \Psi_{s\beta}^+ i_{s\alpha}^+) + (\Psi_{s\alpha}^- i_{s\beta}^- - \Psi_{s\beta}^- i_{s\alpha}^-) \right. \\ & \left. + (\Psi_{s\alpha}^+ i_{s\beta}^- - \Psi_{s\beta}^+ i_{s\alpha}^-) + (\Psi_{s\alpha}^- i_{s\beta}^+ - \Psi_{s\beta}^- i_{s\alpha}^+) \right] \end{aligned} \quad (7.24)$$

In order to remove the stator flux from this last expression, by using equations (7.4) and (7.10)-(7.12), the following relations can be derived:

$$\frac{d\vec{\Psi}_s^+}{dt} = \vec{v}_s^+ - R_s \vec{i}_s^+ \quad (7.25)$$

$$\frac{d\vec{\Psi}_s^-}{dt} = \vec{v}_s^- - R_s \vec{i}_s^- \quad (7.26)$$

At steady state, for positive and negative sequences, these last two expressions hold (Fig. 7.4):

$$-\omega_s \Psi_{s\beta}^+ = v_{s\alpha}^+ - R_s i_{s\alpha}^+ \quad (7.27)$$

$$\omega_s \Psi_{s\alpha}^+ = v_{s\beta}^+ - R_s i_{s\beta}^+ \quad (7.28)$$

$$-\omega_s \Psi_{s\alpha}^- = v_{s\beta}^- - R_s i_{s\beta}^- \quad (7.29)$$

$$\omega_s \Psi_{s\beta}^- = v_{s\alpha}^- - R_s i_{s\alpha}^- \quad (7.30)$$

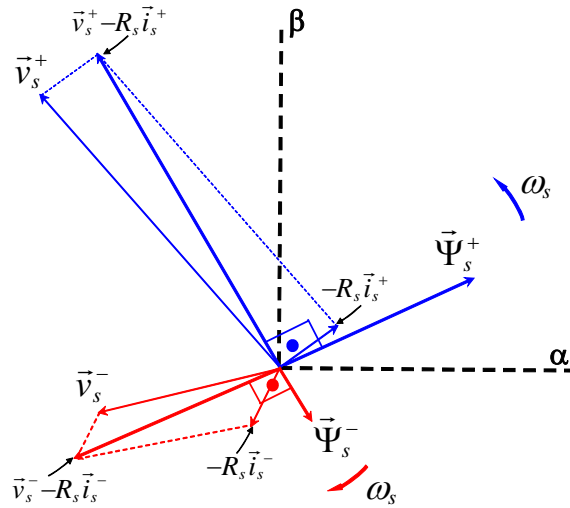


Fig. 7.4. Relation between stator voltage, current and flux space vectors.

Consequently, by substituting equations (7.27)-(7.30) into the torque expression (7.8), the torque can be expressed as:

$$T_{em} = \frac{3}{2} p \frac{1}{\omega_s} (A_{s\_P} - B_{s\_P} + C_{s\_P} - D_{s\_P} + E_{s\_T}) \quad (7.31)$$

with constant term  $E_{s\_T}$ :

$$E_{s\_T} = R_s (|\vec{i}_s^-|^2 - |\vec{i}_s^+|^2) \quad (7.32)$$

Note that when the stator current positive sequence is greater than the negative sequence, the  $E_{s\_T}$  term will produce less electromagnetic torque.

In addition, as can be observed from equations (7.31) and (7.14), the stator active power and the electromagnetic torque are closely related since they share four common terms, i.e.  $A_{s\_P}$ ,  $B_{s\_P}$ ,  $C_{s\_P}$  and  $D_{s\_P}$ . This fact will be exploited later, in order to improve the control performance under unbalanced grid conditions.

## 7.4 Control of the Doubly Fed Induction Machine under Unbalanced Voltage Grid Conditions

As depicted in Fig. 7.1, the control strategy for the DFIM is divided into two different general blocks. The first block performs a DPC technique, which as stated at the beginning of the chapter, controls directly the stator active and reactive power.

After that, the second block performs the required stator power references to deal with the problems generated by the grid voltage unbalance, i.e. electromagnetic torque oscillations and non-sinusoidal stator currents. Hence, with the easy combination of a standard DPC control solution and proper but simple reference generation strategy, wind turbines based on the DFIM will present an improved behavior, which could yield to avoid the necessity of disconnection from the grid.

### 7.4.1 Direct Power Control (DPC)

In order to focus all the study, on the reference generation strategy required to solve the distorted voltage grid operation conditions, the DPC technique employed in this situation will be an easy version of the DPC technique presented in Chapter 5. The control block diagram of the DPC is shown in Fig. 7.5. From the stator active and reactive powers, it is in charge to calculate the pulses for the IGBTs of the two level converter. It is divided into 5 different tasks, represented as 5 different blocks.

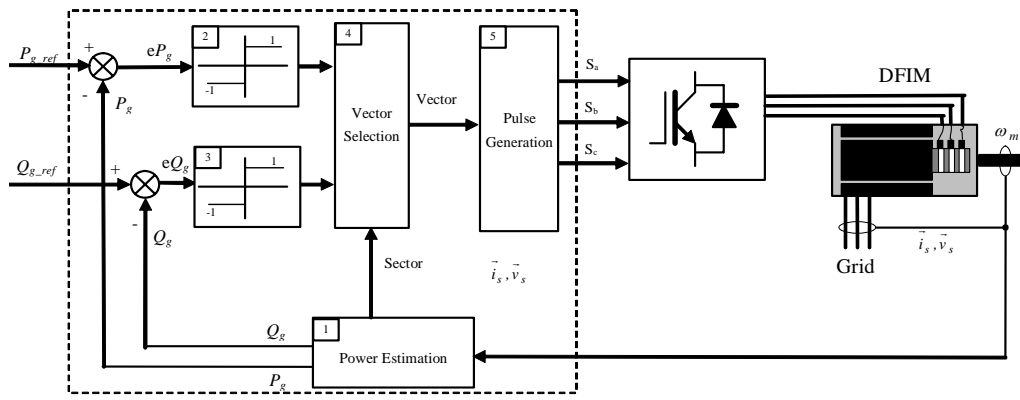


Fig. 7.5. Rotor side DPC block diagram.

In the first block the stator active and reactive powers are calculated, as well as the location of the rotor flux space vector, i.e. the sector. Hence, depending on the position of the rotor flux space vector, the two level converter vectors will produce different active and reactive powers evolutions, as graphically represented in Fig. 7.6.

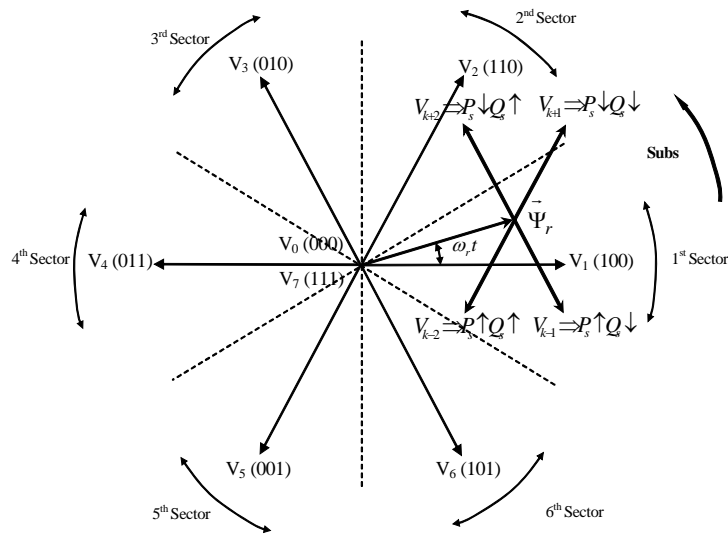


Fig. 7.6. Voltage vectors and their effect on the stator active and reactive power.

After that, the stator active and reactive power references are compared with their estimated values, so the stator power errors are obtained. In this simplified DPC strategy, only one active vector will be used to correct the stator power errors. During the sample period  $h$ , the same active vector will be employed, producing the stator active and reactive power evolutions shown in Fig. 7.7. Note that in this case, non-constant switching frequency behavior will be achieved and the zero vector never is used.

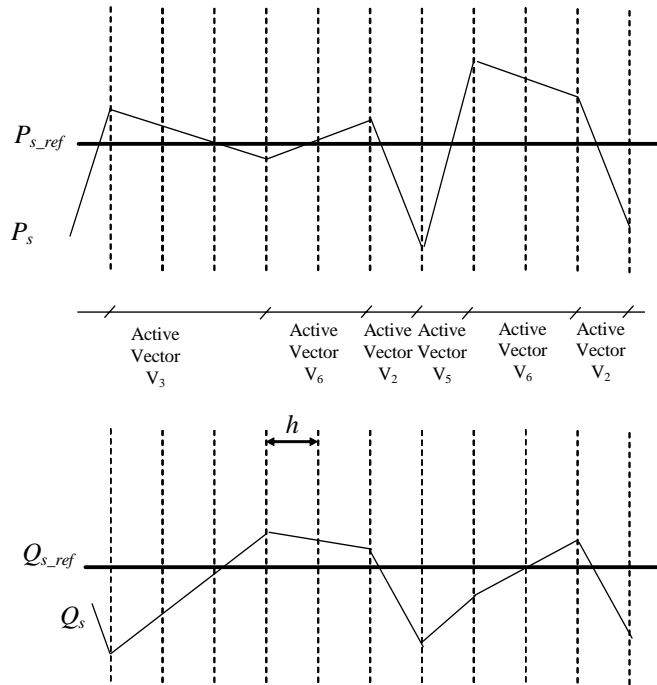


Fig. 7.7. Steady state active and reactive power waveforms in sector 1.

The active voltage vector choice is based on a look-up table mapped by the output of two ON-OFF comparators without hysteresis bands. These tasks are accomplished in blocks 2, 3 and 4 of Fig. 7.5. The look-up table is made up according to TABLE 7.I.

TABLE 7.I  
ACTIVE VECTOR SELECTION AS A FUNCTION OF THE STATOR ACTIVE AND REACTIVE POWER  
ON-OFF CONTROLLERS' OUTPUTS (K = SECTOR)

		$eP_s$	
		1	-1
$eQ_s$	1	$V_{(k-2)}$	$V_{(k+2)}$
	-1	$V_{(k-1)}$	$V_{(k+1)}$

Once the active vector is selected, as mentioned before, during the whole sample period  $h$  is introduced. Block 5 of Fig. 7.5 creates de pulses for the IGBTs of the converter. Consequently, by means of this simple control strategy is possible to directly control both active and reactive powers exchanged with the grid.

#### 7.4.2 Stator Current Negative Sequence Cancellation Strategy

In this subsection, the first version of stator power generation strategy will be analyzed. It is a commonly used strategy already employed by authors such as [28] for the DFIM, or equivalently by some other authors [62], [63] in grid connected converter applications.

According to expressions (7.14) and (7.15), if constant stator active and reactive power references are commanded, since the stator voltage is unbalanced, necessarily the stator currents will present positive and negative sequences as well.

Hence, in the first case study, the required stator active and reactive power references are derived, in order to achieve balanced stator currents, i.e. negative stator current sequence cancellation.

Hence, for given active and reactive power references ( $P_{s\_required}$ ,  $Q_{s\_required}$ ), if  $D_{s\_P}$  and  $D_{s\_Q}$  terms are added as follows:

$$P_{s\_ref} = P_{s\_required} + \frac{3}{2} \cdot D_{s\_P} \quad (7.33)$$

$$Q_{s\_ref} = Q_{s\_required} + \frac{3}{2} D_{s\_Q} \quad (7.34)$$

The DPC control will produce stator active and reactive powers according to equations (7.33) and (7.34). By equaling expression (7.14), (7.15) and (7.33), (7.34), the constant terms yield:

$$P_{s\_required} = \frac{3}{2} (A_{s\_P} + B_{s\_P}) \quad (7.35)$$

$$Q_{s\_required} = \frac{3}{2} (A_{s\_Q} + B_{s\_Q}) \quad (7.36)$$

While the oscillatory terms yield:

$$C_{s\_P} = C_{s\_Q} = 0 \quad (7.37)$$

This last expression, by using equations (7.18) and (7.28), generates the following system of two equations:

$$0 = v_{s\alpha}^+ i_{s\alpha}^- + v_{s\beta}^+ i_{s\beta}^- \quad (7.38)$$

$$0 = v_{s\beta}^+ i_{s\alpha}^- - v_{s\alpha}^+ i_{s\beta}^- \quad (7.39)$$

Which solution necessarily holds:

$$0 = i_{s\alpha}^- = i_{s\beta}^- \quad (7.40)$$

This fact produces that the stator currents interchanged with the grid will be balanced, due to the absence of the negative sequence currents. However, substituting the expression (7.37) in the electromagnetic torque equation (7.31):

$$T_{em} = \frac{3}{2} p \frac{1}{\omega_s} (A_{s\_P} - B_{s\_P} - D_{s\_P} + E_{s\_T}) \quad (7.41)$$

Concludes proving that the electromagnetic torque will not be constant, because the term  $D_{s\_P}$  is not cancelled.

Consequently, as shown in this analysis, the addition of the oscillatory terms  $D_{s\_P}$  and  $D_{s\_Q}$  to the stator power references, produces negative sequence cancellation of the stator currents. On the contrary, it does not cancel the electromagnetic torque oscillations due to the unbalanced grid voltage.

This control performance in general will not be accepted, because the torque oscillations could provoke additional stresses to the mechanical system, especially for higher unbalanced voltage conditions. In the next subsection, the reference generation strategy will be modified, in order to strictly cancel the electromagnetic torque oscillations.

### 7.4.3 Torque Oscillations Cancellation Strategy

By deep analysis of expression (7.18) and (7.19), in order to cancel the electromagnetic torque oscillations, since  $C_{s\_P}$  and  $D_{s\_P}$  depend on both positive and negative stator currents sequences, it is impossible to make zero both oscillating terms at the same time, because it will require zero stator currents imposition. Thus, the only manner to achieve constant electromagnetic torque under unbalanced grid voltage conditions, will be imposing:

$$C_{s\_P} = D_{s\_P} \quad (7.42)$$

This imposition, for a given voltage unbalance, in general will not make zero neither the positive nor the negative sequences of the stator currents. However, for a given active power reference ( $P_{s\_required}$ ), if an oscillating term obtained from the electromagnetic torque and stator power is added as follows (see Fig 7.8):

$$P_{s\_ref} = P_{s\_required} + \left( P_s - \frac{\omega_s}{p} \cdot T_{em} \right) \quad (7.43)$$

Substituting into expression (7.43), the equations (7.14) and (7.31), the stator active power reference expression yields:

$$P_{s\_ref} = P_{s\_required} + \frac{3}{2}(2B_{s\_P} + 2D_{s\_P} + E_{s\_T}) \quad (7.44)$$

Again, this last expression is equal to equation (7.14), thus the oscillating terms yields:

$$C_{s\_P} + D_{s\_P} = 2D_{s\_P} \quad (7.45)$$

What means that with this expression, the condition to cancel the torque oscillations has been obtained.

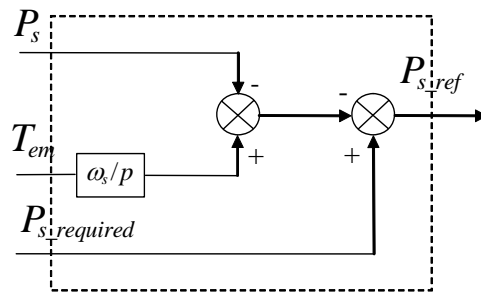


Fig. 7.8. Stator active power generation strategy.

Note that with this reference generation strategy, positive and negative sequence calculations are not needed to avoid the electromagnetic torque oscillations, therefore, the implementation simplicity of the strategy is highly improved.

In addition, as will be later shown in the simulation results, since the stator current unbalance obtained with this power generation strategy is equal to the stator voltage unbalance, the stator currents interchanged with the grid will be unbalanced as well, but sinusoidal.

## 7.5 Control of the Grid Side Converter under Unbalanced Voltage Grid Conditions

In general, in a DFIM based wind turbine [6], the grid side converter is used to control the DC bus voltage ( $V_{bus}$ ) of the back to back converter and the reactive power exchanged thorough this converter to the grid  $Q_g$ . As shown in Fig 7.1, in this research this objective is achieved by means of a DPC method, with references  $P_{g\_ref}$  and  $Q_{g\_ref}$ . However, as required in the rotor side converter, in order to avoid the problems generated by the grid voltage unbalance, a special reference generation strategy will be implemented.

In fact, as shown by several authors [62]-[63], if no special efforts are made, the active power exchanged by the grid side converter  $P_g$  will be polluted by non desired currents harmonics. This is due to presence of the positive and negative sequence components of the currents exchanged with the grid ( $i_{g\_abc}$ ). Hence, by applying the same analysis of subsection 7.4.2 to this side of the converter, it is possible to eliminate the negative sequence component of the grid side converter currents, exchanging balanced and sinusoidal currents, by only adding two oscillating terms to the active and reactive power references.

Added to this, with this unbalanced grid voltage scenario, there is a new challenge that must be considered in DFIM based wind turbines. Since the rotor active power exchanged through the rotor of the machine, can be calculated according to the following expression:

$$P_r = \frac{3}{2} \operatorname{Re} \left\{ \vec{v}_r \cdot \vec{i}_r^* \right\} = \frac{3}{2} (v_{r\alpha} i_{r\alpha} + v_{r\beta} i_{r\beta}) \quad (7.46)$$

Combining this expression with equations (7.4)-(7.9), it is possible to derive the following approximated relation between the stator and rotor active powers:

$$P_r \approx -s P_s \quad (7.47)$$

With  $s$  the slip, calculated as follows:

$$s = \frac{\omega_s - \omega_r}{\omega_s} \quad (7.48)$$

Hence, the stator active power oscillations of expression (7.44), required to achieve constant torque and sinusoidal stator currents, will be instantaneously propagated through the

rotor of the machine as a function of the mechanical speed, according to expression (7.47). This fact will demand additional control efforts that will be analyzed in the following subsections.

### 7.5.1 Direct Power Control (DPC) of the Grid Side Converter

In this case again, as done with the rotor side control strategy, the active and reactive power exchanged with the grid will be directly controlled by means of a simple DPC technique. Thus, the grid side converter active and reactive powers can be calculated by the following well known expressions:

$$P_g = \frac{3}{2} \operatorname{Re} \left\{ \vec{v}_s \cdot \vec{i}_g^* \right\} = \frac{3}{2} (v_{s\alpha} i_{g\alpha} + v_{s\beta} i_{g\beta}) \quad (7.49)$$

$$Q_g = \frac{3}{2} \operatorname{Im} \left\{ \vec{v}_s \cdot \vec{i}_g^* \right\} = \frac{3}{2} (v_{s\beta} i_{g\alpha} - v_{s\alpha} i_{g\beta}) \quad (7.50)$$

The control block diagram is depicted in Fig. 7.9. It can be noticed that exactly the same structure of block diagram from Fig. 7.5, is employed. The active and reactive power of the power exchanged with the grid is calculated in block 1. In addition, the sector where the stator voltage space vector is located is estimated as well.

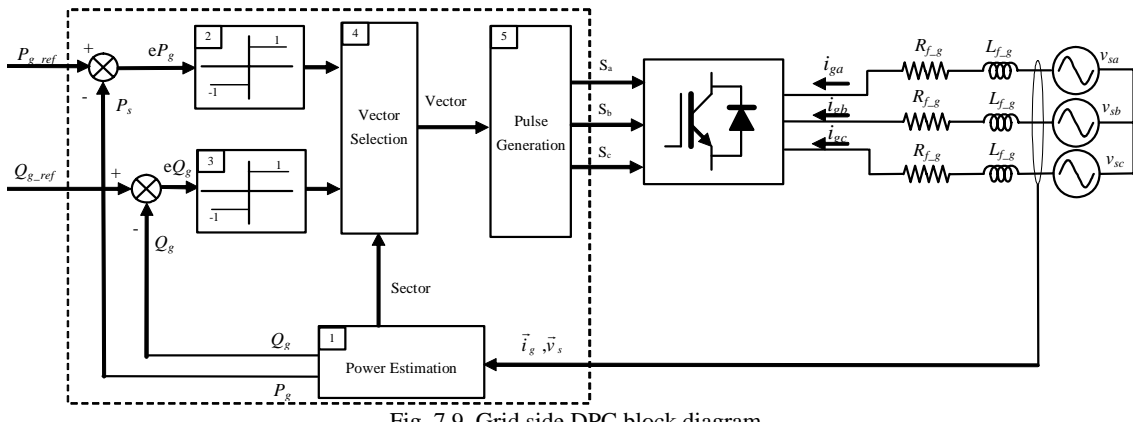


Fig. 7.9. Grid side DPC block diagram.

Then, the active and reactive power errors are introduced to the ON-OFF controllers represented by block 2 and 3. In order to correct the power errors, one active vector will be introduced from the two level converter. The look-up table is served in Table 7.II, and as can be noticed, is equal to the one used for the rotor side DPC control (Table 7.I). It must be stressed that

in this case, the sector that maps the look-up table is defined by the stator voltage as graphically illustrates Fig. 7.10.

TABLE 7.II  
ACTIVE VECTOR SELECTION AS A FUNCTION OF THE STATOR ACTIVE AND REACTIVE POWER  
ON-OFF CONTROLLERS' OUTPUTS (K = SECTOR)

	$eP_g$	
	1	-1
$eQ_g$	$V_{(k-2)}$	$V_{(k+2)}$
	$V_{(k-1)}$	$V_{(k+1)}$

Finally, once the active vector is selected, the fifth block of Fig. 7.9, will generate the corresponding pulses for the IGBTs of the two level converter. Consequently, once again by means of this simple control strategy, it is possible to directly control both active and reactive powers exchanged with the grid.

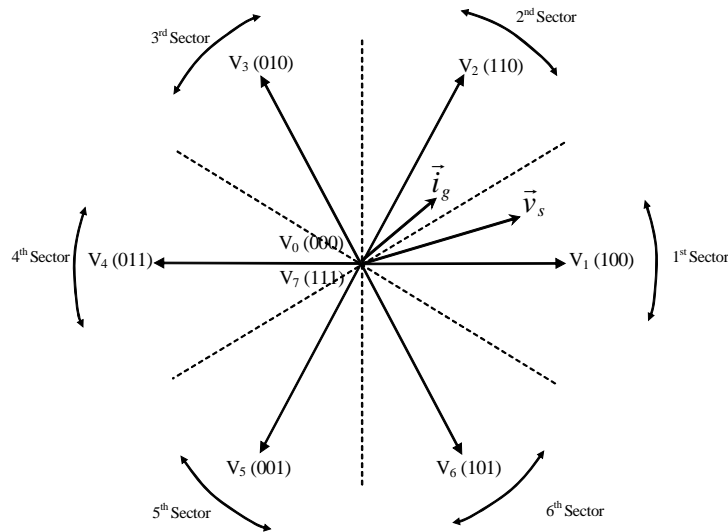


Fig. 7.10. Space vector diagram of the grid side converter.

### 7.5.2 Power References Generation Strategy. Negative Sequence Cancellation.

The proposed reference generation strategy is illustrated in Fig 7.11. Equivalent negative sequence current cancellation strategy of proposed in subsection 7.4.2 has been used. Note that in this case, the positive and negative sequences of  $i_g$  and  $v_s$  must be calculated, to achieve the oscillating terms  $D_{g\_P}$  and  $D_{g\_Q}$ :

$$D_{g\_P} = v_{s\alpha}^- i_{g\alpha}^+ + v_{s\beta}^- i_{g\beta}^+ \quad (7.51)$$

$$D_{g\_Q} = v_{s\beta}^- i_{g\alpha}^+ - v_{s\alpha}^- i_{g\beta}^+ \quad (7.52)$$

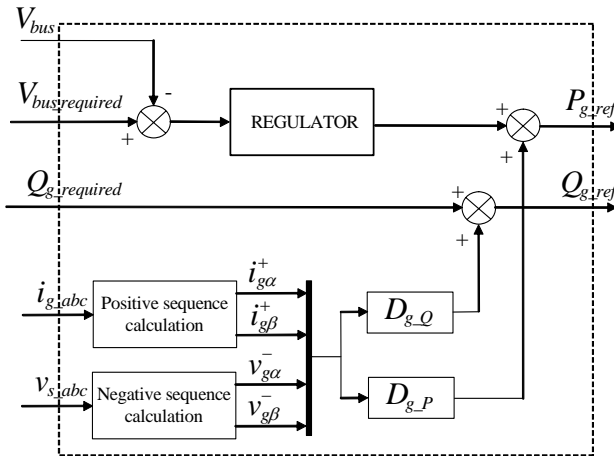


Fig. 7.11. Grid side converter active and reactive power generation strategy.

The main characteristics of this reference generation strategy are summarized as follows:

- 1.- The oscillating terms  $\frac{3}{2}D_{g\_P}$  and  $\frac{3}{2}D_{g\_Q}$ , must be the unique oscillations of the powers  $P_g$  and  $Q_g$ , in order to eliminate the zero sequence component of the exchanged currents  $i_g$ .
- 2.- The  $V_{bus}$  regulator, provides only the mean value of the exchanged active power  $P_g$ , i.e. the mean value of the transmitted rotor active power ( $P_r$ ) plus the active power losses of the back to back converter. For that purpose, it should be tuned with very smooth dynamic, otherwise, it will produce additional oscillations in  $P_g$  that will provoke a non proper cancellation of the negative sequence of the currents.
- 3.- The oscillations of the active power  $P_r$  due to the grid voltage unbalance, will directly appear in oscillations of the  $V_{bus}$  voltage value.

Consequently, by this control procedure is possible to address to main difficulties, unbalance voltage operation conditions, exchanging balanced currents with the grid when the active power exchanged through the rotor is oscillating.

## 7.6 Contribution to Balance the Grid Voltage Unbalance

Once it has been seen that at the same time is possible to eliminate the torque oscillations and exchange sinusoidal currents with the grid (sinusoidal stator currents and balanced grid side converter currents), the next task is to analyze how the generated total currents of the system affect to the unbalance of the grid voltage.

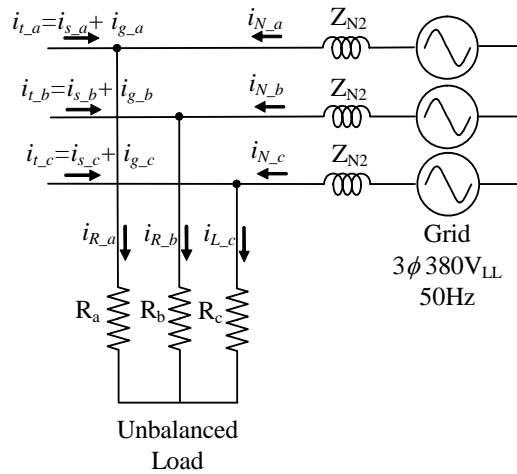


Fig. 7.12. Load node.

Hence, as shown in Fig 7.12, the current demanded by the unbalanced load will be provided partially by the DFIM system (grid side and stator side). Unfortunately, as will be later shown, the unbalance of the stator voltage is equivalent to the unbalance of the generated stator currents. This means that for example, for an unbalanced load with  $R_a \neq R_b = R_c$ , the stator currents will be as illustrated in Fig. 7.13. The grid side converter currents will be balanced, while the total current since in general the grid side converter only operates with 30% of the total power will be still unbalanced, not contributing to reduce the unbalance in the grid voltage.

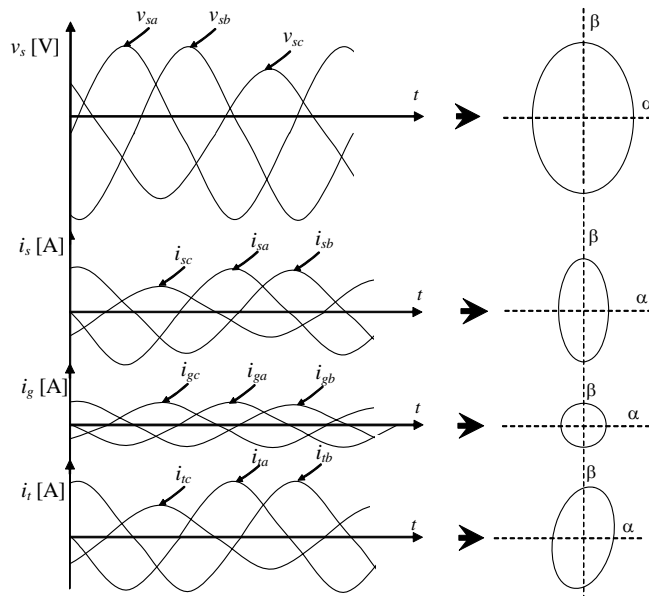


Fig. 7.13. Unbalanced grid voltage and generated stator currents, provoked by a load with  $R_a \neq R_b = R_c$  and torque oscillations cancellation strategy.

Consequently, although the proposed control strategy avoids the necessity to disconnect the wind turbine due to the elimination of the mechanical torque oscillations, only by the stator of the machine is not possible to contribute to palliate the unbalance of the grid.

## 7.7 Simulation Results

### 7.7.1 Unbalanced Voltage Situation

In this section, simulation results will be carried out in order to validate the control strategy proposed in this chapter. The simulated system presents the characteristics served in TABLES 7.III, and 7.IV:

TABLE 7.III  
BACK TO BACK CONVERTER

Rated power	5 kW
DC link Capacitance	0.005 F
Switching Frequency	
Grid Side Filter	
$R_f$	0.010 Ω
$L_f$	0.025 H

TABLE 7.IV  
ELECTRICAL GRID

Phase to phase Voltage	380 V
Network Impedance	
$R_N$	0.010 Ω
$L_N$	0.0045 H
Unbalanced Load	
$R_a$	1.5 Ω
$R_b$	3 Ω
$R_c$	3 Ω

In only one experiment, all proposed control strategies will be tested showing the performance of the system under unbalanced grid voltage conditions. The operation conditions are fixed as follows: the machine operates at 1000 rev/min of constant speed. It contributes with 7.5kW, 0VAR of stator active and reactive power to the load. Under these operation conditions, the active power consumed from the grid by the back to back converter is approximately 2.2kW. The reactive power  $Q_g$  at this point has been set to 0VAR. On the other hand, the DC link voltage is set to 700V.

The proposed different control strategies are commanded in four time intervals:

A.- First, the behavior of the system is shown, with the electromagnetic torque oscillations cancellation strategy together with the grid side converter current negative sequence cancellation strategy.

B.- Second, after 0.4 sec of simulation time, the negative sequence cancellation of the grid side currents strategy is disabled, performing constant  $P_g$  and  $Q_g$  references.

C.- Third, after 0.4sec of simulation time, the electromagnetic torque oscillations cancellation strategy is disabled, commanding constant reference values of  $P_s$ ,  $Q_s$ ,  $P_g$  and  $Q_g$ .

D.- Finally, after 0.4sec of simulation time, the strategy for negative sequence cancellation of the stator currents is enabled.

Hence, with the grid characteristics shown in Table 7.IV, the severe stator voltage unbalance shown in Fig. 7.14(a) is generated ( $v_{sa}=176V_{rms}|0^\circ|$ ,  $v_{sb}=220V_{rms}|-113^\circ|$ ,  $v_{sc}=220V_{rms}|+113^\circ|$ ). Since a three wire connection configuration is used, the zero sequence of the voltage does not appear.

With regards to the DFIM behavior, Fig. 9(c) and (d) show the reactive and active powers tracking performances, in order to achieve A, B, C and D control behaviors mentioned above. During intervals A and B, 100Hz oscillating active power references are set in order to eliminate the torque oscillations and get sinusoidal stator currents. This fact can be observed in Fig. 7.14 (b) and (f), the torque is maintained constant and the stator currents are unbalanced, but they are sinusoidal, until 1.42sec of the simulation. During these two intervals, the stator reactive power reference remains constant. After that, in interval C, both stator power references are kept constant, provoking torque oscillations and non sinusoidal stator currents as shown in Fig 7.14. (b) and (f). During the last interval D, 100Hz frequency oscillations are commanded to the stator active and reactive powers, producing balanced stator currents by a cancellation of the negative sequence. However, although the torque oscillations are slightly reduced they are still highly significant. In the whole experiment, the speed of the machine is externally maintained constant as shown in Fig. 7.14 (e).

With regards to the grid side converter behavior, Fig. 7.15 (a) shows the oscillating behavior of the DC bus voltage. The oscillation amplitude depends on the capacitors of the DC bus of the two level back to back converter, together with the transmitted rotor active power. The oscillating rotor active power transmitted trough the converter to the grid is presented in Fig. 7.15 (b). It can be noticed the oscillating performance of these two magnitudes during the four intervals. On the other hand, interval A performs 100Hz oscillating reactive and active powers, in order to achieve balanced grid side currents as illustrated in Fig. 7.15 (c)-(e). During the rest of the time, the power references are kept constant, provoking unbalanced grid side converter currents.

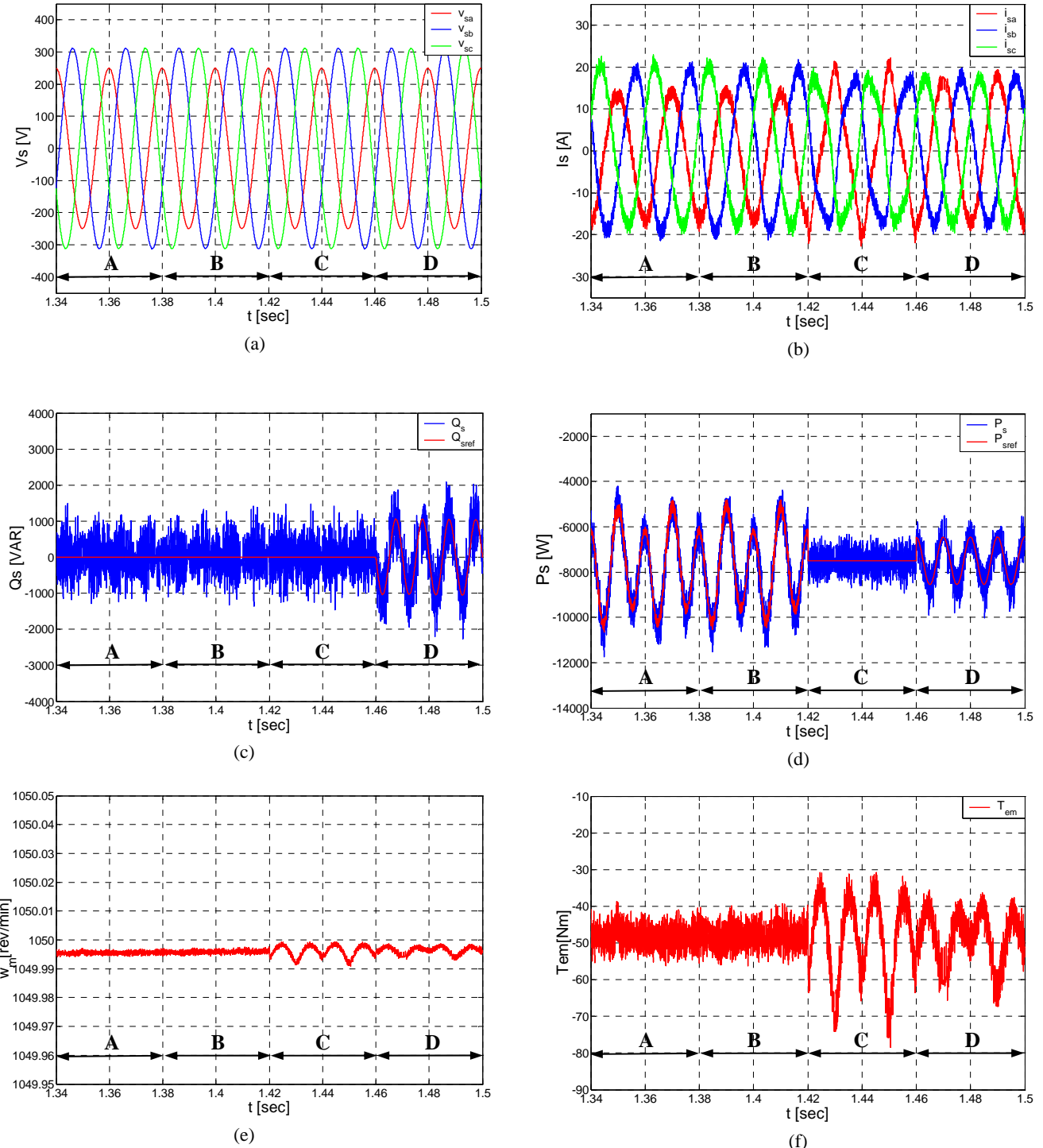


Fig. 7.14. Simulation results under different references generation strategies of the DFIM. (a) Stator voltages, (b) Stator currents, (c) Stator reactive power, (d) Stator active power, (e) Speed, (f) Electromagnetic Torque.

Finally, Fig. 7.16 (a) and (b) shows the  $\alpha$ - $\beta$  plots of the stator unbalanced voltage and the stator currents, in the four time intervals of the experiment. As expected, the three phase voltage unbalance of Fig. 7.14 (a) gives rise to ellipsoid voltage unbalance. According to the commanded reference generation strategies, the stator currents generated in time intervals A and B, result in

equivalent unbalance as the voltage unbalance, yielding to sinusoidal stator currents. On the other hand, constant stator active and reactive powers references of interval C, produce different unbalance to the voltage, producing non-sinusoidal stator currents. Alternatively, in interval D, the negative sequence elimination of the stator currents is performed producing balanced and sinusoidal stator currents.

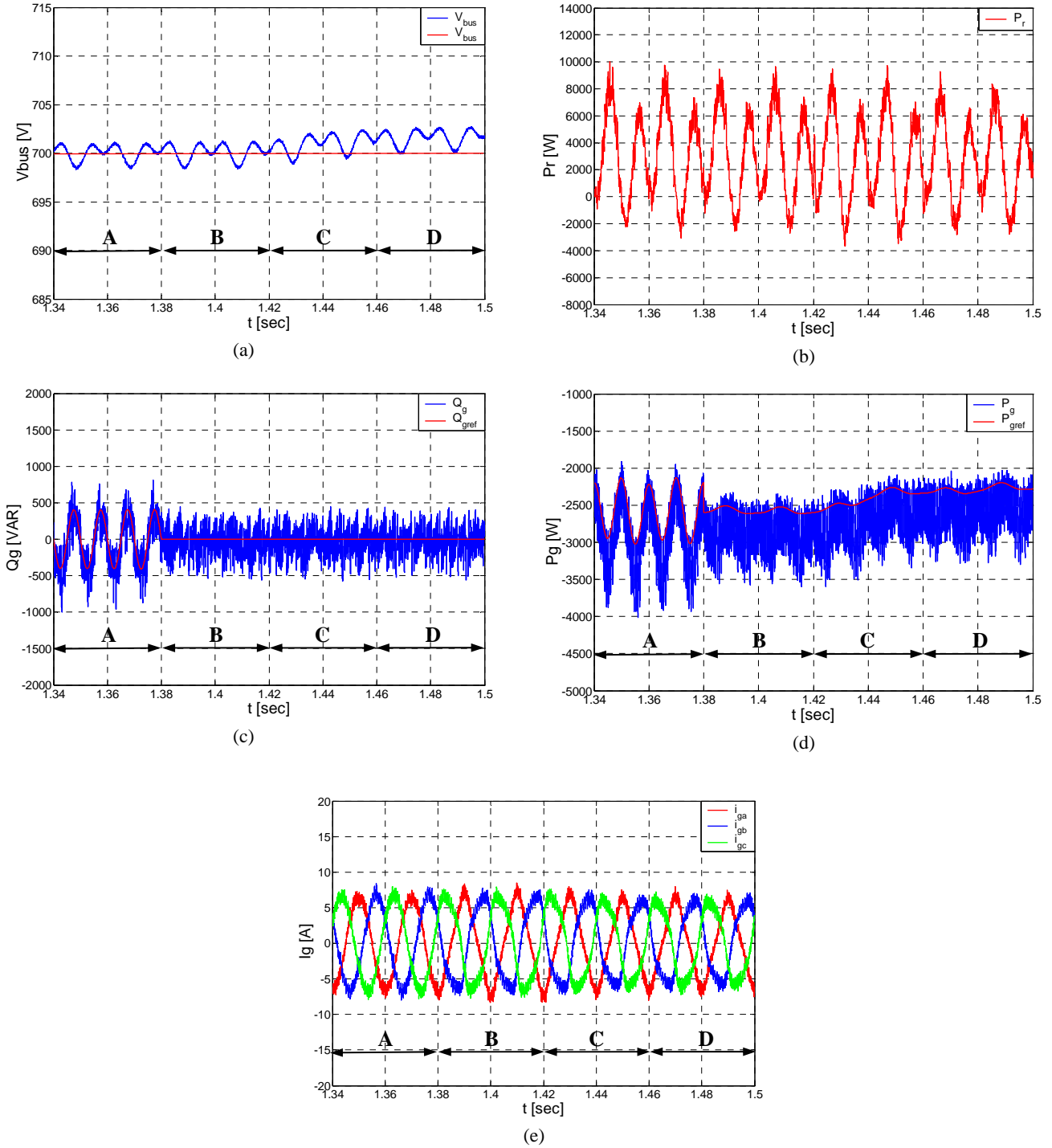


Fig. 7.15. Simulation results under different references generation strategies of the grid side converter. (a) DC bus voltage, (b) Rotor active power, (c) Grid side converter reactive power, (d) Grid side converter active power, (e) Grid side converter currents.

To conclude, Fig. 7.16 (c) and (d), show the unbalance relation between the stator and grid side converter currents, by using the  $\alpha$ - $\beta$  plots and at different grid side converter reactive powers references. Thus, as depicted in Fig. 7.16 (c) with zero reactive power reference  $Q_g$ , the grid side converter currents are smaller than the stator currents shortly, contributing to the total current balance. On the contrary, with greater  $Q_g$  reactive power contribution, the total wind turbine unbalance is mitigated as shown in Fig. 7.16 (d), still maintaining sinusoidal currents.

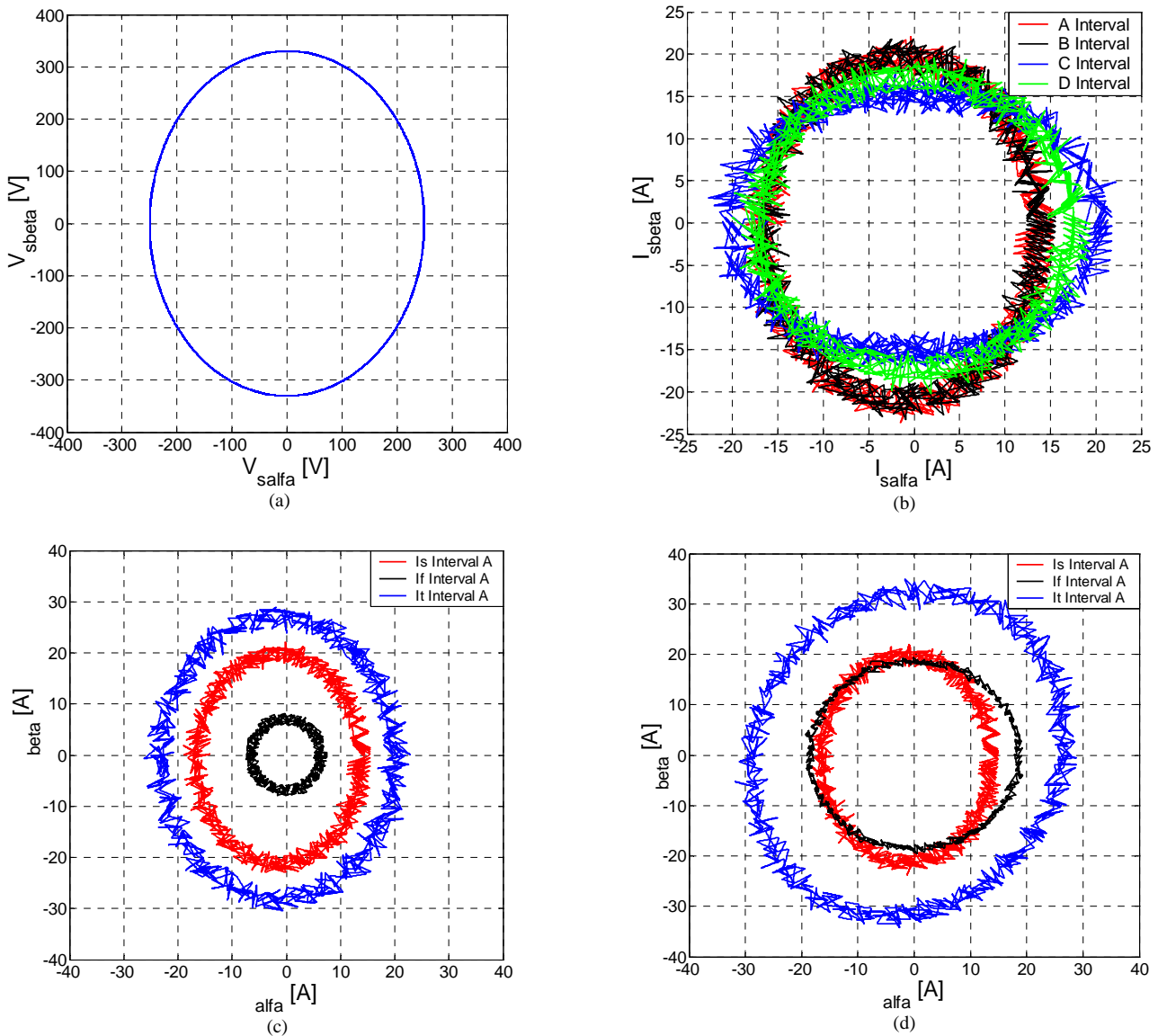


Fig. 7.16. Simulation results under different references generation strategies of the grid side converter. (a)  $\alpha$ - $\beta$  plot of the stator voltage, (b)  $\alpha$ - $\beta$  plot of the stator currents, (c)  $\alpha$ - $\beta$  plot of the stator, grid side converter and total currents ( $Q_g=0$ kVAR), (d)  $\alpha$ - $\beta$  plot of the stator, grid side converter and total currents, ( $Q_g=-7500$ kVAR).

### 7.7.2 Unbalanced Voltage Situation under Presence of Harmonics

In this subsection, the behavior of the system is studied under the presence of harmonics and unbalance at the same time. These two distortions of the grid will be produced by the electric system illustrated in Fig. 7.17. The unbalance is created by the presence of an unbalance load, while the harmonics are generated by the presence of a nonlinear rectifier load. The main characteristics of the system are summarized in TABLE 7.V.

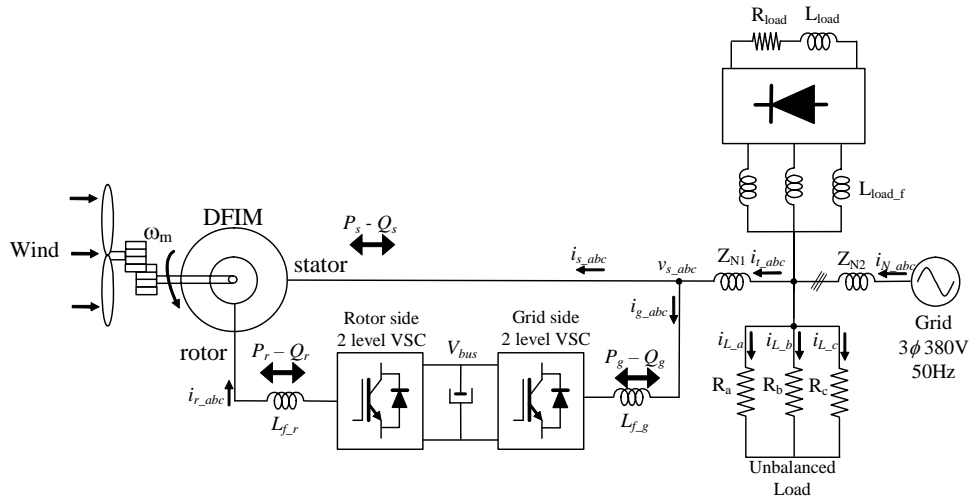


Fig. 7.17. Wind energy generation system under unbalanced grid and presence of harmonics.

In this simulation experiment, the addition of a non sinusoidal current consumption (rectifier) will produce that the voltage seen by the wind turbine ( $v_s$ ) is polluted by a wide range of harmonics. The operation conditions of the experiment are equal as the previous experiment (1000rev/min,  $P_s=7.5\text{kW}$ ,  $Q_s=0\text{kVAR}$ ,  $Q_g=0\text{kVAR}$ ,  $V_{bus}=700\text{V}$ ). Now lower voltage unbalance has been imposed ( $v_{sa}=210\text{V}_{peak} \angle 0^\circ$ ,  $v_{sb}=230\text{V}_{peak} \angle -117^\circ$ ,  $v_{sc}=230\text{V}_{peak} \angle +117^\circ$ ).

TABLE 7.V  
ELECTRICAL GRID

Phase to phase Voltage	380 V
Network Impedance	
$R_N$ ( $R_{N1}$ & $R_{N2}$ )	0.010 $\Omega$
$L_N$ ( $L_{N1}$ & $L_{N2}$ )	0.00025 H
Unbalanced and Nonlinear Loads	
$R_a$	2 $\Omega$
$R_b$	3 $\Omega$
$R_c$	3 $\Omega$
$L_{load}$	0.001 H
$R_{load}$	0.25 $\Omega$
$L_{load\_f}$	0.001 H

The experiment is divided into two different parts, focusing the analysis on the behavior of the doubly fed induction machine:

A.- In the first part, the electromagnetic torque oscillations cancellation strategy is commanded together with the grid side converter current negative sequence cancellation strategy.

B.- Then, the behavior of the system is shown when the electromagnetic torque oscillations cancellation strategy is disabled.

Fig.7.18 (a) shows the  $\alpha$ - $\beta$  plot of the stator voltage polluted by unbalance and by harmonics. Then, Fig.7.18 (b) and (c) illustrates the stator current  $\alpha$ - $\beta$  plots with and without cancellation strategy. It can be noticed that in both cases, as occurred in the previous simulation experiment, the stator currents are unbalanced but when the electromagnetic torque cancellation strategy is disabled, the current harmonics are much higher.

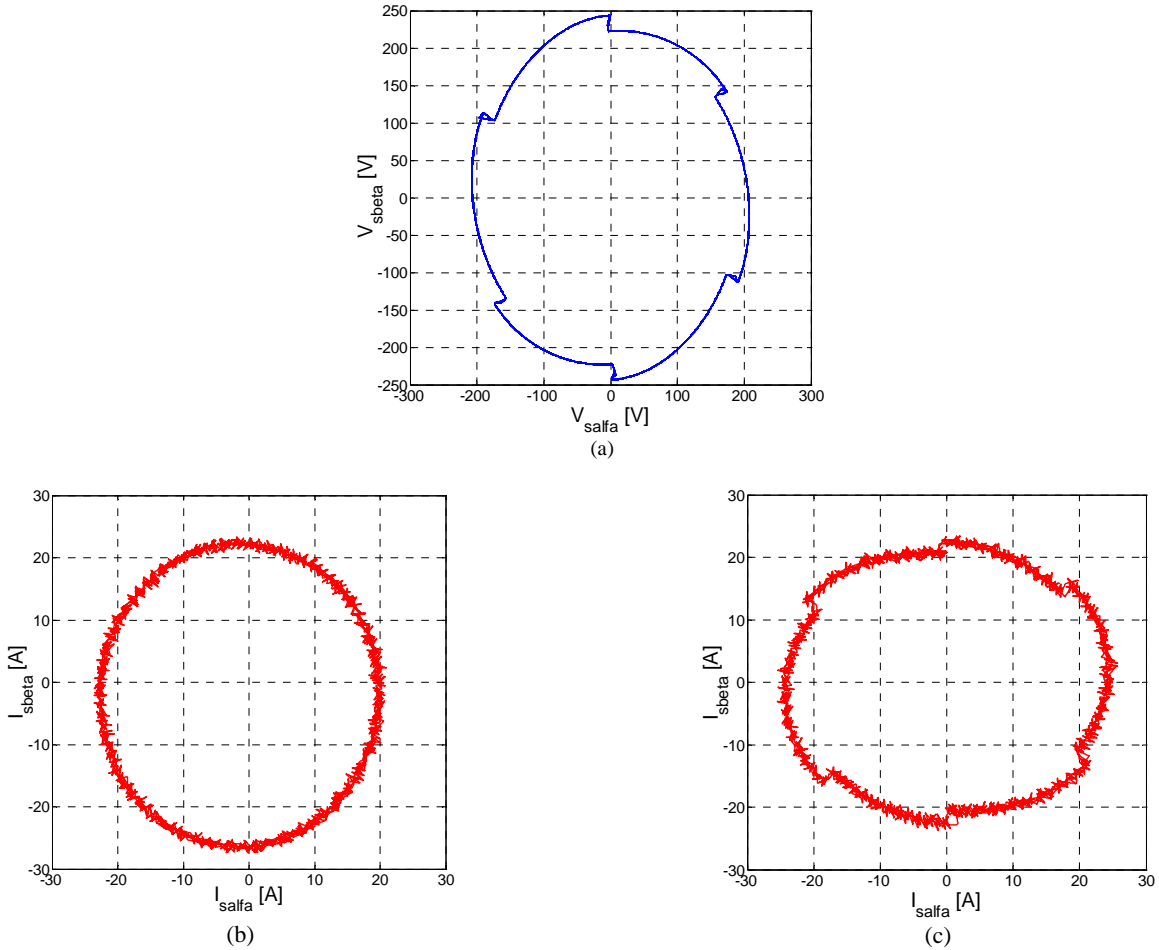


Fig. 7.18. (a)  $\alpha$ - $\beta$  plot of the stator voltage, (b)  $\alpha$ - $\beta$  plot of the stator current with compensation, (c)  $\alpha$ - $\beta$  plot of the stator current without compensation,

On the other hand, these unbalanced voltage and currents are also shown in time domain in Fig. 7.19 (a) and (b). Then, Fig. 7.19 (c) and (d) show the stator power references commanded in both intervals A and B. It can be noticed that under these distorted voltage conditions, the

oscillating stator active power reference is not only composed by 100Hz oscillations. Fig. 7.19 (e), demonstrates that when the cancellation strategy is enabled in interval A, the electromagnetic torque is maintained constant as it was desired, meanwhile in interval B, the oscillating behavior of the torque begins due to the stator voltage distortion.

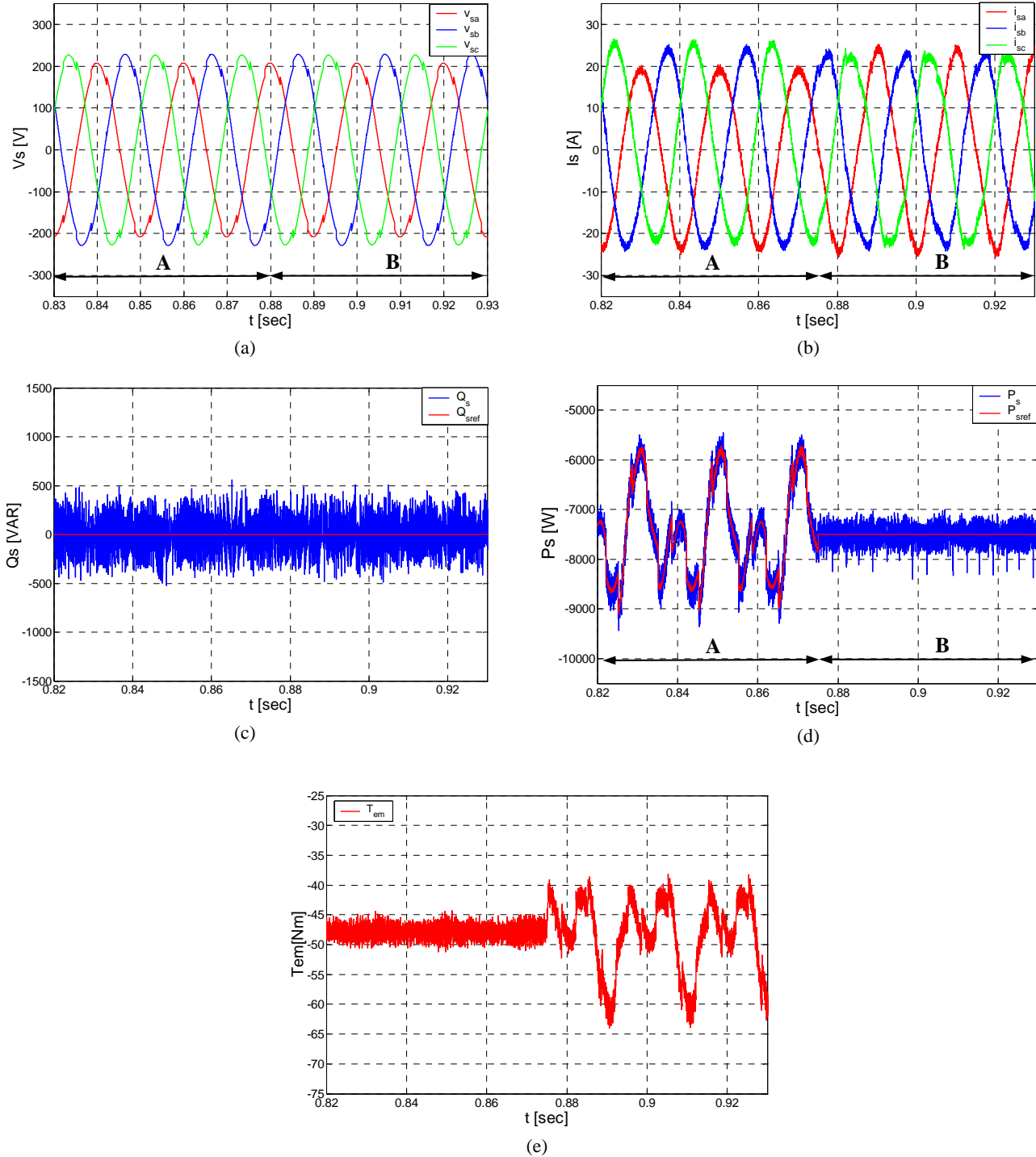


Fig. 7.19. Simulation results under different references generation strategies of the DFIM. (a) Stator voltages, (b) Stator currents, (c) Stator reactive power, (d) Stator active power, (e) Electromagnetic Torque.

Finally, Fig. 7.20 the grid side converter behaviour is shown under these operation conditions. It must be stressed that while it is able to eliminate the negative sequence of the current exchanging balanced currents with the grid, these currents are polluted by the same harmonics present in the voltage.

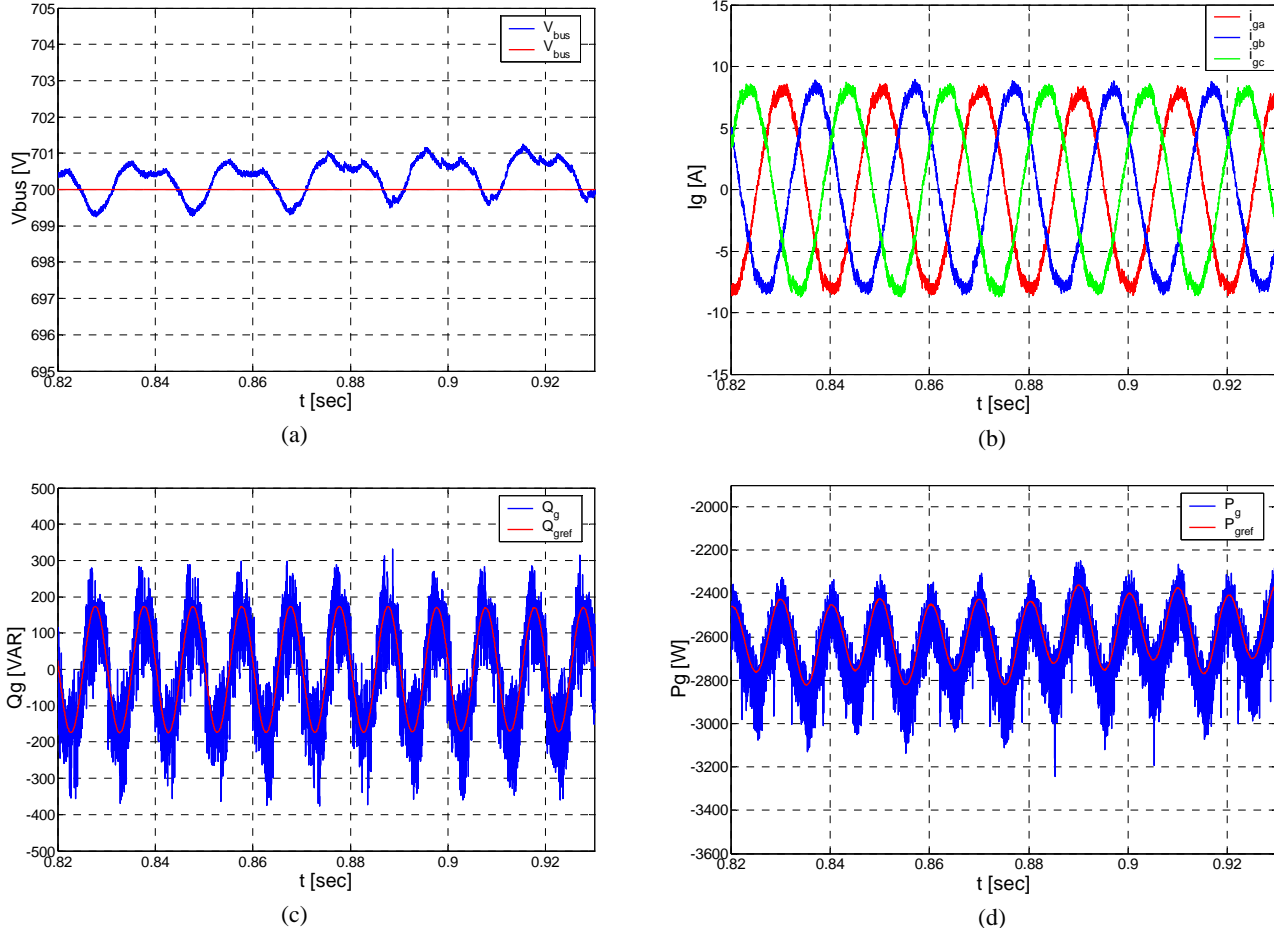


Fig. 7.20. Simulation results under different references generation strategies of the grid side converter. (a) DC bus voltage, (b) Grid side converter currents, (c) Grid side converter reactive power, (d) Grid side converter active power.

## 7.8 Conclusions of the Chapter

In this chapter, a new problem associated to DFIM based wind turbines has been addressed. Under unbalanced voltage grid operation conditions, it has been shown that a simple DPC technique accompanied by a proper active and reactive power reference generation strategy, can eliminate the electromagnetic torque oscillations interchanging sinusoidal currents with the grid.

After testing several reference generation strategies for the rotor side converter control, it has been concluded that the simplest solution performs the best results. Thus, by using an oscillating stator active reference, calculated from the torque estimation, provides electromagnetic torque oscillation elimination and sinusoidal stator current exchange, avoiding the necessity to perform a calculation of the positive and negative sequence components.

On the other hand, from the grid side converter point of view, in order to exchange balanced and sinusoidal currents with the grid, active and reactive power oscillating references have been generated from the positive and negative sequences of voltage and currents, combined with a low dynamic regulator for the DC bus voltage of the back to back VSC. Hence, part of the oscillating active power transmitted by the converter, is not delivered to the grid, provoking DC bus voltage oscillations that do not affect negatively to the system performance.

All this results have been validated by simulation experiments, demonstrating that the DPC techniques developed in previous chapters, can be easily adapted to avoid the difficulties of an unbalanced grid voltage scenario.

Finally, the control solutions developed for the unbalanced problem have also been tested in a more disturbed voltage grid scenario, including harmonics in the grid. It has been shown that the behavior of the system still avoids the electromagnetic torque oscillations, but it cannot eliminate the exchange of currents polluted by the same harmonics present in the grid voltage. In future research, more efforts should be made on this issue, in order to explore the capacity of this system to exchange currents not polluted by harmonics.



## **CONTENTS of Chapter 8**

8	Conclusions and Future Research.....	215
8.1	Contributions.....	215
8.2	Conclusions .....	216
8.3	Future Research.....	217
8.4	Publications .....	218
	References .....	219

# Chapter 8

## 8 Conclusions and Future Research

### 8.1 Contributions

The main scientific contributions of this thesis are:

#### Chapter 3

1. Development of a new dynamic model of the doubly fed induction machine, that considers the iron loss.

#### Chapter 4

2. Development of a new DTC control strategy for the doubly fed induction machine based on the two level converter.
3. Development of two new predictive DTC control strategies for the doubly fed induction machine at constant switching frequency based on the two level converter.

#### Chapter 6

4. Development of a new predictive DPC control strategy for the doubly fed induction machine at constant switching frequency based on the two level converter.

#### Chapter 6

5. Development of a new predictive DTC control strategy and a predictive DPC control strategy for the doubly fed induction machine at constant switching frequency based on the three level NPC converter.

#### Chapter 7

6. Development of a new reference generation strategy based on DPC control, for the doubly fed induction machine, that allows to eliminate electromagnetic torque oscillations exchanging sinusoidal currents with the grid, under unbalanced grid voltage operation conditions.

General contributions:

- State and demonstrate that using **three vectors** instead of two vectors in predictive direct control techniques, allows to operate at low constant switching frequencies.
- State and demonstrate that when low constant switching frequencies are required, **reducing ripples of both directly controlled variables** instead of only one, is critical to achieve the whole good performance of the machine.
- State and demonstrate that direct control techniques present a control structure that can be easily adapted, to address the difficulties generated by a faulty grid scenario.

## 8.2 Conclusions

In this thesis, predictive direct control of the doubly fed induction machine, for wind energy applications has been studied. Once the main contributions of the thesis have been summarized, it can be concluded this direct predictive control theory is very well suited for high power applications, particularly for high performance wind energy generation applications, since addresses several challenges associated to this field:

- It allows to operate in a closed loop system, at low and constant switching frequency.
- It presents the capacity to reduce the ripples of the directly controlled variables, allowing to obtain improved generated power quality.
- The fast dynamic response capacity of “classic” direct control techniques is achieved as well as a good tracking behavior.
- It can be implemented in several voltage source converter topologies such as, the classic two level VSC or the multilevel NPC voltage source converter.
- It can operate with high torque, power and current ripples, conditions that are common in some applications requiring low switching frequency.
- On the contrary, if improved power quality is required, it can consider an inductive filter as a part of the system, achieving good quality of the generated power at low switching frequency.
- It presents reasonably on-line implementation simplicity without the necessity to tune the controllers.

However, it also presents some remarkable drawbacks:

- As it is based on a predictive control method, it requires the knowledge of the model parameters.

- For the same reason, if this control technique is going to be implemented in a set of machines with a considerably high parameter uncertainty, steady state quality deterioration is expected that could be higher than in control techniques not based on model predictions.

- Since it directly controls two variables (torque and flux or active and reactive power), it allows to implement a simple reference generation strategy, in order to cope with performance deteriorations due to voltage grid distortions such as, voltage unbalance and voltage harmonics presence.

In addition, it is necessary to highlight the fact that from both proposed predictive DTC and DPC techniques, it has been observed that the DPC technique allows to achieve better steady state behavior rather the DTC technique.

Consequently, the achieved results demonstrate that these predictive direct control techniques could become an alternative solution to classical control methods in the field of high power applications.

### 8.3 Future Research

Once the proposed predictive direct control techniques have been successfully validated, the following challenges are considered suitable for future research:

- Validate with experimental results, the control strategies developed in Chapter 7, demonstrating the capacity of the system to operate under unbalanced grid voltage conditions.

- Take advantage of the quick dynamic response capacity of these proposed control techniques, in order to contribute to the **fault ride through** capability of the doubly fed induction machine based wind turbines.

- Again, take advance of the good performance capacity of these control techniques, in order to contribute to the grid voltage **harmonic correction** by the doubly fed induction machine based wind turbines. What means that it requires to explore the capacity of the wind energy generations system, to operate as an **active filter** as well.

## 8.4 Publications.

### Chapter 2:

1. G. Abad, M.A. Rodríguez., J. Poza, "High Power and Medium Voltage Wind Turbines based on Predictive Direct Control techniques", *EPE Wind Energy Chapter Seminar*, Delft 2008.

### Chapter 4:

2. G. Abad, M.A. Rodríguez., J. Poza, "Predictive Direct Torque Control of the Doubly Fed Induction Machine with Reduced Torque and Flux Ripples at Low Constant Switching Frequency", in *Conf. IECON*, Paris 2006.
3. G. Abad, M.A. Rodríguez., J. Poza, "Two Level VSC Based Predictive Direct Torque Control of the Doubly Fed Induction Machine with Reduced Torque and Flux Ripples at Low Constant Switching Frequency", *IEEE Trans. Pow. Electron*, vol. 23, no.3, May 2008.

### Chapter 5:

4. G. Abad, M.A. Rodríguez and J. Poza, "Predictive Direct Power Control of the Doubly Fed Induction Machine with Reduced Power Ripple at Low Constant Switching Frequency," in *Proc. IEEE ISIE'07 Conf.*, 2007.
5. G. Abad, M.A. Rodríguez and J. Poza, "Two Level VSC Based Predictive Direct Power Control of the Doubly Fed Induction Machine with Reduced Power Ripple at Low Constant Switching Frequency," *IEEE Trans. Ener. Conv.* vol. 23, no. 2, June 2008.

### Chapter 6:

6. G. Abad, M.A. Rodríguez and J. Poza, "Three Level NPC Converter Based Predictive Direct Power Control of the Doubly Fed Induction Machine at Low Constant Switching Frequency," *IEEE Trans. Ind. Elect.* 2008. (ACCEPTED)

## References

- [1] European Wind Energy Association, “www.ewea.org”
- [2] R. Teodorescu, P. Rodríguez, L. Helle, “Grid Requirements, Monitoring, Synchronization and Control of Wind Turbines under Grid Faults,” Tutorial in *ISIE'07, Conf.* 2007.
- [3] Blaabjerg, F. “Power Electronics in Renewable Energy Systems,” Tutorial in *SAAEI'06 Conf.* 2006.
- [4] A. D. Hansen, L. H. Hansen, “Wind Turbine Concept Market Penetration over 10 Years (1995–2004),” *Wind Energy*, pp. 81-97, 2007.
- [5] H. Polinder, F.F.A. Van der Pijl, G.J. de Vilder, P.J. Tavner, “Comparison of direct-drive and geared generator concepts for wind turbines,” *IEEE Trans. Energy. Conversion*, vol. 21, no.3, pp. 725-733, Sept. 2006.
- [6] R. Pena, J.C. Clare and G.M. Asher, “Doubly fed induction generator using back-to-back PWM converters and its application to variable-speed wind-energy generation,” *Proc. IEE. Elec. Power Appl.*, vol. 143, no. 3, pp. 231–241. May 1996.
- [7] Petersson. A., “Analysis, Modeling and Control of Doubly-Fed Induction Generators for Wind Turbines”, Ph.D. Chalmers University of Technology, Sweden 2003.
- [8] G. Poddar, V.T. Ranganathan, “Direct torque and frequency control of double-inverter-fed slip-ring induction motor drive,” *IEEE Trans. Ind. Elect.* vol. 51, no.6, pp. 1329-1337, Dec. 2004.
- [9] G. Poddar, V.T. Ranganathan, “Sensorless field-oriented control for double-inverter-fed wound-rotor induction motor drive,” *IEEE Trans. Ind. Elect.* vol. 51, no.5, pp. 1089-1096, Oct. 2004.
- [10] G. Poddar, V.T. Ranganathan, “Sensorless double-inverter-fed wound-rotor induction-Machine drive,” *IEEE Trans. Ind. Elect.* vol. 53, no.1, pp. 86-95, Feb. 2006.
- [11] F. Bonnet, P.E. Vidal, M. Pietrzak-David, “Dual Direct Torque Control of Doubly Fed Induction Machine,” *IEEE Trans. Ind. Elect.* vol. 54, no.5, pp. 2482-2490, Oct. 2007.
- [12] R.C. Portillo, M.M. Prats, J.I. Leon, J.A. Sanchez, J.M. Carrasco, E. Galvan, L.G. Franquelo, “Modeling Strategy for Back-to-Back Three-Level Converters Applied to High-Power Wind Turbines” *IEEE Trans. Ind. Elect.* vol. 53, no.5, pp. 1483 - 1491, Oct. 2006.
- [13] J.M. Carrasco, L.G. Franquelo, J.T. Bialasiewicz, E. Galvan, R.C. Portillo-Guisado, M.A.M. Prats, J.I. Leon, N. Moreno-Alfonso, “Power-Electronic Systems for the Grid Integration of Renewable Energy Sources: A Survey,” *IEEE Trans. Ind. Elect.* vol. 53, no.4, pp. 1002-1016, June 2006.
- [14] G. Abad, M. A. Rodríguez, G. Almundoz, U. Viscarret, “Validación experimental de los algoritmos para la integración en la red eléctrica de un aerogenerador de velocidad variable” in *Conf. SAAEI*, Toulouse, France, Sept. 2004.
- [15] S. Seman, J. Niiranen, S. Kanerva, A. Arkkio, J. Saitz, “Performance Study of a Doubly Fed Wind-Power Induction Generator Under Network Disturbances,” *IEEE Trans. Energy. Conversion*, vol. 21, no.4, pp. 883-890, Dec. 2006.
- [16] S. Seman, J. Niiranen, A. Arkkio, “Ride-Through Analysis of Doubly Fed Induction Wind-Power

- Generator Under Unsymmetrical Network Disturbance," *IEEE Trans. Power Syst.*, vol. 21, no.4, pp. 1782-1789, Nov. 2006.
- [17] A. Miller, E. Muljadi, D.S. Zinger, "A variable speed wind turbine power control," *IEEE Trans. Energy. Conversion*, vol. 12, no.2, pp. 181-186, June. 1997.
- [18] D.S. Zinger, E. Muljadi, "Annualized wind energy improvement using variable speeds," *IEEE Trans. Ind. Applic.*, vol. 33, no.6, pp. 1444-1447, Nov-Dec. 1997.
- [19] E. Muljadi and C. P. Butterfield, "Pitch-controlled variable-speed wind turbine generation," *IEEE Trans. Ind. Appl.*, vol. 37, no. 1, pp. 240–246, Jan-Feb. 2001.
- [20] A. D. Hansen, P. Sørensen, F. Iov, F. Blaabjerg, "Control of variable speed wind turbines with doubly-fed induction generators," *Wind Engineering*, vol. 28, no.4, pp. 411-434, 2004.
- [21] J. L. Rodriguez-Amenedo, S. Arnalte, J. C. Burgos, "Automatic generation control of a wind farm with variable speed wind turbines," *IEEE Trans. Energy. Conversion*, vol. 17, no.2, pp. 279 - 284, June. 2002.
- [22] A. D. Hansen, P. Sørensen, F. Iov, F. Blaabjerg, "Centralised power control of wind farm with doubly fed induction generators," *Renewable Energy*, no.31, pp. 935–951, 2006.
- [23] IEC 61400-21 Wind Turbine Generator Systems - Part 21: Measurement and Assessment of Power Quality Characteristics of Grid Connected Wind Turbines.
- [24] M. Zelechowski, "Space Vector Modulated-Direct Torque Controlled (DTC-SVM) Inverter-Fed Induction Motor Drive," *Ph. D. Thesis*, Warsaw, Poland, 2005.
- [25] D. Krug, S. Bernet, S.S. Fazel, K. Jalili, M. Malinowski, "Comparison of 2.3-kV Medium-Voltage Multilevel Converters for Industrial Medium-Voltage Drives," *IEEE Trans. Ind. Elect.* vol. 54, no.6, pp. 2979-2992, Dec. 2007.
- [26] J. Rodriguez, S. Bernet, W. Bin, J.O. Pontt, S. Kouro, "Multilevel Voltage-Source-Converter Topologies for Industrial Medium-Voltage Drives," *IEEE Trans. Ind. Elect.* vol. 54, no.6, pp. 2930-2945, Dec. 2007.
- [27] E. P. Wiechmann, P. Aqueveque, R. Burgos, J. Rodríguez, "On the Efficiency of Voltage Source and Current Source Inverters for High-Power Drives," *IEEE Trans. Ind. Elect.* vol. 55, no.4, pp. 1771-1782, April 2008.
- [28] L. Xu, "Coordinated Control of DFIG's Rotor and Grid Side Converters During Network Unbalance," *IEEE Trans. Power Electron.*, vol. 23, no. 3, pp. 1041 - 1049, May 2008.
- [29] M.P. Kazmierkowski, R. Krishnan, F. Blaabjerg, "Control in Power Electronics Selected Problems," Academic Press, 2002.
- [30] F. Blaschke, "A new method for the structural decoupling of A.C. induction machines," in *Conf. Rec. IFAC*, Dusseldorf, Germany, Oct.1971.
- [31] I. Takahashi and Y. Ohmori, "High-performance direct torque control of an induction motor," *IEEE Trans. Ind. Applicat.*, vol. 25, pp. 257-264, Mar./Apr. 1989.
- [32] M. Depenbrock, "Direct self-control (DSC) of inverter-fed induction machine," *IEEE Trans. Power Electron.*, vol. 3, pp. 420–429, Oct. 1988.
- [33] D. Casadei, F. Profumo, G. Serra and A. Tani, "FOC and DTC: two viable schemes for induction motors torque control," *IEEE Trans. Power Electron.*, vol. 17, no. 5, pp. 779-787, Sept. 2002.

- [34] E. Flach, R. Hoffmann, P. Mutschler, "Direct mean torque control of an induction motor," in *Proc. EPE'97 Conf.*, 1997.
- [35] Habetler, T.G.; Profumo, F.; Pastorelli, M.; Tolbert, L.M.; "Direct torque control of induction machines using space vector modulation", *IEEE Trans. Ind. Applicat.*, vol. 28, no. 5, Sept.-Oct. 1992.
- [36] D. Casadei, G. Serra, K. Tani, "Implementation of a direct control algorithm for induction motors based on discrete space vector modulation," *IEEE Trans. Power Electron.*, vol. 15, no. 4, pp. 769-777, July 2000.
- [37] J. K. Kang and S.K. Sul, "New direct torque control of induction motor for minimum torque ripple and constant switching frequency," *IEEE Trans. Ind. Applicat.*, vol. 35, no.5, pp. 1076-1086, Sept.-Oct. 1999.
- [38] K. B. Lee, J-H. Song, I. Choy and J-Y. Yoo, "Torque ripple reduction in DTC of induction motor driven by three-level inverter with low switching frequency," *IEEE Trans. Power Electron.*, vol. 17, no. 2, pp. 255-264, March 2002.
- [39] C.A. Martins, X. Roboam, T.A. Meynard, A.S. Carvalho, "Switching frequency imposition and ripple reduction in DTC drives by using a multilevel converter," *IEEE Trans. Power Electron.*, vol. 17, no. 2, pp. 286-297, March 2002.
- [40] J. Rodríguez, J. Pontt, S. Kouro, P. Correa, "Direct Torque Control With Imposed Switching Frequency in an 11-Level Cascaded Inverter," *IEEE Trans. Ind. Elect.*, Aug. 2004.
- [41] K. Hatua and V.T. Ranganathan, "Direct Torque Control Schemes for Split-Phase Induction Machine," *IEEE Trans. Ind. Applicat.*, vol. 41, no. 5, pp. 1243-1254, Sept.-Oct. 2005.
- [42] F. Morel, J.M. Retif, X. Lin-Shi, A.M. Llor, , "Fixed switching frequency hybrid control for a permanent magnet synchronous machine," in *Proc. IEEE ICIT'04 Conf.*, 2004.
- [43] M. Pacas and J. Weber, "Predictive direct torque control for the PM synchronous machine," *IEEE Trans. Ind. Electron.* vol. 52, no. 5, pp. 1350-1356, Oct. 2005.
- [44] I. Sarasola, J. Poza,, M.A. Rodríguez, G. Abad "Predictive Direct Torque Control of Brushless Doubly Fed Machine with Reduced Torque Ripple at Constant Switching Frequency," in *Proc. IEEE ISIE'07 Conf.*, 2007.
- [45] S. Chen and G. Joó, "Direct Power Control of Active Filters With Averaged Switching Frequency Regulation," in *Proc. IEEE PESC'04 Conf.*, 2004.
- [46] S. Aurtenechea, M.A. Rodríguez, E. Oyarbide and J. R. Torrealday, "Predictive Control Strategy for DC/AC Converters Based on Direct Power Control," *IEEE Trans. Ind. Electron.*, vol. 54, no. 3, June 2007.
- [47] S.A. Gomez, and J.L.R Amenedo, "Grid synchronization of doubly fed induction generators using direct torque control," in *Proc. IEEE IECON'02 Conf.*, 2002.
- [48] Datta, R. and V.T. Ranganathan, , "Direct power control of grid-connected wound rotor induction machine without rotor position sensors," *IEEE Trans. Power Electron.*, vol. 16, no. 3, pp. 390-399, May 2001.
- [49] L. Xu and P. Cartwright, "Direct Active and Reactive Power Control of DFIG for Wind Energy Generation," *IEEE Trans. Energy Conversion*, vol. 21, no.3, pp. 750-758, Sept. 2006.

- [50] A. Linder and R. Kennel, "Direct model Predictive Control-A new Direct Predictive Control Strategy for Electrical Drives," in *Proc. EPE'05 Conf.*, 2005.
- [51] Idris, N.R.N.; Yatim, A.H.M., "Direct torque control of induction machines with constant switching frequency and reduced torque ripple", *IEEE Trans. Ind. Electron.*, vol 51, 2004
- [52] S. Bernet, "State of the art and developments of medium voltage converters-an overview", *International Conference on PELINCEC*, 2005.
- [53] O. Alonso, "Análisis, diseño y control de convertidores multinivel de tipo NPC", Ph.D. UPNA., Spain, 2005
- [54] Revista Energía. Especial Energía eólica
- [55] [http://www.technologyreview.com/read\\_article.aspx?id=16801&ch=biztech](http://www.technologyreview.com/read_article.aspx?id=16801&ch=biztech)  
Tuesday, May 09, 2006
- [56] T. Gjengedal, "Wind Power Challenges and Opportunities," in *Conf. 1<sup>st</sup> Seminar on Wind Energy*, Delft, Feb. 2008.
- [57] Low Wind Speed Turbine Project Phase II: The application of Medium-Voltage Electrical Apparatus to the Class of Variable Speed Multi-Megawatt Low Wind Speed Turbines. NREL. April 2005.
- [58] E. Levi, "Impact of iron loss on behavior of vector controlled induction machines," *IEEE Trans. Ind. Applicat.*, vol. 31, no. 6, pp. 1287-1296, Dec., 1995.
- [59] K. B. Lee, J-H. Song, I. Choy and J-Y. Yoo, "Improvement of Low-Speed Operation Performance of DTC for Three-Level Inverter-Fed Induction Motors," *IEEE Trans. Ind. Electron.*, vol. 48, no. 5, pp. 255-264, Oct. 2001.
- [60] J. Pou, D. Boroyevich, R. Pindado, "New Feedforward Space-Vector PWM Method to Obtain Balanced AC Output Voltages in a Three-Level Neutral-Point-Clamped Converter," *IEEE Trans. Ind. Electron.* vol. 49, no. 5, pp. 1026-1034, Oct. 2002.
- [61] T.K.A. Brekken, N. Mohan, "Control of a Doubly Fed Induction Wind Generator Under Unbalanced Grid Voltage Conditions" *IEEE Trans. Ener. Conv.* vol. 22, no. 1, pp. 129-135, Mar. 2007.
- [62] P. Rodriguez, A.V. Timbus, R. Teodorescu, M. Liserre, F. Blaabjerg, "Flexible Active Power Control of Distributed Power Generation Systems During Grid Faults" *IEEE Trans. Ind. Electron.* vol. 54, no. 5, pp. 2583 - 2592, Oct. 2007.
- [63] J. E-G. Carrasco, "Control directo de potencia de convertidores conectados a la red" Ph.D. Universidad Carlos III, Madrid, 2007.
- [64] C. L. Fortescue, "Method of Symmetrical Coordinates Applied to the Solution of Polyphase Networks," *Transactions AIEE*, vol. 37, pp. 1.27-1140, 1918.

